

CHARACTERIZATION AND OPTIMIZATION OF CdZnTe
FRISCH COLLAR GAMMA-RAY SPECTROMETERS AND
THEIR DEVELOPMENT IN AN ARRAY OF DETECTORS

by

ALIREZA KARGAR

M.S., Kansas State University, Manhattan, Kansas, 2003

AN ABSTRACT OF A DISSERTATION

submitted in partial fulfillment of the
requirements for the degree

DOCTOR OF PHILOSOPHY

Department of Mechanical and Nuclear Engineering
College of Engineering

KANSAS STATE UNIVERSITY

Manhattan, Kansas

2009

Abstract

Cadmium Zinc Telluride (CdZnTe) has been used for many applications, such as medical imaging and astrophysics, since its first demonstration as a room temperature operating gamma-ray detector in 1992. The wide band gap, high effective Z-number and high resistivity of CdZnTe make it a good candidate for use as a room temperature operated detector with good absorption efficiency, while maintaining a low bulk leakage current at high electric fields. Nevertheless, the low mobility lifetime products $\mu\tau$ of holes in CdZnTe makes detectors position sensitive, unless advanced detector designs are employed. Among those designs is the *Frisch collar* technology which turns the detector into a *single carrier* device by negating the degrading effects of hole trapping and low mobility. The superiority of the Frisch collar technology over other methods include its inexpensive associated electronics and straight forward fabrication process.

The main objective of this research study is to develop a large volume gamma-ray detector with an array of individual CdZnTe Frisch collar gamma-ray spectrometers while still using a single readout. Several goals were to be accomplished prior to the main objective. One goal is to develop a reliable low cost method to fabricate bulk CdZnTe crystals into Frisch collar detectors. Another goal was to investigate the limitations of crystal geometry and the crystal electrical properties to obtain the best spectroscopic performance from CdZnTe Frisch collar detectors. Still another goal was to study all other external parameters such as the collar length, anode to cathode ratio, the insulator thickness and applied voltage on performance of CdZnTe Frisch collar detectors. The final goal was to construct the CdZnTe Frisch collar devices into an array and to show its feasibility of being used for large volume detector.

CHARACTERIZATION AND OPTIMIZATION OF CdZnTe
FRISCH COLLAR GAMMA-RAY SPECTROMETERS AND
THEIR DEVELOPMENT IN AN ARRAY OF DETECTORS

by

ALIREZA KARGAR

M.S., Kansas State University, Manhattan, Kansas, 2003

A DISSERTATION

submitted in partial fulfillment of the
requirements for the degree

DOCTOR OF PHILOSOPHY

Department of Mechanical and Nuclear Engineering
College of Engineering

KANSAS STATE UNIVERSITY
Manhattan, Kansas
2009

Approved by:

Major Professor
Dr. Douglas S. McGregor

Abstract

Cadmium Zinc Telluride (CdZnTe) has been used for many applications, such as medical imaging and astrophysics, since its first demonstration as a room temperature operating gamma-ray detector in 1992. The wide band gap, high effective Z-number and high resistivity of CdZnTe make it a good candidate for use as a room temperature operated detector with good absorption efficiency, while maintaining a low bulk leakage current at high electric fields. Nevertheless, the low mobility lifetime products $\mu\tau$ of holes in CdZnTe makes detectors position sensitive, unless advanced detector designs are employed. Among those designs is the *Frisch collar* technology which turns the detector into a *single carrier* device by negating the degrading effects of hole trapping and low mobility. The superiority of the Frisch collar technology over other methods include its inexpensive associated electronics and straight forward fabrication process.

The main objective of this research study is to develop a large volume gamma-ray detector with an array of individual CdZnTe Frisch collar gamma-ray spectrometers while still using a single readout. Several goals were to be accomplished prior to the main objective. One goal is to develop a reliable low cost method to fabricate bulk CdZnTe crystals into Frisch collar detectors. Another goal was to investigate the limitations of crystal geometry and the crystal electrical properties to obtain the best spectroscopic performance from CdZnTe Frisch collar detectors. Still another goal was to study all other external parameters such as the collar length, anode to cathode ratio, the insulator thickness and applied voltage on performance of CdZnTe Frisch collar detectors. The final goal was to construct the CdZnTe Frisch collar devices into an array and to show its feasibility of being used for large volume detector.

Table of Contents

Table of Contents	v
List of Figures	ix
List of Tables	xvi
Acknowledgements	xviii
Dedication	xix
1 INTRODUCTION	1
1.1 Gamma-Ray Detection	1
1.2 CdZnTe Detectors	2
1.3 Research Objectives	3
2 BACKGROUND OF CdZnTe FRISCH COLLAR DEVICES AND THE PRESENT RESEARCH	6
2.1 Previous Work on Frisch Collar Devices	6
2.2 The Present Work on Frisch Collar Devices	10
3 THEORETICAL CONSIDERATIONS	13
3.1 Induced Charge and Induced Current	13
3.1.1 Green's reciprocity theorem and induced charge	13
3.1.2 The definition of potential, weighting potential, electric field, weighting field and Shockley-Ramo theorem	15
3.1.2.1 Potential and electric field	15
3.1.2.2 Weighting potential and weighting field	16
3.1.2.3 Shockley-Ramo theorem	17
3.1.3 Charge collection efficiency	18
3.1.3.1 Charge collection efficiency for a two-terminal CdZnTe Frisch collar device	19
3.1.3.2 Validity of charge collection efficiency model	25
3.2 Parameters Affecting Charge Collection Efficiency	27
3.2.1 Effect of weighting potential/field distribution on CCE	28
3.2.1.1 Crystal geometry	33
3.2.1.2 Frisch collar length	39
3.2.1.3 Ratio of anode area to cathode area, small pixel effect	41
3.2.1.4 Thickness of insulator/dielectric layer	43

3.2.2	Effect of CdZnTe electrons/holes mobility-lifetime product on CCE	47
3.2.3	Effect of applied voltage (bias) on CCE	50
3.2.4	Effect of crystal length on CCE	52
4	EXPERIMENTAL PROCEDURES AND SETUP, CdZnTe DEVICE FAB- RICATION AND CHARACTERIZATION	54
4.1	CdZnTe Detector Fabrication Process	54
4.1.1	Mechanical treatment	55
4.1.2	Chemical etching	57
4.1.3	Contact deposition	57
4.1.4	Applying insulator and Frisch collar to planar device	58
4.2	CdZnTe Detector Characterization Methods	59
4.2.1	Leakage current measurement	59
4.2.2	Pulse height spectra measurements	60
4.2.3	Charge collection efficiency measurement	62
4.2.4	Surface analysis	65
4.3	Investigating Parameters Affecting CdZnTe Frisch Collar Device Performance	66
4.3.1	Effect of crystal aspect ratio on performance of CdZnTe Frisch collar devices	66
4.3.1.1	Device designs	66
4.3.1.2	Device preparation	67
4.3.1.3	Device testing: spectral measurement	68
4.3.2	Effect of insulator layer thickness on performance of CdZnTe Frisch collar devices	69
4.3.2.1	Device designs and preparation	69
4.3.2.2	Device testing: current-voltage characteristic and spectral measurement	70
4.3.3	Effect of high voltage on performance of CdZnTe Frisch collar devices	72
4.3.4	Effect of crystal length on performance of CdZnTe Frisch collar de- vices; experimental procedures and setups	72
4.3.5	Post fabrication process: surface treatment (passivation)	74
4.3.5.1	Device fabrication	76
4.3.5.2	Post fabrication process 1: Mechanical	76
4.3.5.3	Post fabrication process 2: Chemical	77
4.3.5.4	Post fabrication process 3: Ion-mill	78
4.4	Angular Dependency of the Collimated CdZnTe Detector	78
4.4.1	Two-dimensional assembly	78
4.4.2	Setup arrangement for directional sensitivity of the collimated CdZnTe Frisch collar device	90
4.4.2.1	Device preparations	90
4.4.2.2	Device collimator alignment	90
4.4.2.3	Gold sample preparation	91

4.4.2.4	Collecting data for directional sensitivity of collimated CdZnTe Frisch collar devices	93
4.5	Array of CdZnTe Frisch Collar Detectors and the Corresponding Readout Electronics	94
5	RESULTS AND DISCUSSION	98
5.1	Primary Results of Gamma-Ray Spectroscopy with CdZnTe Detectors	98
5.2	Charge Collection Efficiency Measurement Results and the Effect of High Voltage on CCE	103
5.3	Investigating Parameters Affecting Device Performance	113
5.3.1	Frisch Collar Geometry Effect Results	113
5.3.1.1	Spectral testing results for the Frisch collar geometry effect	113
5.3.2	Results of insulator layer thickness effect on performance of the CdZnTe Frisch collar devices	118
5.3.2.1	Current-voltage characteristic measurement results for devices used for the insulator layer thickness effect	118
5.3.2.2	Spectral testing results for devices with different insulator layer thicknesses	119
5.3.3	Results of crystal length on performance of the CdZnTe Frisch collar devices	128
5.3.4	Post fabrication surface treatment results	129
5.3.4.1	Mechanical treatment results	131
5.3.4.2	Chemical treatment results	133
5.3.4.3	Ion milling results	138
5.3.4.4	Surface characterization results	139
5.3.4.5	Post fabrication surface treatment discussions	140
5.4	CdZnTe Device Efficiency Calculations	143
5.5	Angular Response of W-Collimated CdZnTe Frisch Collar Device Results	149
5.5.1	Angular Response Results	149
5.6	Spectral Results of Array of CdZnTe Detectors	154
5.6.1	Gamma-Ray Response of Array of 16 CdZnTe Detectors	154
6	SUMMARY AND CONCLUSIONS	160
6.1	Summary	160
6.1.1	Optimizing the Two-Terminal CdZnTe Frisch Collar Device to Enhance Induced Charge	161
6.1.2	Fabrication Enhancement	163
6.2	Conclusions	164
6.3	Future Work	164
A	Source of the FORTRAN code for charge collection efficiency simulation	176

B The CdZnTe Frisch Collar Detectors Fabricated at Kansas State University and Used in the Array of Detectors at Brookhaven National Laboratory

180

List of Figures

1.1	Array of collimated Frisch collar detectors.	4
1.2	Array of non-collimated Frisch collar detectors.	5
2.1	The different designs of Frisch collar	8
3.1	Green's Reciprocation Theorem for three electrodes	14
3.2	Shockley-Ramo theorem applied to charge Q_0 on a certain path for a two-terminal system of electrodes	21
3.3	Applying Shockley-Ramo theorem to a two-dimensional Frisch collar device.	22
3.4	The charge collection efficiency CCE profile for a 10.0 mm long planar device at 1000V based on Hecht relation	26
3.5	The charge collection efficiency CCE profile for a 10.0 mm long planar device at 1000V based on the model in Section 3.1.3.1	27
3.6	The weighting potential and weighting field distributions for a $4.7 \times 4.7 \times 9.5 \text{ mm}^3$ CdZnTe device along the central axis (Frisch collar and planar).	29
3.7	The charge collection efficiency CCE profile at 1000V applied to anode for a $4.7 \times 4.7 \times 9.5 \text{ mm}^3$ CdZnTe device along the central axis (Frisch collar and planar).	30
3.8	Pulse height spectra taken with a $4.7 \times 4.7 \times 9.5 \text{ mm}^3$ CdZnTe device from a ^{137}Cs gamma-ray source.	31
3.9	Sample devices for Frisch collar geometry effect study.	34
3.10	The weighting potential profile for Frisch collar CZT1 (19.08 mm \times 19.34 mm \times $L=4.95$ mm)	35
3.11	The weighting potential profile for Frisch collar CZT5 (9.44 mm \times 9.45 mm \times $L=4.88$ mm)	35
3.12	The weighting potential profile for Frisch collar CZT6 (6.65 mm \times 6.89 mm \times $L=4.84$ mm)	36
3.13	The weighting potential profile for Frisch collar CZT7 (5.05 mm \times 5.02 mm \times $L=4.84$ mm)	36
3.14	The weighting potential profile for Frisch collar CZT8 (4.03 mm \times 4.00 mm \times $L=4.76$ mm)	37
3.15	The weighting potential profile for Frisch collar CZT9 (3.51 mm \times 3.51 mm \times $L=4.76$ mm)	37
3.16	The weighting potential profile for Frisch collar CZT10 (2.90 mm \times 2.90 mm \times $L=4.60$ mm)	38
3.17	The weighting potential profile for Frisch collar CZT11 (2.40 mm \times 2.40 mm \times $L=4.60$ mm)	38

3.18	The weighting potential distribution for a $4.7 \times 4.7 \times 9.5 \text{ mm}^3$ CdZnTe Frisch collar device (with $AR=L/W = 2.0$) along the central axis with different collar lengths.	39
3.19	The weighting field distribution for a $4.7 \times 4.7 \times 9.5 \text{ mm}^3$ CdZnTe Frisch collar device (with $AR=L/W = 2.0$) along the central axis with different collar lengths.	40
3.20	The charge collection efficiency <i>CCE</i> profile for a $4.7 \times 4.7 \times 9.5 \text{ mm}^3$ CdZnTe Frisch collar device (with $AR=L/W = 2.0$) along the central axis with different collar lengths.	41
3.21	The weighting potential distribution for a $5.0 \times 5.0 \times 5.0 \text{ mm}^3$ CdZnTe Frisch collar device (with $AR=L/W = 1.0$) along the central axis with different anode areas.	42
3.22	The weighting field distribution for a $5.0 \times 5.0 \times 5.0 \text{ mm}^3$ CdZnTe Frisch collar device (with $AR=L/W = 1.0$) along the central axis with different anode areas.	43
3.23	The charge collection efficiency <i>CCE</i> profile for a $5.0 \times 5.0 \times 5.0 \text{ mm}^3$ CdZnTe Frisch collar device (with $AR=L/W = 1.0$) along the central axis with different anode areas.	44
3.24	The weighting potential distribution for a $4.7 \times 5.0 \times 19.6 \text{ mm}^3$ CdZnTe Frisch collar device (with average aspect ratio $L/W = 4.0$) along the central axis with different insulator thicknesses.	45
3.25	The weighting field distribution for a $4.7 \times 5.0 \times 19.6 \text{ mm}^3$ CdZnTe Frisch collar device (with average aspect ratio $L/W = 4.0$) along the central axis with different insulator thicknesses.	46
3.26	The charge collection efficiency <i>CCE</i> profile for a $4.7 \times 5.0 \times 19.6 \text{ mm}^3$ CdZnTe Frisch collar device (with average aspect ratio $L/W = 4.0$) along the central axis with different insulator layer thicknesses.	47
3.27	The charge collection efficiency <i>CCE</i> profile for a $4.7 \times 4.7 \times 9.5 \text{ mm}^3$ CdZnTe Frisch collar device (with $AR=L/W = 2.0$) along the central axis with different values for holes mobility-lifetime product $\mu_h \tau_h$	48
3.28	The charge collection efficiency <i>CCE</i> profile for a $4.7 \times 4.7 \times 9.5 \text{ mm}^3$ CdZnTe Frisch collar device (with $AR=L/W = 2.0$) along the central axis with different values for electron mobility-lifetime product $\mu_e \tau_e$	49
3.29	The charge collection efficiency <i>CCE</i> profile for a $4.7 \times 4.7 \times 9.5 \text{ mm}^3$ CdZnTe Frisch collar device (with $AR=L/W = 2.0$) along the central axis at different applied voltages.	50
3.30	The weighting potential distribution along the central axis of CdZnTe Frisch collar devices with the same aspect ratios ($L/W = 1.8$) and different lengths.	52
3.31	The charge collection efficiency <i>CCE</i> profile along the central axis of CdZnTe Frisch collar devices with the same aspect ratios ($L/W = 1.8$) and different lengths	53
4.1	The stainless steel block and the L-shaped stainless steel jig.	55

4.2	Lapping/grinding the CdZnTe	56
4.3	Polishing CdZnTe crystals on polishing pads	56
4.4	Contact deposition on CdZnTe crystals using gold chloride solution.	57
4.5	Fabricated CdZnTe Frisch collar detectors	58
4.6	Diagram of the spectral measurements aluminum test box.	60
4.7	Copper Faraday cage and the NIM electronics	61
4.8	The schematic setup for the gamma-ray source, Pb-collimator, and the $4.7 \times 4.7 \times 9.5$ mm ³ CdZnTe Frisch collar detector for the <i>CCE</i> measurement.	63
4.9	The irradiated points on the $4.7 \times 4.7 \times 9.5$ mm ³ CdZnTe Frisch collar device for the <i>CCE</i> measurement.	64
4.10	The lead collimator-detector setup within the aluminum test box for the <i>CCE</i> measurement.	64
4.11	The devices' aspect ratio L/W is kept unchanged by shortening the device sizes.	73
4.12	Diagram of two-dimensional model for the detector-collimator configuration.	79
4.13	Diagram of two-dimensional model for detector-collimator-source positions showing the two critical angles and the source position.	80
4.14	Diagram of two-dimensional model for detector-collimator-source position while the source is in region 1.	81
4.15	Diagram of two-dimensional model for detector-collimator-source position while the source is in region 2.	82
4.16	Diagram of two-dimensional model for detector-collimator-source position while the source is in region 3.	83
4.17	The CdZnTe detector and the virtual CdZnTe detector.	86
4.18	The aluminum test stage inside the Faraday cage.	91
4.19	The aluminum test box with the 4 cm long tungsten collimator.	92
4.20	The 4 cm long tungsten collimator and the CdZnTe detector.	92
4.21	CdZnTe Frisch collar detector fabricated at S.M.A.R.T. laboratory at KSU.	94
4.22	An array of 16-CdZnTe Frisch collar detectors.	95
4.23	An array of 16-CdZnTe Frisch collar detectors, before and after gluing the cathode connections.	95
4.24	The preamplifier board for the array of 16 CdZnTe Frisch collar detectors.	96
4.25	Close view of preamplifier board with two CdZnTe detector modules.	96
4.26	The two detector modules with the preamplifier board in a test box.	97
5.1	Room temperature spectra of a ²⁴¹ Am source from the 3.4mm \times 3.4mm \times 5.7mm CdZnTe semiconductor detector.	99
5.2	Room temperature spectra of a ⁵⁷ Co source from the 3.4mm \times 3.4mm \times 5.7mm CdZnTe semiconductor detector.	99
5.3	Room temperature spectra of a ¹³³ Ba source from the 3.4mm \times 3.4mm \times 5.7mm CdZnTe semiconductor detector at low energies.	100
5.4	Room temperature spectra of a ¹³³ Ba source from the 3.4mm \times 3.4mm \times 5.7mm CdZnTe semiconductor detector at high energies.	101

5.5	Room temperature spectra of a ^{198}Au source from the $3.4\text{mm} \times 3.4\text{mm} \times 5.7\text{mm}$ CdZnTe semiconductor detector at high energies.	101
5.6	Room temperature spectra of a ^{137}Cs source from the $3.4\text{mm} \times 3.4\text{mm} \times 5.7\text{mm}$ CdZnTe semiconductor detector at high energies.	102
5.7	Room temperature spectra of a ^{235}U source from the $3.4\text{mm} \times 3.4\text{mm} \times 5.7\text{mm}$ CdZnTe semiconductor detector at high energies.	103
5.8	Pulse height spectra collected from a collimated ^{137}Cs gamma-ray source with the $4.7 \times 4.7 \times 9.5 \text{ mm}^3$ CdZnTe Frisch collar device along row- r at 1200V.	104
5.9	Pulse height spectra collected from a collimated ^{137}Cs gamma-ray source with the $4.7 \times 4.7 \times 9.5 \text{ mm}^3$ CdZnTe Frisch collar device along row- v at 1200V.	104
5.10	Pulse height spectra collected from a collimated ^{137}Cs gamma-ray source with the $4.7 \times 4.7 \times 9.5 \text{ mm}^3$ CdZnTe Frisch collar device along row- t at 1200V for two hours real time.	105
5.11	Pulse height spectra collected from a collimated ^{137}Cs gamma-ray source with the $4.7 \times 4.7 \times 9.5 \text{ mm}^3$ CdZnTe Frisch collar device.	105
5.12	Pulse height spectra collected from a collimated ^{137}Cs gamma-ray source with the $4.7 \times 4.7 \times 9.5 \text{ mm}^3$ CdZnTe Frisch collar device along row- t at 1000V for one hour real time.	106
5.13	Pulse height spectra collected from a collimated ^{137}Cs gamma-ray source with the $4.7 \times 4.7 \times 9.5 \text{ mm}^3$ CdZnTe Frisch collar device along row- t at 800V for one hour real time.	106
5.14	Pulse height spectra collected from a collimated ^{137}Cs gamma-ray source with the $4.7 \times 4.7 \times 9.5 \text{ mm}^3$ CdZnTe Frisch collar device along row- t at 600V for one hour real time.	107
5.15	Pulse height spectra collected from a collimated ^{137}Cs gamma-ray source with the $4.7 \times 4.7 \times 9.5 \text{ mm}^3$ CdZnTe Frisch collar device along row- t at 400V for one hour real time.	107
5.16	The peak channel of photopeak for the irradiated points of the $4.7 \times 4.7 \times 9.5 \text{ mm}^3$ CdZnTe Frisch collar device probed with a highly collimated gamma-ray source of ^{137}Cs along row- r , row- t and row- v at 1200V.	108
5.17	The peak channel of photopeak for the irradiated points of the $4.7 \times 4.7 \times 9.5 \text{ mm}^3$ CdZnTe Frisch collar device probed with a highly collimated gamma-ray source of ^{137}Cs along row- t at voltages of 1200V, 1000V, 800V, 600V and 400V.	108
5.18	The CCE profile at 1200V applied to the anode (collecting electrode) along the central line of the $4.7 \times 4.7 \times 9.5 \text{ mm}^3$ CdZnTe Frisch collar device and the normalized peak channel of photopeak.	110
5.19	The CCE profile at 1000V applied to the anode (collecting electrode) along the central line of the $4.7 \times 4.7 \times 9.5 \text{ mm}^3$ CdZnTe Frisch collar device and the normalized peak channel of photopeak.	110
5.20	The CCE profile at 800V applied to the anode (collecting electrode) along the central line of the $4.7 \times 4.7 \times 9.5 \text{ mm}^3$ CdZnTe Frisch collar device and the normalized peak channel of photopeak.	111

5.21	The CCE profile at 600V applied to the anode (collecting electrode) along the central line of the $4.7 \times 4.7 \times 9.5 \text{ mm}^3$ CdZnTe Frisch collar device and the normalized peak channel of photopeak.	111
5.22	The CCE profile at 400V applied to the anode (collecting electrode) along the central line of the $4.7 \times 4.7 \times 9.5 \text{ mm}^3$ CdZnTe Frisch collar device and the normalized peak channel of photopeak.	112
5.23	Pulse height spectra collected from CZT1 using a ^{137}Cs source	114
5.24	Pulse height spectra collected from CZT1 using a ^{241}Am source	114
5.25	Pulse height spectra collected from CZT1 using a ^{137}Cs source	115
5.26	Pulse height spectra collected from CZT11 using a ^{241}Am source	115
5.27	Normalized pulse height spectra collected from devices using an ^{137}Cs source	116
5.28	Normalized pulse height spectra collected from devices using an ^{241}Am source	116
5.29	The current-voltage (IV) characteristic curves of Device 1 through Device 6 in planar configurations for the insulator layer thickness effect.	118
5.30	The pulse height spectra of Device 1 ($4.95 \times 4.76 \times L=4.87 \text{ mm}^3$) taken with standard gamma-ray source of ^{137}Cs	119
5.31	The pulse height spectra of Device 2 ($4.70 \times 4.56 \times L=6.03 \text{ mm}^3$) taken with a standard ^{137}Cs gamma-ray source.	120
5.32	The pulse height spectra of Device 3 ($3.36 \times 3.34 \times L=5.68 \text{ mm}^3$) taken with a standard ^{137}Cs gamma-ray source.	120
5.33	The pulse height spectra of Device 4 ($3.96 \times 4.01 \times L=11.60 \text{ mm}^3$) taken with standard ^{137}Cs gamma-ray source.	122
5.34	The pulse height spectra of Device 4 taken with a standard ^{137}Cs gamma-ray source.	122
5.35	The pulse height spectra of Device 5 ($3.92 \times 3.89 \times L=10.82 \text{ mm}^3$) taken with a standard ^{137}Cs gamma-ray source.	123
5.36	The pulse height spectra of Device 5, taken with a standard ^{137}Cs gamma-ray source, for specific dielectric thicknesses.	123
5.37	The pulse height spectra of Device 6 ($5.01 \times 4.73 \times L=19.63 \text{ mm}^3$) taken with a standard ^{137}Cs gamma-ray source.	124
5.38	The pulse height spectra of Device 6, taken with a standard ^{137}Cs gamma-ray source, for specific dielectric thicknesses.	125
5.39	The electric field distribution for Device 4 in Frisch collar configurations along the central axis.	126
5.40	The operating and weighting potential distributions for Device 4 in Frisch collar configurations along the central axis.	127
5.41	The normalized pulse height spectra of Frisch collar Device <i>i</i> , Device <i>ii</i> and Device <i>iii</i> (with the same aspect ratio of 1.8 and different lengths) taken with a standard ^{137}Cs gamma-ray source.	128
5.42	The pulse height spectra of Frisch collar Device <i>ii</i> and Device <i>iii</i> (with the same aspect ratio of 1.8 and different lengths) taken with a standard ^{137}Cs gamma-ray source.	129
5.43	The detector-preamplifier circuit.	130

5.44	Results collected from Detector 1 ($4.75 \times 4.78 \times 9.22 \text{ mm}^3$) showing the current-voltage (I-V) characteristic curves for planar configurations.	131
5.45	Results collected from Detector 1 ($4.75 \times 4.78 \times 9.22 \text{ mm}^3$) showing the pulse height spectra using a ^{137}Cs source.	132
5.46	Results collected from Detector 2 ($5.00 \times 4.55 \times 9.21 \text{ mm}^3$) showing the current-voltage (I-V) characteristic curves for planar configurations.	134
5.47	Results collected from Detector 2 ($5.00 \times 4.55 \times 9.21 \text{ mm}^3$) showing the pulse height spectra using a ^{137}Cs source.	134
5.48	Results collected from Detector 3 ($4.95 \times 4.54 \times 9.22 \text{ mm}^3$) showing the current-voltage (I-V) characteristic curves for planar configurations.	135
5.49	Results collected from Detector 3 ($4.95 \times 4.54 \times 9.22 \text{ mm}^3$) showing the pulse height spectra using a ^{137}Cs source.	135
5.50	Results collected from Detector 4 ($4.97 \times 4.50 \times 9.24 \text{ mm}^3$) showing the current-voltage (I-V) characteristic curves for planar configurations.	136
5.51	Results collected from Detector 4 ($4.97 \times 4.50 \times 9.24 \text{ mm}^3$) showing the pulse height spectra using a ^{137}Cs source.	136
5.52	Results collected from Detector 5 ($5.00 \times 4.56 \times 9.23 \text{ mm}^3$) showing the current-voltage (I-V) characteristic curves for planar configurations.	137
5.53	Results collected from Detector 5 ($5.00 \times 4.56 \times 9.23 \text{ mm}^3$) showing the pulse height spectra using a ^{137}Cs source.	137
5.54	Results collected from Detector 6 ($4.92 \times 4.98 \times 9.82 \text{ mm}^3$) showing the current-voltage (I-V) characteristic curves for planar configurations.	138
5.55	Results collected from Detector 6 ($4.92 \times 4.98 \times 9.82 \text{ mm}^3$) showing the pulse height spectra using a ^{137}Cs source.	139
5.56	The solid angle between a point isotropic source and a CdZnTe bar detector with a rectangular aperture with the source aligned along the center of the detector.	144
5.57	Room temperature spectrum from standard radiation source of ^{137}Cs taken with the $3.4 \times 3.4 \times 5.7 \text{ mm}^3$ CdZnTe semiconductor Frisch collar detector.	146
5.58	Room temperature spectrum from standard radiation source of ^{133}Ba taken with the $3.4 \times 3.4 \times 5.7 \text{ mm}^3$ CdZnTe semiconductor Frisch collar detector.	146
5.59	Room temperature spectrum from standard radiation source of ^{57}Co taken with the $3.4 \times 3.4 \times 5.7 \text{ mm}^3$ CdZnTe semiconductor Frisch collar detector.	147
5.60	Room temperature spectrum from standard radiation source of ^{241}Am taken with the $3.4 \times 3.4 \times 5.7 \text{ mm}^3$ CdZnTe semiconductor Frisch collar detector.	147
5.61	The measured CdZnTe Frisch collar detector full energy peak intrinsic efficiency at different gamma-ray energies.	148
5.62	Room-temperature spectra of ^{198}Au gamma-ray emissions from the $3.4 \times 3.4 \times 5.8 \text{ mm}^3$ CdZnTe semiconductor detector inside the 8 cm long tungsten collimator at three different sourcedetector angles.	149
5.63	The experimental angular dependency of net photopeak counts from ^{198}Au for the 4 and 8 cm long tungsten collimators.	152

5.64	The experimental and theoretical angular dependency of net photopeak counts from ^{198}Au gamma-ray sources using the 4 cm long tungsten collimators. . .	153
5.65	The experimental and theoretical angular dependency of net photopeak counts from ^{198}Au gamma-ray sources using the 8 cm long tungsten collimators. . .	153
5.66	Individual responses of 32 CdZnTe Frisch collar detectors (two arrays of 4x4 device) to an uncollimated ^{137}Cs source.	155
5.67	Individual responses of 32 CdZnTe Frisch collar detectors (two arrays of 4x4 device) to an uncollimated ^{241}Am source.	156
5.68	Individual responses of 32 CdZnTe Frisch collar detectors (two arrays of 4x4 device) to an uncollimated ^{133}Ba source.	157
5.69	Overall responses of 16 detectors (one array of 4x4 device) to ^{137}Cs source. .	158
5.70	Overall responses of 16 detectors (one array of 4x4 device) to ^{133}Ba source. .	158
5.71	Overall responses of 16 detectors (one array of 4x4 device) to ^{241}Am source.	159

List of Tables

3.1	CdZnTe devices with the same length L and different aspect ratios L/W . . .	33
4.1	The operating voltage applied to the detectors and the spectral testing time for the Frisch collar geometry effect study.	67
4.2	The device names and dimensions to study the effect of insulator layer thickness on performance of CdZnTe Frisch collar devices.	69
4.3	The insulator layer thickness for Device 1 to Device 6.	70
4.4	The experimental setup to study the effect of insulator layer thickness on the performance of CdZnTe Frisch collar devices.	71
4.5	The device names, dimensions, and the experimental setup to study the effect of device length on performance of CdZnTe Frisch collar devices.	73
4.6	CdZnTe devices' names, dimensions, and surface treatment methods.	75
4.7	Post fabrication process 1: Mechanical treatment and the technique applied to the lateral surface of Detector 1.	77
5.1	The FWHM and peak-to-valley of collected spectra with Device 4 and Device 5.	121
5.2	The FWHM and peak-to-valley of collected spectra with Device 6.	124
5.3	Summary of energy resolution, peak-to-valley, and maximum leakage current for Detector 2 after each surface treatment.	132
5.4	Summary of FWHM energy resolution, peak-to-valley, and maximum leakage current for Detector 2 through Detector 5.	133
5.5	EDS results of the atomic concentration from EMP technique.	140
5.6	Devices' total resistance and surface resistance for Detector 1 through Detector 6.	142
5.7	Summary of the values to determine the intrinsic full energy peak efficiency.	148
5.8	The net counts in the full energy peak obtained from ^{198}Au sources at different source-detector angles with the 8 cm long tungsten collimator.	150
5.9	The net counts in the full energy peak obtained from ^{198}Au sources at different source-detector angles with the 4 cm long tungsten collimator.	151

Acknowledgments

I would like to gratefully acknowledge and express my deep appreciation to Professor Douglas McGregor for his efforts, enthusiasm, trust, encouragement, mentoring and guidance during my Ph.D. studies at Kansas State University. He provided me with the opportunity to grow as a researcher. In fact, none of this work would have been possible without his patience, tolerance and technical support. This dissertation is a part of the research carried out under his direction throughout the completion of this degree.

Many thanks to the sponsors of this research project and for providing the financial and technical support of this research project. This work was funded in part by the U.S. Department of Energy through NEER Grants DE-FG07-03ID14498 and DE-FG07-04ID14599, and by Brookhaven National laboratory.

I wish to extend my appreciation to my other committee members: Dr. Ken Shultis, who always had some challenging questions, and also for his support, inspiration and great assistance to me during the period of my graduate study; Dr. William Dunn, who always provided me great opportunities to enhance my technical skills and knowledge; and Drs. Chris L. Lewis and Medhat M. Morcos, for their insight and patience in reading and editing my thesis.

I would like to thank Dr. Henry Chen of Redlen Technologies for providing spectroscopy grade CdZnTe materials to this project. I owe Dr. Aleksey Bolotnikov of Brookhaven National laboratory (BNL) many thanks for taking the data with the array of CdZnTe Frisch collar detector presented at the end of Chapter 5.

Many thanks to all my colleagues at S.M.A.R.T. laboratory at KSU for their support, inspiration and great assistance to me, not only technically but also personally. They all have taught me many things. I appreciate all their friendships and collective encouragement to learn. Especially, I would like to thank Adam Brooks, Dr. Mark Harrison (University of Florida), Walter McNeil, Elsa Ariesanti, Martin Ohmes, Andrew Jones, Chris Ward, Adam

Graebner, Rans Lowell, Kyle Kohman and Roger Keyes for sharing their technical wisdom, willingness to help me, practical advice and contributions to this project.

Finally I would like to thank my parents and family members for their constant encouragements, continued support, and faith in me. My most heartfelt acknowledgment goes to my wife Faranak, whose patience, companionship, understanding and love has turned my journey through graduate school into a pleasure. And of course my unconditional love to my son Neakon, born on October 6, 2004, whose arrival coincided with the early preparation of this research study.

Dedication

This dissertation is dedicated to my parents:

Mohammad Kargar

and

Nahideh Sameie

Chapter 1

INTRODUCTION

1.1 Gamma-Ray Detection

While experimenting with Lenard and Crookes tubes, Wilhelm Conrad Röntgen, a German physicist, produced and detected X-rays for the first time in 1896. He was rewarded for his discovery with the first ever Nobel Prize in physics in 1901. While studying radiation emitted from radium, Paul Villard discovered γ -ray (gamma-ray) in 1900. In 1903 Rutherford named this radiation discovered by Villard's as gamma-rays. Röntgen [1] observed small ionization while measuring the electric conductivity of quartz and mica in 1913 and later the influence of radiation on the electric conductivity of certain crystals. Later, Jaffé [2] (1932) systematically investigated the observation of radiation in solids, and further summarized and documented the work done by previous scientists including Röntgen and Joffé. In particular, Jaffé [2], in a series of experiments with thin sheets of mica and quartz, observed that the current passing through crystal biased with a high electric field is noticeably altered by α -rays.

Despite early discoveries, no significant achievement in developing solid state radiation detectors occurred until 1945, when Van Heerden introduced AgCl in his PhD dissertation: The Crystal Counter. Heerden detected α particles emitted by ^{210}Po with the first semiconductor detector, AgCl, while the detector was cooled at low temperatures. Subsequently, the first room temperature operated γ -ray detector was successfully tested by Harding in

1960 using GaAs crystals as detecting medium [3]. Later in 1967, Akutagawa showed the first CdTe room temperature gamma-ray detector [4].

1.2 CdZnTe Detectors

Cadmium zinc telluride (CdZnTe) as a room-temperature operated gamma-ray detector was first introduced in 1992 [5]. Since then, CdZnTe has shown great promise for many applications such as medical imaging, industrial tomography, and astrophysics. Room temperature detectors are widely used for gamma-ray spectroscopy in nondestructive analysis of nuclear materials, portable applications and field surveys [6–8]. Due to $\text{Cd}_{1-x}\text{Zn}_x\text{Te}$'s relatively wide band gap (about 1.55 eV, depending on Zn concentration x), it is a good candidate for a room temperature operated detectors. This characteristic makes the CdZnTe devices so demandable which facilitate the detector to operate well without complicated cryocooling systems to cool the detectors to liquid nitrogen temperature. Also, the material's high resistivity (about $1.0 \times 10^{11} \Omega \text{ cm}$) provides a low bulk leakage current while operating in high electric field (or bias), which subsequently decreases the effect of noise. Additionally, the high atomic number Z of Cd ($Z_{\text{Cd}}=48$) and Te ($Z_{\text{Te}}=52$), makes the fabricated CdZnTe detector a remarkable gamma-ray absorption medium. The high Z (average) and high resistivity, along with the wide band gap, of CdZnTe material make it a good candidate for gamma-ray spectroscopy. The material, however, suffers from low mobility-lifetime products $\mu\tau$ of charge carriers, especially for holes. Thus, the energy resolution of planar CdZnTe devices is degraded by poor charge-carrier transport properties (CdZnTe hole mobility μ and lifetime τ , are generally poor).

Researchers have presented various methods to improve the energy resolution of CdZnTe devices. These methods are the small pixel effect [9], co-planar grids [10], geometric weighting, and the Frisch collar effect [11–13], all of which generally concentrate on negating the degrading effects of hole trapping and low mobility. All approaches are based on minimizing the effect of poor mobility-lifetime product $\mu\tau$ of the holes by modifying the device

design and electrode configuration (rather than making external corrections), and turning the detector into a *single carrier* device.

However, the Frisch collar technique is superior to the others, due to its robustness, low cost and simplicity. Frisch collar spectrometers [11, 12, 14–25] are one of the most promising types of single carrier devices that are easy to fabricate and require simple, commercially available readout electronics. Other types of single carrier devices, such as pixelated devices, are either hard to fabricate and/or require expensive, complicated readout electronics.

For some specific applications such as medical imaging where a large detecting area is desired, pixelated devices are the most commonly used method. However, there are several issues with large detectors using pixelated devices or similar single carrier devices. First, acquiring a large-volume CdZnTe single crystal is costly. The second issue with such a CdZnTe crystal is the availability of the material; in most cases, the crystal is difficult and sometimes impossible to acquire. Furthermore, it may require very expensive and complicated readout electronics. Fabricating and handling a large-volume pixelated CdZnTe device is also time consuming and requires complicated equipment. Finally, there are some technical issues and limitations with pixelated devices, such as charge-sharing and cross-talking (since the pixels share the active region of the device). To overcome the complexities of pixelated devices for a large detecting area, an array of bar shaped CdZnTe Frisch collar detectors are proposed. However, such an array of CdZnTe *Frisch collar* detectors (collimated/non-collimated) is still under development and is not commercially available.

1.3 Research Objectives

In the proposed method (Fig. 1.1 and Fig. 1.2), each pixel is basically dedicated to one previously fabricated Frisch collar detector. Such a design resolves several issues of other types of single carrier devices. First, acquiring smaller volume CdZnTe single crystals for several Frisch collar detectors is less costly than obtaining the same amount of total detecting volume with one large-volume single crystal. This fact reduces the capital cost of the

project significantly. Also, the fabricating process of CdZnTe Frisch collar detectors is simple and does not necessarily require time-consuming photolithography processing and other expensive clean-room costs. Finally, there is no charge-sharing effect between the pixels, because each pixel has its own individual active volume. For an array of collimated Frisch collar detectors, the effect of cross-talking (through Compton scatter gamma-rays from one pixel volume to another) can be minimized by using a high atomic number material, such as tungsten, for the collimators. This reduction in cross-talking is due to absorption of scattered gamma-ray in the collimator materials. However, the complexity of the readout electronics for such an array still remains.

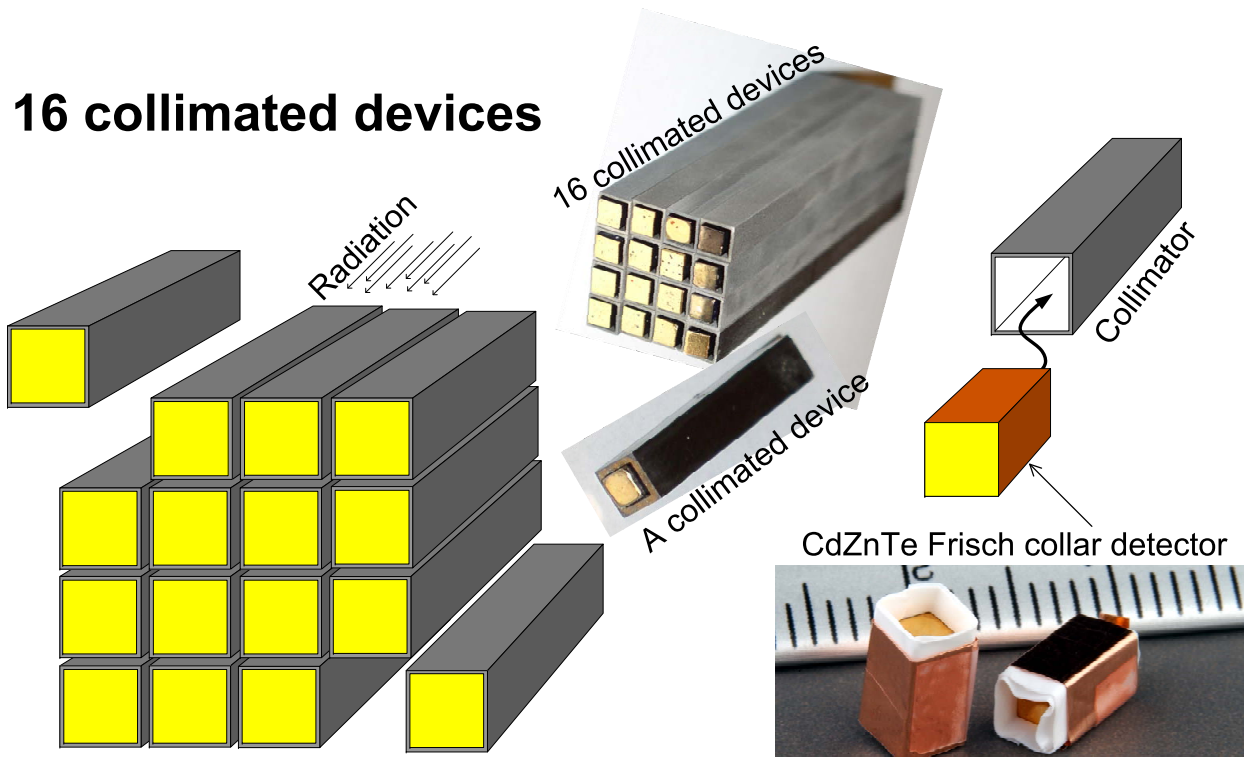


Figure 1.1: Array of collimated Frisch collar detectors.

The main objectives of this work are summarized as follows.

- Develop a reliable, low-cost fabrication method for CdZnTe Frisch collar detectors.
- Characterize CdZnTe Frisch collar devices for different geometries and configurations.
- Investigate the robustness of the Frisch collar effects on CdZnTe devices.

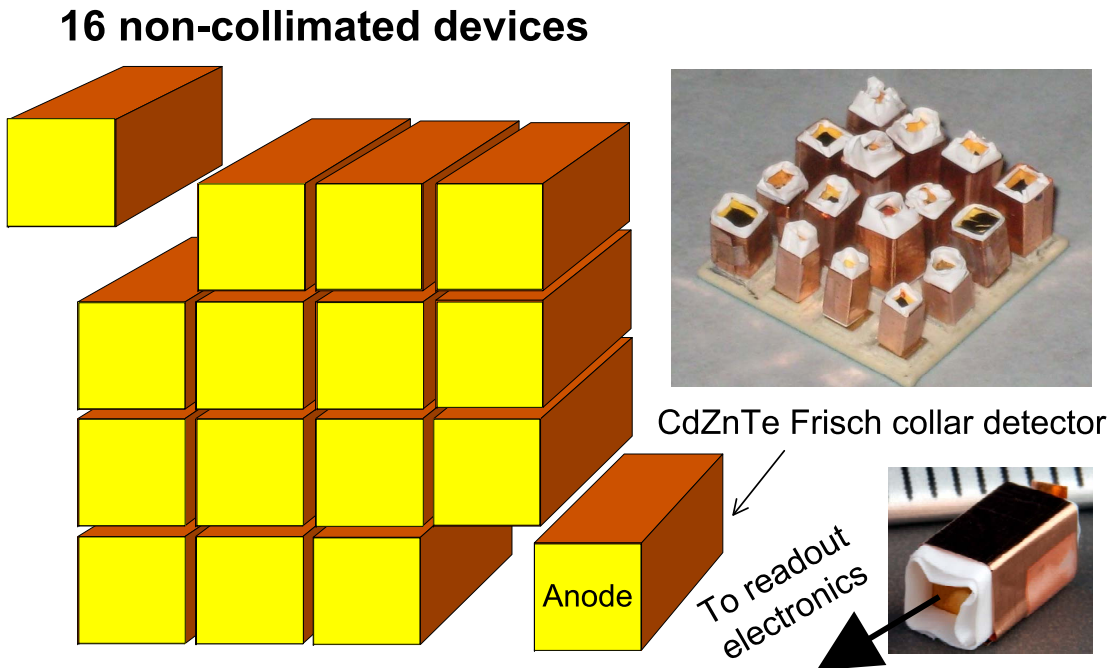


Figure 1.2: Array of non-collimated Frisch collar detectors.

- Optimize the CdZnTe Frisch collar devices' performance.
- Construct the CdZnTe Frisch collar devices into an array.

The results of this study are presented in six chapters. Chapter one introduces the existing problem and the primary objectives of the study. Chapter two reviews the literature on principles of Frisch collar devices and introduces the present research. Chapter three describes the theoretical considerations and the procedures to model the device. Chapter four describes the experimental setups and instrumentation, equipment and facilities, and the measurement procedures. Chapter five details the results of the experiments and compares them with theoretical simulations and previous research. Chapter six summarizes the study results and makes recommendations for future research.

Chapter 2

BACKGROUND OF CdZnTe FRISCH COLLAR DEVICES AND THE PRESENT RESEARCH

This chapter briefly reviews previous work on Frisch collar detectors and describes the basics of the Frisch collar device. The first part gives a brief history of the Frisch collar (or Frisch grid or Frisch ring) detector and the basic concept based on major previous research. The second part of this chapter describes the present work and the studies conducted on Frisch collar devices.

2.1 Previous Work on Frisch Collar Devices

As previously mentioned, the Frisch collar spectrometer is one of the most promising designs of single carrier devices. Indeed, the CdZnTe Frisch collar detector has been widely used in radiation detection by many other research groups [11, 12, 14-25] since its inception [11, 12]. The idea behind the Frisch collar effect in semiconductors comes from the Frisch grid effect in ion chambers [26]. Specifically, the dependence of the signal (pulse height) on the position of interaction in an electron sensitive ion chamber can be eliminated by dividing the chamber volume, using a Frisch grid. The grid can be designed and built in such a way that most of the radiation interactions occur in the volume between the grid and the cathode of the chamber. Such a design requires the grid to be virtually transparent to the electrons, while

the grid is maintained at an intermediate potential between the anode and the cathode, to keep the electric field uniform. The grid also needs to be closer to the anode, while the anode is set as the readout electrode. In this design, the signals (pulse height) are produced primarily from the motion of the electrons over the small distance between the grid and the anode. The Frisch grid effect in ion chambers provided the base for the invention of Frisch collar design in semiconductor detectors.

Reported research on the performance of Frisch collar devices focuses on initial design, the effect of bulk, surface leakage current and charge collection efficiency. The first design of the Frisch grid effect in semiconductor devices was reported in the literature [11, 12] as contacting grid devices (Fig. 2.1b and Fig. 2.1c). Semiconductor Frisch collar (ring/grid) devices using contacting grids applied directly to a semiconductor surface, as illustrated in Fig. 2.1b and Fig. 2.1c, have voltage limitations imposed by leakage currents flowing between the grid and the collecting anodes [11–19, 21]. The non-contacting grid proposed by [19, 20, 22, 23] has a thin high resistive insulator between the conductive collar (ring/grid) and the CdZnTe detector (Fig. 2.1d). Subsequently, non-contacting grids [20, 22–25] have less limitation on applied voltage. One of the unique characteristics about the non-contacting grid device, the so-called Frisch collar device, is that the device’s total leakage current does not increase as the Frisch collar is applied to a planar device. This important feature allows a variety of configurations for conductive collars.

Next, the effect of bulk and surface leakage current on the performance of CdZnTe (Frisch collar) devices was studied by [24, 27], and results showed that the bulk and surface leakage current are the main limiting factors on performance of CdZnTe devices. Fluctuations in the charge losses due to electron trapping, as the electron cloud drifts toward the anode, was mentioned as the additional factor degrading the performance of the long-drift CdZnTe (Frisch collar) device. In another study by the same research group [28], several effects was proposed to have impact on the performance of Frisch-collar devices. Among those are the aspect ratio of the device, the thickness of the insulating layer, and the portion of

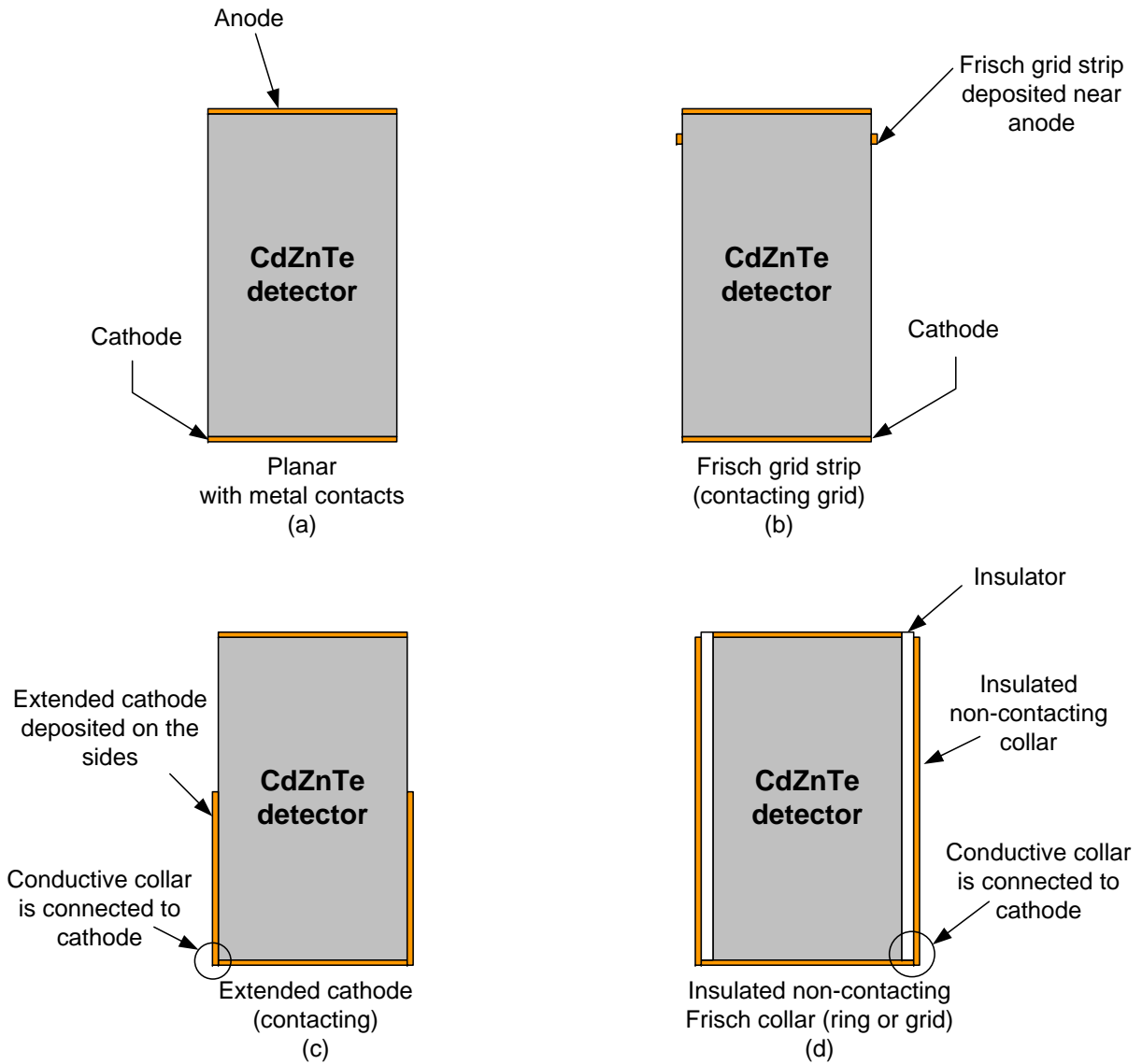


Figure 2.1: The different designs of Frisch collar (ring/grid) as reported in the literature. The anode is the top metal contact for all the detectors shown in this figure. (a) A planar device with deposited metal contacts on both ends as the electrodes. (b) The Frisch grid strip as in [12]. The grid is grounded or maintained at an intermediate potential between the anode and the cathodes. No insulator is used between the grid and the detector. (c) The extended cathode (non-insulated Frisch collar) in which no insulator is used between the conductive collar and the detector. (d) The insulated non-contacting Frisch collar with a deposited insulator between the conductive collar and the detector surfaces [20, 23].

the device covered by the conductive collar (length of collar) (see Fig. 2.1c, d). In another study [23], the effect of the conductive collar length on device spectroscopic performance was systematically investigated; however, the results were only for a specific device size ($3.0 \times 3.0 \text{ mm}^2 \times L = 6.0 \text{ mm}$) and can not be generalized for other geometries.

The effects of the dielectric layer thickness, the conductive collar length, and the ring position (see Fig. 2.1) on spectroscopic performance of a $4.0 \times 4.0 \text{ mm}^2 \times L = 6.0 \text{ mm}$ CdZnTe detector were investigated by [20]. However, in that study [20] a lack of enough experimental data led to no clear conclusion, and further experimental results with higher energy gamma-rays was proposed as future work.

The charge collection efficiency (CCE) of Frisch collar devices was first reported by [16, 18] for a trapezoidal-shaped Frisch grid CdZnTe gamma-ray detector. In a systematic series of experiments, the detector was probed with a collimated 59.5 keV gamma-ray source of ^{241}Am along the bottom and sides. Because 97% of the 59.5 keV gamma-rays are absorbed within the 1.0 mm of the CdZnTe detector surface, most of the charge carriers were excited within 1.0 mm of the detector surface. The results proved that charge-carriers were collected from all locations along the surface. A similar study was conducted by [29] and the charge collection efficiency profile along the length of a bar-shaped Frisch collar device was determined, using highly collimated gamma-rays of 412 keV. In that study, unlike in a planar configuration, the charge collection efficiency profile along the length of a Frisch collar device is considerably improved. The study was performed for a $3.4 \times 3.4 \text{ mm}^2 \times L = 5.5 \text{ mm}$ CdZnTe Frisch collar device with a variety of conductive collar lengths. The study also showed that a $3.4 \times 3.4 \text{ mm}^2 \times L = 5.5 \text{ mm}$ device with full-length Frisch collar ($L_f = L$) has the best charge collection efficiency profile compare to the devices with Frisch collar length L_f , less than the total device length L . The study clearly confirms the robustness of Frisch collar technology. However, further investigation for different device geometries and aspect ratios, as well as testing for higher gamma-ray energies was merited. In the following, a systematic intensive study on CdZnTe Frisch collar device is presented with the focus on

the issues that was not addressed previously. These issues can be summarized as, device optimization for the best aspect ratio, insulator layer thickness, Frisch collar length and the ratio of anode area to cathode area. Further investigation is performed on the device post fabrication surface treatment and the directional sensitivity of collimated device.

2.2 The Present Work on Frisch Collar Devices

Researchers whose previous work is summarized in Section 2.1 studied CdZnTe Frisch collar detectors and determined some characterizations of Frisch collar devices. However, further characterizations are required to investigate and predict the CdZnTe Frisch collar detector's response in a variety of conditions. In this research work, intensive studies have been conducted to characterize and optimize CdZnTe Frisch collar detectors in variety of conditions and for different geometries. Further, this research assesses the feasibility of CdZnTe Frisch collar devices in an array of detectors. The theoretical consideration and the numerical models for all devices for all studies are discussed in Chapter 3, while the experimental setup and procedures are shown in Chapter 4, and the results are presented in Chapter 5.

Some major issues that have not been previously investigated on Frisch collar devices are covered in this dissertation. Among those are the impacts of crystal geometry or aspect ratio (length over width) on performance of Frisch collar devices. This research shows a minimum aspect ratio at which the Frisch collar effect starts showing its performance. The research also shows a range of geometries for which the Frisch collar enhances the device spectroscopic performance significantly.

Further device characterization investigates the impact of dielectric layer thickness on performance of Frisch collar detectors, revealing an optimum dielectric layer thickness for Frisch collar devices, at which the device shows its best spectroscopic performance. This research also shows that the optimum thickness strongly depends on the crystal geometry and aspect ratio. The experiments are carried out for several CdZnTe Frisch collar devices. The optimum dielectric layer thickness was experimentally determined for each device and

the results were verified through three-dimensional geometry modeling of the potential and electric field.

The surface passivation and final surface treatment on the lateral sides of CdZnTe/CdTe gamma-ray detectors have been studied by many research groups. However, none of the studies addressed the impact of final surface treatment on CdZnTe *Frisch* collar devices. Existing research lacks information on how surface treatment affects the device spectroscopic performance while a higher energy gamma-ray source (like ^{137}Cs) is used. Therefore, this research covers systematic studies on spectroscopic performance and current voltage (IV) for characteristic behavior of Frisch collar devices as a result of surface treatments. In particular, a variety of final surface treatments and oxidizing agents were applied to different CdZnTe detectors, and the effects on the IV characteristic behavior and spectral performance of Frisch collar devices at 662 keV are reported.

More device characterization was performed by probing the non-contacting Frisch collar with a highly collimated 662 keV gamma-ray source of ^{137}Cs . The spectroscopic response was investigated by probing a $4.7 \times 4.7 \times 9.5 \text{ mm}^3$ CdZnTe Frisch collar device along the lateral side using a ^{137}Cs source and a 0.6 mm Pb-collimator. Then the results were confirmed by simulating the charge collection efficiencies of the device under the operated condition.

To investigate the possibility of using the Frisch collar devices in imaging applications, the spatial resolution of a $3.4 \times 3.4 \text{ mm}^2 \times L = 5.8 \text{ mm}$ collimated CdZnTe Frisch collar detector was investigated for two different tungsten collimators (8 cm and 4 cm) using a ^{198}Au gamma-ray source. A two-dimensional model for the detector-collimator-source geometry was developed and applied. Results showed that the angular resolution of a collimated CdZnTe Frisch collar gamma-ray spectrometer depends strongly on the collimator length. The dependency of angular response on collimator length along with simplicity of detector geometry makes the bar-shaped Frisch detectors an excellent candidate for large area imaging applications.

Finally, an array of 16-channel CdZnTe Frisch collar detectors was successfully constructed and tested using readout electronics developed at the Brookhaven National laboratory (BNL). The readout electronics are designed to support 32 CdZnTe detectors being operated simultaneously. These readout electronics were built to be a substitute for the preamplifier, amplifier, and high voltage supply in commercial Nuclear Instrument Modules (NIM) bins while supporting 32 detectors simultaneously.

Chapter 3

THEORETICAL CONSIDERATIONS

3.1 Induced Charge and Induced Current

This section covers Green's reciprocity theorem, the definition of weighting potential, the definition of weighting field, Shockley-Ramo theorem, and induced charge. The application of Shockley-Ramo theorem to a gamma-ray detector while using the weighting potential/field distribution within the device, facilitate to evaluate the charge collection efficiency (*CCE*) distribution for a gamma-ray detector. Based on this *CCE* distribution, the device respond to gamma-ray can be predicted and subsequently, the device can be designed for its optimum configuration to obtain the best spectral performance.

3.1.1 Green's reciprocity theorem and induced charge

Green's Reciprocity Theorem states that if a series of charges $Q_1, Q_2, Q_3, \dots, Q_n$ on a system of conductors produces potentials of $V_1, V_2, V_3, \dots, V_n$ on each of the conductors respectively (initial condition) and likewise another series of charges $Q'_1, Q'_2, Q'_3, \dots, Q'_n$ on the same system of conductors gives potentials of $V'_1, V'_2, V'_3, \dots, V'_n$ respectively (final condition) [30], then

$$\sum_{i=1}^n Q_i V'_i = \sum_{i=1}^n Q'_i V_i . \quad (3.1)$$

Assume that four points in space are labeled as points 1 through 4, with points 1 through 3 stationed on three conductors and the potential at point 1 is held constant at V_1 through an external bias supply (Fig. 3.1). A finite number of dielectric layers with specific values of permittivity κ exist between the conductors (two dielectric layers are shown in Fig. 3.1 with different permittivities κ_1 and κ_2). Point 4 is an arbitrary point where the numerical value of potential is known. Application of Equation 3.1 for the system shown in Fig. 3.1 yields

$$Q_1 V_1' = Q_1' V_1 + Q_4' V_4 . \quad (3.2)$$

Because $V_1 = V_1'$, then,

$$Q_1 - Q_1' = Q_4' \left(\frac{V_4}{V_1} \right) . \quad (3.3)$$

The term $(Q_1 - Q_1')$ is called the change in induced charge ΔQ_1 , which can be sensed

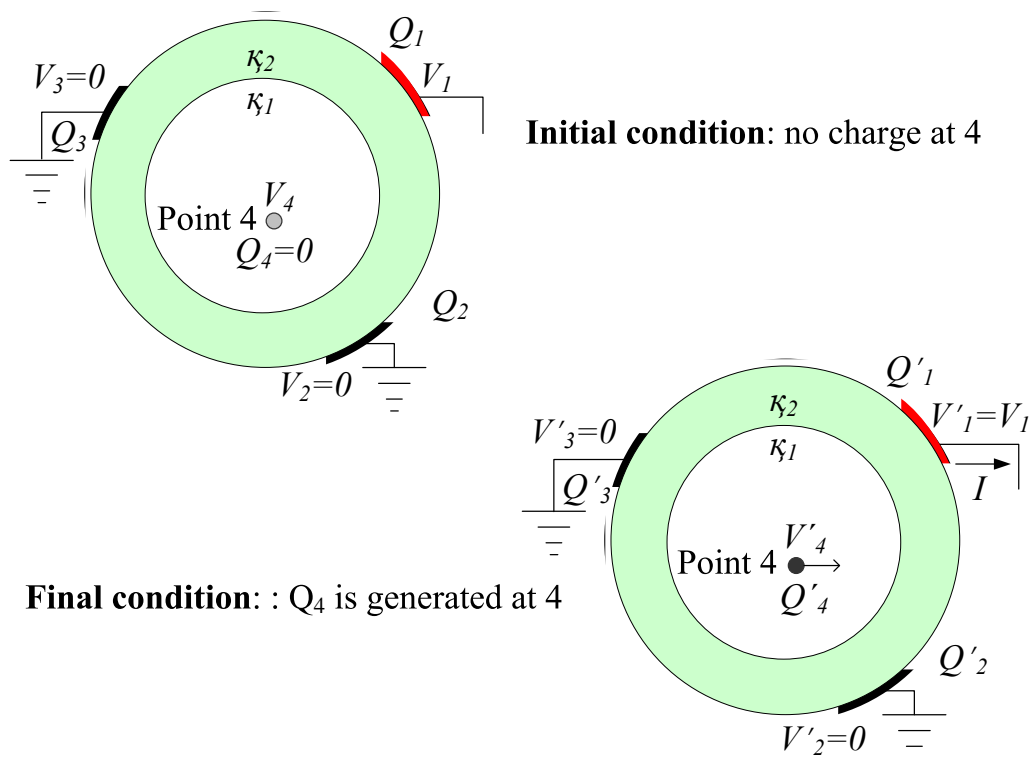


Figure 3.1: Green's Reciprocation Theorem [30] for three electrodes resembling a two-terminal Frisch collar device. Two of the electrodes are held at zero potential, while the collecting electrode senses the generation and motion of the charge generated at point 4.

on conductor 1 by a charge sensitive preamplifier. Notably, this amount of charge ΔQ_1 is first induced as a result of generation of charge Q'_4 at point 4 (such as that produced by a radiation interaction). As Q'_4 moves in space, it induces current I on conductor 1, which is the derivative of induced charge with respect to time.

3.1.2 The definition of potential, weighting potential, electric field, weighting field and Shockley-Ramo theorem

3.1.2.1 Potential and electric field

The electric field $\mathbf{E}(\mathbf{r})$ is defined as the force $\mathbf{F}(\mathbf{r})$ per unit charge at a given point \mathbf{r} , which is a vector function of position [31]. The force $\mathbf{F}(\mathbf{r})$ on a point charge q at \mathbf{r} in space due to the existing electric field $\mathbf{E}(\mathbf{r})$ at \mathbf{r} can be written in the following form,

$$\mathbf{F}(\mathbf{r}) = q\mathbf{E}(\mathbf{r}) . \quad (3.4)$$

Now, based on Coulomb's law, if $\mathbf{F}(\mathbf{r})$ is the force on a point charge q at \mathbf{r} due to another point charge Q at \mathbf{R} , then,

$$\mathbf{F}(\mathbf{r}) = \frac{qQ}{4\pi\epsilon_0} \frac{\mathbf{r} - \mathbf{R}}{|\mathbf{r} - \mathbf{R}|^3} , \quad (3.5)$$

where Q and q are charges and can have positive or negative values. $\epsilon_0 = 8.85419 \times 10^{-12} \text{ F m}^{-1}$ is the permittivity of free space (vacuum). From Equations 3.5 and 3.4, the electric field at \mathbf{r} due to a point charge Q at \mathbf{R} can be defined by the following equation,

$$\mathbf{E}(\mathbf{r}) = \frac{Q}{4\pi\epsilon_0} \frac{\mathbf{r} - \mathbf{R}}{|\mathbf{r} - \mathbf{R}|^3} . \quad (3.6)$$

The differential form of Gauss's law of electrostatics in vacuum can be written as [31],

$$\nabla \cdot \mathbf{E}(\mathbf{r}) = \rho(\mathbf{r})/\epsilon_0 , \quad (3.7)$$

where $\mathbf{E}(\mathbf{r})$ can be defined in terms of the scalar potential $V(\mathbf{r})$ as,

$$\mathbf{E}(\mathbf{r}) = -\nabla V(\mathbf{r}) . \quad (3.8)$$

In the presence of a dielectric, Gauss's law can be written as,

$$\nabla \cdot \mathbf{D}(\mathbf{r}) = \rho(\mathbf{r}) , \quad (3.9)$$

where $\mathbf{D}(\mathbf{r})$ is the electric displacement [31], and for an *isotropic* dielectric medium with permittivity of $\kappa(\mathbf{r})$, it is defined as,

$$\mathbf{D}(\mathbf{r}) = \kappa(\mathbf{r}) \epsilon_0 \mathbf{E}(\mathbf{r}) . \quad (3.10)$$

By combining equations 3.8 through 3.12, Poisson's equation can be derived as

$$\nabla \cdot [\kappa(\mathbf{r}) \epsilon_0 \nabla V(\mathbf{r})] = -\rho(\mathbf{r}) . \quad (3.11)$$

In the case of a medium with a *uniform* dielectric constant (κ does not change with position \mathbf{r}), Equation 3.9 is reduced to,

$$\nabla^2 V(\mathbf{r}) = -\rho(\mathbf{r})/(\kappa\epsilon_0) . \quad (3.12)$$

For media with various different dielectric materials (Fig. 3.1), Equation 3.11 must be solved for each region with appropriate boundary conditions at the interface between the different materials. The results for different media with uniform dielectric constants indicate that the normal component of $\mathbf{D}(\mathbf{r})$ and the tangential component of $\mathbf{E}(\mathbf{r})$ should satisfy the boundary conditions derived from the full set of Maxwell equations [31], namely

$$[\mathbf{D}_2(\mathbf{r}) - \mathbf{D}_1(\mathbf{r})] \cdot \mathbf{n}_{21} = \sigma , \quad (3.13)$$

$$[\mathbf{E}_2(\mathbf{r}) - \mathbf{E}_1(\mathbf{r})] \times \mathbf{n}_{21} = 0 , \quad (3.14)$$

where \mathbf{n}_{21} is the unit normal vector to the interface surface directing from medium 1 to medium 2, and σ is the macroscopic charge density at the interface surface.

3.1.2.2 Weighting potential and weighting field

If a system of conductors (electrodes) 1, 2, 3, ..., n in space at $\mathbf{r}_1, \mathbf{r}_2, \mathbf{r}_3, \dots, \mathbf{r}_n$ is held at potentials $V_1, V_2, V_3, \dots, V_n$ with the space charges $\rho(\mathbf{r})$ distribution among them, then the potential distribution $V(\mathbf{r})$ in the medium with permittivity distribution of $\kappa(\mathbf{r})$ can be evaluated by solving Poisson's equation (see Equation 3.11), with appropriate boundary conditions (each electrode is set to its corresponding potential).

Unlike the actual potential, the weighting potential profile (distribution) depends on the conductor (electrode) of interest that is sensing the moving charge. For instance, in Fig. 3.1, it is electrode 1 that is of interest, and therefore, the weighting potential distribution would be calculated with respect to electrode 1. For the system of conductors in Fig. 3.1, as charge Q'_4 is generated and moved, the change in induced charge on electrode 1 can be expressed through Equation 3.3 by $(Q_1 - Q'_1)$ or ΔQ_1 . The change in induced charge ΔQ_1 can be sensed on conductor 1 by a charge sensitive preamplifier. The normalized potential (V_4/V_1) is called *weighting potential* ψ [32, 33], which is dimensionless and is normalized such that $0 \leq \psi \leq 1$. Notably, V_4 is the potential at point 4 with initial condition ($Q_4 = 0$). Therefore, to evaluate the weighting potential at point 4, an arbitrary point, one solves Poisson's equation (see Equation 3.11), with no space charge, the appropriate boundary conditions, $V(\mathbf{r}_2) = V(\mathbf{r}_3) = 0$ and $V(\mathbf{r}_1) = V_1$, and the appropriate permittivities of the materials. Poisson's equation reduces to Laplace's equation in the absence of space charge,

$$\nabla \cdot [\kappa(\mathbf{r}) \epsilon_0 \nabla \psi(\mathbf{r})] = 0 , \quad (3.15)$$

with the boundary condition of $\psi = 1$ at the collecting electrode and $\psi = 0$ for all other electrodes. The boundary conditions for the problem with regions of different dielectric constants (κ_1 and κ_2) are discussed in Section 3.1.2.1.

Similar to the definition of electric field $\mathbf{E}(\mathbf{r})$, the *weighting field* $\mathbf{E}_w(\mathbf{r})$ (normalized electric field [32, 33]) can be found by applying Equation 3.8 to the *weighting potential* $\psi(\mathbf{r})$,

$$\mathbf{E}_w(\mathbf{r}) = -\nabla \psi(\mathbf{r}) . \quad (3.16)$$

The vector $\mathbf{E}_w(\mathbf{r})$ has the norm (length) of $E_w(\mathbf{r})$ with the unit of cm^{-1} . The commercial package, Integrated Engineering Software LORENTZ, was employed for three-dimensional geometry potential modeling [34] for all the studies in the work described.

3.1.2.3 Shockley-Ramo theorem

The procedure explained in Section 3.1.1 about the induced charge is based on the hypothesis proposed first by Shockley [35]. Later and in a separate work, Ramo [36] proposed the same

idea with a slightly different approach; however, the results were almost identical. Ramo's method [36] of calculating the induced current on a conductor due to an electron's motion is as follows. Assume a series of conductors, among which a single electron is moving with a known path and velocity v_e . Then, the instantaneously induced current I on a desired electrode can be evaluated by:

$$I = ev_e E_w , \quad (3.17)$$

where e is the charge of the electron, and E_w is the component of normalized electric field in the direction of velocity as the electron moves along its path. The normalized electric field E_w , also referred to as the weighting field [32, 33], can be evaluated in the same way as the electric field with the following conditions, (1) the electron is removed (assuming no space charge), and (2) the desired conductor is raised to unit potential, and (3) all other conductors are grounded. The Shockley-Ramo theorem [35, 36] has become the most popular method for evaluating the induced current in radiation detectors. The Shockley-Ramo theorem application to semiconductor devices is described by [37–41].

3.1.3 Charge collection efficiency

The charge collection efficiency $CCE(\mathbf{r})$ at a given point \mathbf{r} within a gamma-ray detector is defined as the normalized change in induced charge resultant from the gamma-ray interaction at that point. For instance, if Q_0 is generated by a single photon interaction at point \mathbf{r} within the device, and $Q_{tot}(\mathbf{r})$ is the total induced charge sensed by the collecting electrode after the remaining charges are collected including the trapping effect, then the charge collection efficiency $CCE(\mathbf{r})$ at point \mathbf{r} is defined by:

$$CCE(\mathbf{r}) = \frac{Q_{tot}(\mathbf{r})}{Q_0} . \quad (3.18)$$

In most compound semiconductors, there is significant charge carrier trapping, which degrades the device performance due to incomplete charge collection. Therefore, the $CCE(\mathbf{r})$ is almost always smaller than unity. For planar devices (Fig. 2.1a), the Hecht equation can

be used [41–44],

$$CCE(x) = \frac{E(x)}{L} \left[\mu_e \tau_e \left(1 - \exp \left[\frac{x - L}{E(x) \mu_e \tau_e} \right] \right) + \mu_h \tau_h \left(1 - \exp \left[\frac{-x}{E(x) \mu_h \tau_h} \right] \right) \right], \quad (3.19)$$

where L is the distance between the electrodes (detector length), x is the interaction location in the detector measured from the cathode, $E(x)$ is the magnitude of the electric field at point x and $\mu_{e,h}\tau_{e,h}$ is the mobility-lifetime product of the electrons and holes. The charge collection efficiency plots for a planar detector based on the Hecht equation are well presented in [41]. Obviously, the $CCE(x)$ at a given point x within the planar detector is significantly affected by the charge carrier transport property $\mu\tau$, applied bias (or electric field $E(x)$), and detector geometry (primarily the detector thickness L), as can be seen from the Hecht equation.

3.1.3.1 Charge collection efficiency for a two-terminal CdZnTe Frisch collar device

This section discusses the methods and assumptions used to develop the charge collection efficiency for a two-terminal CdZnTe Frisch collar device. Note that a *two-terminal* Frisch collar device referred to in this work is shown in Fig. 2.1b, c and d, with *the conductive ring and the cathode grounded (zero voltage potential)* for all cases. The electric/weighting field within the Frisch collar device is not uniform. Hence, to predict the device behavior through the charge collection efficiency, one needs first to solve Poisson’s and/or Laplace’s equations (see Equations 3.11 and 3.15) to determine the magnitude and distribution of the electric/weighting field. Afterwards, Shockley-Ramo theorem is applied to determine and plot the charge collection efficiency profiles.

The following assumptions are used to evaluate the electric/weighting field and the influence of the cloud of electrons/holes pairs generated from a radiation interaction. The perturbation of electric field due to the stationary space charges is considered negligible compared to the electric field from an externally applied voltage; hence, stationary space charges are neglected. Hence, Poisson’s equation (see Equation 3.11) reduces to Laplace’s

equation (see Equation 3.15) to determine the electric field distribution. Also, for a two-terminal device (with both the cathode and conductive collar *grounded*), the electric field has the same shape as the weighting field, differing only in magnitude and units. For such a two-terminal device, one can conclude,

$$\mathbf{E}(\mathbf{r}) = V(\mathbf{r}) \mathbf{E}_w(\mathbf{r}) , \quad (3.20)$$

where, $V(\mathbf{r})$ is the applied voltage in V (volt), $\mathbf{E}(\mathbf{r})$ is the electric field in V cm⁻¹, and $\mathbf{E}_w(\mathbf{r})$ is the weighting field in cm⁻¹ (all parameters at point \mathbf{r}).

The second assumption is to combine the effect of recombination and long term trapping of the charge carriers, while neglecting the effect of de-trapping. Hence, the charge carrier life-time (or mean free drift time or mean transient time) τ is used to consider the average time interval in which the current is induced on the desired electrode before the charge carrier is lost. Therefore, if Q_0 charges exist at time $t = 0$, the amount of charge $Q(t)$ at time $t = \Delta t$ is,

$$Q(t) = Q_0 \exp \left[\frac{-\Delta t}{\tau} \right] . \quad (3.21)$$

It is also assumed that the diffusion of the charge cloud is negligible compared to the drift caused by the external applied bias. This assumption is valid for detectors with a large area for the collecting electrode, such as Frisch collar detectors with a minimum of 9 mm² electrode area (a detector with 9 mm² collecting electrode area is the smallest detector used in this study). However, the negligible diffusion assumption may cause significant error for long drift detectors with a small collection area (such as those in pixelated devices) [9].

With the above assumptions, and application of the Shockley-Ramo theorem [45–47] to charge Q_0 in Fig. 3.2, the induced current on the collecting electrode can be written as,

$$I = \frac{dQ}{dt} = Q_0 [\mathbf{v}(\mathbf{r}) \cdot \nabla \psi(\mathbf{r})] , \quad (3.22)$$

where $\mathbf{v}(\mathbf{r})$ is the velocity of the charge carrier Q_0 at point \mathbf{r} , I is the induced current on collecting electrode, and dQ is the change in induced charge (sensed by collecting electrode).

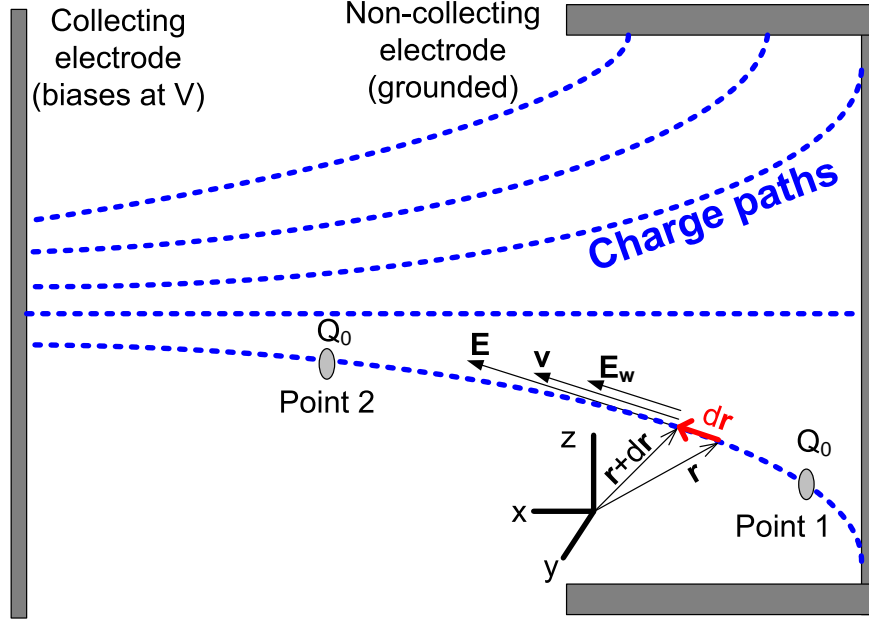


Figure 3.2: Shockley-Ramo theorem applied to charge Q_0 on a certain path for a two-terminal system of electrodes while the weighting field and the electric field vectors are in the same direction and have the relation in Equation 3.20 (two-terminal Frisch collar device).

Because the velocity is $d\mathbf{r}/dt$ (see Fig. 3.2) and with Equation 3.16, one can rewrite Equation 3.22 for the instantaneous induced current as,

$$I = \frac{dQ}{dt} = Q_0 \left[\frac{d\mathbf{r}}{dt} \cdot \mathbf{E}_w(\mathbf{r}) \right]. \quad (3.23)$$

By using Equation 3.23 one can evaluate the *induced current* caused by the motion of charge Q_0 within a two-terminal device (both Frisch collar and planar configuration), knowing the weighting field vector, $\mathbf{E}_w(\mathbf{r}) = E_{wx}\mathbf{i} + E_{wy}\mathbf{j} + E_{wz}\mathbf{k}$ along the charge carriers' path, $\mathbf{r} = x\mathbf{i} + y\mathbf{j} + z\mathbf{k}$ (where \mathbf{i} , \mathbf{j} and \mathbf{k} are the unit vectors in x , y and z directions). By simplifying the problem and considering only the charge carriers along the *central line* of a two-terminal device as in Fig. 3.3, Equation 3.23 reduces to,

$$I = \frac{dQ}{dt} = \frac{dx}{dt} Q_0 E_w(x). \quad (3.24)$$

The change in *induced charge* $\Delta Q(x)$ for Q_0 charges moving along the *central x-axis* over

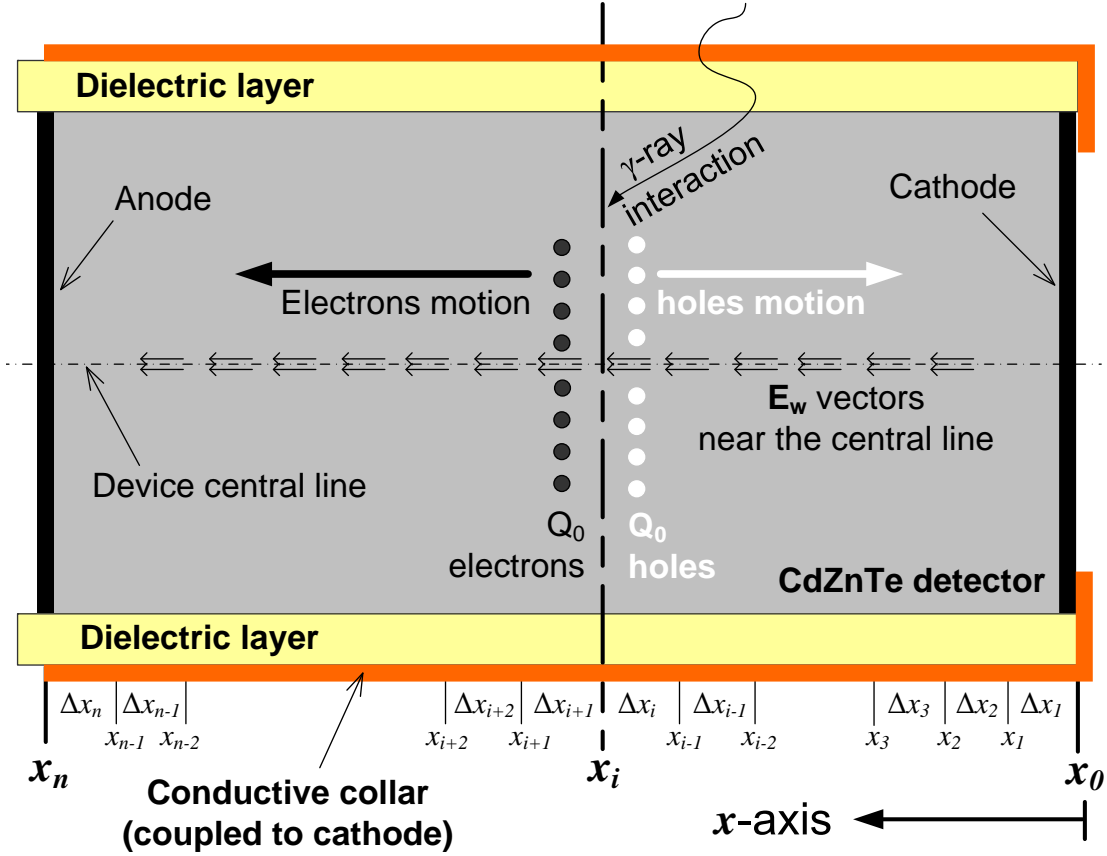


Figure 3.3: Applying Shockley-Ramo theorem to a two-dimensional Frisch collar device along the *central axis* $\mathbf{E}_w(\mathbf{r}) = E_{wx}(x)\mathbf{i} = E_w(x)\mathbf{i}$. The conductive Frisch collar is coupled to the cathode and both are grounded.

the interval Δx at x is,

$$\Delta Q(x) = Q_0 E_w(x) \Delta x = Q_0 \Delta\psi(x) , \quad (3.25)$$

where Δx is the length of segments on device's central line, as shown in Fig. 3.3, with the device length L divided into n equal segments, *i.e.*,

$$\Delta x_1 = \Delta x_2 = \dots = \Delta x_i = \Delta x_n = \Delta x = L/n . \quad (3.26)$$

Obviously, $\Delta Q(x)$ is the change in induced charge on the collecting electrode (anode in this case) as charge Q_0 moves within the device. Now, assume that a gamma interaction occurs at an arbitrary point x_i , and Q_0 charge is generated. Charge carriers are trapped as they

move toward their corresponding electrodes as described by Equation 3.21. Therefore, the Shockley-Ramo relation in Equation 3.25 (which is along the device's *central line*), can be written for charge carriers as follows (considering the trapping effects),

$$\Delta Q_{e,h}(x) = \Delta x E_w(x) Q_0 \exp \left[\frac{-\Delta t_{e,h}}{\tau_{e,h}} \right], \quad (3.27)$$

in which,

$$\Delta t_{e,h} = \frac{\Delta x}{[v_x(x)]_{e,h}} = \frac{\Delta x}{\mu_{e,h} E_x(x)}, \quad (3.28)$$

where $v_x(x)$ is the velocity of electrons and holes in the x -direction along the device's central line, and $E_x(x)$ is the magnitude of the electric field in the x -direction along the device's central line. It is important to remember that along the device's central line, the electric field, the weighting field, and the velocity have only an x -component ($\mathbf{E}(\mathbf{r}) = \mathbf{E}(x) = E_x(x)\mathbf{i} = E(x)\mathbf{i}$ and $\mathbf{E}_w(\mathbf{r}) = E_{wx}(x)\mathbf{i} = E_w(x)\mathbf{i}$ and $\mathbf{v}(\mathbf{r}) = \mathbf{v}(x) = v_x\mathbf{i} = v\mathbf{i}$). Therefore, the Shockley-Ramo theorem in Equation 3.27 can be stated as

$$\Delta Q_{e,h}(x) = \Delta x E_w(x) Q_0 \exp \left[\frac{-\Delta x}{\mu_{e,h}\tau_{e,h} E(x)} \right]. \quad (3.29)$$

It is also known that the total induced charge $Q_{tot}(x_i)$ (due to radiation interaction at x_i in Fig. 3.3) has contributions from both electrons $Q_e(x_i)$ and holes $Q_h(x_i)$,

$$Q_{tot}(x_i) = Q_e(x_i) + Q_h(x_i). \quad (3.30)$$

The electron and hole contribution to charge induction is the summation of $\Delta Q_e(x_i)$ and $\Delta Q_h(x_i)$ over the entire path of their motion from when they are generated until they are trapped (or collected). In other words, if an interaction occurs at x_i in Fig. 3.3, then the holes travel from $x = x_i$ to the cathode at $x = 0$, while the electrons travel from $x = x_i$ to the anode at $x = L$. Therefore the total induced charge $Q_{tot}(x_i)$, due to Q_0 charges generated at x_i , can be expressed as (see Fig. 3.3)

$$Q_{tot}(x_i) = \sum_{k=1}^i \Delta Q_h(x_k) + \sum_{k=i+1}^n \Delta Q_e(x_k). \quad (3.31)$$

Note that appropriate signs are needed for the charge carrier type (negative or positive) and the direction of charge carrier (see Fig. 3.3). By applying Equation 3.29, the contribution of electrons and holes to the change in induced charge can be separated and added over the entire length of the device, L . The change in induced charge with trapping in each segment 1 to n in Fig. 3.3 after an interaction at some arbitrary point x_i can be evaluated, given a known material (*i.e.*, the $\mu_{e,h}\tau_{e,h}$), geometry, and applied bias (*i.e.*, distribution of $E_w(x)$ and $E(x)$). This contribution to charge induction is detailed in each segment (see Fig. 3.3 and the right hand side of Equation 3.31), from point x_i where Q_0 is generated and moves toward the two respective electrodes at x_0 and x_n . The total induced charge due to *hole* motion is $\sum_{k=1}^i \Delta Q_h(x_k)$, and the change in induced charge due to motion of holes in segment Δx_k is $\Delta Q_h(x_k)$, which can be written as,

$$\Delta Q_h(x_k) = \Delta x E_w(x_k) Q_0 \exp \left[\frac{-\Delta x}{\mu_h \tau_h} \left(\sum_{j=k+1}^i \frac{1}{E(x_j)} \right) \right], \quad k = 1, \dots, i. \quad (3.32)$$

The total induced charge due to *electron* motion is $\sum_{k=i+1}^n \Delta Q_e(x_k)$, and the change in induced charge due to motion of holes in segment Δx_k is $\Delta Q_e(x_k)$, which can be written as,

$$\Delta Q_e(x_k) = \Delta x E_w(x_k) Q_0 \exp \left[\frac{-\Delta x}{\mu_e \tau_e} \left(\sum_{j=k-1}^{i+1} \frac{1}{E(x_j)} \right) \right], \quad k = i + 1, \dots, n. \quad (3.33)$$

Hence, the right hand side of Equation 3.31 can be evaluated by the summation of all the ΔQ_e 's and ΔQ_h 's within Δx_1 to Δx_n , as shown above. One can also factor out the term Q_0 in all the $\Delta Q_{e,h}$, and meanwhile divide both sides of Equation 3.31 by Q_0 to get the charge collection efficiency $CCE(x_i)$ at point x_i due to a gamma-ray interaction at this point, namely

$$CCE(x_i) = \frac{Q_{tot}(x_i)}{Q_0} = \frac{\sum_{k=1}^i \Delta Q_h(x_k) + \sum_{k=i+1}^n \Delta Q_e(x_k)}{Q_0}. \quad (3.34)$$

Equation 3.34 can be used to plot the $CCE(x)$ along the central line of any symmetrically made detector (including Frisch collar and planar detector). The parameters that must be known and/or evaluated before using Equation 3.34 are $\Delta x = L/n$ (n is the number of segments along the device central line), $E_w(x)$ and $E(x)$. To evaluate $E_w(x)$ and $E(x)$, Equations 3.15, 3.16 and 3.20 can be applied that required the device geometry, applied voltage, electrode configurations, and the dielectric constant κ of all materials. The last parameter that needs to be known is the electrical property of the semiconductor material $\mu_{e,h}\tau_{e,h}$.

3.1.3.2 Validity of charge collection efficiency model

To validate the model presented in Section 3.1.3.1, the CCE results simulated by the presented model are compared to some of the known and previously published results, such as those for the planar device in [41] and the Frisch collar device presented in [29]. Later, in Chapter 5, the $CCE(x)$ (or CCE) results simulated by the present model are used to predict the experimental results observed with highly collimated probing of a CdZnTe Frisch collar device along its central line. The model is written in a FORTRAN code (see Appendix A) in which the electric field and the weighting field along the device central line are in an input file. These input files are the data outputs from the LORENTZ package [34]. Other input parameters used to model the CCE include electrical properties of the semiconductor material $\mu_{e,h}\tau_{e,h}$, device length L , and the number of segments n . The number of segments n must be the same for both the FORTRAN code and the outputs of LORENTZ.

In the present section, a $5 \times 5 \times 10 \text{ mm}^3$ *planar* device is simulated for the CCE plots using both the Hecht equation 3.19 (see [41]) and the model presented in Section 3.1.3.1. Before presenting the results of CCE plots for the $5 \times 5 \times 10 \text{ mm}^3$ *planar* device, it is best to review the terms presented by [41]. To replicate the CCE plots (or normalized pulse height) in [41], the carrier extraction factor ρ is reintroduced as,

$$\rho_{e,h} = \frac{v_{e,h}\tau_{e,h}}{L} = \frac{E}{L} \mu_{e,h}\tau_{e,h} . \quad (3.35)$$

Equation 3.19 can be rewritten as,

$$CCE(x) = \rho_e \left(1 - \exp \left[\frac{x - L}{L \rho_e} \right] \right) + \rho_h \left(1 - \exp \left[\frac{-x}{L \rho_h} \right] \right), \quad (3.36)$$

where L is the distance between the electrodes (detector length), x is the interaction location in the detector measured from the cathode, as described in Equation 3.19. Fig. 3.4 illustrates the plots of $CCE(x)$ predicted by Equation 3.36 for a variety of carrier extraction factors $\rho_e = \rho_h$ (see [41]). The constraint $\rho_e = \rho_h$, for a $5 \times 5 \times 10 \text{ mm}^3$ planar detector can be satisfied by considering 1000 V applied voltage and assuming corresponding values of $\mu_e \tau_e = \mu_h \tau_h$. Fig. 3.5 shows the plots of CCE through the model in Section 3.1.3.1, which is applied to the $5 \times 5 \times 10 \text{ mm}^3$ planar detector for a variety of $\mu_e \tau_e = \mu_h \tau_h$. Figs. 3.4 and 3.5 represent identical CCE plots using the Hecht equation and the model in Section 3.1.3.1.

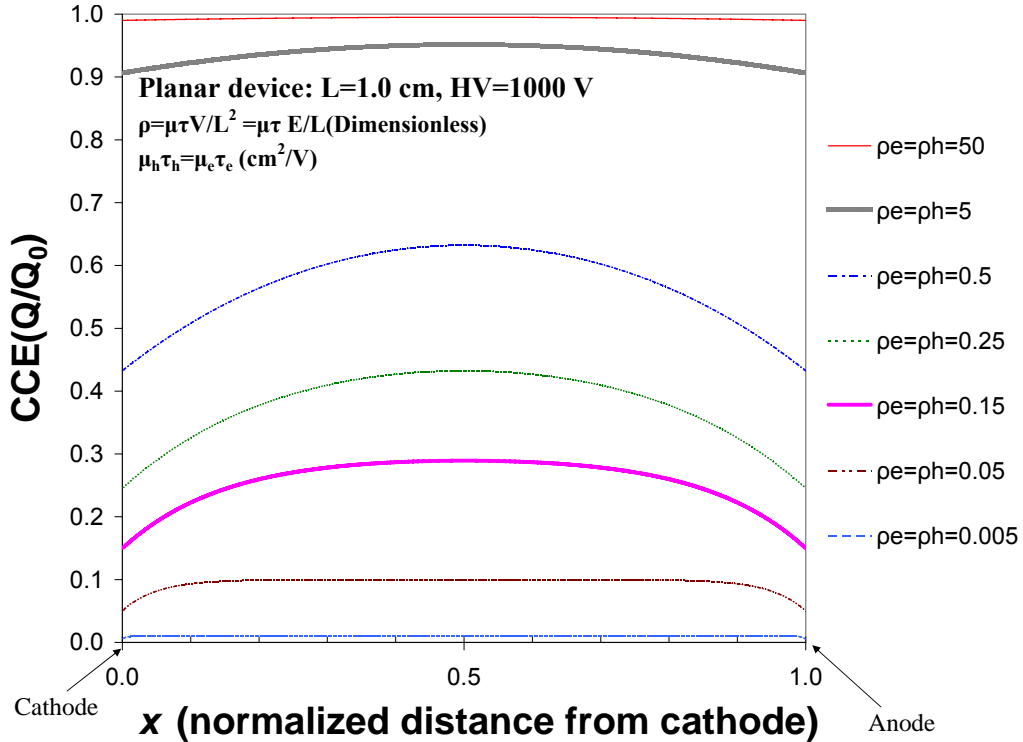


Figure 3.4: The charge collection efficiency CCE profile for a 10.0 mm long planar device at 1000 V, applied to anode (collecting electrode). The CCE is plotted based on the Hecht relation (Equation 3.36). The mobility-lifetime product $\mu_{e,h}\tau_{e,h}$ for electrons and holes is assumed to be the same, which results in equal carrier extraction factor $\rho_{e,h}$, resembling similar conditions to previously presented values for $\rho_{e,h}$ in [41].

In the first part of this section, the impact of the weighting potential/weighting field distribution on *CCE* plots is discussed. The parameters that affect this distribution are detailed and explained. Later, sections 3.2.2 and 3.2.3 discuss the parameters that do *not* affect weighting potential/weighting field distribution, but that do directly affect *CCE* and subsequently the Frisch collar device performance. Later, Section 3.2.4 discusses the impacts of device length on *CCE* plots. Device length has a dual and complex impact on *CCE*; as the device becomes longer, the weighting potential/weighting field distribution is altered favorably, but charge carrier trapping increases.

3.2.1 Effect of weighting potential/field distribution on CCE

The distribution of the weighting potential/weighting field within the device is one of the most important factors that affects device *CCE* and the change in induced charge on collecting electrode. Therefore, this section determines the weighting potential and the weighting field distribution within a $4.7 \times 4.7 \times 9.5 \text{ mm}^3$ CdZnTe detector (both planar and Frisch collar configurations). Then, device *CCEs* are evaluated and plotted using the model presented in Section 3.1.3.1. Finally, the pulse height spectrum of a fabricated CdZnTe device is presented and compared for the detector in both planar and Frisch collar configurations. The $4.7 \times 4.7 \times 9.5 \text{ mm}^3$ CdZnTe detector is a typical device size used in most of the studies in this thesis, although many other device sizes and geometries are also modeled and later tested to confirm the theoretical model.

The weighting potential and the weighting field distribution within the device are determined along the central line through full three-dimensional geometry modeling using LORENTZ (Section 3.1.2). The dielectric constants of CdZnTe and the insulator between the detector and Frisch ring (Teflon in this case) is considered 11.0 and 1.8 (in Equation 3.15) for all weighting potential and weighting field calculations [48]. These distributions are plotted in Fig. 3.6 for the $4.7 \times 4.7 \times 9.5 \text{ mm}^3$ CdZnTe detector. The electric field distributions can easily be evaluated by Equation 3.20 since both planar and Frisch collar CdZnTe detec-

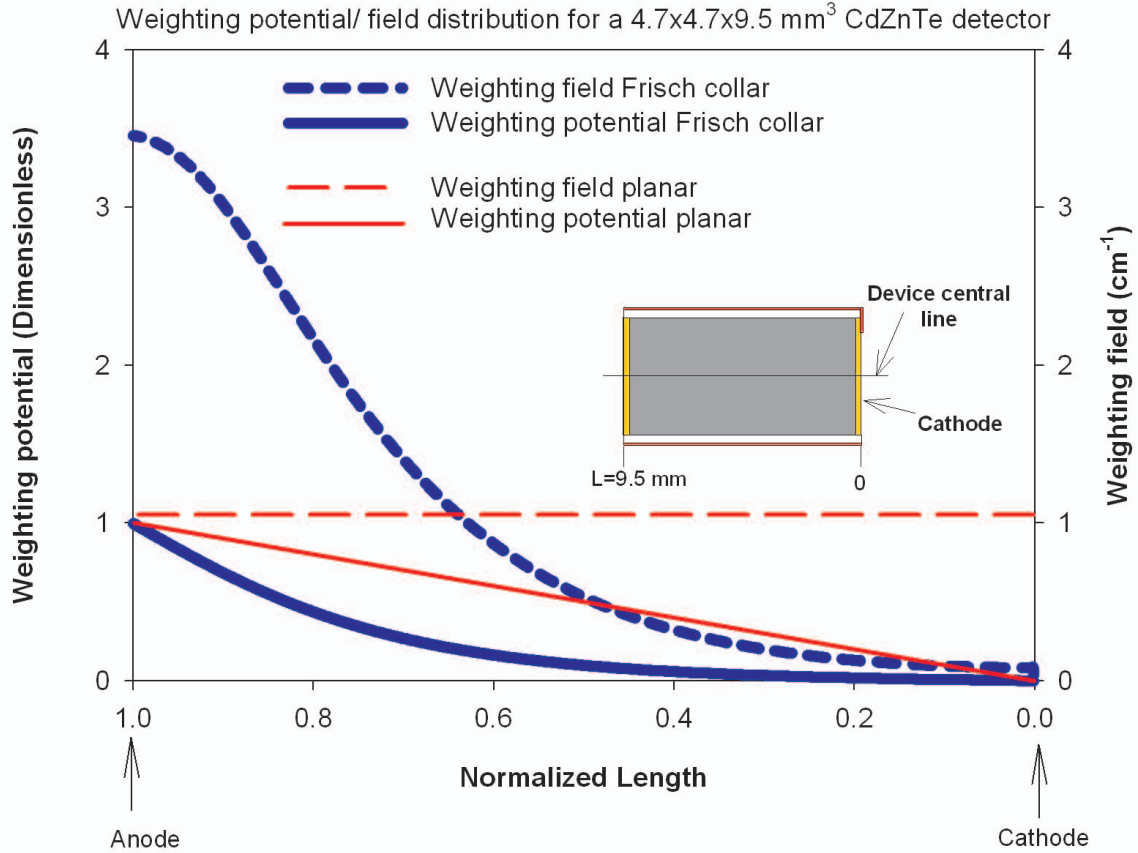


Figure 3.6: The weighting potential and weighting field distributions for a $4.7 \times 4.7 \times 9.5 \text{ mm}^3$ CdZnTe device along the central axis (Frisch collar and planar). The weighting potential and weighting field distributions for the Frisch collar device are modeled by considering a 0.35 mm insulator layer and 9.5 mm Frisch collar length (entire device length). The graph shows how the weighting potential distribution is altered into a nonlinear distribution due to the conductive collar. The graph also shows how the uniform field in planar device is altered to a nonuniform field distribution by applying the Frisch collar.

tors are two-terminal devices. Next, the CCE plots and the pulse height spectra are shown in Figs. 3.7 and 3.8, respectively. Clearly, based on Equation 3.25, most of the charge induction occurs where there is the greatest *change* in weighting potential $\Delta\psi$. In other words, the majority of charge induction, as the charge carriers are drifted toward their corresponding electrodes, occurs when the weighting field E_w has its *maximum* values.

It is easy to comprehend the impact of the Frisch collar on planar devices from Fig. 3.6 and Equation 3.25. Hence, the Frisch collar alters the linear distribution of weighting po-

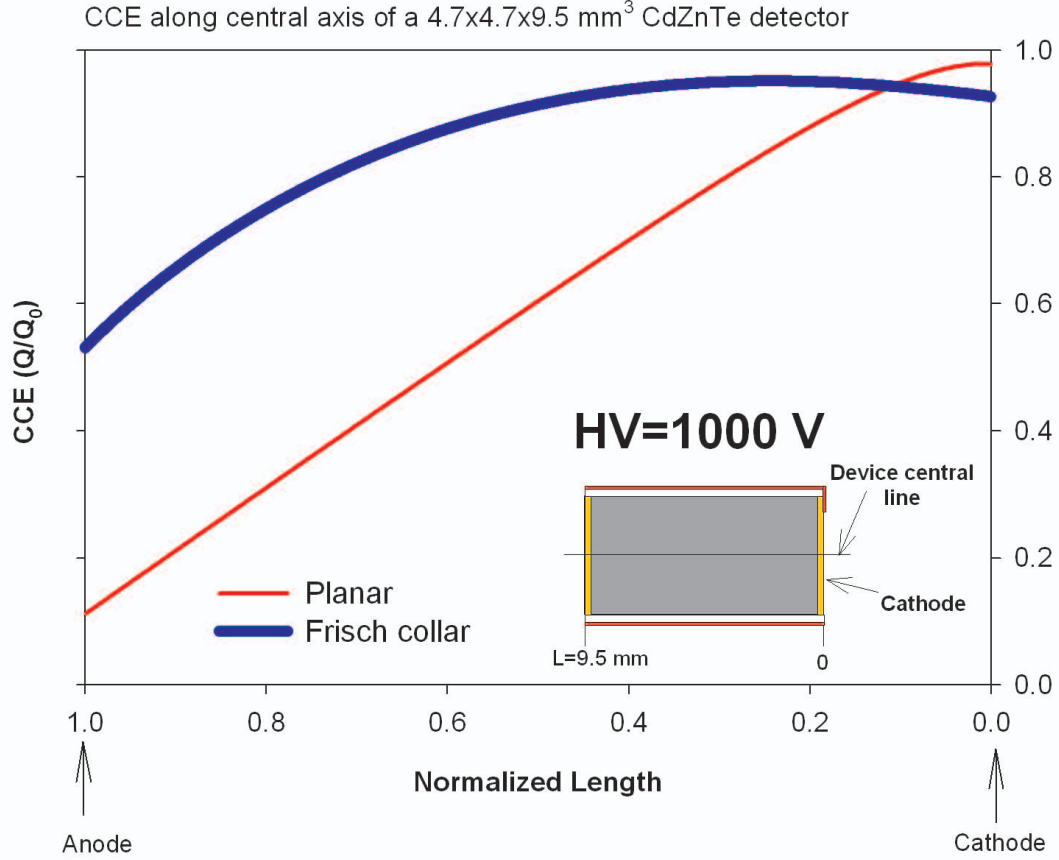


Figure 3.7: The charge collection efficiency CCE profile at 1000V applied to anode (collecting electrode) for a $4.7 \times 4.7 \times 9.5 \text{ mm}^3$ CdZnTe device along the central axis. The CCE is plotted based on the model presented in Section 3.1.3.1. The $\mu\tau$ values of 0.045 and $0.0001 \text{ cm}^2 \cdot \text{V}^{-1}$ are assumed for the electrons and holes, respectively. The plot shows significant enhancement in CCE of the detector when the Frisch collar is applied to the planar device.

tential in a planar device into a non-linear distribution for the same device in a Frisch collar configuration (see Figs. 3.3 and 3.6), for which the majority of the change in weighting potential is near the anode region. As a result, those charge carriers drifting towards the anode (electrons in this case) contributes to the induced charge more than those charge carriers drifting towards the cathode (holes). Therefore, the low mobility and higher trapping effect of the holes are negated in the Frisch collar device compared to the planar configuration. These effects alter the CCE plots of a planar device to a more *uniform* CCE plot for the corresponding Frisch collar device (Fig. 3.7). The more uniform CCE plot results in better

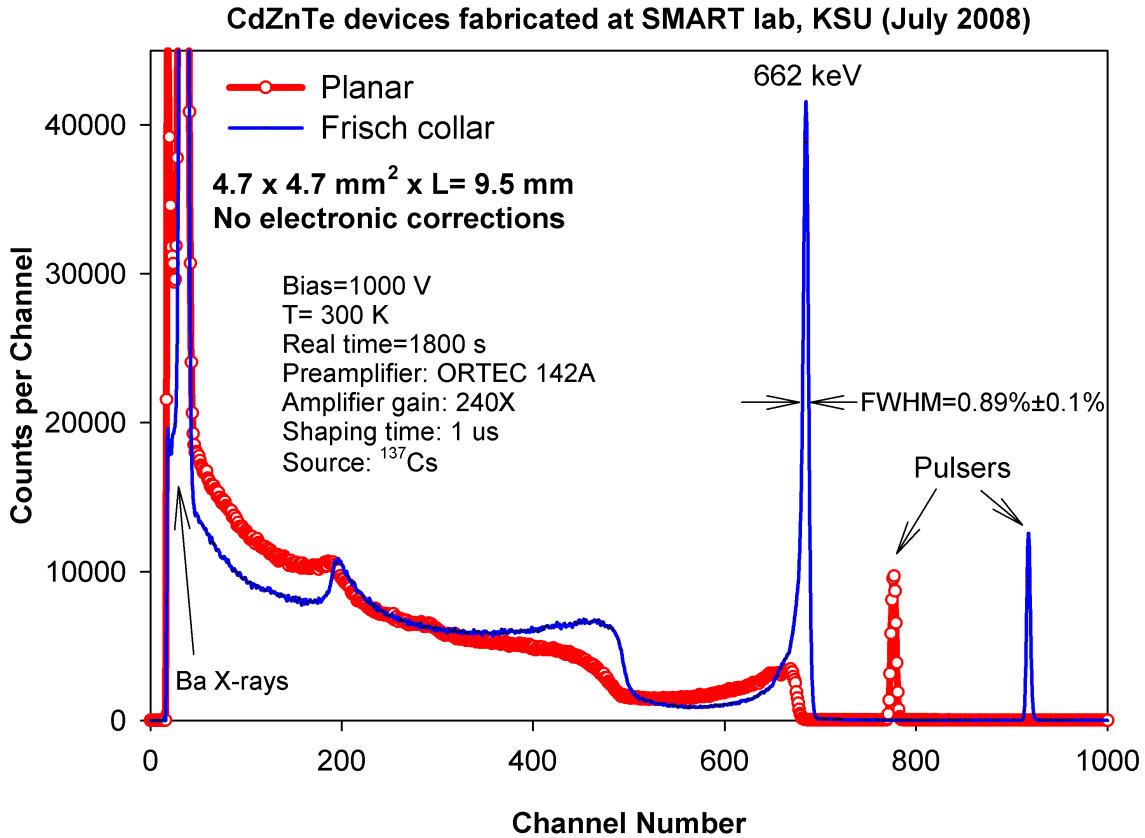


Figure 3.8: Pulse height spectra taken with a $4.7 \times 4.7 \times 9.5 \text{ mm}^3$ CdZnTe device being fully irradiated with a ^{137}Cs source. A 0.89% FWHM energy resolution is achieved at 662 keV.

pulse height spectra as illustrated in Fig. 3.8, since the charge induction (linearly related to the photoelectric peak channel on a multichannel channel analyzer, MCA) depends less on position of interaction. It should be noted that the main criterion of CdZnTe material that allows the fabricated device to benefit from the Frisch collar effect is the high mobility-lifetime product $\mu\tau$ of the electrons compared to holes. In other words, the higher electron mobility-lifetime product (compared to hole mobility-lifetime product) enables it to be an excellent candidate for a single carrier device to compensate for the effect of hole trapping and low mobility.

The previous discussion shows how the Frisch collar alters the weighting potential/weighting field distribution and makes the CdZnTe planar device into a single carrier device. Thus, the parameters affecting this distribution are of interest and need to be studied in detail. These parameters are listed in this section, and their impacts on weighting potential/weighting field distribution and subsequently the *CCE* plots are discussed. Some of these parameters are also investigated experimentally and the results of the experiments are presented in Chapter 5.

The parameters directly affecting the weighting potential/weighting field distribution are as follows: the crystal geometry and the aspect ratio of bar shaped crystal, the Frisch collar length, the ratio of the anode area to the cathode area (or the small pixel effect), the thickness of the insulator layer, and the dielectric constant of the insulator layer. Other parameters with no effect on weighting potential/weighting field distribution but impacts the *CCE* plots and subsequently device performance, such as mobility-lifetime product $\mu\tau$ of the CdZnTe materials and applied voltage, are discussed toward the end of Section 3.2. Regarding the effect of one parameter, it is assumed that the other parameters remain constant, since the parameters are independent of each other. Device length L is the only exception that changes the aspect ratio and has direct impact on *CCE*; therefore, it needs further clarification and is discussed in Section 3.2.4.

3.2.1.1 Crystal geometry

As mentioned at the beginning of Section 3.2.1, one of the most promising designs of single carrier devices is the Frisch collar device, which benefits from the nonlinearity of weighting potential near the anode region. This nonlinearity along the length of the device enables the electrons to contribute to the majority of the charge induction, thereby improving device performance.

The weighting potential profiles for several different device geometries and aspect ratios were modeled. The numerical values of the weighting potential distribution were then plotted for the central plane. The device performance as a function of the aspect ratio, before and after applying Frisch collars for various CdZnTe devices, are experimentally investigated. The experimental method and setup are detailed in Section 4.3.1, and the results of the experiment are presented in Section 5.3.1. Fig. 3.9 shows the designed pattern for fabricating CdZnTe crystals to prepare the starting devices. As shown in Fig. 3.9, the device’s length L is kept constant, and the device width W is reduced in size, thereby increasing the aspect ratio L/W . The second prepared device is also illustrated in Fig. 3.9 and labeled as CZT5. The dimensions and names of the subsequently designed detectors are presented in Table 3.1.

Table 3.1: CdZnTe devices with the same length L (4.8 ± 0.2) and different L/W to render the impact of geometry on weighting potential profiles along device central plane.

Device label	Device dimensions (mm)	Average aspect ratio (L/W)
CZT1	$19.08 \times 19.34 \times 4.95$	0.26
CZT5	$9.44 \times 9.45 \times 4.88$	0.52
CZT6	$6.65 \times 6.89 \times 4.84$	0.71
CZT7	$5.05 \times 5.02 \times 4.84$	0.96
CZT8	$4.03 \times 4.00 \times 4.76$	1.19
CZT9	$3.51 \times 3.51 \times 4.76$	1.36
CZT10	$2.90 \times 2.90 \times 4.60$	1.59
CZT11	$2.40 \times 2.40 \times 4.60$	1.92

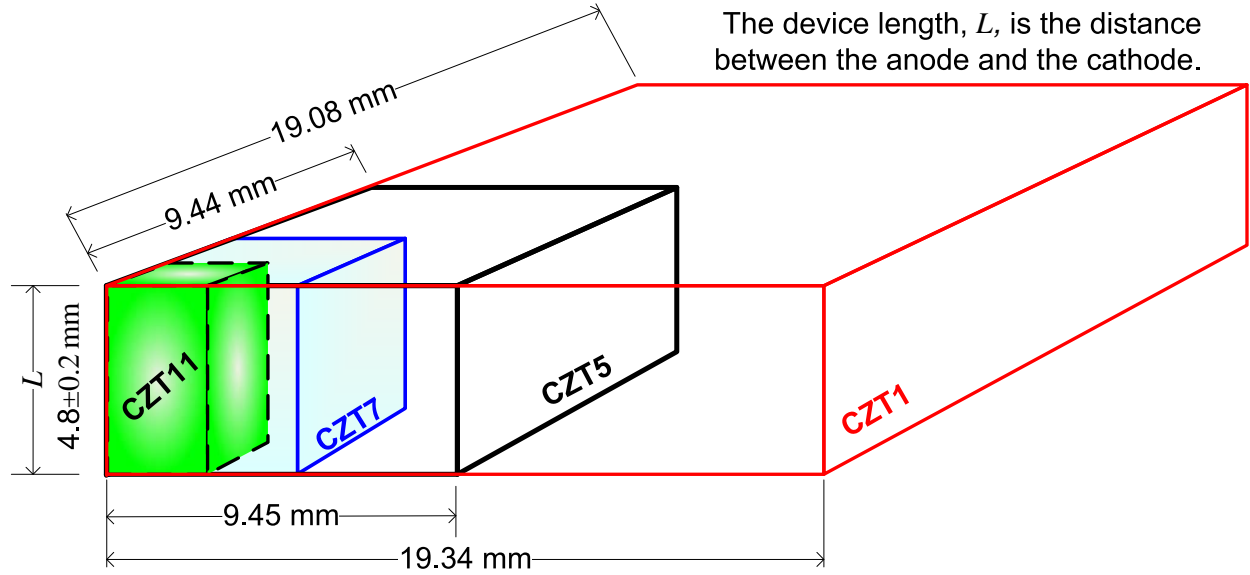


Figure 3.9: Sample devices showing the CZT1 (entire sample) and CZT5 (second device).

In Table 3.1 and Fig. 3.9, the length L is kept constant while the aspect ratio is increased. The effect of length is studied separately in Section 3.2.4 due to its simultaneous effect on CCE and weighting potential distribution. The weighting potential profiles for the central plane of devices in Table 3.1 are evaluated and plotted in Figs. 3.10 through 3.17. Clearly, the nonlinearity of the weighting potential distribution does *not* penetrate into the device bulk for the devices with aspect ratios near 1.0 or less (Figs. 3.10 through 3.13). Those devices with aspect ratio greater than 1.0, but less than 1.5, have nonlinear weighting potential distributions within the bulk, although some change still occurs in the bulk (Figs. 3.14 and 3.15). Devices with aspect ratios greater than 1.5 show a more uniform distribution of weighting potential within the bulk; hence, better performance is expected (Figs. 3.16 and 3.17). These predictions based on the weighting potential distribution are experimentally verified and presented in Sections 4.3.1, and the results are shown in Section 5.3.1.

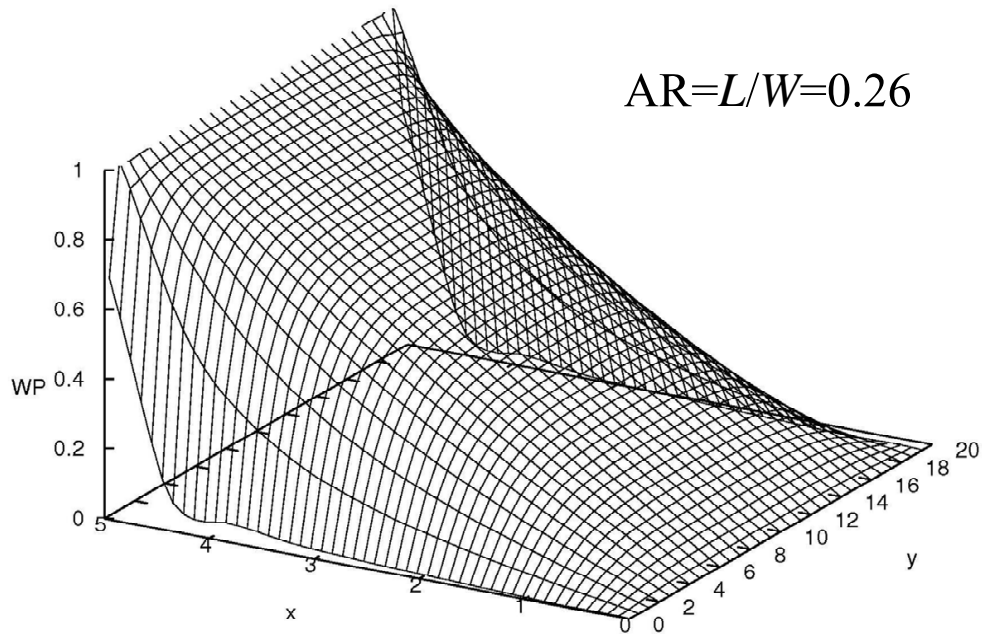


Figure 3.10: The weighting potential profile for Frisch collar CZT1 (19.08 mm \times 19.34 mm \times $L=4.95$ mm) for the central plane on z-axis (plane $z=9.54$ mm). The device length, L , is along the x-axis. The cathode is on $x=0$; the anode is on $x=L$ plane.

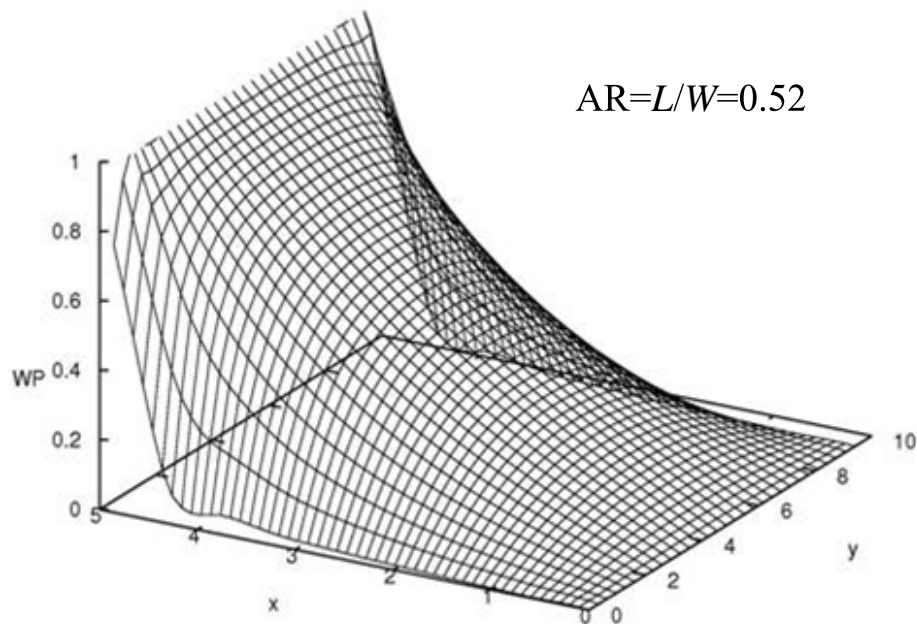


Figure 3.11: The weighting potential profile for Frisch collar CZT5 (9.44 mm \times 9.45 mm \times $L=4.88$ mm) for the central plane on z-axis (plane $z=4.72$ mm). The device length, L , is along the x-axis. The cathode is on $x=0$; the anode is on $x=L$ plane.

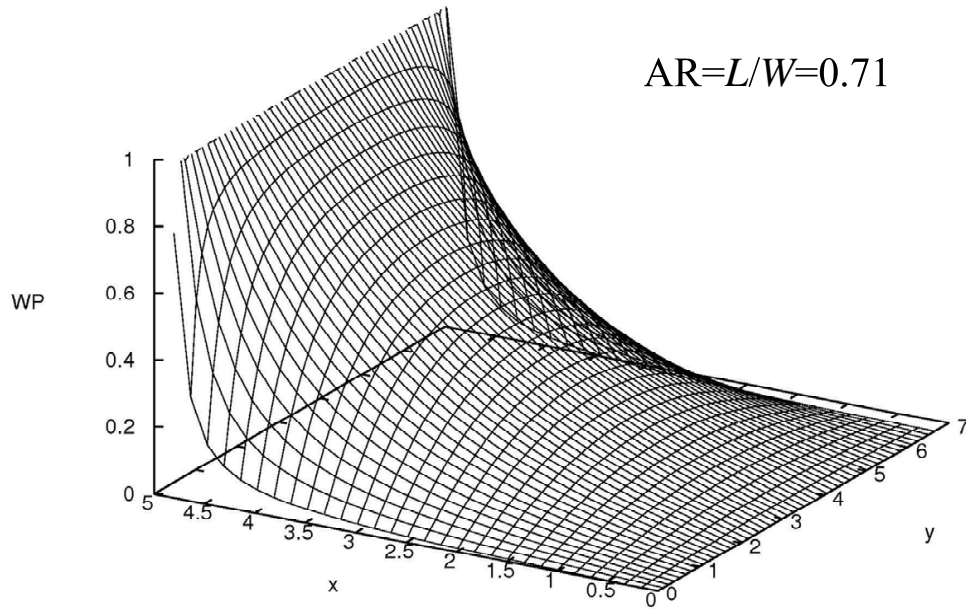


Figure 3.12: The weighting potential profile for Frisch collar CZT6 ($6.65 \text{ mm} \times 6.89 \text{ mm} \times L=4.84 \text{ mm}$) for the central plane on z -axis (plane $z=4.72 \text{ mm}$). The device length, L , is along the x -axis. The cathode is on $x=0$; the anode is on $x=L$ plane.

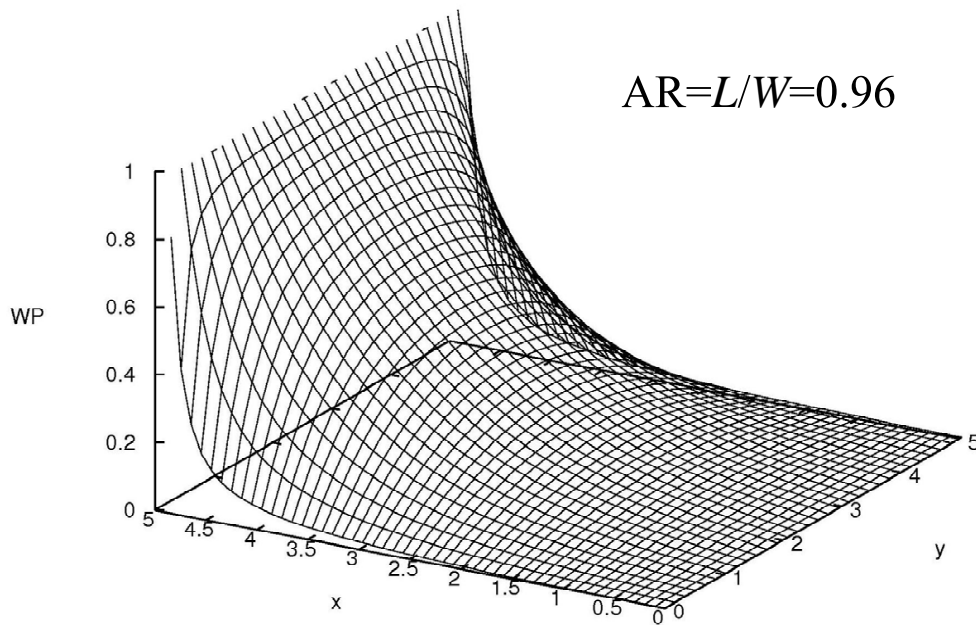


Figure 3.13: The weighting potential profile for Frisch collar CZT7 ($5.05 \text{ mm} \times 5.02 \text{ mm} \times L=4.84 \text{ mm}$) for the central plane on z -axis (plane $z=4.72 \text{ mm}$). The device length, L , is along the x -axis. The cathode is on $x=0$; the anode is on $x=L$ plane.

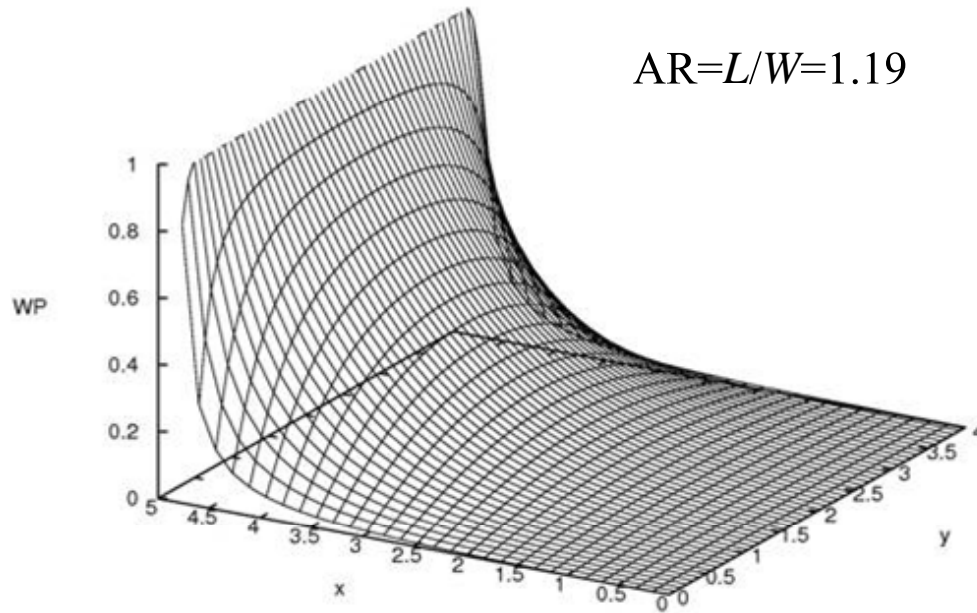


Figure 3.14: The weighting potential profile for Frisch collar CZT8 (4.03 mm × 4.00 mm × $L=4.76$ mm) for the central plane on z-axis (plane $z=4.72$ mm). The device length, L , is along the x-axis. The cathode is on $x=0$; the anode is on $x=L$ plane.

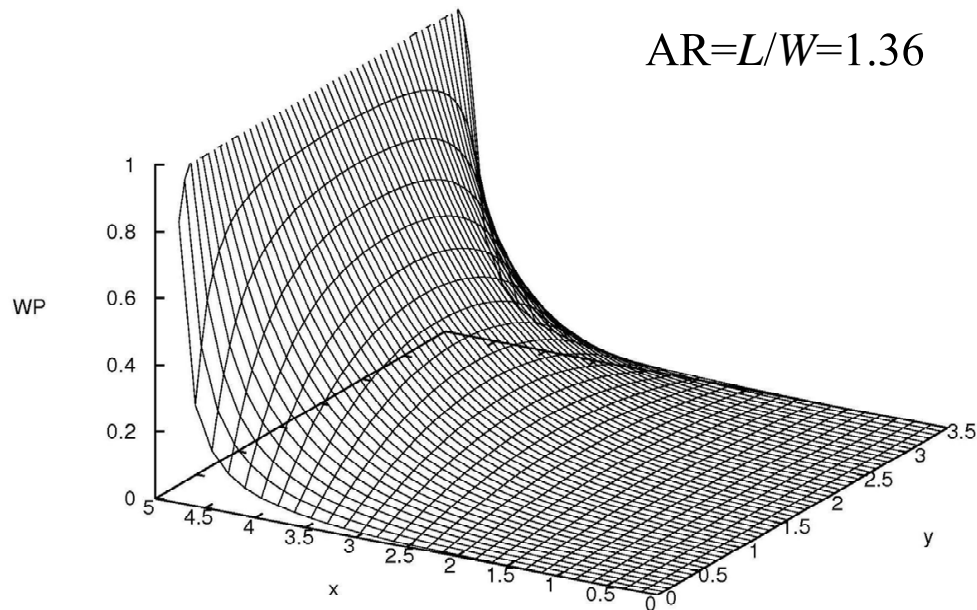


Figure 3.15: The weighting potential profile for Frisch collar CZT9 (3.51 mm × 3.51 mm × $L=4.76$ mm) for the central plane on z-axis (plane $z=4.72$ mm). The device length, L , is along the x-axis. The cathode is on $x=0$; the anode is on $x=L$ plane.

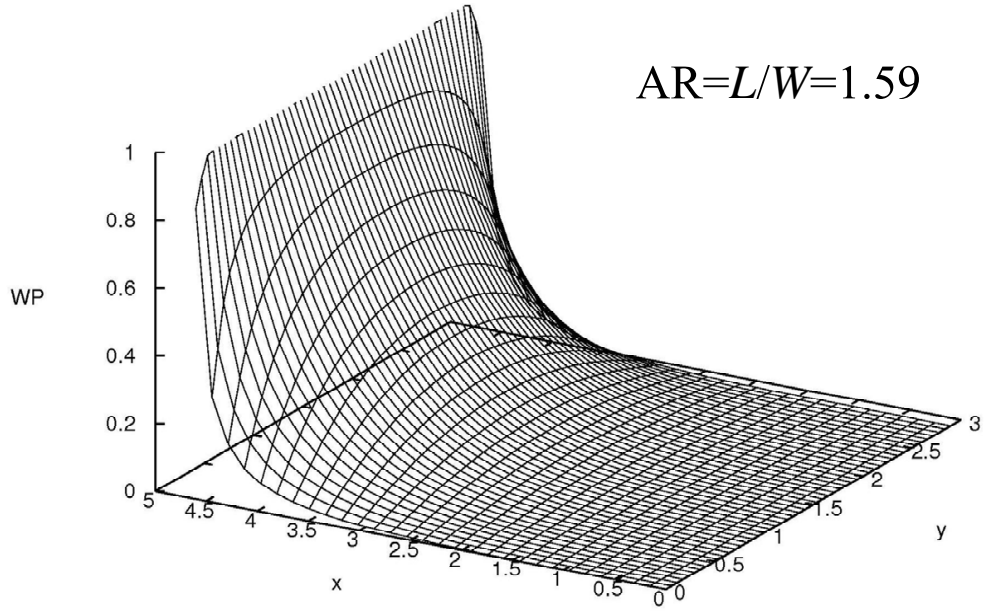


Figure 3.16: The weighting potential profile for Frisch collar CZT10 ($2.90 \text{ mm} \times 2.90 \text{ mm} \times L=4.60 \text{ mm}$) for the central plane on z-axis (plane $z=4.72 \text{ mm}$). The device length, L , is along the x-axis. The cathode is on $x=0$; the anode is on $x=L$ plane.

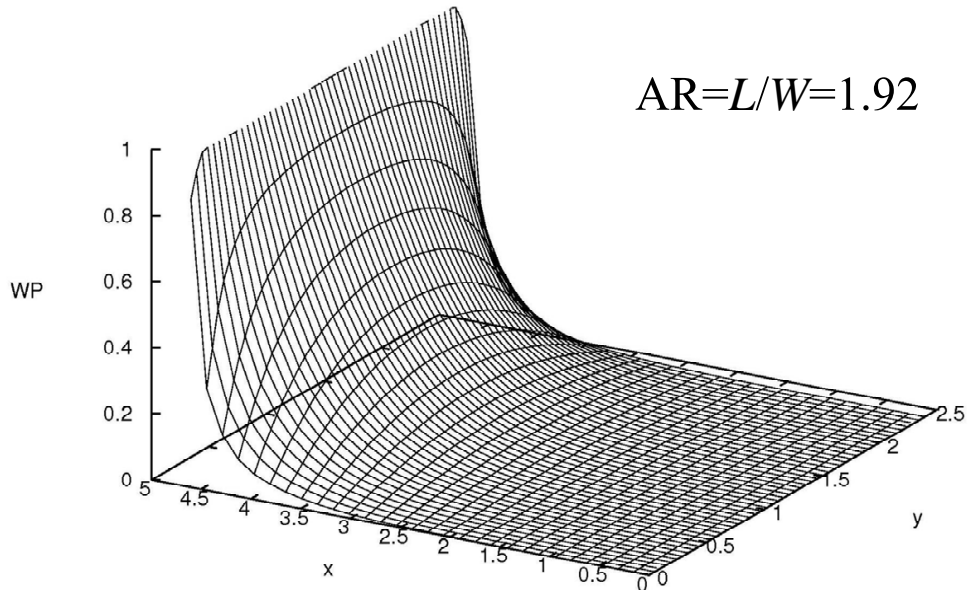


Figure 3.17: The weighting potential profile for Frisch collar CZT11 ($2.40 \text{ mm} \times 2.40 \text{ mm} \times L=4.60 \text{ mm}$) for the central plane on z-axis (plane $z=4.72 \text{ mm}$). The device length, L , is along the x-axis. The cathode is on $x=0$; the anode is on $x=L$ plane.

3.2.1.2 Frisch collar length

Given that the length of the Frisch collar L_F has a great impact on device performance [23, 29], it is easy to conclude that as the length of the Frisch collar decreases to a fraction of the device length L , the effect of the Frisch collar starts to change. Eventually, as the length approaches zero, the Frisch collar device mimics a planar device. In this section, the CCE plots for a $4.7 \times 4.7 \times 9.5 \text{ mm}^3$ device with a variety of Frisch collar lengths are presented along with weighting potential/weighting field calculations. Figs. 3.18, 3.19 and 3.20, show the weighting potential, weighting field and CCE plots for a $4.7 \times 4.7 \times 9.5 \text{ mm}^3$ CdZnTe device along the central line.

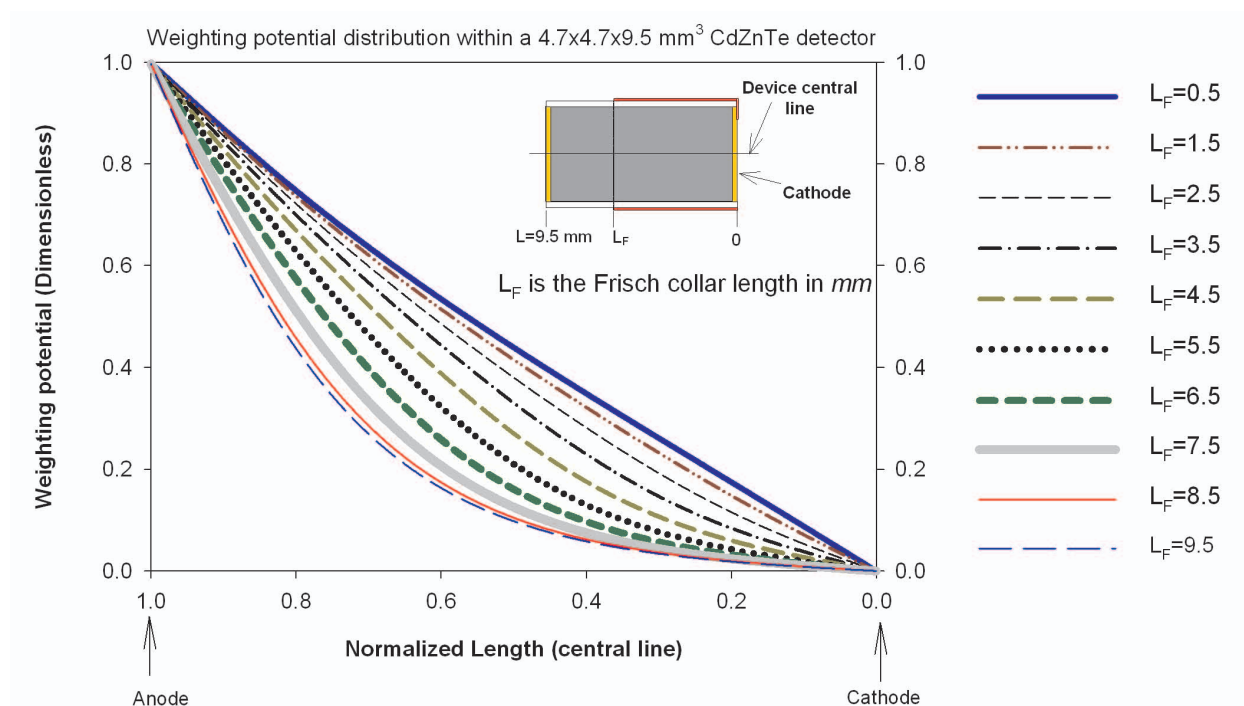


Figure 3.18: The weighting potential distribution for a $4.7 \times 4.7 \times 9.5 \text{ mm}^3$ CdZnTe Frisch collar device (with $AR=L/W = 2.0$) along the central axis with different collar lengths and a 0.35 mm insulator layer thickness. The distribution is calculated using LORENTZ.

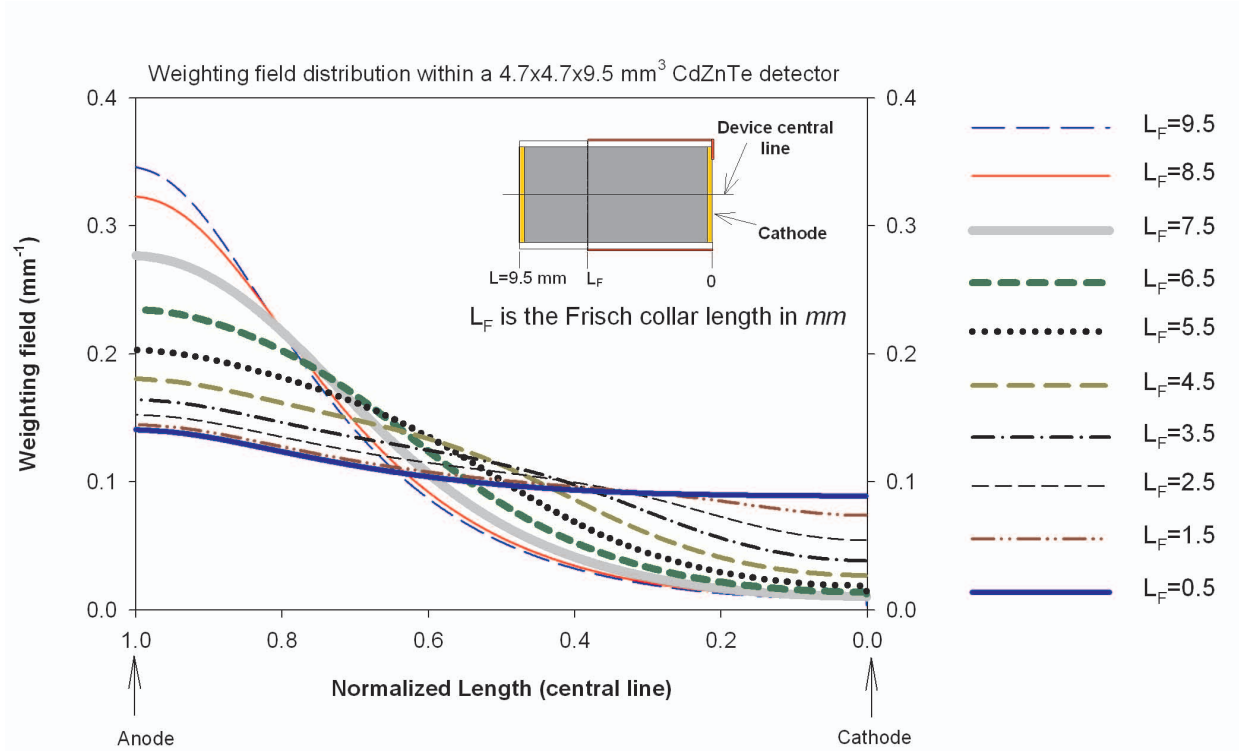


Figure 3.19: The weighting field distribution for a $4.7 \times 4.7 \times 9.5 \text{ mm}^3$ CdZnTe Frisch collar device (with $AR=L/W = 2.0$) along the central axis with different collar lengths and a 0.35 mm insulator layer thickness. The distribution is calculated using LORENTZ.

It is shown in Fig. 3.20 that for a $4.7 \times 4.7 \times 9.5 \text{ mm}^3$ CdZnTe device, the conductive collar length L_F around the device length (in this case 9 mm) predicts the best spectral performance (flat CCE response for about two-thirds of the device volume as in Fig. 3.20). Devices with aspect ratios close to 2.0 demonstrate best performance with a full Frisch collar, as reported in [23, 29], which helps to substantiate these research findings.

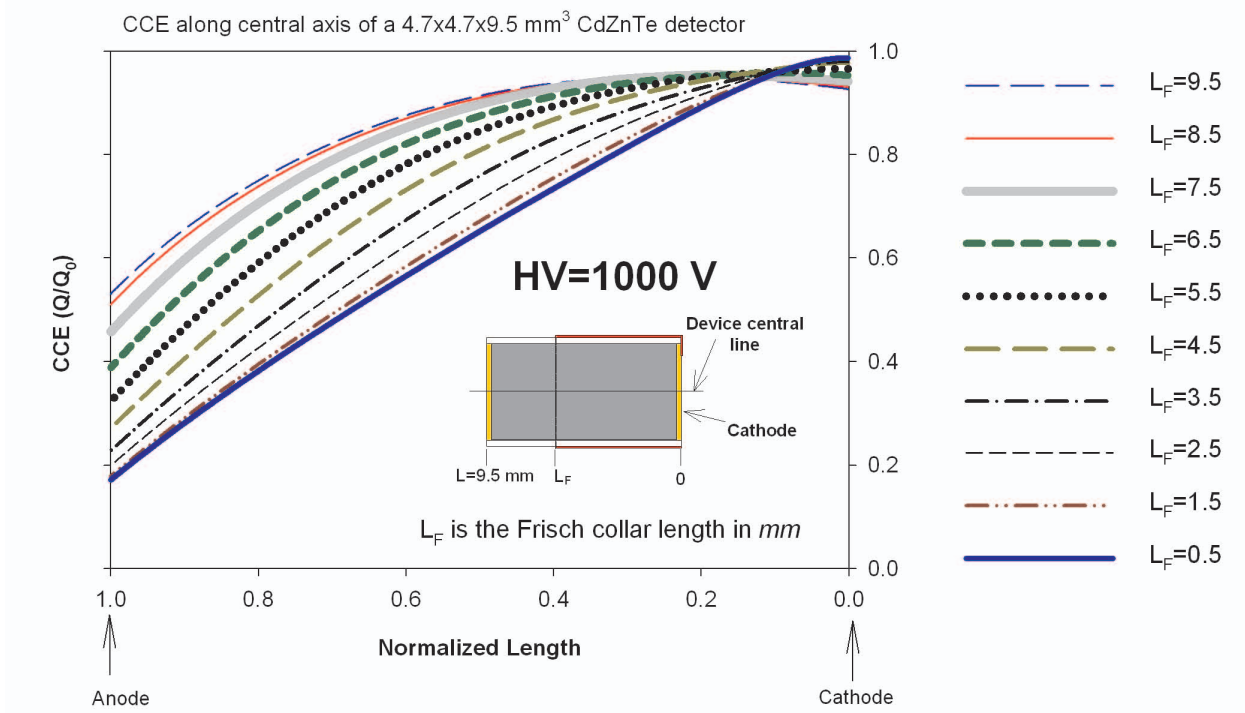


Figure 3.20: The charge collection efficiency CCE profile for a $4.7 \times 4.7 \times 9.5 \text{ mm}^3$ CdZnTe Frisch collar device (with $AR=L/W = 2.0$) along the central axis with different collar lengths.

3.2.1.3 Ratio of anode area to cathode area, small pixel effect

It is shown in Figs. 3.10 and 3.13 (Section 3.2.1.1) that devices with aspect ratios near 1.0 and lower, having weighting potential whose nonlinear property does not penetrate into the bulk of the device. The effect can be remedied by making the area of the anode smaller than that of the cathode, thereby allowing the device to benefit from the small pixel effect as well as Frisch collar effect. The simultaneous Frisch collar effect and small pixel effect enable the device to benefit from the nonlinearity of weighting potential and turn it into a single carrier device. Figs. 3.21, 3.22, and 3.23 show the weighting potential distributions, weighting field, and CCE plots for a $5.0 \times 5.0 \times 5.0 \text{ mm}^3$ CdZnTe Frisch collar device along the central line for three different anode to cathode area ratios.

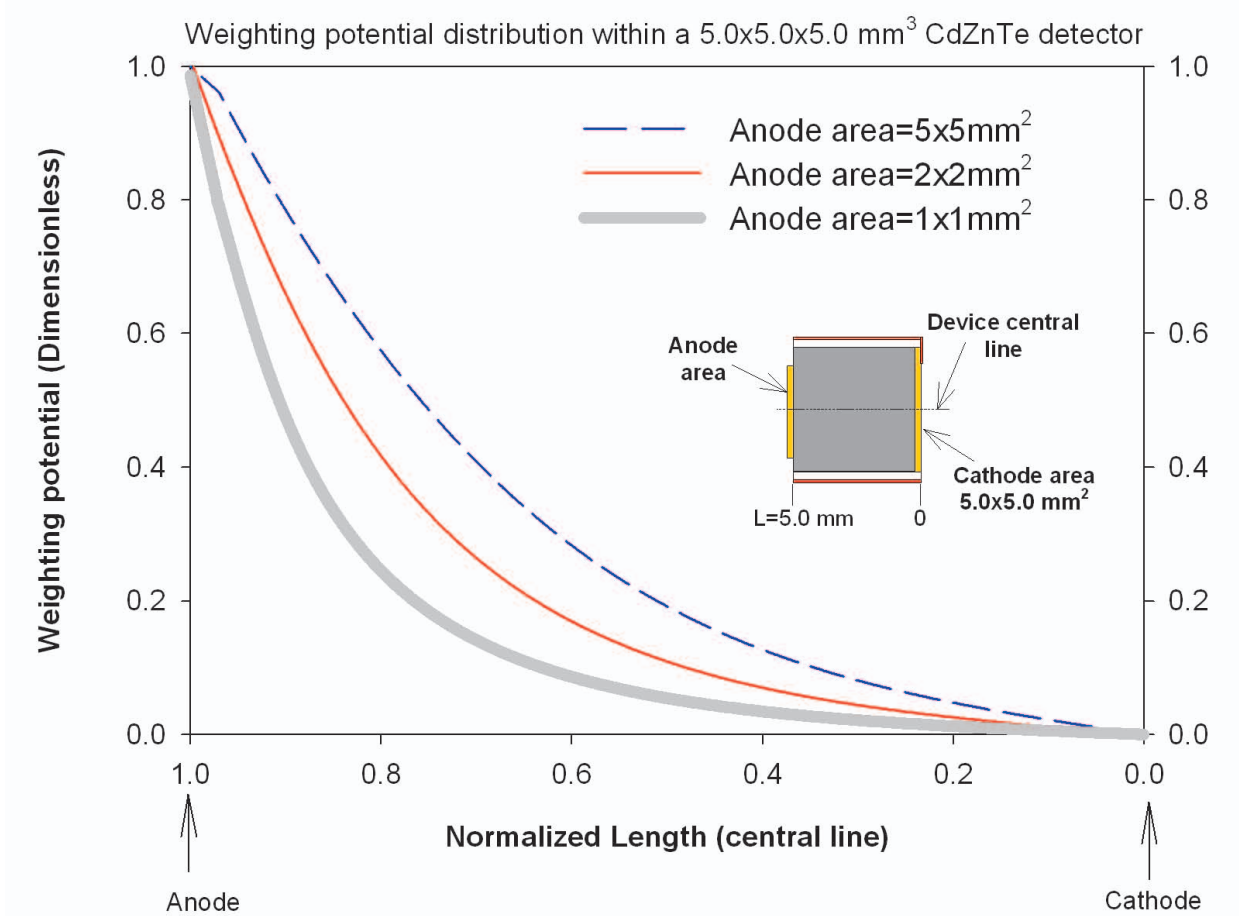


Figure 3.21: The weighting potential distribution for a $5.0 \times 5.0 \times 5.0 \text{ mm}^3$ CdZnTe Frisch collar device (with $AR=L/W = 1.0$) along the central axis with different anode areas. The distribution is calculated using LORENTZ considering a 0.35 mm insulator layer thickness. The graph shows the small pixel effect along with the Frisch collar effect on weighting potential distribution.

It is shown in Fig. 3.23 that for a $5.0 \times 5.0 \times 5.0 \text{ mm}^3$ CdZnTe device with small aspect ratios (around 1.0), where the Frisch collar effect is not prevalent, the small pixel effect can potentially turn the detector into a single carrier device. Fig. 3.23 indicates that decreasing the anode area enhances the *CCE* profile and offers a method to optimize the *CCE* for devices with aspect ratios less than 1.0.

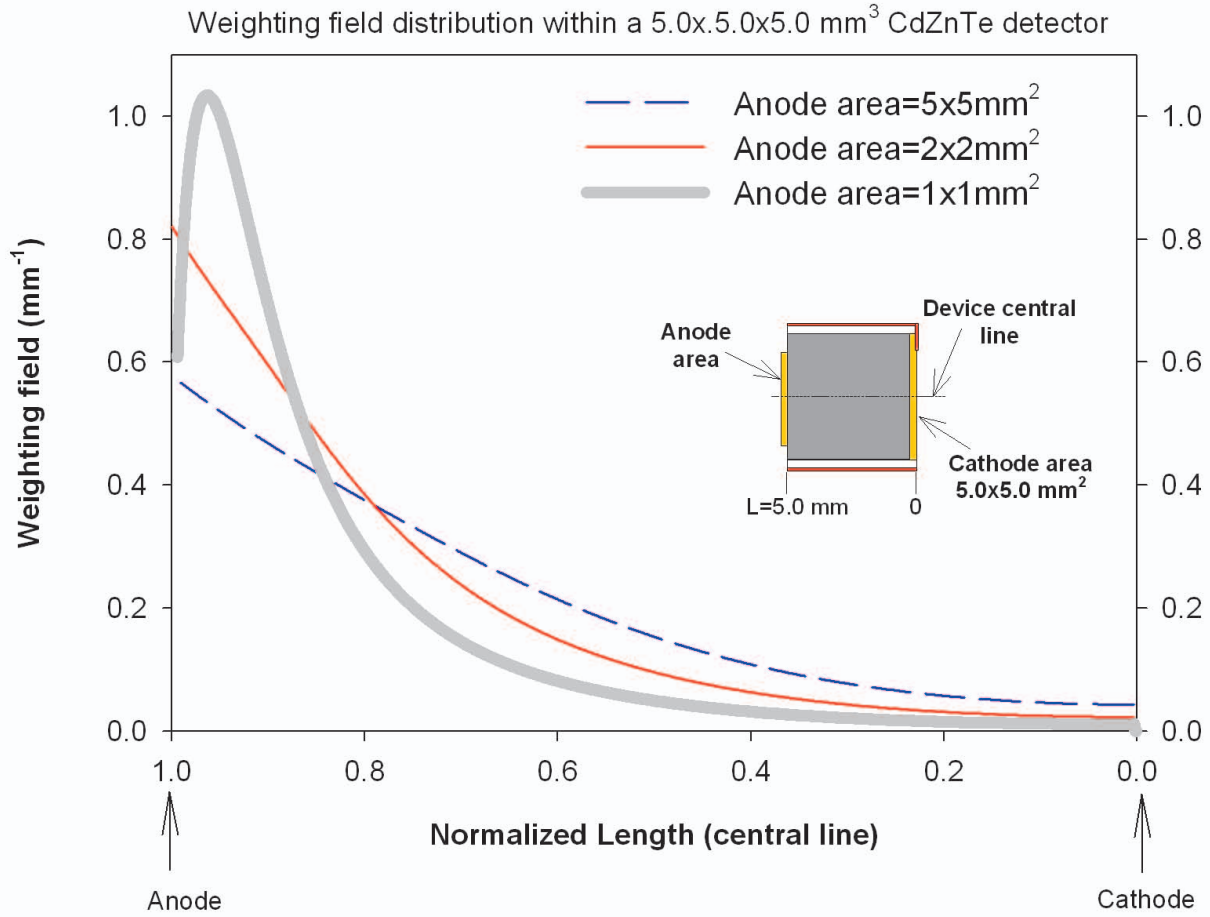


Figure 3.22: The weighting field distribution for a $5.0 \times 5.0 \times 5.0 \text{ mm}^3$ CdZnTe Frisch collar device (with $AR=L/W = 1.0$) along the central axis with different anode areas. The distribution is calculated using LORENTZ considering a 0.35 mm insulator layer thickness. The graph shows the small pixel effect along with the Frisch collar effect on weighting field distribution.

3.2.1.4 Thickness of insulator/dielectric layer

The thickness of the dielectric layer between the bare CdZnTe semiconductor crystal and the conductive collar has been reported to impact the device performance [20]. As the dielectric layer thickness of the two-terminal Frisch collar device increases, the overall device AR decreases. Correspondingly, a decrease in AR affects the uniformity of the weighting potential distribution (Section 3.2.1.1). Unfortunately, this change degrades the device performance,

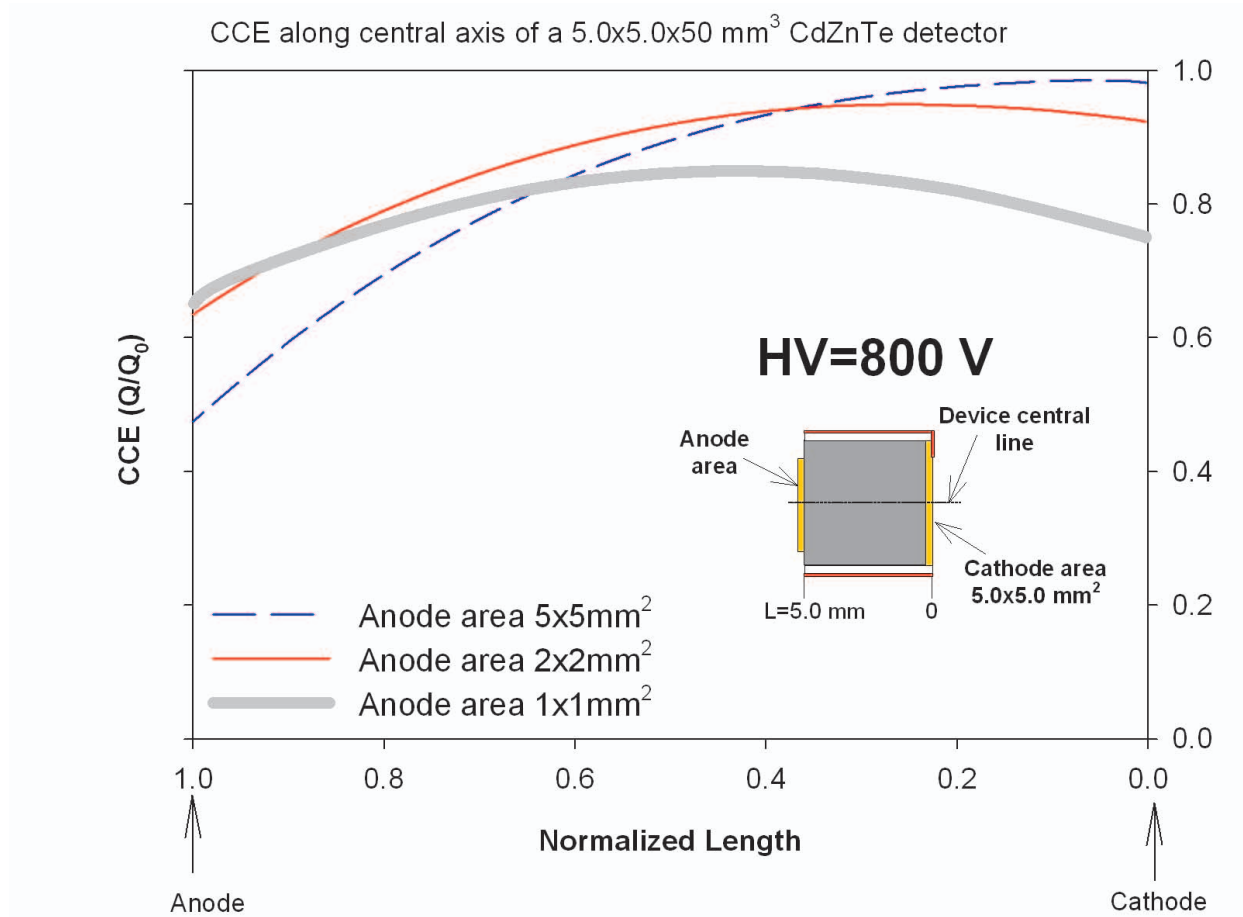


Figure 3.23: The charge collection efficiency CCE profile for a $5.0 \times 5.0 \times 5.0 \text{ mm}^3$ CdZnTe Frisch collar device (with $AR=L/W = 1.0$) along the central axis with different anode areas. The graph shows how the small pixel effect along with the Frisch collar effect alters the CCE profile.

especially if the aspect ratio of the device is significantly altered. Similarly, the great difference between the dielectric constant of CdZnTe and the insulator layer also forces the weighting potential toward a linear distribution as the dielectric thickness increases. However, the operating potential profile moves toward a linear distribution, thereby increasing the electric field near the cathode region, which improves the device performance by improving charge carrier transport. Hence, increasing the dielectric thickness has two different effects on device performance, whereby one effect improves device performance (electric field), and the other deteriorates device performance (weighting potential).

In this section, the impact of the insulator layer thickness on *CCE* plots is investigated. The results of simulations are confirmed through experimental data, presented in Chapters 4 and 5. Figs. 3.24, 3.25, and 3.26 show the weighting potential distributions, weighting field, and *CCE* plots for a $4.7 \times 5.0 \times 19.6 \text{ mm}^3$ CdZnTe device along the *central line* for different insulator thicknesses.

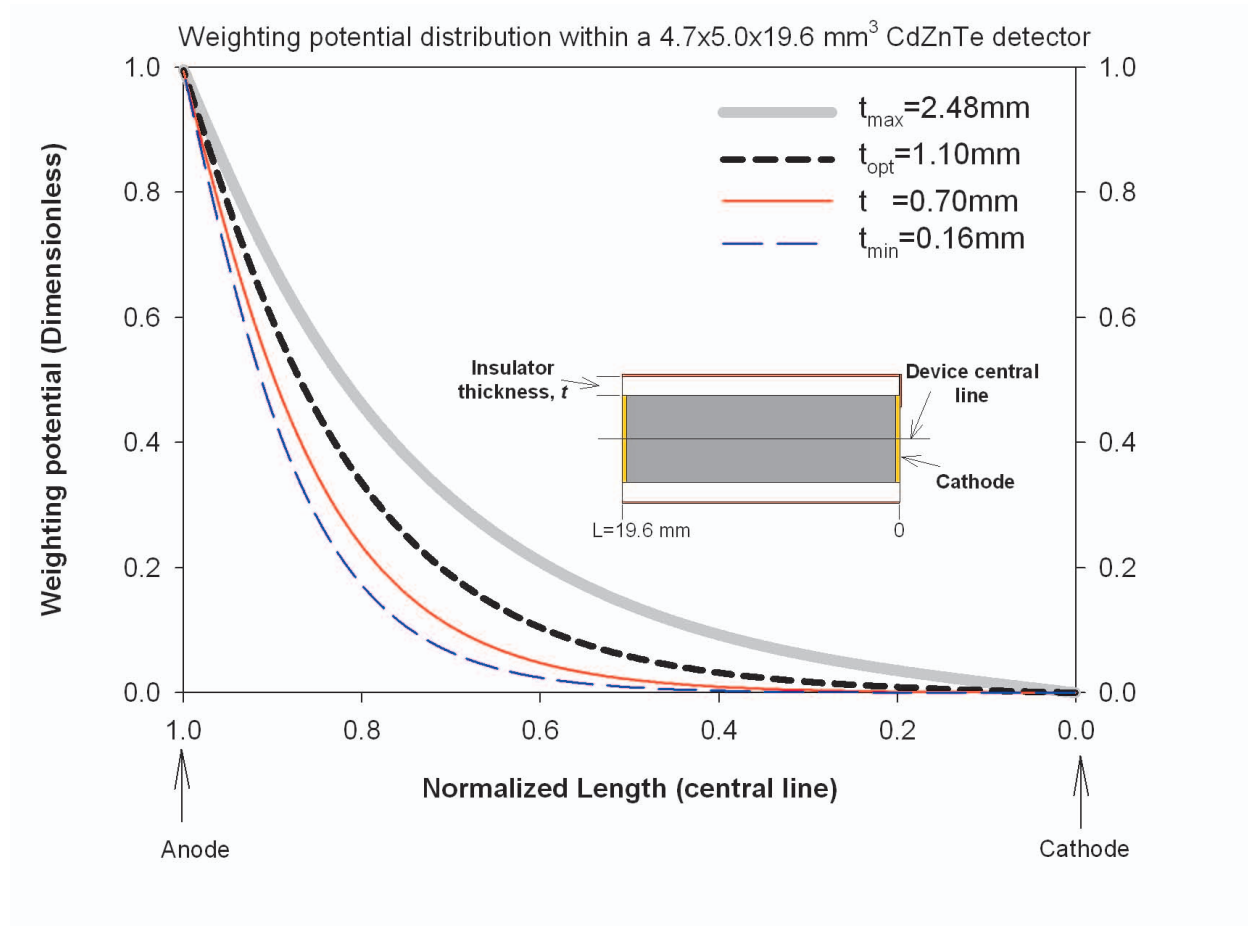


Figure 3.24: The weighting potential distribution for a $4.7 \times 5.0 \times 19.6 \text{ mm}^3$ CdZnTe Frisch collar device (with average aspect ratio $L/W = 4.0$) along the central axis with different insulator thicknesses. The distribution is calculated using LORENTZ.

Fig. 3.24 shows the *CCE* plots for the $4.7 \times 5.0 \times 19.6 \text{ mm}^3$ CdZnTe Frisch collar device along the central axis with different insulator layer thicknesses. The device has an $AR=4.0$, which results in low electric/weighting field distributions near the cathode region when applying a thin insulator layer (Fig. 3.25). Consequently, the *CCE* near the cathode

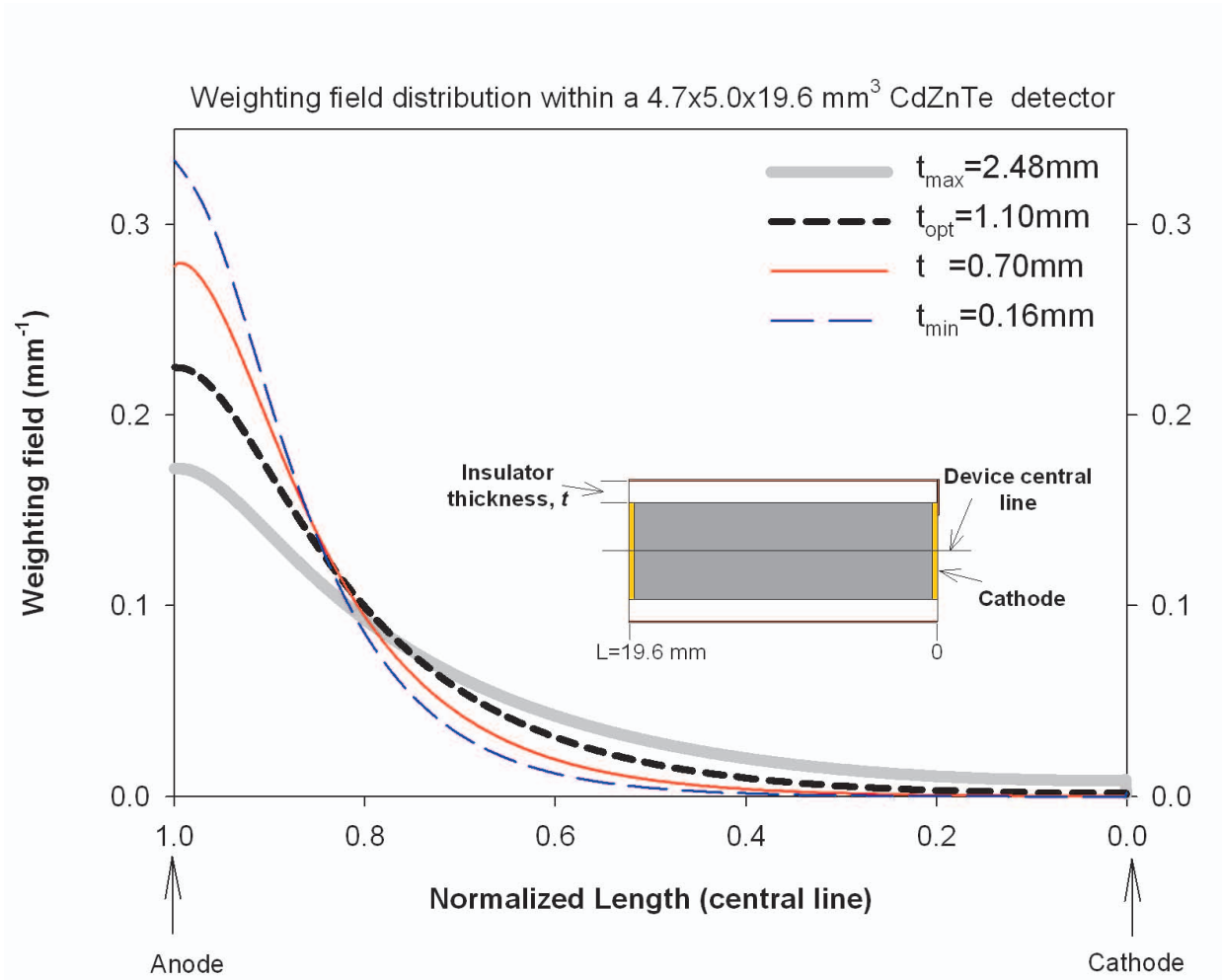


Figure 3.25: The weighting field distribution for a $4.7 \times 5.0 \times 19.6 \text{ mm}^3$ CdZnTe Frisch collar device (with average aspect ratio $L/W = 4.0$) along the central axis with different insulator thicknesses. The distribution is calculated using LORENTZ.

region is expected to be low, as plotted in Fig. 3.26. Fig. 3.26 indicates that increasing the dielectric layer thickness enhances the *CCE* profile and offers a method to optimize the device performance. Note that, for the simulations of the effect of insulator thickness on *CCE*, all other parameters (including the device geometry, Frisch collar length, applied bias, and material properties) are assumed to be the same.

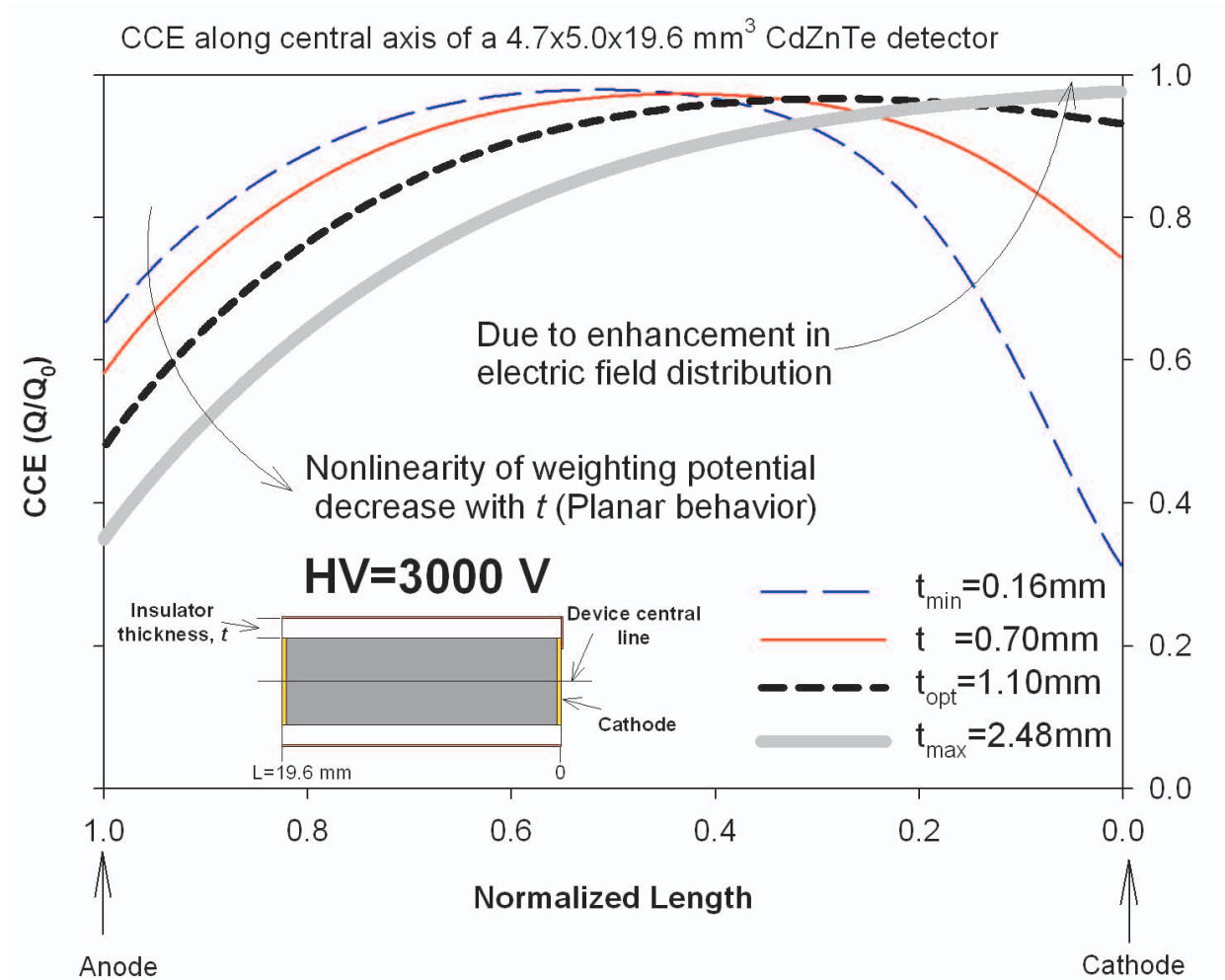


Figure 3.26: The charge collection efficiency CCE profile for a $4.7 \times 5.0 \times 19.6 \text{ mm}^3$ CdZnTe Frisch collar device (with average aspect ratio $L/W = 4.0$) along the central axis with different insulator layer thicknesses. The graph shows an optimum insulator layer thickness for the best CCE profile.

3.2.2 Effect of CdZnTe electrons/holes mobility-lifetime product on CCE

The electrical properties of the CdZnTe material, primarily the electron/hole mobility-lifetime products $\mu_{e,h}\tau_{e,h}$, are the most important material properties and have a great impact on device performance. The effect is investigated in this section through CCE modeling of a $4.7 \times 4.7 \times 9.5 \text{ mm}^3$ CdZnTe Frisch collar device. Since $\mu_{e,h}\tau_{e,h}$ have no direct effect on weighting potential and weighting field distributions, these distributions are similar

to those previously presented in Fig. 3.6. The numerical values of these distributions, previously presented in Section 3.1.3.1, are used to plot the CCE . Figs. 3.27 and 3.28 present the CCE profile for the $4.7 \times 4.7 \times 9.5 \text{ mm}^3$ CdZnTe Frisch collar device along the central axis for different values of $\mu_{e,h}\tau_{e,h}$.

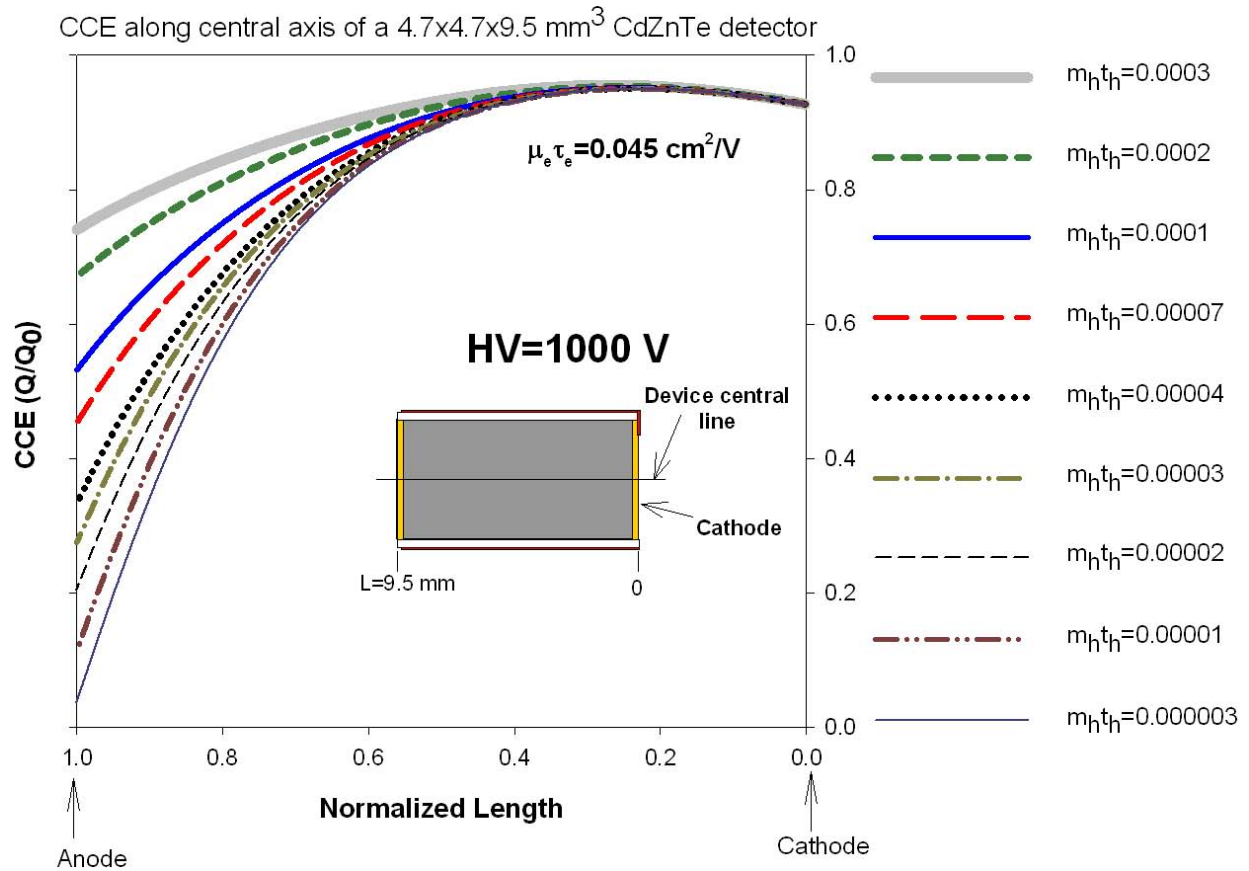


Figure 3.27: The charge collection efficiency CCE profile for a $4.7 \times 4.7 \times 9.5 \text{ mm}^3$ CdZnTe Frisch collar device (with $AR=L/W = 2.0$) along the central axis with different values for holes mobility-lifetime product $\mu_h \tau_h$. The plots show CCE enhancement for the higher values of $\mu_h \tau_h$.

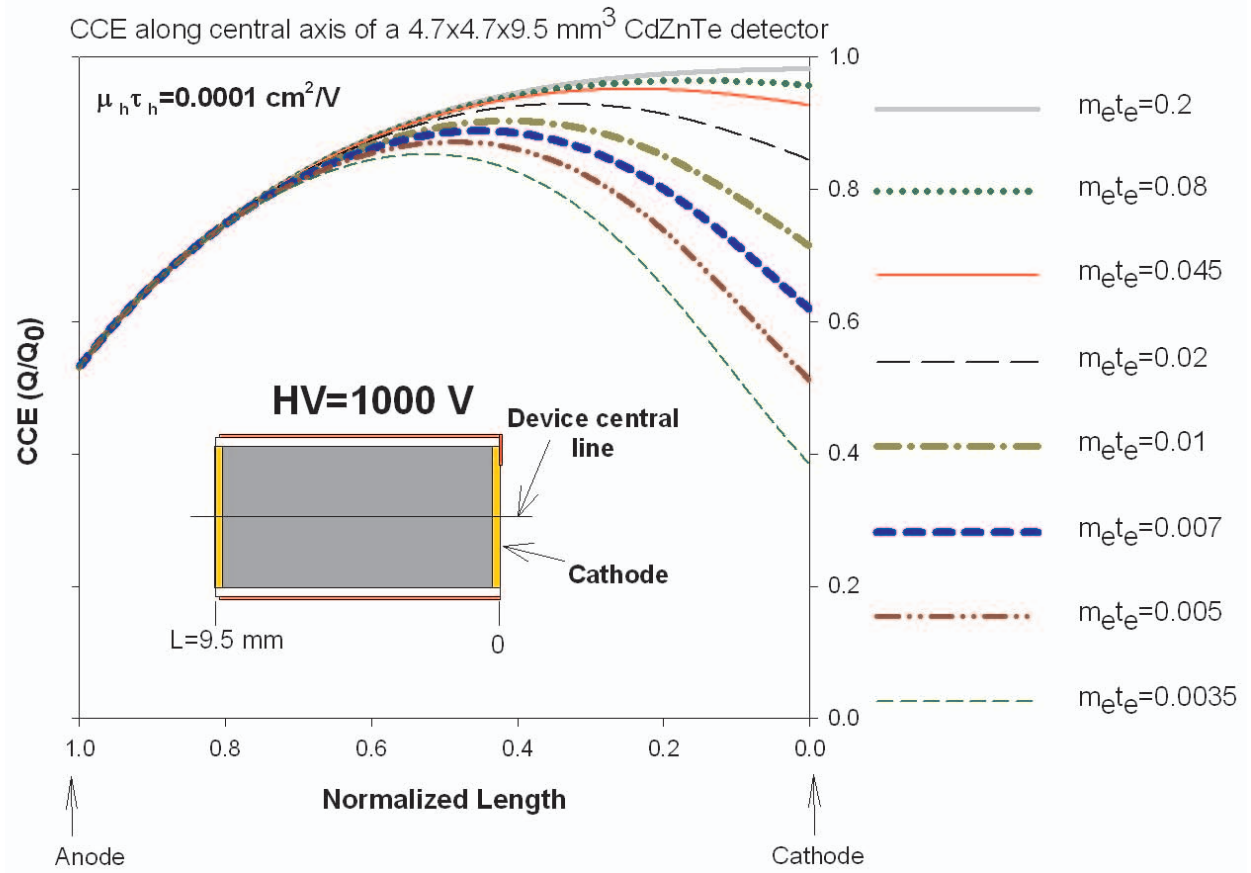


Figure 3.28: The charge collection efficiency CCE profile for a $4.7 \times 4.7 \times 9.5 \text{ mm}^3$ CdZnTe Frisch collar device (with $AR=L/W = 2.0$) along the central axis with different values for electron mobility-lifetime product $\mu_e \tau_e$. The plots show CCE deterioration for the lower values of $\mu_e \tau_e$.

Fig. 3.27 shows the impact of the $\mu_h \tau_h$ on CCE profiles, while the electron mobility-lifetime product is assumed to be constant ($\mu_e \tau_e = 0.045 \text{ cm}^2 \text{ V}^{-1}$). Similarly, Fig. 3.28 shows the impact of the $\mu_e \tau_e$ on CCE profiles, while the hole mobility-lifetime product is assumed to be constant ($\mu_h \tau_h = 0.0001 \text{ cm}^2 \text{ V}^{-1}$). However, the CCE plots in Fig. 3.27 and Fig. 3.28 show that the $\mu_h \tau_h$ has less impact on CCE (compare to $\mu_e \tau_e$), and consequently has less impact on device performance. The plots on Fig. 3.27 with low $\mu_h \tau_h$ values show that the CCE profiles remain relatively uniform for more than half the device volume. Whereas low $\mu_e \tau_e$ value deteriorates the CCE and device performance as in Fig. 3.28. Hence, CdZnTe Frisch collar device performance is limited by electron transport properties.

3.2.3 Effect of applied voltage (bias) on CCE

In semiconductor radiation detectors, the primary need of voltage is to separate the electrons and holes generated due to radiation interaction. As a result of existing voltage, the electrons and holes are drifted towards their corresponding electrodes. At low voltages (or electric fields) the electrons and holes recombine or undergo significant trapping. Consequently, little to no charge is induced on the collecting electrode. The secondary effect of applied voltage HV is its impact on the CCE profile after the electrons and holes are drifted toward corresponding electrodes. Fig. 3.29 shows the CCE profile for a $4.7 \times 4.7 \times 9.5 \text{ mm}^3$ CdZnTe Frisch collar device along the central axis at different applied voltages.

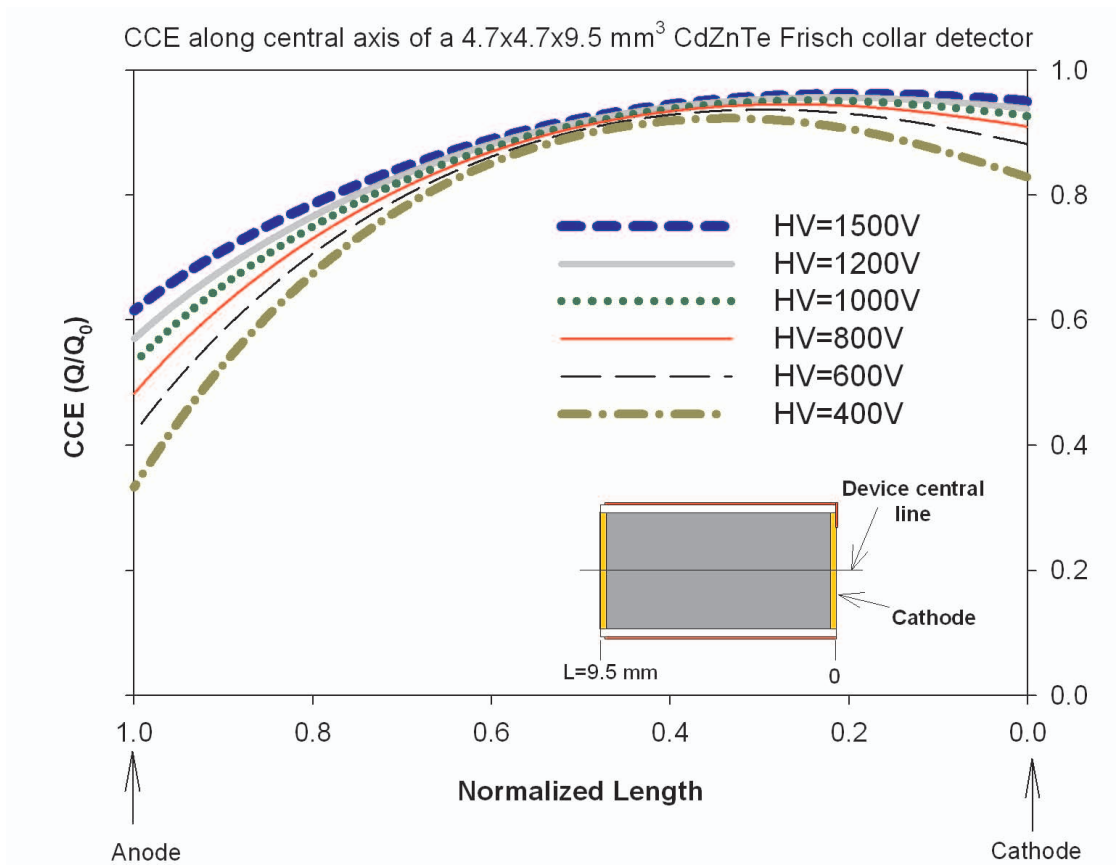


Figure 3.29: The charge collection efficiency CCE profile for a $4.7 \times 4.7 \times 9.5 \text{ mm}^3$ CdZnTe Frisch collar device (with $AR=L/W = 2.0$) along the central axis at different applied voltages. The plots show CCE is enhanced at higher voltages. The mobility-lifetime product $\mu_{e,h}\tau_{e,h}$ of 0.045 and $0.0001 \text{ cm}^2 \cdot \text{V}^{-1}$ are assumed for the electrons and holes, respectively.

The effect can be predicted through Equation 3.20, where higher applied voltages result in higher electric fields E and subsequently higher charge carrier velocities ($v_{e,h} = \mu_{e,h} E$). This allows better charge collection and greater change in induced charge ΔQ (Equation 3.29, page 23). Consequently, the CCE is enhanced for higher applied voltages (Fig. 3.29). The Frisch collar device is modeled under applied voltages of 1500V, 1200V, 1000V, 800V, 600V, and 400V to the collecting electrode (anode in this case). The plots in Fig. 3.29 shows that the CCE is enhanced at higher applied voltages. Fig. 3.29 also shows that above some voltage (about 1200V for this device) the CCE is not significantly enhanced, but rather reaches a relatively uniform and flat response. The experimental procedures and results for this effect are presented in Sections 4.3.3 and 5.2 .

3.2.4 Effect of crystal length on CCE

As mentioned earlier in this section, device length has a dual and complex impact on CCE . Primarily, crystal (device) length L directly affects device aspect ratio AR (L/W). Consequently, the change in AR significantly alters the weighting potential/weighting field distributions and affects the CCE . Alternatively, more charge carriers are trapped in a longer device with longer traveling distance, because the mobility-lifetime product of the charge carriers are limited. Hence, to exclusively study the impact of length on CCE , four different Frisch collar devices are assumed to have identical aspect ratios of 1.8 for simulation purposes. Figs. 3.30 and 3.31 show the weighting potential and the CCE profile along the central line of all devices with the same aspect ratios and different lengths.

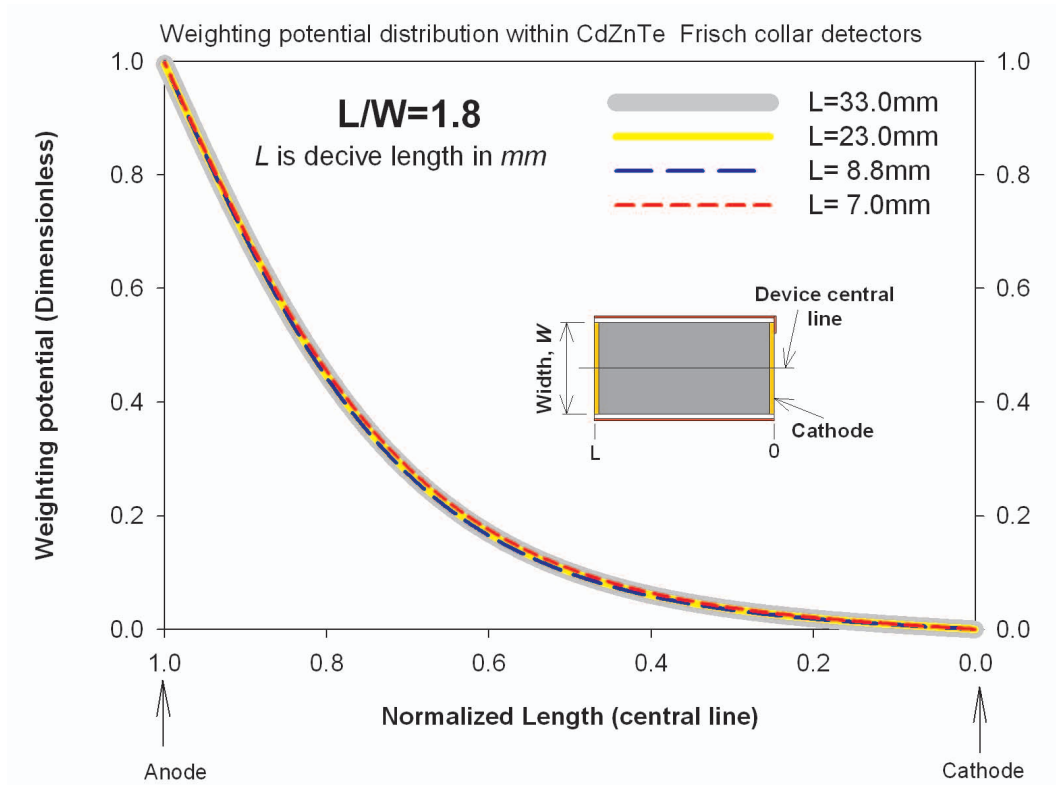


Figure 3.30: The weighting potential distribution along the central axis of CdZnTe Frisch collar devices with the same aspect ratios ($L/W = 1.8$) and different lengths. The distribution is calculated using LORENTZ considering different thicknesses of insulator layer proportional to Frisch collar devices lengths. The graph shows identical weighting potential distribution for devices with the same AR .

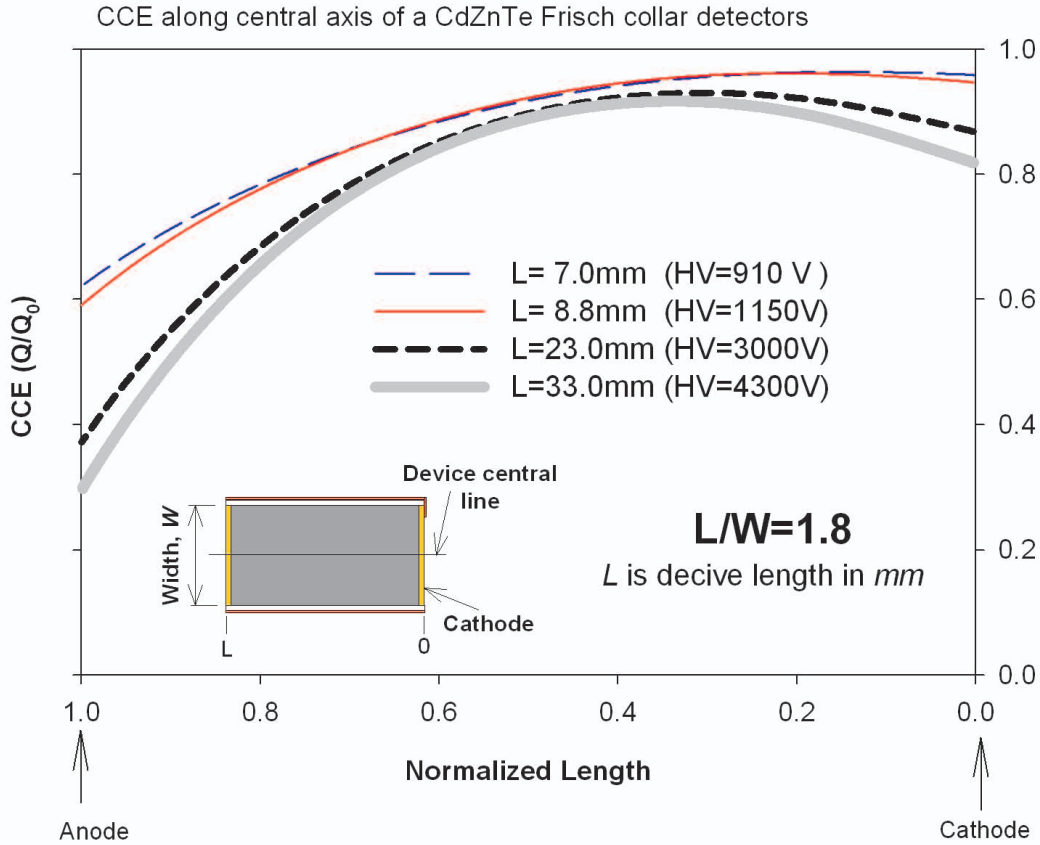


Figure 3.31: The charge collection efficiency CCE profile along the central axis of CdZnTe Frisch collar devices with the same AR ($L/W = 1.8$) and different lengths. The high voltages applied to the collecting electrode (anode) are proportional to Frisch collar device length. The plots show that CCE is enhanced for devices with shorter length. The $\mu_{e,h}\tau_{e,h}$ of 0.045 and $0.0001 \text{ cm}^2 \text{ V}^{-1}$ are assumed for the electrons and holes, respectively.

Three of the devices were actually fabricated and tested, and the experimental results are in Chapter 5. The largest Frisch collar device ($18.3 \times 18.3 \times 33.0 \text{ mm}^3$), however, was not fabricated due to lack of material. As expected, the weighting potential distributions are almost identical; however, the CCE plots are different. Due to similarity in shape with a known ratio of magnification for all four devices, the weighting potential distributions resemble each other. However, since longer devices suffer more from trapping effects, the CCE profiles are not the same, and shorter devices show more uniform response to gamma-rays (Fig. 3.31).

Chapter 4

EXPERIMENTAL PROCEDURES AND SETUP, CdZnTe DEVICE FABRICATION AND CHARACTERIZATION

This chapter offers a detailed description of the fabrication process of Frisch collar CdZnTe gamma-ray detectors, including alternative methods of each process. The chapter also discusses the methods to characterize the fabricated devices. Finally, the chapter details the experimental setup and characterization of a 16-channel CdZnTe Frisch collar detectors.

4.1 CdZnTe Detector Fabrication Process

The process of fabricating a CdZnTe Frisch collar detector can be divided into three main steps: planar device fabrication, post fabrication process (surface treatment) and conductive (Frisch) collar utilization. The planar device fabrication can be divided into mechanical treatment, chemical treatment, and contact deposition, which are detailed in Section 4.1.1 through Section 4.4. The post fabrication process (surface treatment) and the alternative methods are explained in Section 4.3.5, and applying an insulator and a conductive (Frisch) collar is detailed in Section 4.1.4.

4.1.1 Mechanical treatment

Bulk CdZnTe material acquired from Redlen Technologies and eV Products, labeled as counter grade, was used to fabricate several Frisch ring detectors. The material was initially inspected with an infrared (IR) microscope to locate regions containing relatively few visible defects. A diamond wire saw was then utilized to section volumes of low defect density from the bulk samples. The extracted pieces were next shaped through grinding and lapping into right parallelepipeds. The sliced material was first ground using an L-shaped stainless steel jig shown in Fig. 4.1, to form the piece into a rectangular bar shape. The L-shaped stainless steel jig was mounted on a stainless steel block as shown in Fig. 4.1.

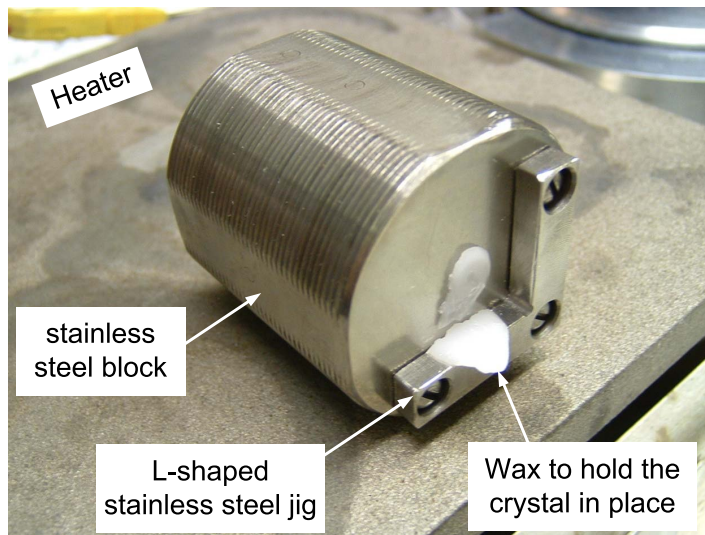


Figure 4.1: The stainless steel block and the L-shaped stainless steel jig used for grinding/lapping CdZnTe crystals.

Silicon carbide (SiC) papers of 2400 and 4000 grit were used in the grinding step and continuously cleaned by running water. This process was performed using a lapping machine, as shown in shown in Fig. 4.2. The ends of the bar-shaped crystals were hand lapped with alumina powders suspended in deionized (DI) water, starting with 3 μm powders, and after a progression of diminishing sized powders, ending with 0.05 μm powder on BUEHLER Chemomet polishing cloths (Fig. 4.3). The 1 μm and 0.3 μm alumina powder solutions

were used as intermediate polishing steps, and at least $1\ \mu\text{m}$ of material was polished away from each of the sides. Because mechanical polishing causes surface damage extending into the crystal bulk typically three times the size of the powder being used [49], it was important to remove all of the surface damage caused in the previous step. Afterwards, the samples were rinsed with DI water and isopropyl alcohol before chemical etching.

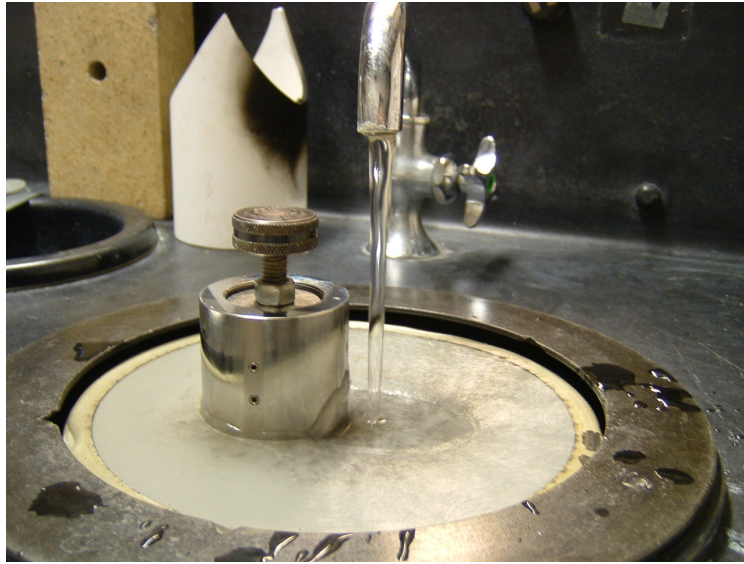


Figure 4.2: Lapping/grinding the CdZnTe crystals on the lapping machine



Figure 4.3: Polishing CdZnTe crystals on polishing pads

4.1.2 Chemical etching

The last step of mechanical polishing (0.05 μm powder) also causes surface damage; hence polishing was followed by a chemical etching step with a 2% volume of bromine/methanol solution for two minutes. The samples were then rinsed once more with isopropanol.

4.1.3 Contact deposition

Gold was deposited on the ends of the crystal to form the ohmic contacts through an electroless deposition technique using gold chloride (AuCl_3) solution. Gold was deposited by applying AuCl_3 solution for eight minutes on each contact. It is believed that the AuCl_3 reacts with the cadmium on surface of CdZnTe crystals based on the following reaction,



which results in the gold ions to be precipitated [50]. Then, the gold diffuses into the crystal introducing dopant sites which produces an ohmic (tunnelling) contact [51]. A sample of CdZnTe block undergoing electroless deposition (plating) is shown in Fig. 4.4.

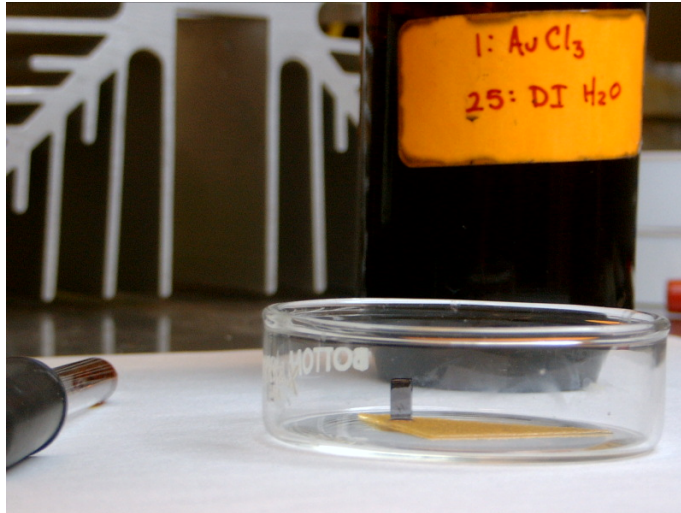


Figure 4.4: Contact deposition on CdZnTe crystals using gold chloride solution.

4.1.4 Applying insulator and Frisch collar to planar device

The planar detector was wrapped with thin Teflon tape, which acted as an insulating boundary. The Teflon was extended beyond the anode about 1.0 mm to avoid discharge between the collar and the anode. A thin copper shim was cut to size and used as the Frisch collar (Fig. 4.5), which extended the length of the device and was connected to the device cathode. In this manner, the Frisch collar was held at the cathode potential (or ground).

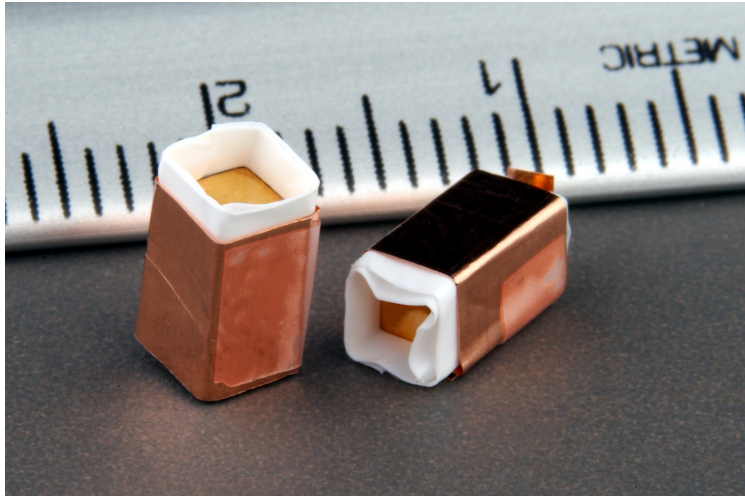


Figure 4.5: Fabricated CdZnTe Frisch collar detectors using copper shim and Teflon tape

The planar device can be turned into a Frisch collar device by applying any insulator layer that has high resistivity and low dielectric constant, and by applying a conductive layer on the insulator. The alternative processes for applying the insulator layer and conductive collar have been published previously in the literature [52]. In the method employed in [52], thin layers of Parylene-N and Parylene-C were deposited as the insulator layer using Specialty Coating Systems PDS 2010 LABCOTER 2. The conductive (Frisch) collar was also applied with conductive paint and sprays such as nickel-based paint, silver-based paint, and Silverdag.

4.2 CdZnTe Detector Characterization Methods

On fabricated devices, three main measurement methods are employed for characterization purposes: the leakage current, the pulse height spectrum, and the charge collection efficiency. For the devices with post fabrication processes (surface treatment), Scanning Electron Microscopy (SEM) analysis has been performed on the surfaces, which is mentioned in Section 4.2.4. Pulse height spectral measurements (Section 4.2.2) were conducted for each device reported in all studies. In spite of varied equipment for spectral measurement (especially preamplifiers), the main setup and Nuclear Instrument Modules are essentially the same. In this section, the general methods of taking a pulse height spectrum and measuring leakage current are explained. Later, sections describe individual measurements, the details of the equipment, and the differences in experimental procedures.

4.2.1 Leakage current measurement

A Keithley I-V Curve Tracer was used to perform the current-voltage (I-V) measurements. The machine automatically sweeps through voltage increments, with a delay at each point before logging a value. The delay at each point was set to 0.5 seconds for all studies, while the voltage increment was set from 2.0 to 5.0 V (varied for different studies). The maximum regulated voltage was set up to ± 1100 V depending on device size. The machine can perform the current-voltage measurement for devices with different configurations, such as bare and wired, in both planar and Frisch collar configurations. The Keithley I-V Curve Tracer is equipped with a platform (probe station) where the bare device (not wired) can easily be tested for an I-V curve. The machine can also be connected to an aluminum test box to measure the leakage current of wired devices (wired devices should be mounted inside the aluminum test box).

4.2.2 Pulse height spectra measurements

The fabricated CdZnTe detectors (both planar and Frisch collar) were positioned in an aluminum test box for spectral collection of various radionuclides (Fig. 4.6). The detector within the box was connected to a preamplifier (the type of preamplifier is mentioned in each study), and the aluminum test box and preamplifier were placed inside a copper Faraday cage to shield the test box from low energy electromagnetic waves and subsequently minimize electronic noise. The measurement system consisted of an amplifier, an oscilloscope, a multi-channel analyzer (MCA), a high voltage supply, a pulse generator, and a personal computer, all positioned outside the Faraday cage (Fig. 4.7). Gamma sources were always placed in the same position, either outside the aluminum test box (Fig. 4.6) or inside the aluminum test box, such that the detector cathode faced the source.

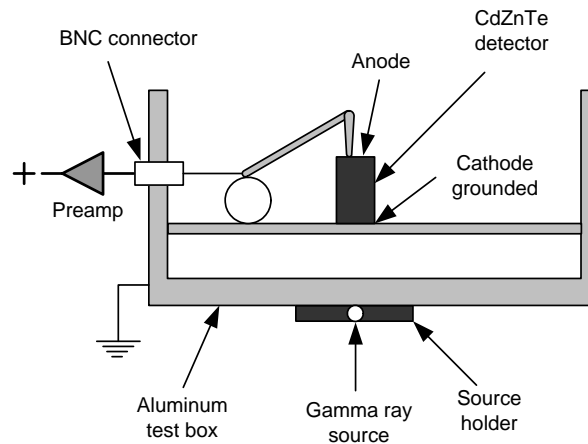


Figure 4.6: Diagram of the aluminum test box used for spectral measurements.

During the experiment, the temperature and the relative humidity were recorded for each study, and operating parameters were held constant throughout the entire individual experiments. Additionally, the amplifier shaping time of $1 \mu\text{s}$ was held constant for all studies, while the high voltage bias, amplifier gain, and the lower level discriminator (LLD) were varied in different studies depending on detector size, dead time, and system noise.

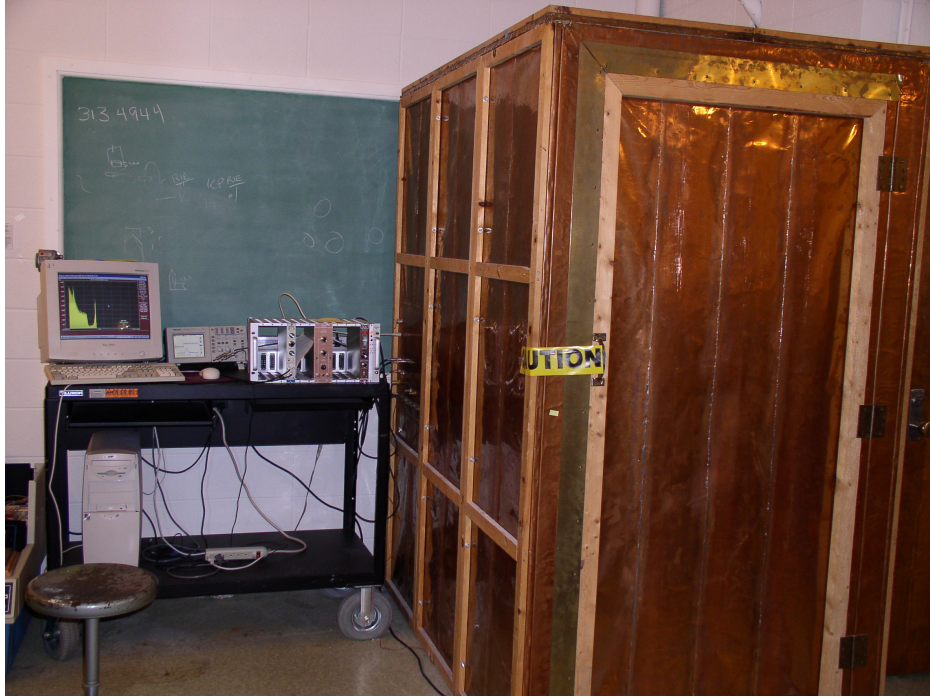


Figure 4.7: Copper Faraday cage and the NIM electronics outside the cage

Accordingly, the values of high voltage bias and amplifier gain are mentioned in each study separately. The spectral testing time also varied for different detectors and studies.

Pulse height spectra were collected from gamma-rays sources of ^{241}Am , ^{137}Cs , ^{57}Co , ^{133}Ba , ^{198}Au , and ^{235}U . The ^{241}Am , ^{137}Cs , ^{57}Co , and ^{133}Ba , samples were standard commercially available calibration sources. The ^{198}Au was prepared through an (n,γ) reaction by irradiating gold foil samples in the Kansas State University TRIGA Mk II nuclear reactor core (see Section 4.4.2.3). The ^{235}U source was in the form of a 93% enriched ^{235}U -nitride solution. As explained, the electronic settings were consistent for all measurements, and energy resolutions for gamma-ray photopeaks (see Chapter 5) are reported with no electronic corrections. While, the primary results of gamma-ray spectroscopy with CdZnTe detectors are reported in Section 5.1, the results of each individual study are presented in Chapter 5 under each study section.

4.2.3 Charge collection efficiency measurement

A $4.7 \times 4.7 \times 9.5$ mm³ CdZnTe Frisch collar device was fabricated as in Section 4.1, and the CdZnTe raw materials for this study were acquired from Redlen Technologies. A 43.0 mm long collimator was made by casting lead with a 0.6 mm diameter rod inserted, which was later removed, leaving behind a 0.6 mm hole. The 43.0 mm long Pb-collimator was designed to attenuate 99.6% of 662 keV gamma-rays, except for the solid angle of the 0.6 mm hole (Fig. 4.8). The 0.6 mm hole in the collimator allowed the CdZnTe detector to be fully irradiated for a 0.72 mm diameter circular area (Fig. 4.9). The Pb-collimator was mounted on a linear stage with two degrees of freedom (Fig. 4.10). This way, the $4.7 \times 4.7 \times 9.5$ mm³ CdZnTe Frisch collar device could be probed by the highly collimated ¹³⁷Cs gamma-ray source with a desired increment along the device length and width, which are illustrated in Fig. 4.9. The Frisch collar device was irradiated for seven columns (1 through 7) along the device length (9.5 mm) and for three rows (*r*, *t* and *v*) along the device width (4.7 mm). The Frisch collar detector was also placed 8.7 mm away from the Pb-collimator (Fig. 4.8) and was held in place for the entire experiment (Fig. 4.10). The ¹³⁷Cs gamma-ray source was placed between the collimator and the linear stage so that the source was aligned with the collimator hole. The detector, gamma-ray source, Pb-collimator, and linear stage were placed inside an aluminum test box (see Fig. 4.10).

Before the probing experiment began, pulse height spectra were taken using a ¹³⁷Cs gamma-ray source placed directly underneath the fabricated CdZnTe device (both planar and Frisch collar configurations). The pulse height spectra for full irradiated with 662 keV gamma-rays are shown in Fig. 3.8, which also shows the sub-0.9% full width half maximum (FWHM) energy resolution at 662 keV for the Frisch collar device (with no electronic correction) using a commercial ORTEC 142A preamplifier. The measurement setups and the counting time are also indicated in Fig. 3.8.

Afterwards, the $4.7 \times 4.7 \times 9.5$ mm³ CdZnTe Frisch collar device was probed with a highly collimated ¹³⁷Cs gamma-array source to investigate the uniformity of the Frisch collar

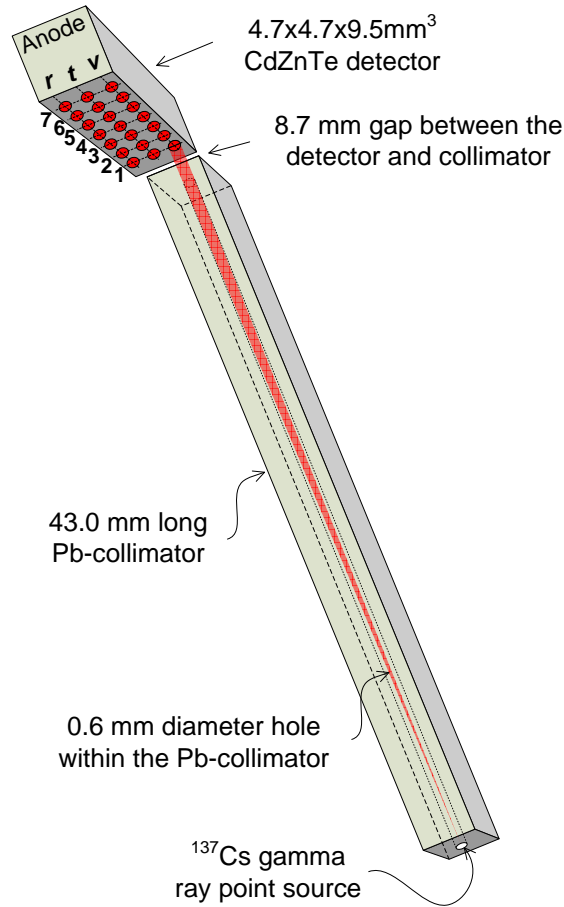


Figure 4.8: The schematic setup for the gamma-ray source, Pb-collimator, and the $4.7 \times 4.7 \times 9.5 \text{ mm}^3$ CdZnTe Frisch collar detector for the *CCE* measurement. A $2 \text{ MBq } ^{137}\text{Cs}$ gamma-ray source was placed at the end of a 0.6 mm circular hole in a 43.0 mm long Pb-collimator. The CdZnTe Frisch collar detector was held in place 8.7 mm away from Pb-collimator. The Pb-collimator and gamma-ray source were mounted on a linear stage with two degrees of freedom to irradiate desired points shown on the CdZnTe device.

device's response to high energy gamma-rays. The following setup and testing equipment were used for the probing experiment. The aluminum test box was connected to an eV-550 preamplifier through an SHV connector. The aluminum test box and the preamplifier were then placed inside a copper Faraday cage where the preamplifier was connected to a high-voltage supply amplifier (Canberra Model 2021) and a pulse generator. An oscilloscope, a multichannel analyzer (MCA), and a personal computer were used to monitor and acquire the data.

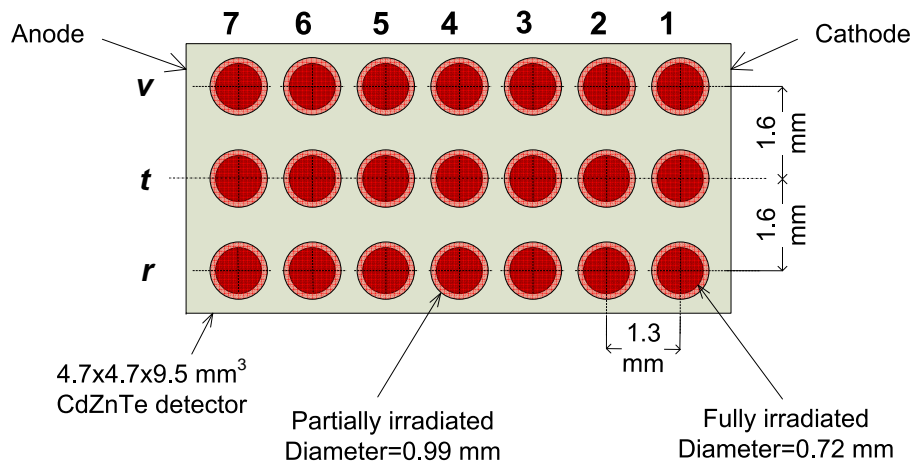


Figure 4.9: The irradiated points on the $4.7 \times 4.7 \times 9.5 \text{ mm}^3$ CdZnTe Frisch collar device for the *CCE* measurement. The collimated gamma-ray source on a linear stage allows irradiating the desired points shown on the CdZnTe device. Here, the Frisch collar device was irradiated in increments of 1.3 mm along the length and 1.6 mm along the width. The partially irradiated area is due to the size of the ^{137}Cs gamma-ray source, which was comparable to that of the collimator hole (0.6 mm).

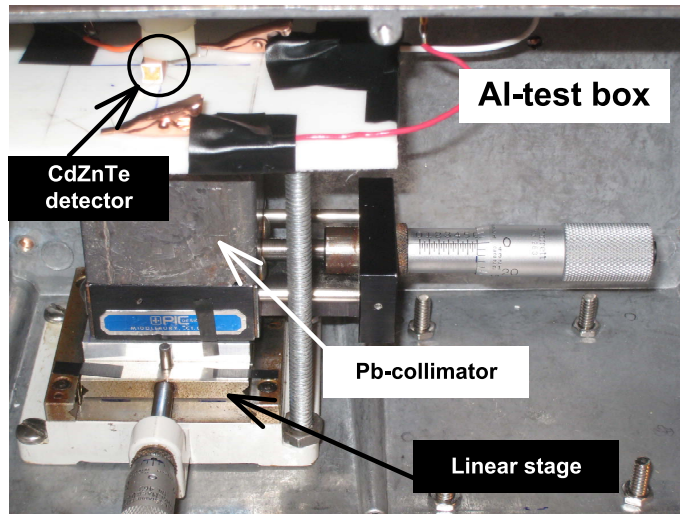


Figure 4.10: The lead collimator-detector setup within the aluminum test box for the *CCE* measurement. As shown the Pb-collimator is mounted on a linear stage with two degrees of freedom, and the CdZnTe Frisch collar detector is held in place immobile, ready to be probed by the highly collimated gamma-ray.

To conduct the probing experiment, the device's lateral side (columns 1 through 7 and rows r , t and v on Figs. 4.8 and 4.9) was probed with collimated 662 keV gamma-rays, and pulse height spectra were taken for two hours real time while the device was biased at 1200V (twenty one data points). Displacement of the source was performed by moving the collimated source using the two-dimensional linear stage in increments of 1.3 mm along the device length (columns 1 through 7 on Figs. 4.8 and 4.9), and increments of 1.6 mm along the device width (rows r , t and v on Figs. 4.8 and 4.9). The resulting pulse height spectra are presented in Section 5.2, consisting of 21 data points, with the detector at 1200V. Each individual measurement was two hours long.

4.2.4 Surface analysis

A Hitachi S-3400N Scanning Electron Microscope (SEM) was used in conjunction with an IXRF EDS2008 detector and its commercial software using Energy Dispersive Spectroscopy (EDS) as part of the Electron Microprobe (EMP) technique. The detector was positioned within the SEM such that approximately 25% of the surface area was imaged using the EDS. An acceleration of 10 kV and 70 mA was used for the electron source, and a Gaussian curve fit algorithm was selected for peak fitting. Additionally, automatic element selection as well as manual peak identification for Cd, Zn, and Te were performed, allowing a count rate of approximately 3000 counts per second over a two minute collection time. This characterization was conducted for the post fabrication surface treatment on devices in Section 4.3.5, and the results of surface analysis are presented in 5.3.4.

4.3 Investigating Parameters Affecting CdZnTe Frisch Collar Device Performance

In this section the parameters that affect the performance of CdZnTe Frisch Collar devices are experimentally investigated. Among these are the crystal geometry (aspect ratio and length), insulator layer thickness, high voltage, crystal, and surface treatment.

4.3.1 Effect of crystal aspect ratio on performance of CdZnTe Frisch collar devices

To investigate the effect of crystal aspect ratio on performance of CdZnTe Frisch collar devices, specific designs were considered to fabricate the required devices. The CdZnTe crystal was then sliced and fabricated into the designed devices. The experimental procedure for device preparation and testing (current voltage characteristic measurement and pulse height spectrum measurement) are detailed in this section.

4.3.1.1 Device designs

A specific strategy was followed to investigate the effect of the crystal aspect ratio on Frisch collar devices' spectral performance. Specifically, many devices were fabricated and tested in both planar and Frisch collar configurations. Fig. 3.9 shows the slicing pattern on the starting CdZnTe crystal to prepare the designed device. The details of device preparation and testing are explained in sections 4.3.1.2 and 4.3.1.3. Note that for every single fabricated device, the same series of spectral measurements was performed for both planar and Frisch collar configurations. However, the current-voltage characteristic measurements were only performed for bare devices. This section details the device designs and dimensions for all of the fabricated CdZnTe detectors.

A piece of CdZnTe crystal ($19.08 \times 19.34 \times 4.95 \text{ mm}^3$) was acquired from Redlen Technologies and was polished. Initially, the device was fabricated as a planar detector (CZT1 in Fig. 3.9) and subsequently a Frisch collar detector. Thus, CZT1 is the starting CdZnTe device for this investigation. To fabricate the required devices, CZT1 was sliced into

smaller crystals and fabricated into planar devices. The device length L was kept constant, and the device width W was reduced, thereby increasing the aspect ratio (L/W). The second device prepared is also illustrated in Fig. 3.9 and labeled as CZT5. However, the dimensions and names of subsequently fabricated detectors are in Table 3.1. The operating conditions and gamma-ray sources used for this study are also in Table 4.1.

Table 4.1: The operating voltage applied to the detectors and the spectral testing time for the Frisch collar geometry effect study.

Detector name	Applied bias (V)	Spectral testing time (s)
CZT1	800 (400 for ^{241}Am)	1800 for ^{137}Cs -900 for ^{241}Am
CZT5	800	1800 for ^{137}Cs -900 for ^{241}Am
CZT6	800	3600 for ^{137}Cs -1800 for ^{241}Am
CZT7	800	5200 for ^{137}Cs -2600 for ^{241}Am
CZT8	800	7200 for ^{137}Cs -3600 for ^{241}Am
CZT9	800	9000 for ^{137}Cs -4500 for ^{241}Am
CZT10	800	10800 for ^{137}Cs -5400 for ^{241}Am
CZT11	800	12600 for ^{137}Cs -6300 for ^{241}Am

4.3.1.2 Device preparation

The CdZnTe devices were prepared as in Section 4.1. Again, the same fabrication process was applied in each step to prepare the smaller device. Then, the lateral sides of the devices were polished with a final slurry of 1.0 μm powder. The ends, however, were finished with a fine slurry of 0.05 μm powders. Lapping and polishing was concluded when the detector dimensions reached the final desired dimensions summarized in Table 3.1. Next, current-voltage (IV) measurements and spectral measurements were performed on the planar devices. The Frisch collar device was prepared by wrapping the planar device with two layers of thin Teflon tape slightly past the full length of the device. Next, a thin Copper shim was applied as the Frisch collar covering the full length of the device and subsequently connected to the device cathode. After taking spectral measurements on the Frisch collar device, the detector was resized (through slicing/grinding) to form the subsequent detector dimensions.

4.3.1.3 Device testing: spectral measurement

The pulse height spectra for two cases of planar and Frisch collar devices were acquired using standard calibration gamma-ray sources of ^{241}Am and ^{137}Cs . The CdZnTe detectors (planar and Frisch collar), were placed in an aluminum test box for spectral collection, while the detector cathode faced the gamma-ray source, which was placed in the same location outside the aluminum test box as in Fig. 4.6. The aluminum test box was then connected to an Ortec model 142A preamplifier through a BNC connector, and both were placed inside a Copper Faraday cage, which shields the low energy electromagnetic waves and subsequently minimizes the noise. The preamplifier was connected to a high-voltage supply, amplifier, and pulse generator sitting outside of the Faraday cage. An oscilloscope, a multichannel analyzer (MCA), and a personal computer were used to monitor and acquire the data. The temperature and the relative humidity were recorded as $27\pm 1^\circ\text{C}$ and $60\pm 1\%$, respectively for all experiments. An amplifier gain of 106 and shaping time of $1\ \mu\text{s}$ were held constant for the spectral measurements and the amplifier polarity was set to positive. The operating high voltage bias was kept at 800 V (except for the one case mentioned in Table 4.1) and kept the same for either detector whether planar or Frisch collar. The operating biases are listed in Table 4.1. The spectral testing time also varies for different detectors. The spectra were taken for a longer period of time for the smaller detectors to maintain good counting statistics. The spectral testing times are listed in Table 4.1. The spectra for all devices are presented in Section 5.3.1.

4.3.2 Effect of insulator layer thickness on performance of CdZnTe Frisch collar devices

4.3.2.1 Device designs and preparation

To determine the effect of insulator (dielectric) thickness on the performance of Frisch collar CdZnTe devices, six planar devices in a variety of sizes were fabricated from raw CdZnTe materials acquired from Redlen Technologies and with different dielectric layer thicknesses. The planar devices were labeled as Device 1 through Device 6. The sizes of the planar devices and the names of the subsequently fabricated Frisch collar devices are given in Table 4.2.

Table 4.2: The device names and dimensions to study the effect of insulator layer thickness on performance of CdZnTe Frisch collar devices. The aspect ratio is the planar device length L over device *average* width W .

Planar Device Name	Dimension (mm)	No. of Frisch Collar Devices	Frisch Collar Device Names	Aspect Ratio
Device 1	$4.95 \times 4.76 \times L=4.87$	4	Device 1 #1 to #4	1.0
Device 2	$4.70 \times 4.56 \times L=6.03$	4	Device 2 #1 to #4	1.3
Device 3	$3.36 \times 3.34 \times L=5.68$	6	Device 3 #1 to #6	1.7
Device 4	$3.96 \times 4.01 \times L=11.60$	13	Device 4 #1 to #13	2.9
Device 5	$3.92 \times 3.89 \times L=10.82$	11	Device 5 #1 to #11	2.8
Device 6	$5.01 \times 4.73 \times L=19.63$	7	Device 6 #1 to #7	4.0

Both planar and Frisch collar devices were prepared as in Section 4.1, and Teflon tape was used as the dielectric layer. Then, the dimensions of each Teflon-wrapped device were measured using a micrometer to evaluate the thickness of the dielectric layer. Once the dielectric layer was applied, the conductive copper shim was cut to size and used as the Frisch collar covering the entire lateral surface of the device and connecting to the device cathode. As each Frisch collar device was prepared, a spectral performance measurement was conducted. The conductive collar was then removed to fabricate each next Frisch collar device by either adding or removing Teflon layer(s). Finally, a new conductive copper shim

was added to complete the new Frisch collar device. The dielectric layer thicknesses for Device 1 to Device 6 in Frisch collar configurations are also summarized in Table 4.3.

Table 4.3: The insulator layer thickness for Device 1 to Device 6.

Frisch collar #	Dielectric Thickness, t in (mm)					
	Device 1	Device 2	Device 3	Device 4	Device 5	Device 6
#1	0.27	0.27	0.38	1.54	1.36	2.5
#2	0.16	0.16	0.32	1.34	1.16	1.6
#3	0.1	0.1	0.27	1.14	0.95	1.4
#4	0.05	0.05	0.22	0.94	0.81	1.25
#5	N/A	N/A	0.16	0.8	0.7	1.1
#6	N/A	N/A	0.1	0.7	0.6	0.95
#7	N/A	N/A	N/A	0.59	0.5	0.45
#8	N/A	N/A	N/A	0.5	0.39	N/A
#9	N/A	N/A	N/A	0.38	0.27	N/A
#10	N/A	N/A	N/A	0.27	0.16	N/A
#11	N/A	N/A	N/A	0.22	0.08	N/A
#12	N/A	N/A	N/A	0.16	N/A	N/A
#13	N/A	N/A	N/A	0.08	N/A	N/A

4.3.2.2 Device testing: current-voltage characteristic and spectral measurement

Two measurements were taken with each device: a ^{137}Cs pulse height spectrum and a current-voltage (I-V) curve as explained in Sections 4.2.1 and 4.2.2. The I-V curve measurement was performed only for the planar devices, while a ^{137}Cs spectrum was recorded for every device in all planar and Frisch collar configurations.

The pulse height spectra were acquired for devices in both planar and Frisch collar configurations using standard ^{137}Cs calibration sources. The CdZnTe detectors were mounted in an aluminum test box such that the detector cathode faced the gamma-ray source, which was placed outside the project box, except for Device 6, in which the source was placed directly underneath the detector. The aluminum test box was then connected to a preamplifier with an appropriate connector. Device 1 to Device 3 were tested using an ORTEC 142A preamplifier through a BNC connector, while Device 4 to Device 6 were tested using

a Canberra 2001A preamplifier through an SHV connector. The aluminum test box and the preamplifier were then placed inside a copper Faraday cage to minimize electronic noise, and the preamplifier was connected to a high-voltage supply, amplifier (Canberra Model 2021), and a pulse generator. An oscilloscope, a multichannel analyzer (MCA), and a personal computer were used to monitor and acquire the data.

The temperature and the relative humidity were recorded as $23\pm 2^\circ$ C and 50 ± 5 %, respectively for all experiments, and an amplifier shaping time of $1 \mu\text{s}$ was held constant for all spectra collected. However, the amplifier gain, the operating bias, and the device to source distance were different. The bias was held constant for each device when operated either as a planar or as a Frisch collar device. While data collection time varied for different detectors, collection time was the same for each device in both planar and all Frisch collar configurations. Settings and data collection times are in Table 4.4, and the results of the spectral measurements are discussed in Section 5.3.2.

Table 4.4: The experimental setup to study the effect of insulator layer thickness on the performance of CdZnTe Frisch collar devices. A different standard ^{137}Cs gamma-ray source was used for Device 6, and only this device was placed directly on the source.

Planar Device Name	Amplifier Gain	Bias (V)	Device to Source Distance (mm)	Real Time (s)
Device 1	100X	736	23.6 ± 0.1	3600
Device 2	100X	905	23.6 ± 0.1	3600
Device 3	100X	1000	23.6 ± 0.1	3600
Device 4	50X	1600	20.8 ± 0.1	1800
Device 5	50X	1500	20.8 ± 0.1	1800
Device 6	10X	3000	0	900

The I-V Curve Tracer was used to perform the I-V curve measurements (as in Section 4.2.1) with the voltage increment set to 5.0 V and the delay at each voltage point set to 0.5 seconds. Additionally, the maximum/minimum regulated voltage was set to ± 1000 V for these measurements. The results of the I-V curve measurements are in Section 5.3.2.

4.3.3 Effect of high voltage on performance of CdZnTe Frisch collar devices

The CdZnTe Frisch collar device was probed with a ^{137}Cs gamma-ray source at different high voltages as mentioned in Section 4.2.3. Specially, the $4.7 \times 4.7 \times 9.5 \text{ mm}^3$ CdZnTe Frisch collar device in Section 4.2.3 was probed along the central line (row t on Figs. 4.8 and 4.9) at 1000V, 600V, 800V and 400V with collimated 662 keV gamma-rays. Pulse height spectra were taken for one hour real time at each radiated point for the previously mentioned high voltages with the highly collimated ^{137}Cs gamma-ray source. The resulting pulse height spectra are presented in Section 5.2.

4.3.4 Effect of crystal length on performance of CdZnTe Frisch collar devices; experimental procedures and setups

The device preparation for this study is the same as that presented in Section 4.3.1; however, the aspect ratios of the fabricated devices are unchanged (see Fig. 4.11). Accordingly, two devices (Device ii to Device iii) were fabricated and tested through reshaping, Device iii being fabricated from resizing Device ii . However, another device (with the same aspect ratio) was fabricated from a separate ingot (Device i). During fabrication, the aspect ratio was unchanged ($L/W = 1.8$) by shortening both device length and width. The designed slicing/grinding patterns to fabricate the detectors are illustrated in Fig. 4.11, and the fabricated CdZnTe Frisch collar detectors names and dimensions are in Table 4.5.

Next, the pulse height spectra for two cases of planar and Frisch collar devices were acquired by using a standard calibration gamma-ray source of ^{137}Cs . The CdZnTe detectors (planar and Frisch collar) were placed in an aluminum test box for spectral collection, while the detector cathode faced the gamma-ray source. The test box was then connected to a preamplifier with an appropriate connector. Device i was tested using a Canberra 2001A preamplifier through an SHV connector, while Device ii and Device iii were tested using an ORTEC 142A preamplifier through a BNC connector. The aluminum test box and the preamplifier were then placed inside a copper Faraday cage to minimize electronic noise

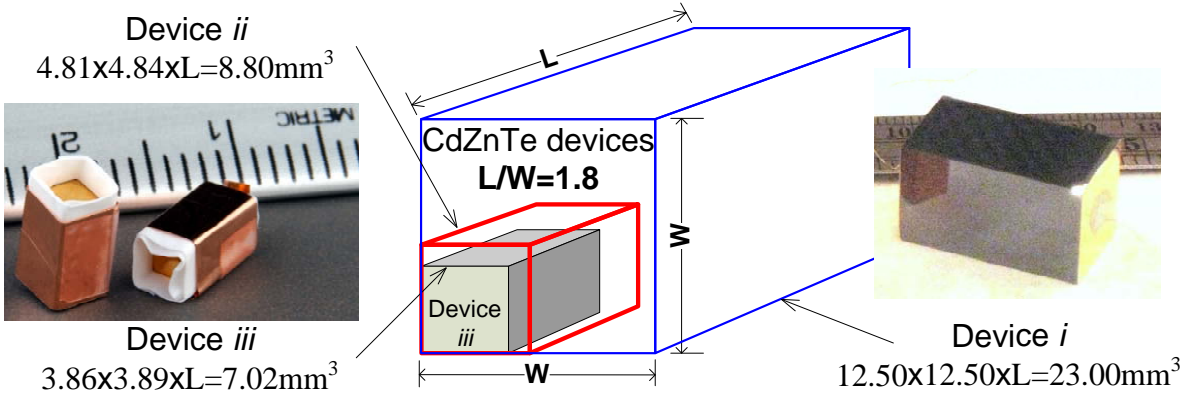


Figure 4.11: The devices' aspect ratio L/W is kept unchanged by shortening the device sizes.

with the preamplifier being connected to a high-voltage supply, amplifier (Canberra Model 2021), and a pulse generator. Again, an oscilloscope, a multichannel analyzer (MCA), and a personal computer were used to monitor and acquire the data. The temperature and the relative humidity were recorded as $27 \pm 5^\circ \text{C}$ and $60 \pm 5\%$, respectively for all experiments. An amplifier gain of 106X for the measurement with Device *ii* and Device *iii* was held constant, while for the spectral measurement with Device *i*, the amplifier gain was set to 150X. However, an amplifier shaping time of $1 \mu\text{s}$ was held constant for all the spectral measurements. The spectral testing times and the applied voltages are in Table 4.5, while the spectra taken with all devices are presented in Section 5.3.3.

Table 4.5: The device names, dimensions, and the experimental setup to study the effect of device length on performance of CdZnTe Frisch collar devices. A different standard ^{137}Cs gamma-ray source, preamplifier, and Al-test box were used for Device *i*.

Detector name	Dimensions (mm)	Applied bias (V)	Testing time (s)
Device # <i>i</i>	$12.50 \times 12.50 \times L=23.00$	3000	1800
Device # <i>ii</i>	$4.81 \times 4.84 \times L=8.80$	968	3600
Device # <i>iii</i>	$3.86 \times 3.89 \times L=7.02$	772	7200

4.3.5 Post fabrication process: surface treatment (passivation)

CdZnTe device total leakage current consists mainly of bulk leakage current and surface leakage current. As mentioned, the bulk leakage current depends strongly on bulk material resistivity, while the morphology and stoichiometry at the surface of the device affects the surface leakage current. Subsequently, this section investigates final surface treatment on CdZnTe spectrometers following contact formation. To reduce the surface leakage current and enhance the detector performance, surface treatments (passivation) have been widely used in the fabrication process of CdZnTe detectors, applied mostly after contact deposition. Three major surface passivation methods have been reported for CdZnTe: deposition of a dielectric material such as SiN and SiO₂ [53], in situ growth of wide band gap II-VI compound semiconductor heterostructures such as ZnS [54], and native oxide film coatings [55–60]. The first two techniques require costly equipment, and sometimes elevated temperatures. Unfortunately, such an environment can potentially degrade the CdZnTe detector’s spectroscopic performance. Hence, they are not widely used for surface passivation of CdZnTe; therefore, the focus of this section is native oxide film coating techniques.

Hydrogen peroxide (H₂O₂) was first used as an oxidizing agent on the surfaces of CdTe [56], and later in another study, on the surfaces of CdZnTe [55]. Surface oxidation using low energy atomic oxygen was shown to result in a lower level of leakage current compared to the H₂O₂ treatments, which subsequently resulted in better detector performance [61]. These studies on oxidizing of CdZnTe [55, 57, 62, 63] provide a basis for further studies with different oxidizing agents such as NH₄F/H₂O₂ [58–60]. These studies demonstrated how surface treatments affect the CdZnTe device leakage current. However, few works have been conducted on spectroscopic performance of CdZnTe planar detectors as a result of surface treatment. Furthermore, no systematic study has been performed on how surface treatment affects the spectroscopic performance of CdZnTe *Frisch* collar detectors. Therefore, this section presents the experimental methods applied to investigate the impact of final surface treatments on CdZnTe *Frisch* collar device. In particular, the

section address varieties of mechanical and chemical surface treatments and their effects on the performance of CdZnTe as a Frisch collar spectrometer along with their impacts on leakage current. The atomic concentration of elements at the surface was determined using the Electron Microprobe (EMP) technique before and after each treatment.

Consequently, six CdZnTe detectors were fabricated in planar and Frisch collar configurations using CdZnTe crystals acquired from Redlen Technologies. The names and specifications of the fabricated detectors are in Table 4.6. The details of detector preparations are explained later in this section (see Section 4.3.5.1), and device testing (taking pulse height spectra and current-voltage characteristic curves) is explained in Section 4.3.5.2 through 4.3.5.4. The results of the device testing for the post fabrication surface treatment are in Section 5.3.4, and the surface characterization of the devices is explained in section 4.2.4. Once the original Frisch collar detector was fabricated and tested, surface treatment (passivation) was performed only on the lateral sides of each planar detector, while the detector contacts (ends) were protected using LOGITECH Plasticized bonding wax (Detector 6 contacts were protected with APIEZON mounting wax). Later, the passivated planar detectors were fabricated into Frisch collar detectors, and the same series of spectral and I-V measurements were performed.

Table 4.6: CdZnTe devices' names, dimensions, and surface treatment methods. The uncertainty in detector dimensions is ± 0.02 mm, and L is the detector length.

Original CdZnTe detector name	Planar dimensions (mm)	Lateral surface treatment	Method
Detector 1	$4.75 \times 4.78 \times L=9.22$	Mechanical	Polishing
Detector 2	$5.00 \times 4.55 \times L=9.21$	Chemical	$\text{NH}_4\text{F}/\text{H}_2\text{O}_2$
Detector 3	$4.95 \times 4.54 \times L=9.22$	Chemical	H_2O_2
Detector 4	$4.97 \times 4.50 \times L=9.24$	Chemical	$\text{NaClO}_3/\text{H}_2\text{O}_2$
Detector 5	$5.00 \times 4.56 \times L=9.23$	Chemical	$\text{KClO}_3/\text{H}_2\text{O}_2$
Detector 6	$4.92 \times 4.98 \times L=9.82$	Mechanical	Ion milling

4.3.5.1 Device fabrication

Six different CdZnTe Frisch collar detectors were fabricated as described in Section 4.1, and the CdZnTe detectors were labeled Detector 1 through Detector 6 (Table 4.6). The same fabrication process was applied to prepare each detector in the original planar configuration. For each original detector preparation, the lateral sides were polished with a final slurry of 1.0 μm alumina powder, while the ends were finished with a fine slurry of 0.05 μm alumina powders; However, no further surface treatment was performed after the chemical etching (2% bromine/methanol) and contact depositions (AuCl_3). Therefore, the lateral sides of each original detector have native bromine etched surfaces. The Frisch collar detector was subsequently fabricated with Teflon tape covering slightly past the full length of the device (see Section 4.1.4), while a thin copper shim used as the Frisch collar covered the full length of the device (Section 4.1.4). The same dielectric thickness and the same conductive collar length were used to fabricate each planar detector into a Frisch collar detector before and after each surface treatment. For Detector 2 through Detector 5, gold wires (Alfa Aesar, 0.005in diameter, 99.99% metal base) were attached to the anode and cathode using conductive silver epoxy (Epoxy Technology, EPO-TEK H20E). To make a strong connection between the Au wires and the contacts, the detectors were baked in an oven with an inert atmosphere (nitrogen) at 90° C for 5 hours.

4.3.5.2 Post fabrication process 1: Mechanical

Polishing and grinding were performed on the lateral sides of Detector 1. LOGITECH Plasticised Bonding Wax protected the contacts from the post fabrication surface treatment, and then five different grinding/polishing methods were performed. This detector was labeled after each surface treatment as Detector 1 #2 through Detector 1 #6 (Detector 1 #1 has the native bromine etched surface). Once each treatment was performed, the bonding wax was removed, and the planar device was fabricated into a Frisch collar detector. Later, the same spectral and current-voltage (I-V) measurements were performed on Detector 1 #2 through

Detector 1 #6 (as detailed in Section 4.2). Note that before each treatment, bonding wax was applied to protect the gold contacts; therefore, the same contacts were recovered for Detector 1 #1 through Detector 1 #6. The summary of each surface treatment and its application method (grinding with SiC paper and/or polishing with alumina powder) are in Table 4.7.

Table 4.7: Post fabrication process 1: Mechanical treatment and the technique applied to the lateral surface of Detector 1. Six detectors were fabricated through different treatment on Detector 1, labeled as Detector 1 #1 to Detector 1 #6

Detector 1 #	Steps	Treatment	Method	Type
Detector 1 #1	Step 1	Etching	2%Br/Meth	Native surface
Detector 1 #2	Step 2	Grinding	SiC	1200 Grit
Detector 1 #3	Step 3	Grinding	SiC	2400 Grit
Detector 1 #4	Step 4	Grinding	SiC	4000 Grit
Detector 1 #5	Step 5	Polishing	Alumina	1 micron
Detector 1 #6	Step 6	Polishing	Alumina	0.05 micron

4.3.5.3 Post fabrication process 2: Chemical

The chemical surface treatment (passivation) was performed on Detector 2 through Detector 5 as the final surface treatment (see Table 4.6). LOGITECH Plasticised Bonding Wax protected the contacts from the chemical surface treatment. The passivation solutions were prepared by adding 10.76 g of the chemicals (NH_4F , NaClO_3 , and KClO_3) in turn listed in Table 4.6 in 68 ml of deionized (DI) water and 32 ml of hydrogen peroxide (H_2O_2). For Detector 3, only H_2O_2 was used as the oxidation agent. Each chemical passivation solution was applied to the crystal surfaces for 10 minutes. Once the treatment was performed on each detector, the bonding wax was removed, and the planar device was fabricated into the Frisch collar detector. Later, the same spectral and current-voltage (I-V) measurements were performed on Detector 2 through Detector 5 (Section 4.2). Before each surface treatment, bonding wax was applied to protect the gold contacts; therefore, the same contacts were recovered for Detector 2 through Detector 5 before and after passivation. The results are in Section 5.3.4.

4.3.5.4 Post fabrication process 3: Ion-mill

Ion milling of lateral sides was performed on Detector 6 using a Millatron ion mill equipped with a Kaufman ion source. A PIEZON mounting wax protected the contacts from the surface treatment. Xenon gas was used as the ion source, while a beam current of 81 mA, a beam voltage of 250 V, and an accelerator voltage of 250 V were held constant during the milling process. Detector 6 was clamped to a cooled stage and milled for 90 minutes on each lateral side. After ion milling one side, the ion chamber was opened and the detector was flipped to mill all other lateral sides. After milling all four lateral sides, the protective mounting wax was removed from the contacts, and the same spectral measurements and current-voltage (I-V) measurements were performed on Detector 6 as well as surface analysis using EDS on Detector 6. Later, the lateral sides of Detector 6 were polished with 1.0 μm alumina powders while the contact was protected as explained. Current-voltage (I-V) measurements and a pulse height spectrum were collected for Detector 6, and the results are in Section 5.3.4.

4.4 Angular Dependency of the Collimated CdZnTe Detector

In the following section, the directional sensitivity of a $3.4 \times 3.4 \times 5.8 \text{ mm}^3$ W-collimated Frisch collar CdZnTe detector is investigated for two different collimator lengths: a 4 cm Tungsten collimator and an 8 cm Tungsten collimator. Further, the relevant equations, setups, and procedures are presented to help determine the relative change in detector count rate as a function of irradiation angle.

4.4.1 Two-dimensional assembly

Figs. 4.12 through 4.16 show basic two-dimensional diagrams of the detector-collimator-source assembly, which are used to analyze the expected count rate response. Using a point gamma-ray source in the model, Figs. 4.12 through 4.16 show that as the point source moves

on a circular path with respect to the detector center point, three different exposure regions can be defined. These regions depend on the geometry and positions of the collimator and detector, and the position of the source with respect to the detector-collimator assembly.

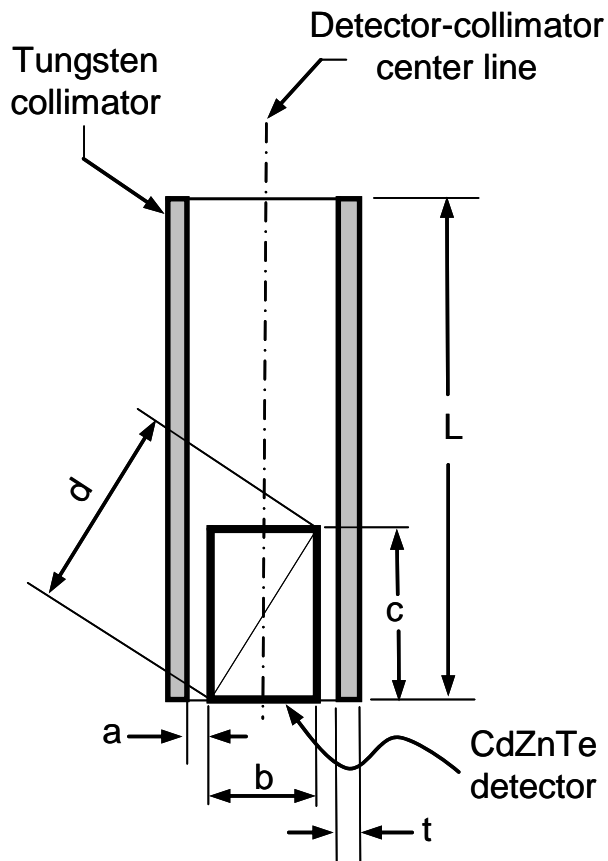


Figure 4.12: Diagram of two-dimensional model for the detector-collimator configuration. The values b and c are the CdZnTe detector dimensions (in this work, 3.4 mm and 5.8 mm), L is the collimator length, and t is collimator thickness.

For the designated source path, two critical angles are identified, labeled here as α_{c1} and α_{c2} (Fig. 4.13). Angle α , the *source-detector angle*, is defined as the angle between the point source and the detector-collimator center line (Fig. 4.13), where the angle apex is at the detector center. The first critical angle α_{c1} occurs at the point along the arc at which the tungsten collimator begins to shield the detector from the point source (Fig. 4.13). The second critical angle α_{c2} occurs at the point along the arc at which the detector becomes

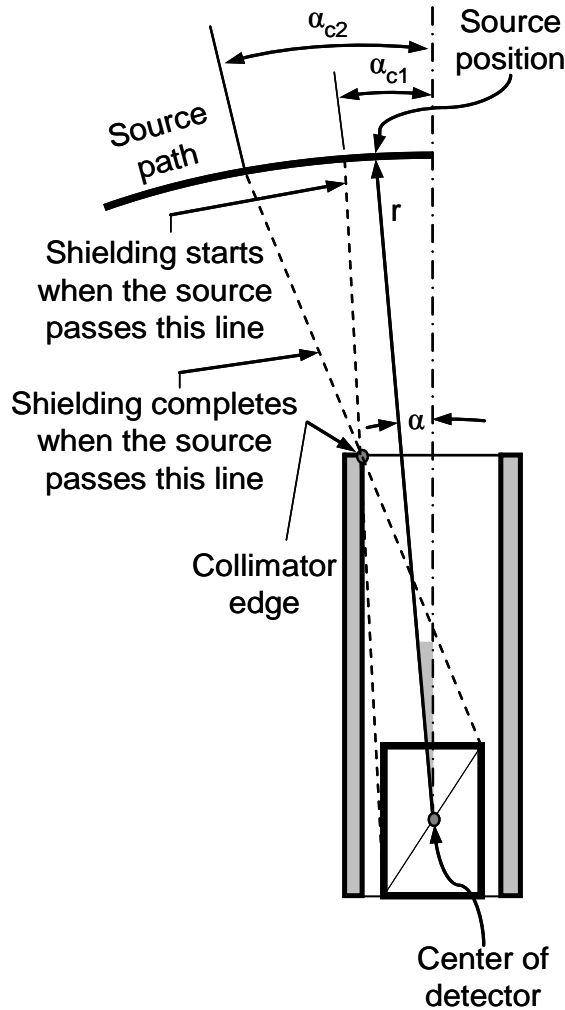


Figure 4.13: Diagram of two-dimensional model for detector-collimator-source positions showing the two critical angles and the source position with respect to detector-collimator assembly ($r=50$ cm).

completely shielded by the collimator (Fig. 4.13). Angle α is the only independent variable as the source moves along its circular path of constant radius r for each particular test.

In the first region shown in Fig. 4.14, the source-detector angle ranges between zero degrees and α_{c1} . Consequently, the detector is entirely exposed to the point source. The second region, shown in Fig. 4.15, describes the source-detector angles between α_{c1} and α_{c2} . Here, the detector is only partially shielded from the point source. In this second region, the total gamma-ray flux emitted from the source is partially attenuated before reaching

the detector. Finally, the third region shown in Fig. 4.16 is described by those angles that are between α_{c2} and 90° . Here, all gamma-ray emissions will intersect the collimator before reaching the detector in this third region; hence the flux will be attenuated.

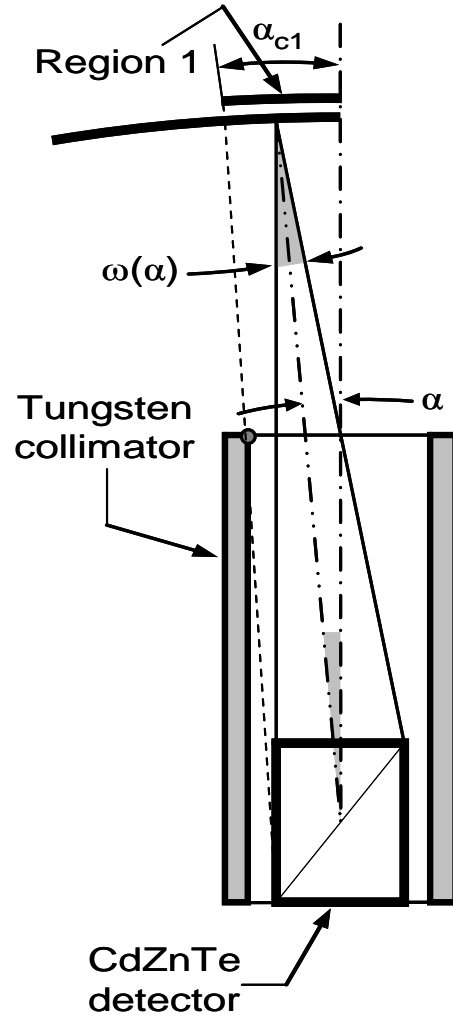


Figure 4.14: Diagram of two-dimensional model for detector-collimator-source position while the source is in region 1.

The following assumptions were made to derive the relation between the counts and the source-detector angle. First, it was assumed that the decrease in counts observed will be a relative function with respect to the total gamma-ray attenuation coefficient, which is a function of the collimator and detector material and the gamma-ray energy. In other

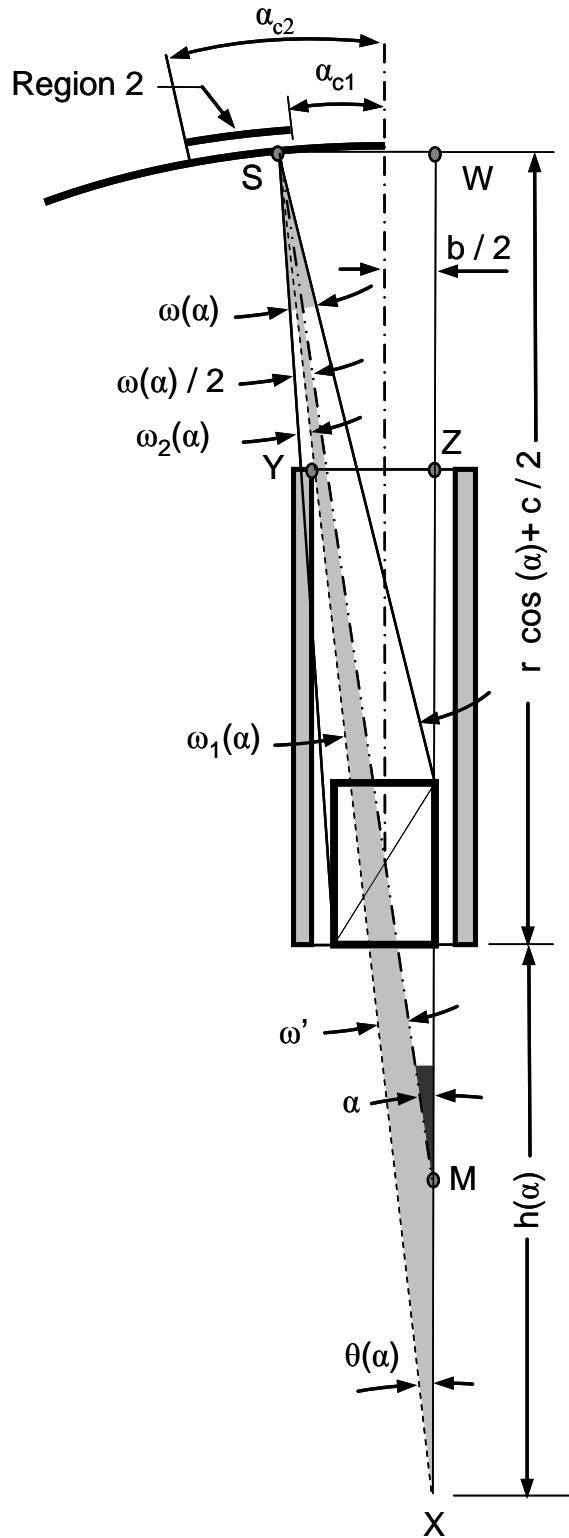


Figure 4.15: Diagram of two-dimensional model for detector-collimator-source position while the source is in region 2.

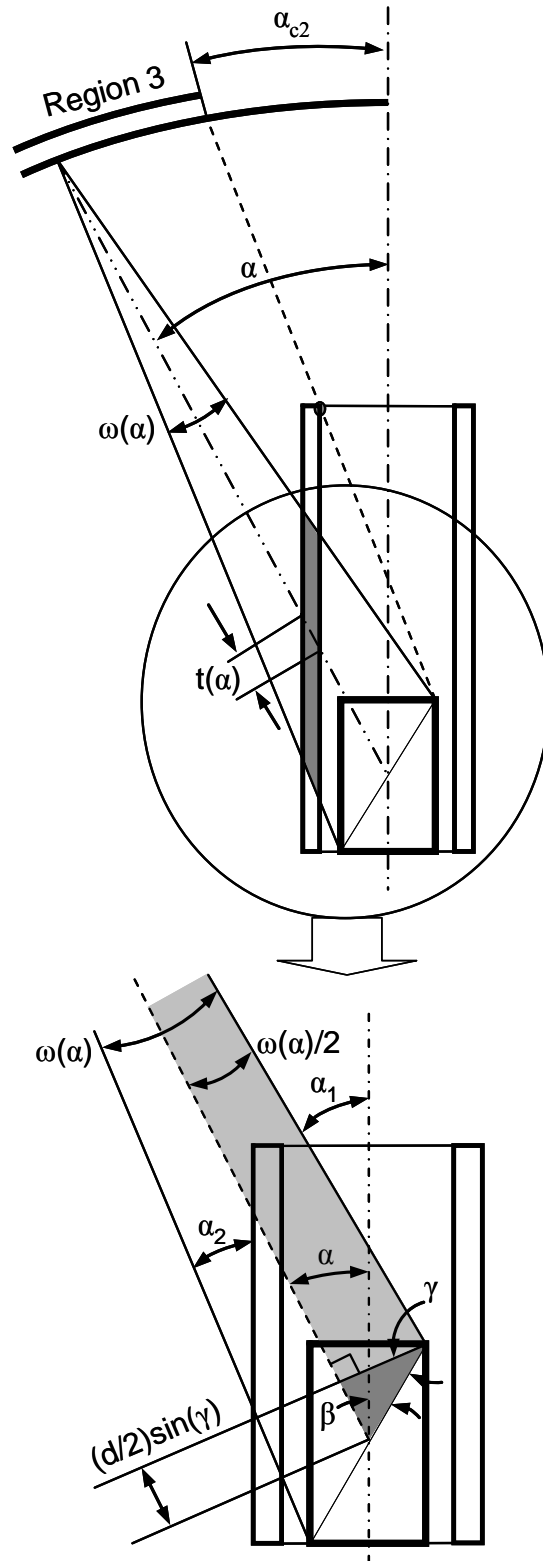


Figure 4.16: Diagram of two-dimensional model for detector-collimator-source position while the source is in region 3.

words, the expected gamma-ray interactions in the detector can be normalized and scaled appropriately for various gamma-ray energies and collimator materials. Next, to simplify the geometry, the two angles α_1 and α_2 shown in Fig. 4.16 are approximated as equal to the source-detector angle α , an approximation that incorporates little error provided that the *exposure angle* between the point source and the detector, $\omega(\alpha)$, is small. Indeed, for geometries used in the experiment, also shown in Figs. 4.14 through 4.16, the exposure angles are approximately 0.5 ± 0.1 degrees, hence allowing such a simplifying assumption to be used. Using this assumption, for a specific source position and angle α in the third region (Fig. 4.16), the gamma-ray flux is attenuated through an average shielding thickness, $t(\alpha)$, termed the *effective thickness*.

The exposure angle, $\omega(\alpha)$, can be described as follows. Retaining the definitions given in Figs. 4.12 and 4.13, the shaded regions in the lower portion of Fig. 4.16, which form two right triangles (note that the corner of the larger triangle is located at the point source), yield:

$$(d/2) \cos(\gamma) = \left[r - \left(\frac{d}{2} \right) \sin(\gamma) \right] \tan [\omega(\alpha)/2] \quad , \quad (4.1)$$

where,

$$\gamma = 90^\circ - (\alpha + \beta) \quad , \quad (4.2)$$

and β is defined as,

$$\beta = \arctan(b/c) \quad . \quad (4.3)$$

By substituting β and γ into Equation 4.1 and rearranging, the following equation can be obtained for the exposure angle,

$$\omega(\alpha) = 2 \arctan \left[\frac{d/2 \sin(\arctan(b/c) + |\alpha|)}{r - d/2 \cos(\arctan(b/c) + |\alpha|)} \right] \quad , \quad (4.4)$$

where b and c are the dimensions of the CdZnTe bar detector (Fig. 4.12), d can be evaluated

as $(b^2 + c^2)^{1/2}$, and r is the distance between the source and the detector center (Fig. 4.13). Closer inspection reveals that $\omega(\alpha)$ is an even function, due to symmetry, and increases with α . The angular limits under investigation range from $\pm 17^\circ$; hence $\omega(\alpha)$ has values of 0.39° and 0.57° at α -values of 0° and $\pm 17^\circ$, respectively.

Since the incident gamma-rays on the CdZnTe detector would be absorbed based on the detector efficiency, ϵ , it would be important to consider the effect of the CdZnTe total linear attenuation coefficient for the incident gamma-ray energy. Since the exposure angle $\omega(\alpha)$ is small, and the detector-source distance, r , is much greater than the detector sizes, b and c , it would be an appropriate assumption to consider parallel beams of gamma-rays impinging upon the detector at a given angle, α (Fig. 4.17).

To evaluate the detector efficiency, ϵ , at angles other than zero degrees, the following assumption is made. The detector is rotating toward the source in a way that the detector face is always perpendicular to the parallel beam of incident gamma-rays for the same $\omega(\alpha)$ evaluated by Equation 4.4. This assumption is illustrated in Fig. 4.17. The equivalent CdZnTe detector at the source-detector angles other than zero degrees is shown by the hatched rectangle in Fig. 4.17 and named as the virtual detector. The virtual CdZnTe detector needs to have the same amount of volume (or area in 2-dimensional analysis) as the original CdZnTe detector. The virtual CdZnTe detector should also have the same exposure angle $\omega(\alpha)$ to the point source and the exact detector-source distance, r , as the original CdZnTe detector. To maintain the equal detector-source distances, the center of the two detectors needs to be at the same point (Fig. 4.17). To find the dimensions of the virtual detector, geometrical relations were employed. For the triangle ABC in Fig. 4.17, $AB = AC \cos(\gamma)$ or $AB = d \cos(\gamma)$. Considering the same volume for both detectors, the following expression is valid:

$$AB t_v = b c \quad , \quad (4.5)$$

where b and c are the original CdZnTe detector dimensions (Fig 4.12), and t_v is the thickness of the virtual detector exposed to the point source and varying with angle α (Fig. 4.17);

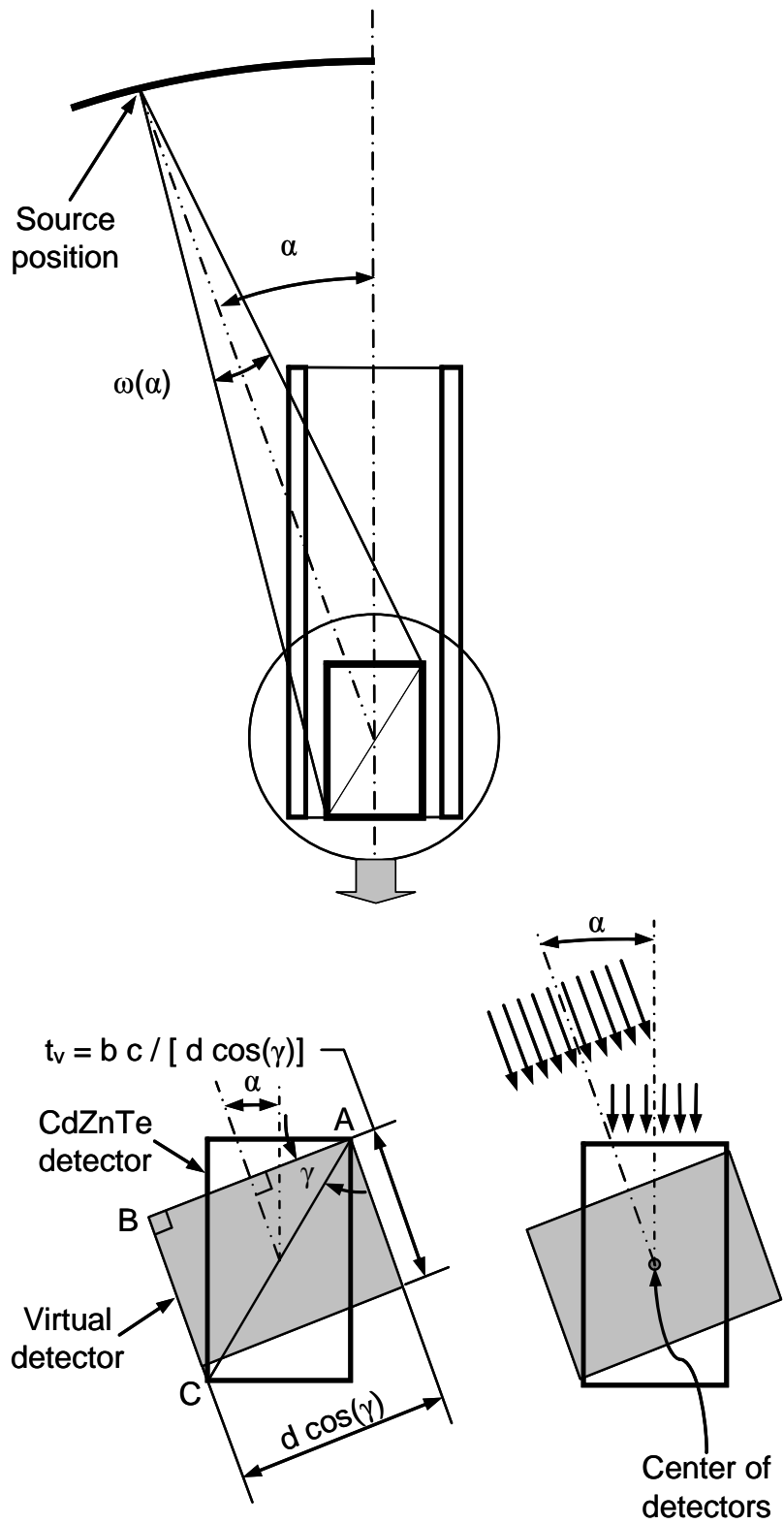


Figure 4.17: The CdZnTe detector and the virtual CdZnTe detector (bottom figures) at any angle α . The total areas of the two detectors are equal.

Therefore,

$$t_v = \frac{b c}{d \cos(\gamma)} \quad . \quad (4.6)$$

Note that the angle, γ , is defined in Equation 4.2 and is a function of the angle, α .

The dimensions of the virtual detector are well-defined. As mentioned, it is assumed that the parallel beams are impinging upon the virtual detector of thickness t_v , for any angle α . Hence, if one gamma-ray interaction within the CdZnTe detector generates a detectable pulse, then the CdZnTe detector efficiency is given by [64, 65] as:

$$\epsilon(\alpha) = 1 - \exp[-\sigma_c t_v] \quad . \quad (4.7)$$

Where, σ_c is the CdZnTe total linear attenuation coefficient for the incident gamma-ray energy. For CdZnTe in this study, the total linear attenuation coefficient for the gamma-ray energy of 412keV emitted by ^{198}Au is given as 0.60 cm^{-1} [66]. Lastly, the virtual detector approximation is only a simplistic analytical method to predict gamma-ray response, whereas a more rigorous and accurate result may be found through numerical methods.

The detector count rate in the first region (Fig. 4.14) is proportional to the product of the CdZnTe detector efficiency and exposure angle in the first region. However, in the second region (Fig. 4.15), the tungsten collimator dramatically impacts the total number of counts observed, although the detector is only partially shielded by the tungsten collimator. In the third region, the gamma-ray flux is completely shielded by the tungsten collimator, yet the effective thickness, $t(\alpha)$, decreases with increasing α (Fig. 4.16). The decrease in effective thickness in the third region results in an increase in count rate as α increases. Consequently, the predicted number of counts, $N(\alpha)$, in the first and third regions (Figs. 4.14 and 4.16) can be expressed as,

$$N(\alpha) = \eta \omega(\alpha) \epsilon(\alpha) \quad \text{for} \quad 0^\circ \leq \alpha \leq \alpha_{c1} \quad , \quad (4.8)$$

and,

$$N(\alpha) = \eta \omega(\alpha) \epsilon(\alpha) \exp[-\sigma_w t(\alpha)] \quad \text{for} \quad \alpha_{c2} \leq \alpha \leq \alpha_{max} \quad , \quad (4.9)$$

where η is a normalization factor, and σ_w is the total linear attenuation coefficient of the collimator material at the desired energy. The gamma-ray energy of interest in this work is the 412 keV emission from ^{198}Au , in which the attenuation coefficient for tungsten is 3.5319 cm^{-1} . The effective thickness, $t(\alpha)$, can be easily obtained from Fig. 4.16 as,

$$t(\alpha) = \frac{t}{\sin(\alpha)} \quad , \quad (4.10)$$

where t is the nominal collimator wall thickness (Fig. 4.12).

The value of $N(\alpha)$ can be obtained in the second region from Fig. 4.15 by considering the entire exposure angle as a sum of the angle for which part of the detector is unshielded ($\omega_1(\alpha)$ on Fig. 4.15) and the angle for which attenuation occurs ($\omega_2(\alpha)$ on Fig. 4.15), such that,

$$\omega(\alpha) = \omega_1(\alpha) + \omega_2(\alpha) \quad . \quad (4.11)$$

In Equation 4.11, $\omega_1(\alpha)$ is defined as the angle between the point source and the portion of the detector for which no shielding occurs, and $\omega_2(\alpha)$ is the angle between the point source and the portion of the detector that is shielded by the collimator. From Fig. 4.15, $\omega_1(\alpha)$ and $\omega_2(\alpha)$ can be evaluated as,

$$\omega_1(\alpha) = 0.5 \omega(\alpha) + \omega' \quad , \quad (4.12)$$

and,

$$\omega_2(\alpha) = 0.5 \omega(\alpha) - \omega' \quad , \quad (4.13)$$

where from the shaded triangle, SMX , in Fig. 4.15,

$$\omega' = \alpha - \theta(\alpha) \quad . \quad (4.14)$$

In the triangle defined as XYZ in Fig. 4.15 with the dimensions given in Fig. 4.12, $\theta(\alpha)$ can be written as,

$$\theta(\alpha) = \arctan \left[\frac{b+a}{L+h(\alpha)} \right] \quad . \quad (4.15)$$

By applying the fundamental theorem of similar triangles to XYZ and XSW in Fig. 4.15, where $\frac{SW}{XW} = \frac{YZ}{XZ}$, $h(\alpha)$ can be found by solving the following equation,

$$\frac{r \sin(\alpha) + b/2}{h(\alpha) + c/2 + r \cos(\alpha)} = \frac{b+a}{L+h(\alpha)} \quad , \quad (4.16)$$

as,

$$h(\alpha) = \frac{L [r \sin(\alpha) + b/2] - (b+a) [r \cos(\alpha) + c/2]}{(b+a) - (r \sin(\alpha) + b/2)} \quad , \quad (4.17)$$

where L is the length of the collimator (Fig. 4.12). Given the above expressions, the normalized total counts, $N(\alpha)$, in the second region are described by,

$$N(\alpha) = \eta \epsilon(\alpha) [\omega_1(\alpha) + \exp[-\sigma_W t(\alpha)] \omega_2(\alpha)] \quad for \quad \alpha_{c1} \leq \alpha \leq \alpha_{c2} \quad . \quad (4.18)$$

Over the range of source-detector angles, Equations 4.8, 4.9, and 4.18 are the main expressions for predicting the behavior of the normalized total number of counts with respect to source-detector angle variations.

4.4.2 Setup arrangement for directional sensitivity of the collimated CdZnTe Frisch collar device

This section details CdZnTe device preparation, collimator alignment, gold sample preparation, and data collection for directional sensitivity of collimated Frisch collar device.

4.4.2.1 Device preparations

The CdZnTe Frisch collar detector preparation for this experiment is similar to that described in Section 4.1. A $3.4 \times 3.4 \times 5.8 \text{ mm}^3$ Frisch collar detector was fabricated from bulk CdZnTe material acquired from eV Products. Later, thin Au wires were attached to the anode and cathode using conductive silver epoxy. To make a strong connection between the Au wires and the contacts, the device was baked in an oven at 50°C for 11 hours.

4.4.2.2 Device collimator alignment

Two different lengths of tungsten collimators were selected to help determine the spatial resolution of collimated Frisch collar detectors. The first collimator type was 4 cm long with a 4.8 mm inside width and a 1 mm wall thickness. The second was 8 cm long with a 4.7 mm inside width and a 0.5 mm wall thickness. Both collimators were fabricated by Tungsten Co. using Electrical Discharge Machining (EDM) techniques. Since the angular dependency experiment was conducted for both 4 cm and 8 cm long collimators, the experimental arrangement described below was performed for both collimators individually.

To investigate the directional-sensitivity of gamma-ray detection with respect to the source-detector angle, it was important to perform the experiment with the detector-source distance considerably larger than the dimensions of the detector. In this manner, the exposure angle, $\omega(\alpha)$, could be kept small to reduce any measurement error of the source-detector angle. Therefore, an aluminum test stage, shown in Fig. 4.18, was designed and built such that the detector-source distance was constant (50 cm) for a variety of source-detector angles. A laser pointer (Fig. 4.18) facilitated accurate source positioning with respect to the collimator center line.

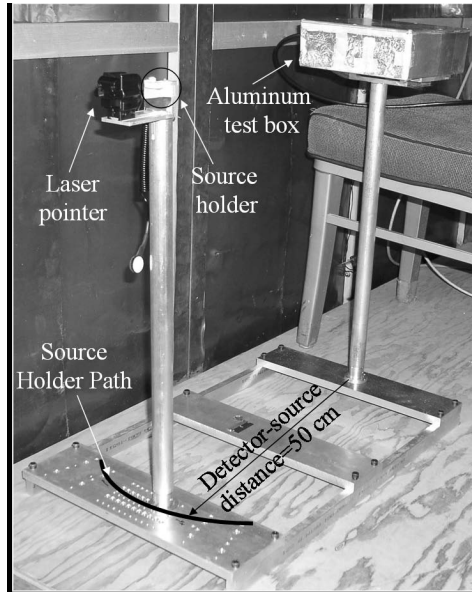


Figure 4.18: The aluminum test stage inside the Faraday cage and the source holder and laser pointer for source positioning.

Once the collimator was aligned, its position was fixed inside the aluminum test box as illustrated in Figs. 4.19 and 4.20. To reduce the effect of shielding from the aluminum box, a window was cut and covered with thin aluminum foil, thereby reducing the aluminum thickness between the source and detector while retaining electro-magnetic shielding. Next, the fabricated CdZnTe detector with a Frisch collar and Au connecting wires was placed inside the tungsten collimator such that the cathode faced the gamma-ray point source (Fig. 4.20). Then, the CdZnTe detector sides were covered with plastic wrapping before positioning inside the collimator to insulate the device and center the detector. Once in place, the CdZnTe detector was ready for spectral data collection.

4.4.2.3 Gold sample preparation

Activated ^{198}Au gamma-ray sources were prepared through neutron activation by irradiating 13 ± 2 mg samples of Au foils in the Kansas State University TRIGA Mk II nuclear reactor core. Activation was conducted for five minutes under a measured fast neutron flux of $3.5 \times 10^{12} \text{ cm}^{-2} \text{ s}^{-1}$ and thermal neutron flux of $4.3 \times 10^{12} \text{ cm}^{-2} \text{ s}^{-1}$. The Au samples were

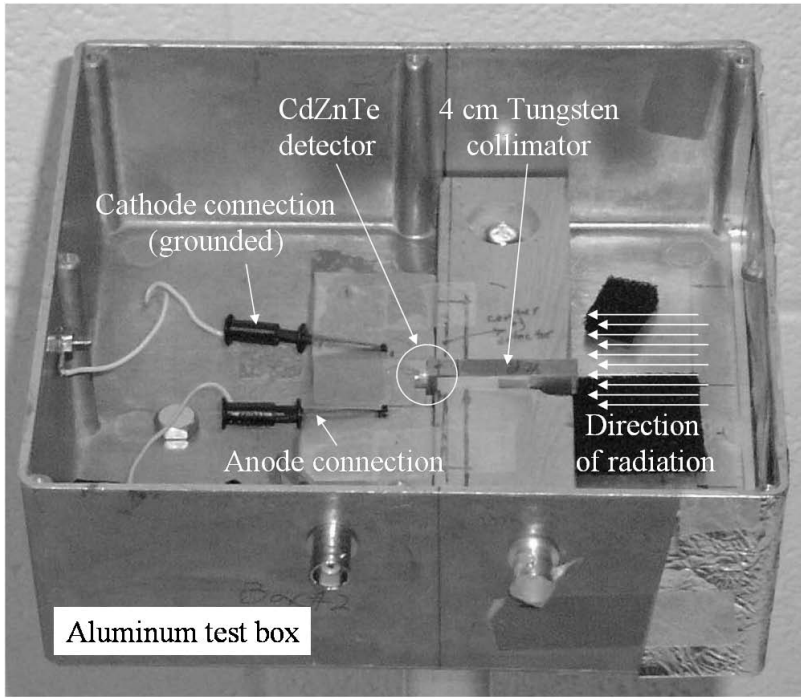


Figure 4.19: The aluminum test box with the 4 cm long W-collimated CdZnTe detector.

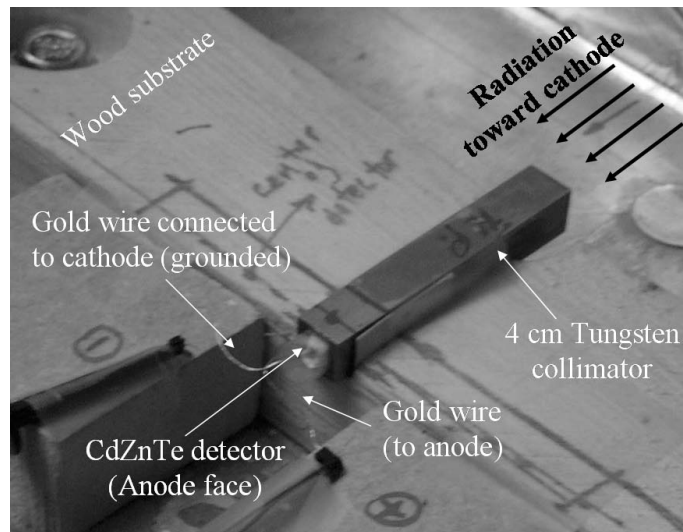


Figure 4.20: The 4 cm long tungsten collimator and the CdZnTe detector with the gold wires. The cathode faces in the direction of radiation.

sliced from commercially available (Alpha Aesar), 99.95% purified, 0.025 mm thick Au foil. To avoid contamination, the Au foils were sliced and weighed in a class 1000 clean room.

4.4.2.4 Collecting data for directional sensitivity of collimated CdZnTe Frisch collar devices

The detector was connected to an ORTEC model 142A preamplifier. To minimize electronic noise, the aluminum test stage and preamplifier were placed inside a copper Faraday cage. The measurement system consisted of an amplifier, an oscilloscope, a multichannel analyzer (MCA), a high voltage supply, and a personal computer, all positioned outside the Faraday cage. The temperature and the relative humidity were recorded as 27°C and 60%, respectively. Also, operating parameters were held constant at a voltage bias of 1000 V, amplifier gain of 700X, and shaping time of 1 μ s.

All data collected in this study were taken with the same CdZnTe Frisch collar detector. The gamma-ray calibration sources have low activity and hence were unable to provide adequate counts in a reasonable time period to investigate the device spatial resolution. Thus, pulse height spectra were collected from the activated Au foils (see Section 4.4.2.3) at a variety of source-detector angles, each for 60 minutes using the two different tungsten collimators. The ^{198}Au sample was placed in the sample holder shown in Fig. 4.18 for each angular measurement. Then, all Au foils were corrected for mass differences by normalizing the observed counts to a 13 mg Au sample with the accuracy of the mass scale being limited to ± 0.5 mg. Error propagation was used to determine the error contributions from the radiation counting and Au foil mass measurement error. The results are in Section 5.5.

4.5 Array of CdZnTe Frisch Collar Detectors and the Corresponding Readout Electronics

The details of electronic fabrication and setup for an array of 4x4 CdZnTe Frisch collar detectors (total of sixteen devices) have been published previously in [67]. The primary purpose of developing an array of CdZnTe detectors is to increase the detecting area and the detection efficiency. The readout electronics for testing the array of CdZnTe detectors were developed and built at Brookhaven National Laboratory (BNL). This readout electronics are capable of testing two arrays of 4x4 CdZnTe detectors. Two arrays of 4x4 CdZnTe Frisch collar detectors (thirty two CdZnTe detectors) were tested with the readout electronics developed at BNL. Similar electronics are still under development at Kansas State University (KSU) at the Electronics Design Laboratory (EDL). Specifically, sixteen of the CdZnTe Frisch collar detectors have been fabricated and tested *individually* at the S.M.A.R.T. lab at KSU in the same fashion as described in Sections 4.1 and 4.2. One of these detectors is shown in Fig. 4.21. The sixteen detectors fabricated at S.M.A.R.T. lab KSU have average dimensions of $(4.7\pm 0.2) \times (4.7\pm 0.2) \times (9.5\pm 0.05)$ mm³.



Figure 4.21: CdZnTe Frisch collar detector fabricated at S.M.A.R.T. laboratory at KSU. The picture is taken at Brookhaven National laboratory (BNL) after delivery of the devices.

The sixteen Frisch collar detectors fabricated at KSU along with sixteen other Frisch collar detectors were later assembled into two arrays of 4x4 detectors at BNL. The module of 16-detectors is shown in Figs. 4.22 and 4.23. A low dielectric material (Roger 4003) was used for the printed circuit board (PCB) substrate to keep noise level low (Figs. 4.22).

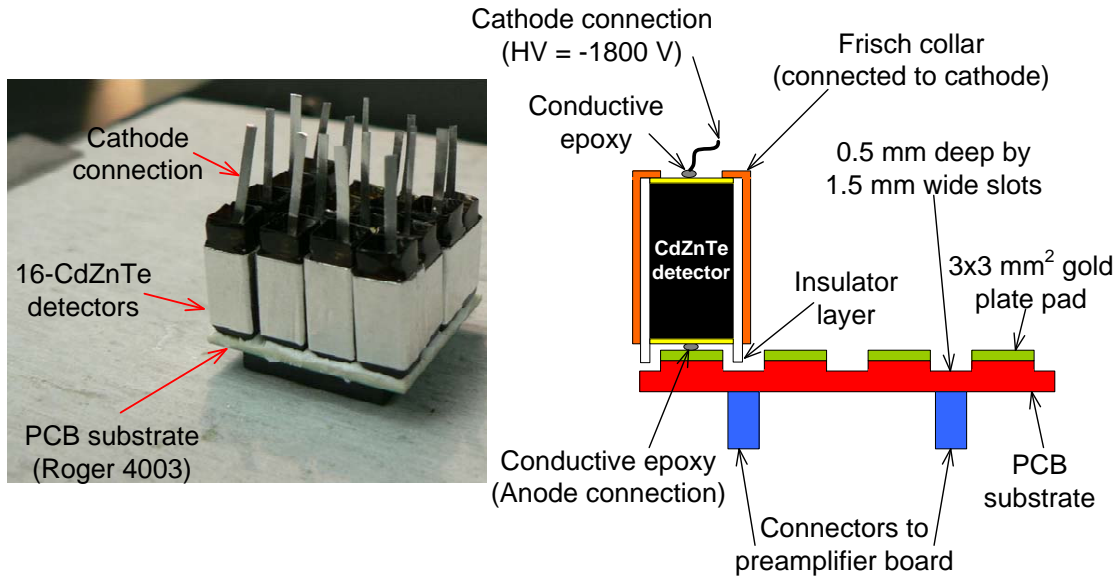


Figure 4.22: An array of 16-CdZnTe Frisch collar detectors. The detectors were mounted on the printed circuit board (PCB) at Brookhaven National laboratory (BNL).

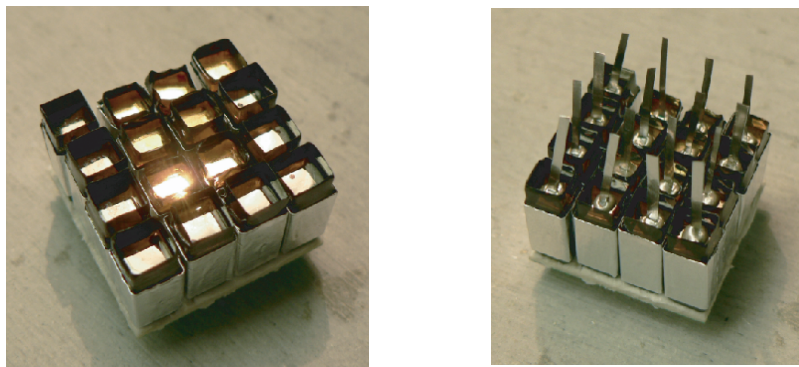


Figure 4.23: An array of 16-CdZnTe Frisch collar detectors, before and after gluing the cathode connections. Courtesy of Aleksey Bolotnikov at BNL.

The Data Acquisition (DAQ) system designed for the radiation detection consists of two Application Specific Integrated Circuits (ASICs). Both ASICs were developed at BNL; the first one was a 16-channel low noise preamplifier for CdZnTe detector readout, and the second one was a Peak Detector/Derandomizer (PDD). The preamplifier board and its components are shown in Fig. 4.24. The test box including preamplifier board, PDD board, two detector modules, and controller board is shown in Fig.4.25.

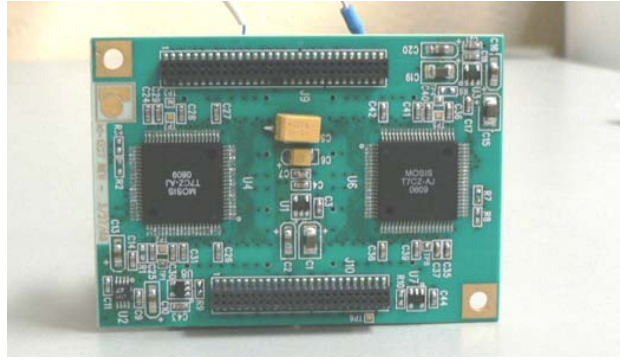


Figure 4.24: The preamplifier board for the array of 16 CdZnTe Frisch collar detectors.

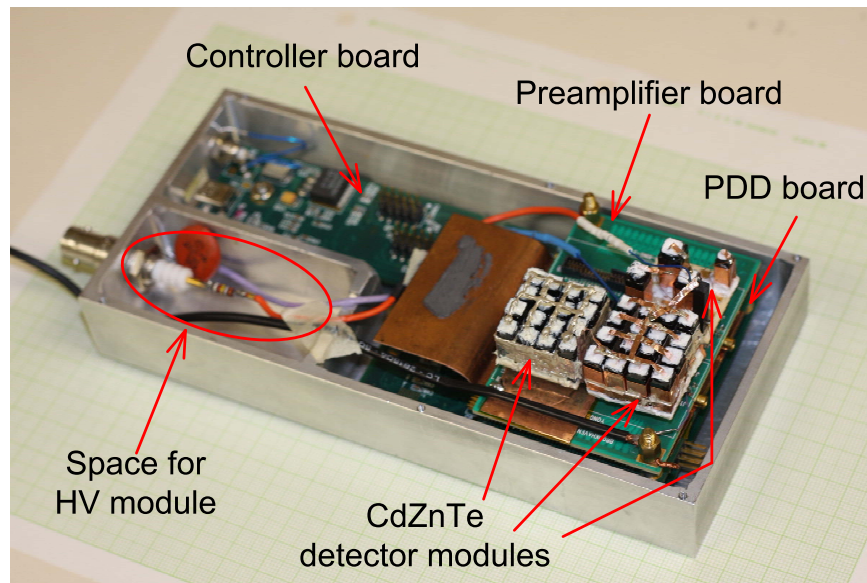


Figure 4.25: Close view of preamplifier board with two CdZnTe detector modules. Sixteen of the individual detectors were fabricated and tested at S.M.A.R.T. laboratory at KSU. The two modules of 16-detectors were mounted at Brookhaven National laboratory (BNL). Courtesy of Aleksey Bolotnikov at BNL.

The preamplifier ASIC keeps the output stable to a maximum of 150 nA leakage current from the CdZnTe detectors (due to its continuous reset system). Also the preamplifier ASIC input transistor and the shaping circuit are optimized for the CdZnTe detector application to keep the noise level low. The preamplifier ASIC used a programmable gain (33 mV/fC to 200 mV/fC) and peaking time ($0.6 \mu\text{s}$ to $4.0 \mu\text{s}$) to amplify and shape the signals from each 16-channel detector module [67].

The output signals from the two preamplifier ASICs are processed and buffered in a PDD (Peak Detector/Derandomizer) ASIC. The PDD ASIC, a 32:1 multiplexer, uses analog techniques to concentrate the data before digitization; thus, for signals arriving at any of its 32 channel inputs, the PDD ASIC provides amplitude and timing signals in analog format and a channel number in digital format. The amplitude and timing from the PDD ASIC are digitized by two 12-bit analog-to-digital converters (ADC) mounted on the controller board (see Fig. 4.25). Then, a Field-Programmable Gate Array (FPGA) on the controller board collects and sends all the digitized information to a computer through a universal serial bus (USB), which is controlled by a microcontroller. The computer has DAQ software to control the system and process the data [67]. The final electronic readout package within the test box is presented in Fig. 4.26.



Figure 4.26: The two detector modules with the preamplifier board in a test box. Courtesy of Aleksey Bolotnikov at BNL.

The results of the primary spectral test on the sixteen CdZnTe Frisch collar detectors with ^{137}Cs are shown in Appendix B (the setups are explained on the figures). These primary spectral test were performed at S.M.A.R.T. lab at KSU. As explained in this section, the detector arrays were later tested at BNL. The detector arrays were biased at -1800 V, and the peaking time of the preamplifiers was set to $2.4 \mu\text{s}$. The results of the uncollimated ^{137}Cs , ^{241}Am , and ^{133}Ba gamma-ray sources are presented in Section 5.6 [67].

Chapter 5

RESULTS AND DISCUSSION

5.1 Primary Results of Gamma-Ray Spectroscopy with CdZnTe Detectors

The primary results of gamma-ray spectroscopy with a $3.4\text{mm} \times 3.4\text{mm} \times 5.7\text{mm}$ CdZnTe semiconductor Frisch collar detector are published [25]. For this study, pulse height spectra were collected from gamma-rays sources of ^{241}Am , ^{57}Co , ^{133}Ba , ^{198}Au , ^{137}Cs and ^{235}U , and the ^{241}Am , ^{57}Co , ^{133}Ba , and ^{137}Cs samples were standard commercially available, calibration sources. The ^{198}Au was prepared through an (n,γ) reaction by activating a 13 mg sample of gold foil in the Kansas State University TRIGA Mk II nuclear reactor core. The ^{235}U source was a 93 % enriched ^{235}U -nitride solution. As explained in Section 4.2.2, the electronic settings were consistent for all measurements, and energy resolutions reported for gamma-ray photopeaks are without any electronic corrections.

An energy resolution of 9.1 % (5.41 keV) FWHM for the 59.5 keV spectral line of ^{241}Am was obtained, which is shown in Fig. 5.1 and does not consider any contributions from electronic noise. Thus, the low noise floor and the high resolution of the device allow the discernment of Cd and Te X-ray escape peaks, as labeled near 35 keV. Next, Fig. 5.2 shows ^{57}Co spectrum where the energy resolution at the 122 keV photopeak is 4.9 % (5.99 keV) FWHM, and the 136 keV photopeak is clearly observed as a small peak on the right side of the 122 keV photopeak. The Cd and Te X-ray escape peaks are also visible.

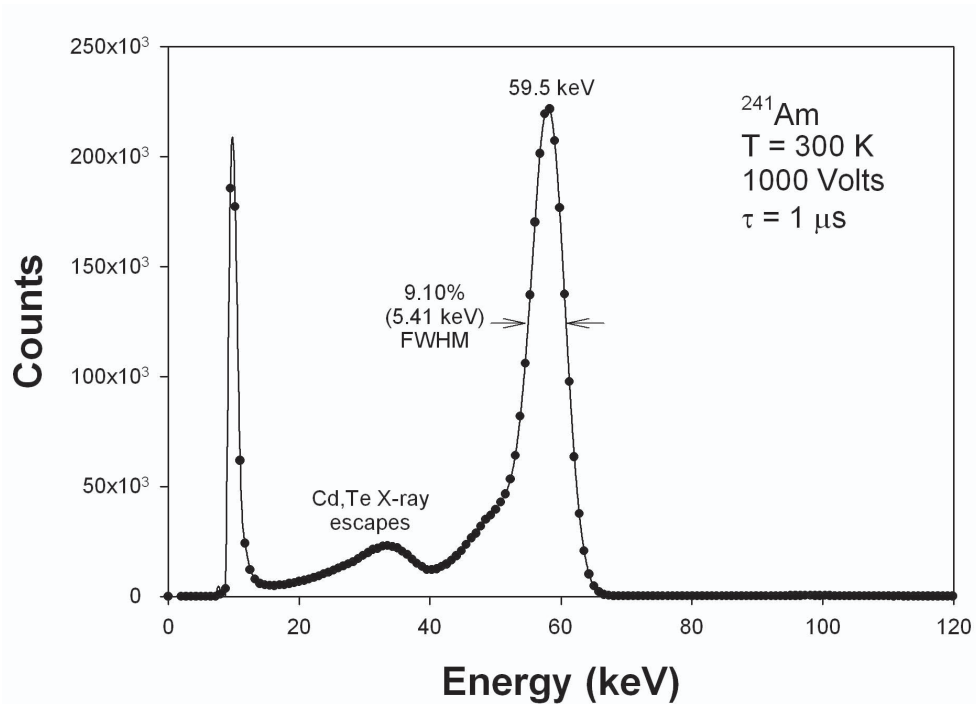


Figure 5.1: Room temperature spectra of a ^{241}Am source from the $3.4\text{mm} \times 3.4\text{mm} \times 5.7\text{mm}$ CdZnTe semiconductor detector.

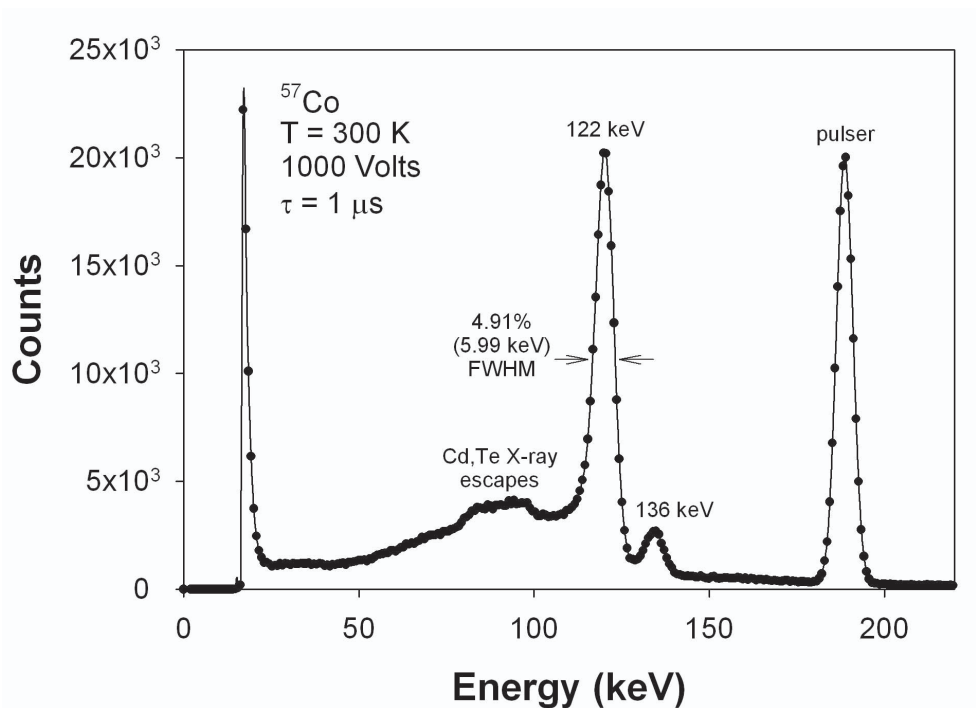


Figure 5.2: Room temperature spectra of a ^{57}Co source from the $3.4\text{mm} \times 3.4\text{mm} \times 5.7\text{mm}$ CdZnTe semiconductor detector.

Figs. 5.3 through 5.6 display the energy spectra for ^{133}Ba , ^{198}Au and ^{137}Cs , respectively. First, an energy resolution of 7.6% (6.04 keV) FWHM was achieved for the 80 keV photopeak of ^{133}Ba as shown in Fig. 5.3. Then, the 356 keV photopeak of ^{133}Ba exhibited an energy resolution of 2.3% (8.29 keV) FWHM (see Fig. 5.4). The full energy peaks corresponding to the 276 keV, 302 keV, and 382 keV emission energies of ^{133}Ba are also clearly present in Fig. 5.4. Additionally, the 20 keV low noise cut-off makes the device capable of detecting the cesium (Cs) X-rays seen in Fig. 5.3. Next, the ^{198}Au spectrum is illustrated in Fig. 5.5 where the 412 keV full energy peak resolution is 2.3% (9.31 keV) FWHM. Again, the Cd and Te X-ray escapes are observable as is the 662 keV photopeak of ^{137}Cs with 1.4% (9.6 keV) FWHM energy resolution. The Compton continuum and backscatter peak are clearly seen in Fig. 5.6. Due to low noise, barium X-rays are also easily identified.

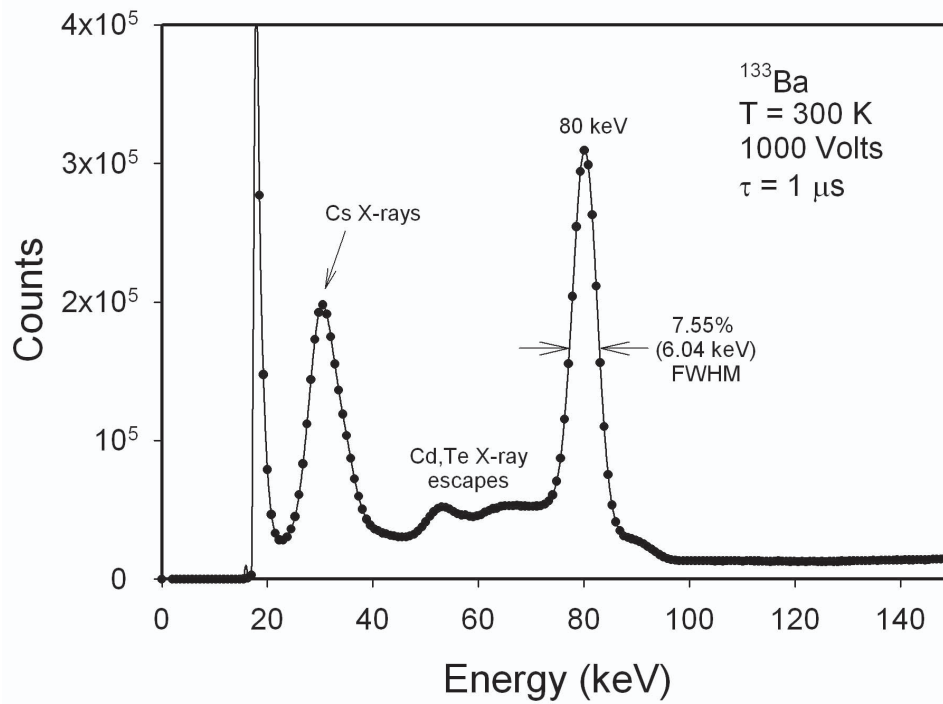


Figure 5.3: Room temperature spectra of a ^{133}Ba source from the $3.4\text{mm} \times 3.4\text{mm} \times 5.7\text{mm}$ CdZnTe semiconductor detector at low energies.

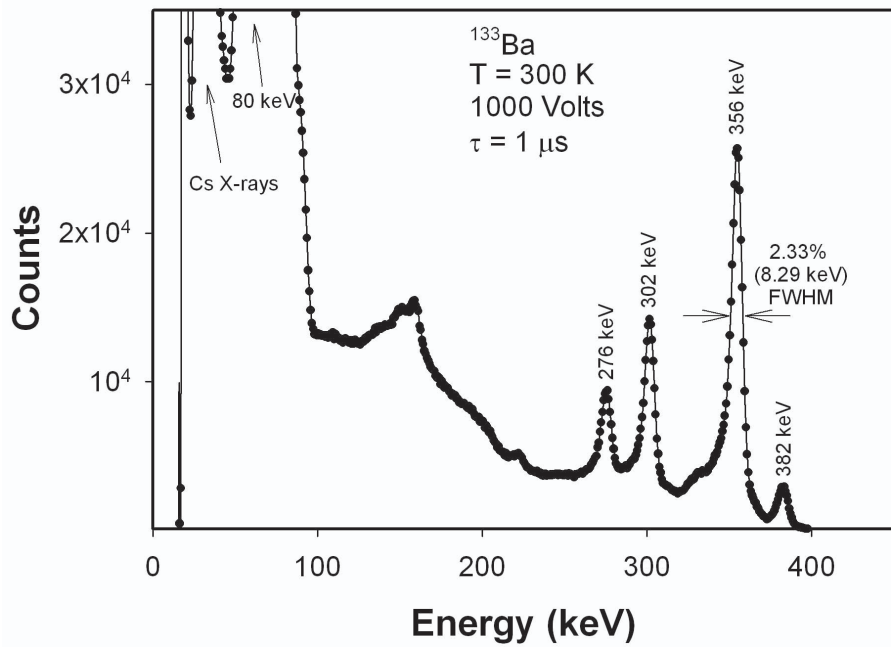


Figure 5.4: Room temperature spectra of a ^{133}Ba source from the $3.4\text{mm} \times 3.4\text{mm} \times 5.7\text{mm}$ CdZnTe semiconductor detector at high energies.

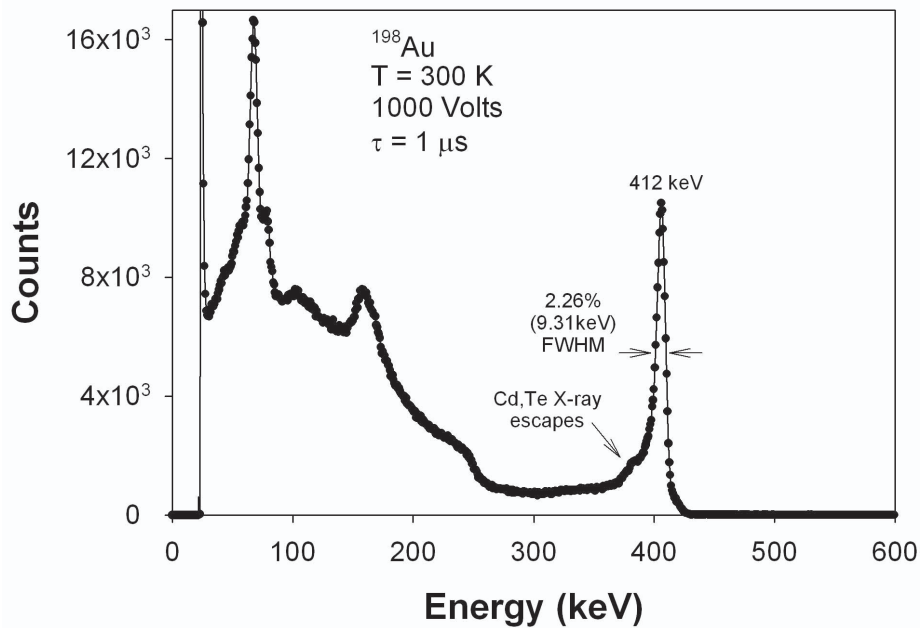


Figure 5.5: Room temperature spectra of a ^{198}Au source from the $3.4\text{mm} \times 3.4\text{mm} \times 5.7\text{mm}$ CdZnTe semiconductor detector at high energies.

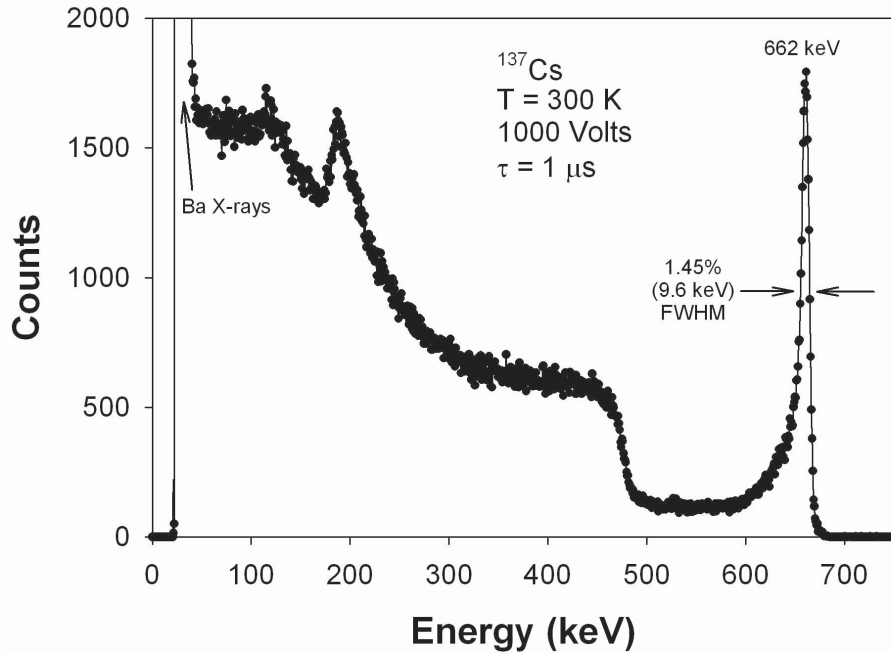


Figure 5.6: Room temperature spectra of a ^{137}Cs source from the $3.4\text{mm} \times 3.4\text{mm} \times 5.7\text{mm}$ CdZnTe semiconductor detector at high energies.

Fig. 5.7 shows the energy spectrum of ^{235}U obtained from a low-activity 93% enriched ^{235}U -nitride solution. The distance between the detector and the source was approximately 5 cm, and the exposure time was 20 hours. All expected energy emissions along with their branching ratios are illustrated in Fig. 5.7. The clearly distinguishable spectral lines of ^{235}U (Fig. 5.7) confirm that the insulated Frisch collar design incorporating bar-shaped CdZnTe material is fully capable of radioactive material identification.

Given that the energy resolution presented for the photopeaks is without any electronic correction. The pulser energy resolution (2.9% FWHM at 191 keV) in Fig. 5.2 represents noise contributions to the detector resolution. The standard deviation, SD (FWHM=2.3 SD), corresponding to the resolution of a full energy peak, is the quadrature sum of the standard deviation values for the detector and the value due to the noise,

$$SD^2 = SD_{\text{detector}}^2 + SD_{\text{noise}}^2 \quad , \quad (5.1)$$

in which the standard deviation, SD , has the units of energy. Clearly, in the present

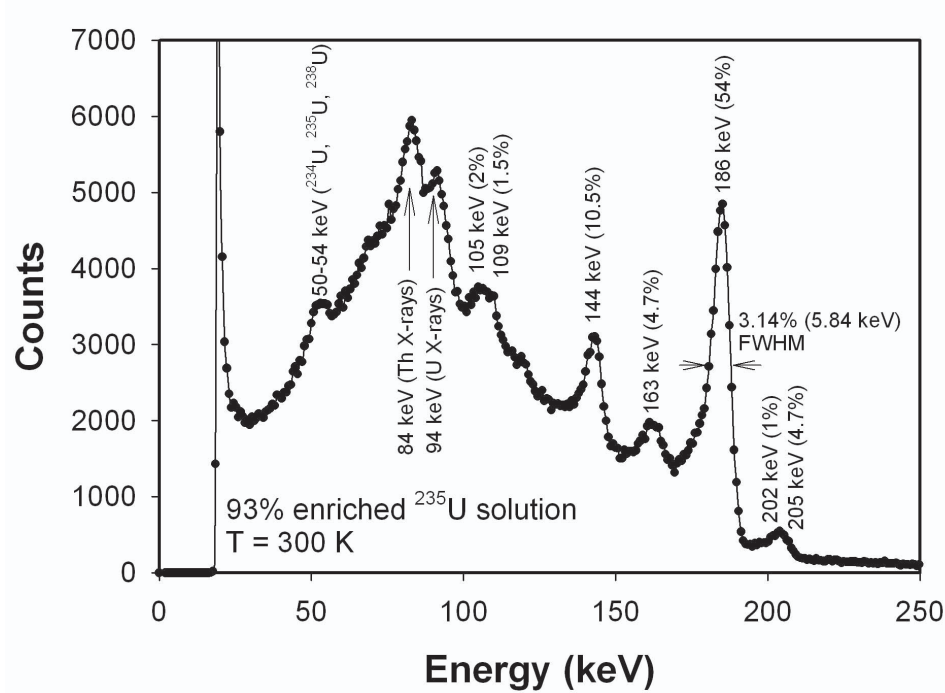


Figure 5.7: Room temperature spectra of a ^{235}U source from the $3.4\text{mm} \times 3.4\text{mm} \times 5.7\text{mm}$ CdZnTe semiconductor detector at high energies.

case, electronic noise contributes significantly to the resolution degradation; hence, reducing electronic noise in the present system significantly improved energy resolution.

5.2 Charge Collection Efficiency Measurement Results and the Effect of High Voltage on CCE

The primary results of characterizing a $4.7\text{mm} \times 4.7\text{mm} \times 9.5\text{mm}$ CdZnTe Frisch collar detector with a highly collimated 662 keV gamma-ray have been submitted for publishing [68], and the experimental setup and procedure are in Section 4.2.3. Subsequently, collected spectra (Figs. 5.8 through 5.15) from the collimated ^{137}Cs gamma-ray source with the $4.7 \times 4.7 \times 9.5 \text{ mm}^3$ CdZnTe Frisch collar device (see sections 4.2.3 and 4.3.3) prove the uniformity of device response to gamma-rays, which is further confirmed by plotting the peak channel number of each spectrum versus the irradiated points as in Figs. 5.16 and 5.17.

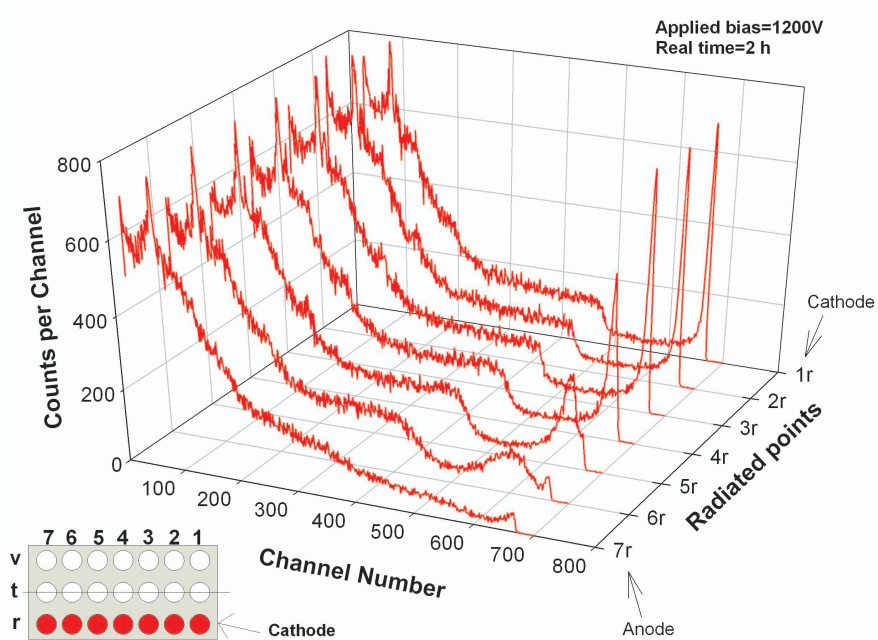


Figure 5.8: Pulse height spectra collected from a collimated ^{137}Cs gamma-ray source with the $4.7 \times 4.7 \times 9.5 \text{ mm}^3$ CdZnTe Frisch collar device. The Frisch collar device was probed with a highly collimated gamma-ray source along row-*r* at 1200V for two hours real time.

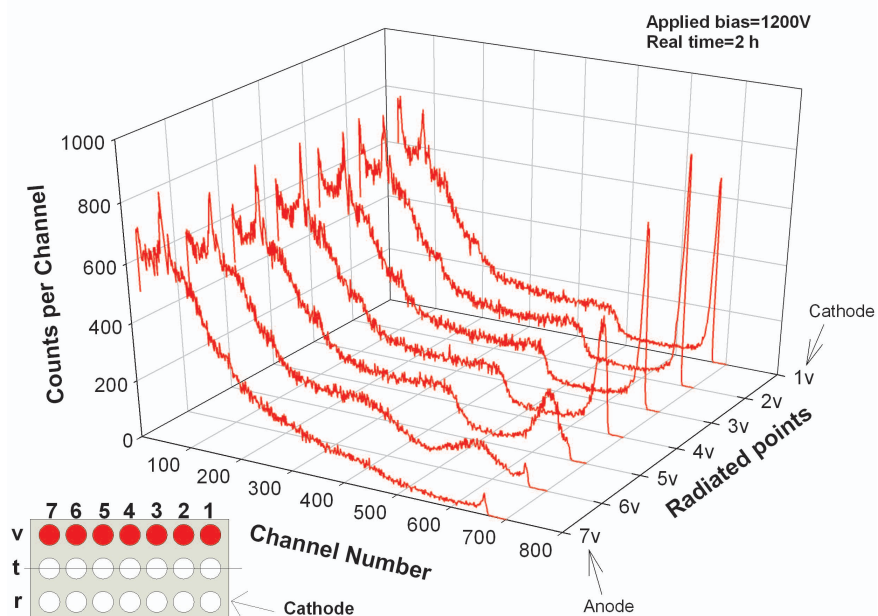


Figure 5.9: Pulse height spectra collected from a collimated ^{137}Cs gamma-ray source with the $4.7 \times 4.7 \times 9.5 \text{ mm}^3$ CdZnTe Frisch collar device. The Frisch collar device was probed with a highly collimated gamma-ray source along row-*v* at 1200V for two hours real time.

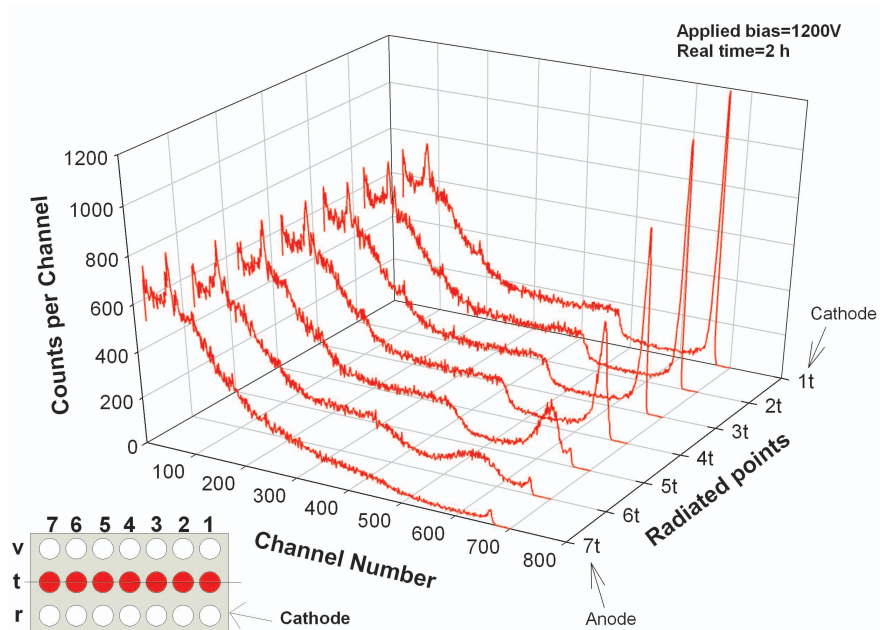


Figure 5.10: Pulse height spectra collected from a collimated ^{137}Cs gamma-ray source with the $4.7 \times 4.7 \times 9.5 \text{ mm}^3$ CdZnTe Frisch collar device. The Frisch collar device was probed with a highly collimated gamma-ray source along row- t at 1200V for two hours real time.

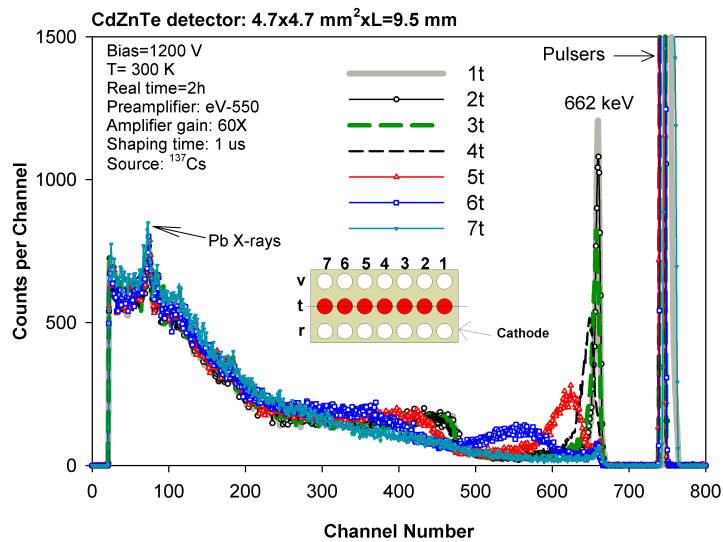


Figure 5.11: Pulse height spectra collected from a collimated ^{137}Cs gamma-ray source with the $4.7 \times 4.7 \times 9.5 \text{ mm}^3$ CdZnTe Frisch collar device along row- t at 1200V. The Frisch collar device was probed with a highly collimated gamma-ray source along row- t at 1200V for two hours real time. The measurement setup and equipment are on the figure.

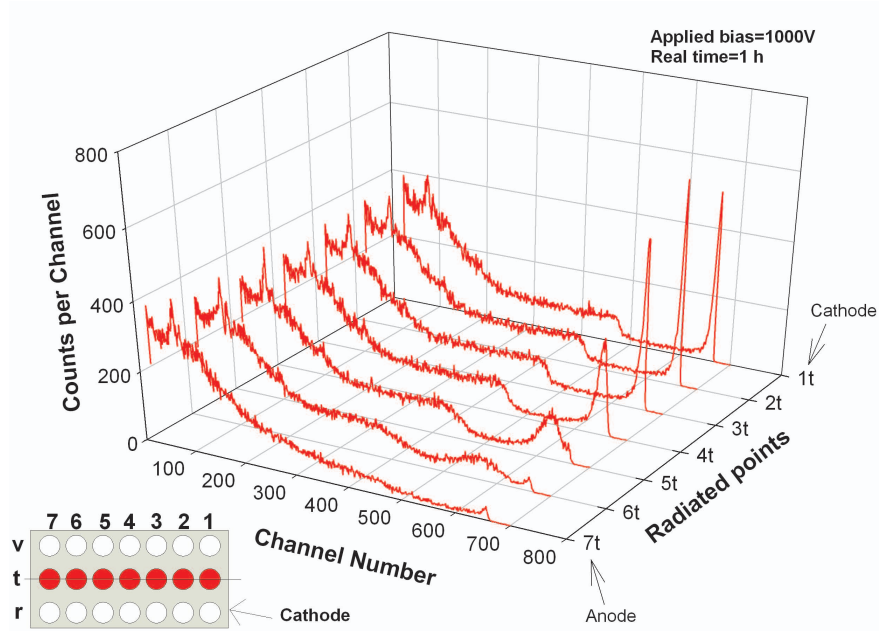


Figure 5.12: Pulse height spectra collected from a collimated ^{137}Cs gamma-ray source with the $4.7 \times 4.7 \times 9.5 \text{ mm}^3$ CdZnTe Frisch collar device. The Frisch collar device was probed with a highly collimated gamma-ray source along row- t at 1000V for one hour real time.

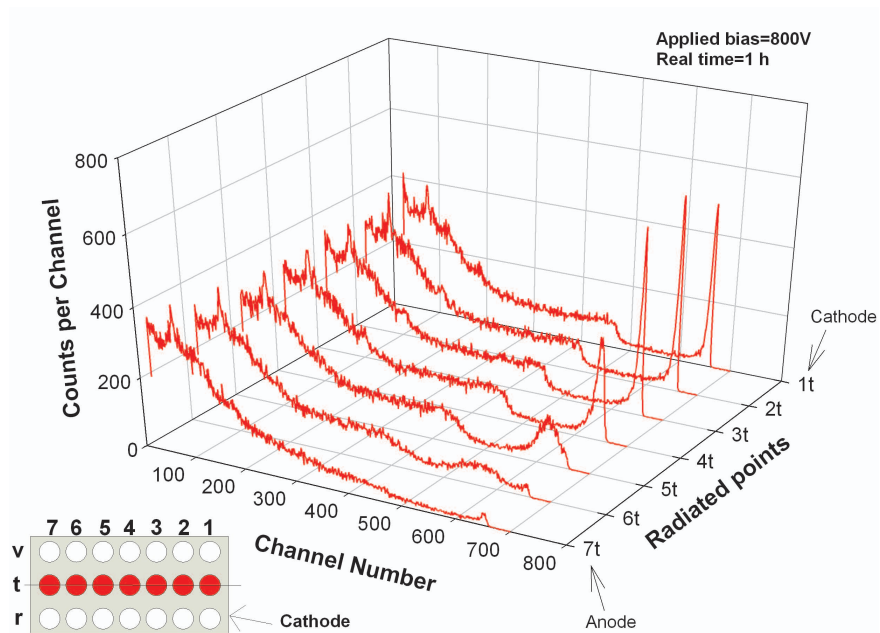


Figure 5.13: Pulse height spectra collected from a collimated ^{137}Cs gamma-ray source with the $4.7 \times 4.7 \times 9.5 \text{ mm}^3$ CdZnTe Frisch collar device. The Frisch collar device was probed with a highly collimated gamma-ray source along row- t at 800V for one hour real time.

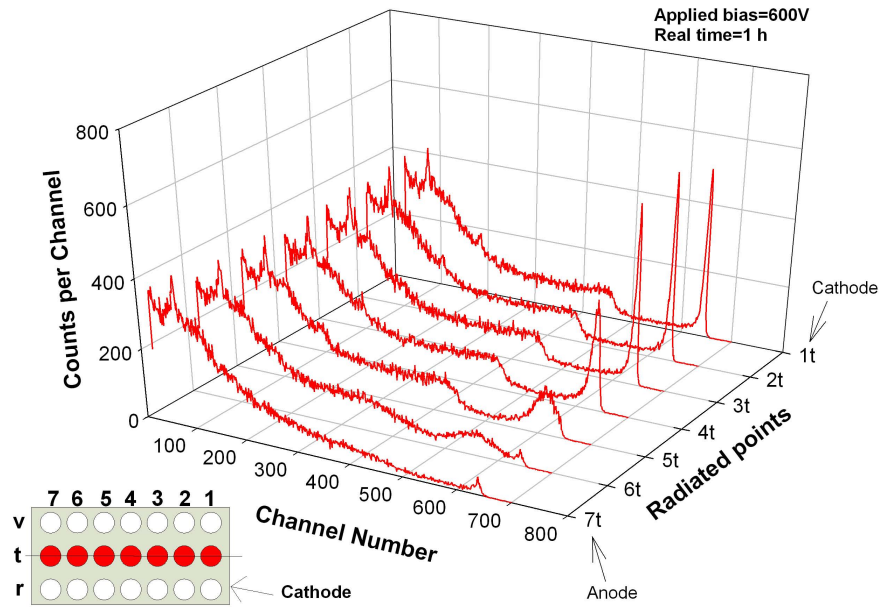


Figure 5.14: Pulse height spectra collected from a collimated ^{137}Cs gamma-ray source with the $4.7 \times 4.7 \times 9.5 \text{ mm}^3$ CdZnTe Frisch collar device. The Frisch collar device was probed with a highly collimated gamma-ray source along row- t at 600V for one hour real time.

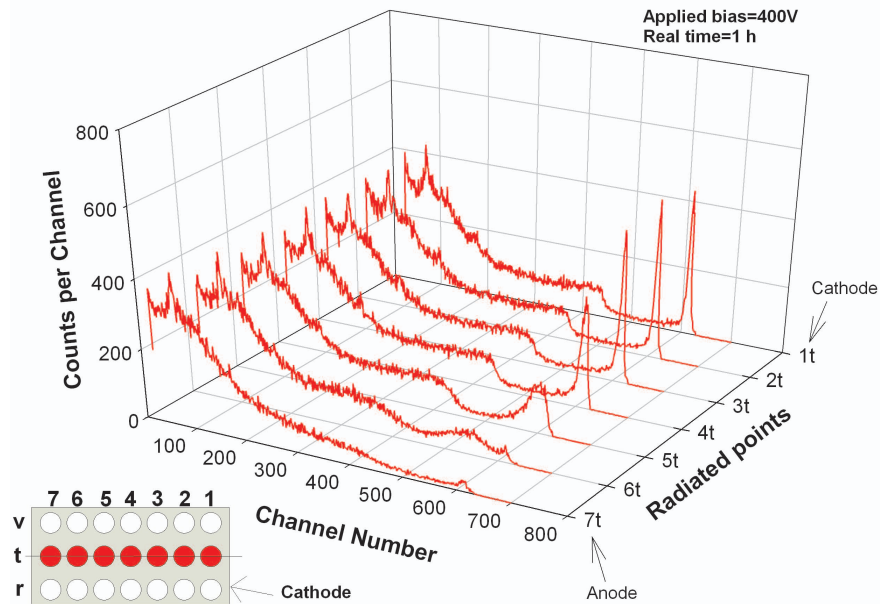


Figure 5.15: Pulse height spectra collected from a collimated ^{137}Cs gamma-ray source with the $4.7 \times 4.7 \times 9.5 \text{ mm}^3$ CdZnTe Frisch collar device. The Frisch collar device was probed with a highly collimated gamma-ray source along row- t at 400V for one hour real time.

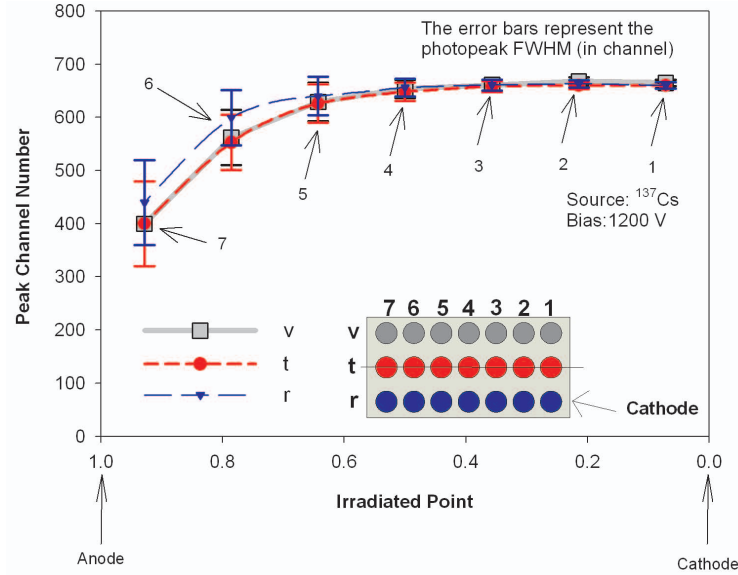


Figure 5.16: The peak channel of photopeak for the irradiated points of the $4.7 \times 4.7 \times 9.5 \text{ mm}^3$ CdZnTe Frisch collar device. The Frisch collar device was probed with a highly collimated gamma-ray source of ^{137}Cs along row-*r*, row-*t* (central line) and row-*v* at 1200V. The error bars represent the photopeak FWHM in channel.

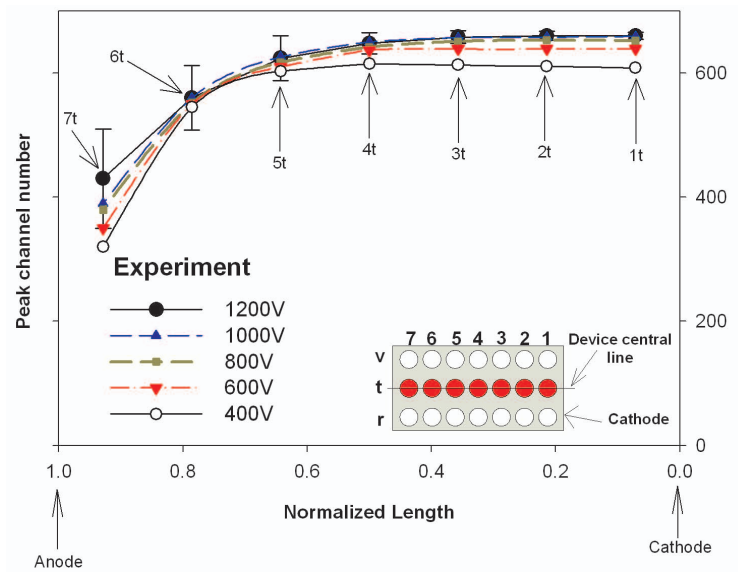


Figure 5.17: The peak channel of photopeak for the irradiated points of the $4.7 \times 4.7 \times 9.5 \text{ mm}^3$ CdZnTe Frisch collar device. The Frisch collar device was probed with a highly collimated gamma-ray source of ^{137}Cs along row-*t* (central line) at different voltages of 1200V, 1000V, 800V, 600V and 400V applied to anode (collecting electrode). The error bars represent the photopeak FWHM in channel and are for the data points collected at 1200V.

As plotted in Fig. 5.16, the peak channel of the photo peak remained unchanged as the collimated gamma-ray source probed almost two-thirds of the device length (from column 1 to column 5) and for the entire device width (columns r , t and v). This consistency in peak channel number on each collected spectrum with respect to irradiated points along the device width and length is clearly visible from the spectra presented in Figs. 5.8 through 5.11, as well.

The peak channel number on each collected spectrum along the device central line (row t) at different applied voltages (Section 4.3.3) is presented in Fig. 5.17, where the peak channel of the photo peak remained unchanged as the collimated gamma-ray source probed almost two-thirds of the device length (from column 1 to column 5) even at the low applied voltage of 400V. This uniform response is also observed from the spectra presented in Figs. 5.10 through 5.15. Comparing the experimental results presented in Fig. 5.17 and the theoretical prediction of the CCE for the same device in Fig. 3.29 reveals that the device response follows the prediction for a variety of applied voltages. Indeed, the comparison between the theoretical prediction of CCE (explained in Section 3.1.3) and the experimental results (normalized peak channel number) is well illustrated in Figs. 5.18 through 5.22. The experimental results together with the theoretical confirmation on the $4.7 \times 4.7 \times 9.5$ mm³ CdZnTe Frisch collar device clearly prove that in spite of non-uniform electric field distribution within the device as well as relatively low electric field distribution near the cathode region [69], the Frisch collar device responds very uniformly to gamma-rays. Even though the electric field distribution is relatively low near the cathode region, device performance is actually enhanced in that region. In other words, the overall enhancement on device spectral performance is so remarkable that sub-0.9% FWHM energy resolution at 662 keV is achieved without any electronic correction (Fig. 3.8) for the $4.7 \times 4.7 \times 9.5$ mm³ CdZnTe Frisch collar device used in this study.

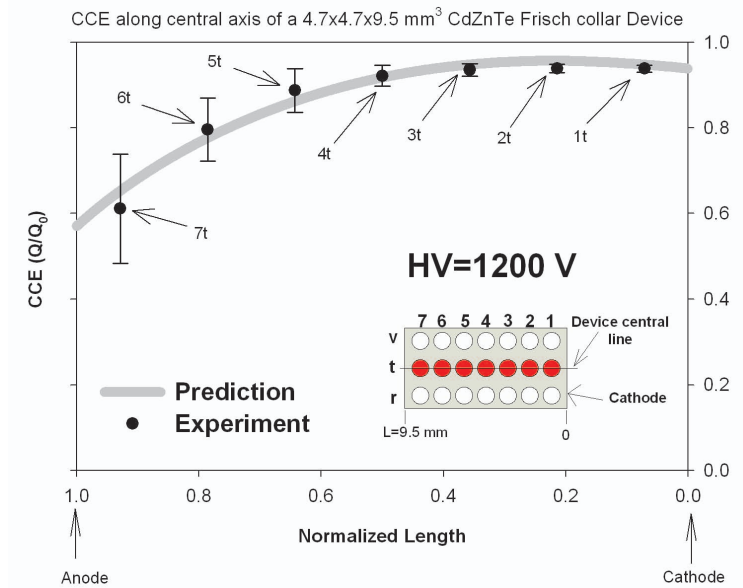


Figure 5.18: The CCE profile at 1200V applied to the anode (collecting electrode) along the central line of the $4.7 \times 4.7 \times 9.5 \text{ mm}^3$ CdZnTe Frisch collar device. The experimental data points are the normalized peak channel of photopeak for the irradiated points (row- t) of the Frisch collar device. The error bars represent the photopeak FWHM at 662 keV.

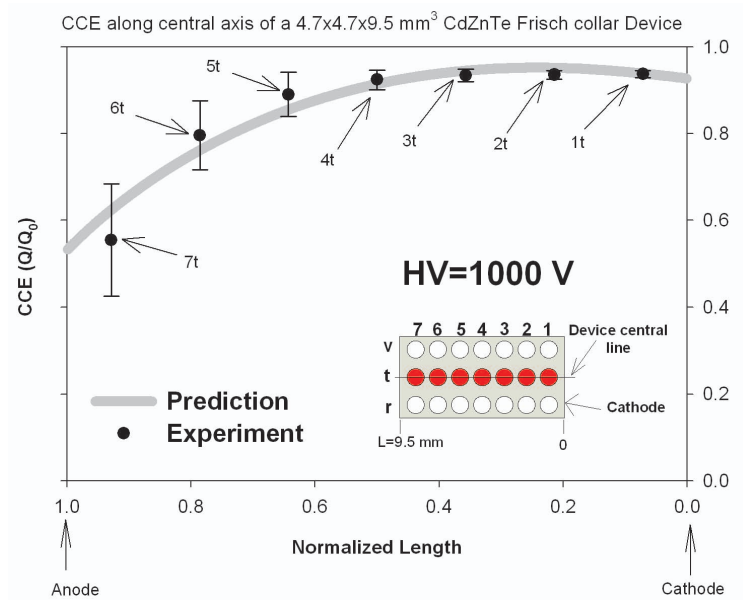


Figure 5.19: The CCE profile at 1000V applied to the anode (collecting electrode) along the central line of the $4.7 \times 4.7 \times 9.5 \text{ mm}^3$ CdZnTe Frisch collar device. The experimental data points are the normalized peak channel of photopeak for the irradiated points (row- t) of the Frisch collar device. The error bars represent the photopeak FWHM at 662 keV.

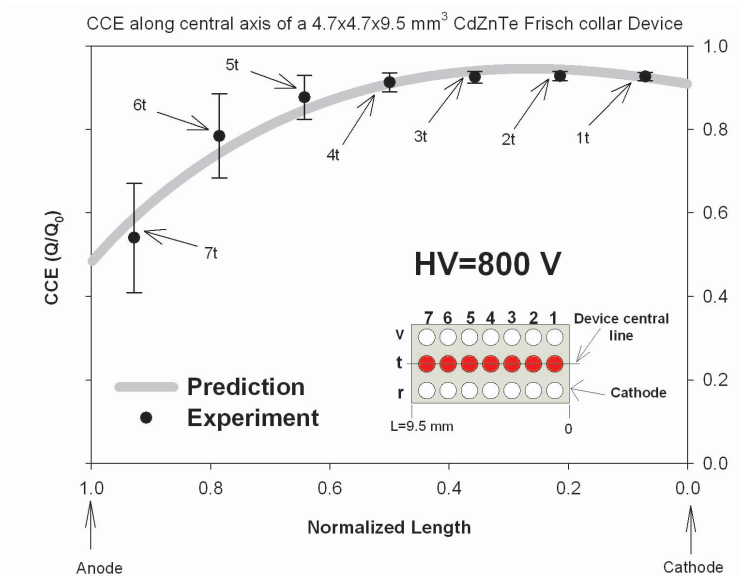


Figure 5.20: The CCE profile at 800V applied to the anode (collecting electrode) along the central line of the $4.7 \times 4.7 \times 9.5 \text{ mm}^3$ CdZnTe Frisch collar device. The experimental data points are the normalized peak channel of photopeak for the irradiated points (row-*t*) of the Frisch collar device. The error bars represent the photopeak FWHM at 662 keV.

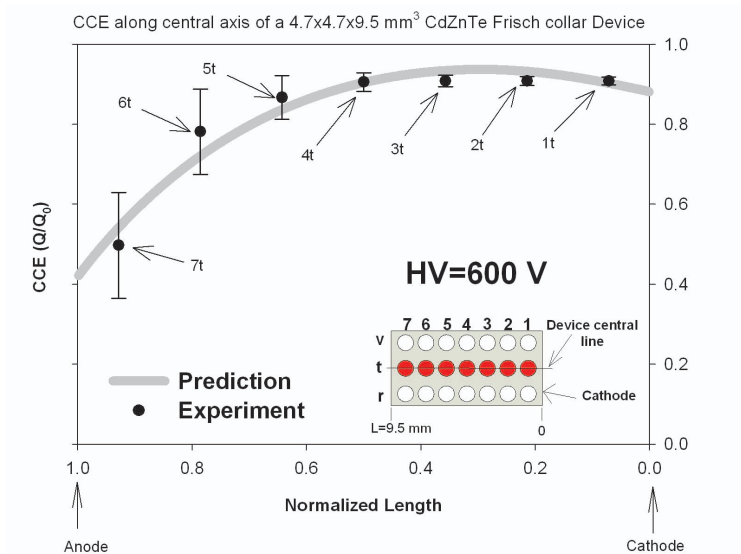


Figure 5.21: The CCE profile at 600V applied to the anode (collecting electrode) along the central line of the $4.7 \times 4.7 \times 9.5 \text{ mm}^3$ CdZnTe Frisch collar device. The experimental data points are the normalized peak channel of photopeak for the irradiated points (row-*t*) of the Frisch collar device. The error bars represent the photopeak FWHM at 662 keV.

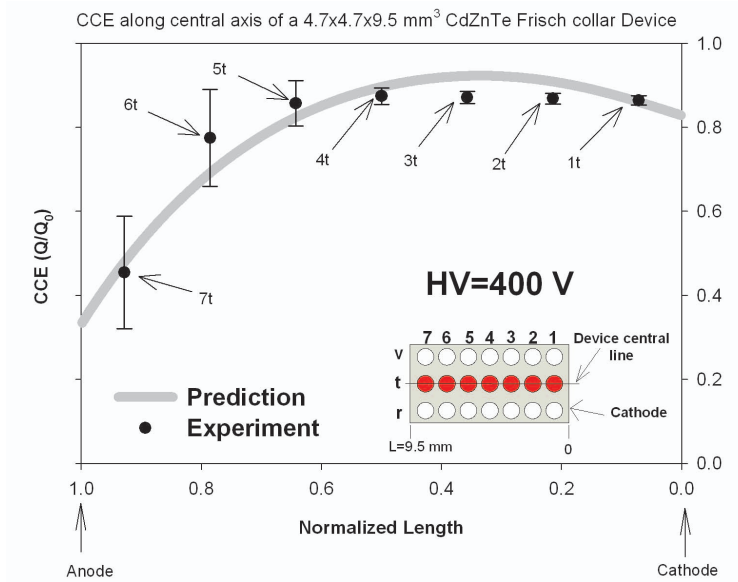


Figure 5.22: The CCE profile at 400V applied to the anode (collecting electrode) along the central line of the $4.7 \times 4.7 \times 9.5 \text{ mm}^3$ CdZnTe Frisch collar device. The experimental data points are the normalized peak channel of photopeak for the irradiated points (row- t) of the Frisch collar device. The error bars represent the photopeak FWHM at 662 keV.

Nonetheless, a feature on all spectra (Figs. 5.8 through 5.15), especially near the anode radiated data points (columns 5, 6 and 7), needs to be addressed. On all spectra collected from irradiating the device near the anode a little hump representing the 662 keV remains unchanged. The feature appears due to the non-collided 662 keV gamma-rays, which screen through the lead collimator edges and interact within regions of the device outside the probed area. These low flux un-collided 662 keV gamma-rays interact in other regions of the device with better CCE profile (regions between columns 1 to 5) causing a secondary spectrum, clearly seen as a new feature at column 6 of all spectra (Figs. 5.8 through 5.15).

5.3 Investigating Parameters Affecting Device Performance

This section addresses the results of the studies (experiments and the theoretical confirmations) on parameters with significant impact on performance of CdZnTe Frisch collar device. Among those are the effects of crystal geometry (device aspect ratio), insulator layer thickness, device length and surface treatment.

5.3.1 Frisch Collar Geometry Effect Results

The results of crystal geometry and the aspect ratio on the performance of the CdZnTe Frisch collar detector were published previously in [70]. The theoretical considerations for this study are in Section 3.2.1.1, and the experimental procedure and setup are in Section 4.3.1, while the results follow in this section.

5.3.1.1 Spectral testing results for the Frisch collar geometry effect

Fig. 5.23 through Fig. 5.28 display the energy spectra for the devices mentioned in Section 4.3.1 and shown in Fig. 3.9 with standard gamma-ray sources of ^{241}Am and ^{137}Cs . Fig. 5.27 shows that the Frisch collar effect begins to occur for the devices with a minimum aspect ratio near 1.0 for the 662 keV gamma-rays. Furthermore, the Frisch collar enhances the device performance further when the device aspect ratio (AR) is greater than 1.5. The energy spectra collected from ^{137}Cs for the devices with the smallest and greatest aspect ratios (CZT1 and CZT11, respectively) are also shown in Figs. 5.23 and 5.25. Clearly, the Frisch collar offers no appreciable energy resolution enhancement for 662 keV gamma-rays for CZT1 with AR=0.26 (Figs. 5.23 and 5.27); however, the energy resolution enhancement is significant (2.3% FWHM at 662 keV) for the Frisch collar CZT11 with AR=1.92 (Figs. 5.25 and 5.27).

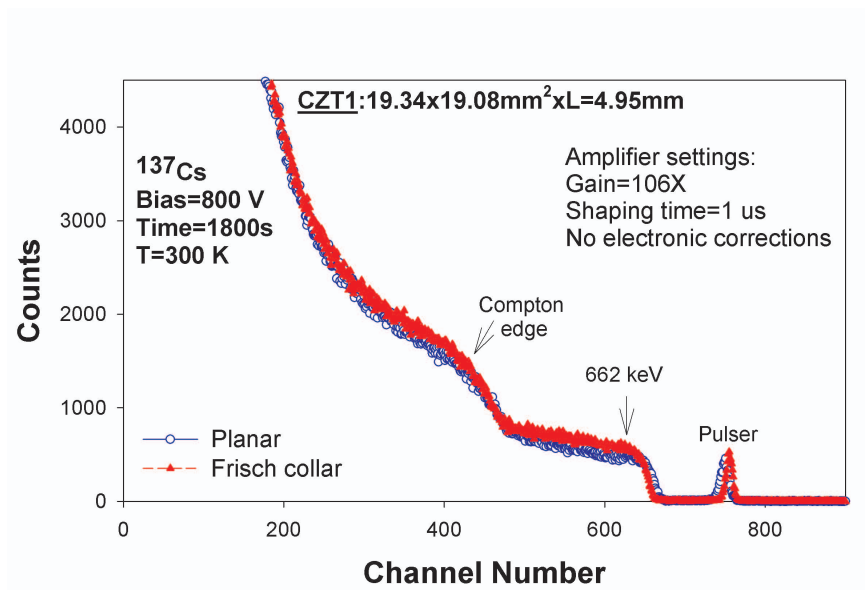


Figure 5.23: Pulse height spectra collected from CZT1 using a ^{137}Cs source for both planar and Frisch collar configurations.

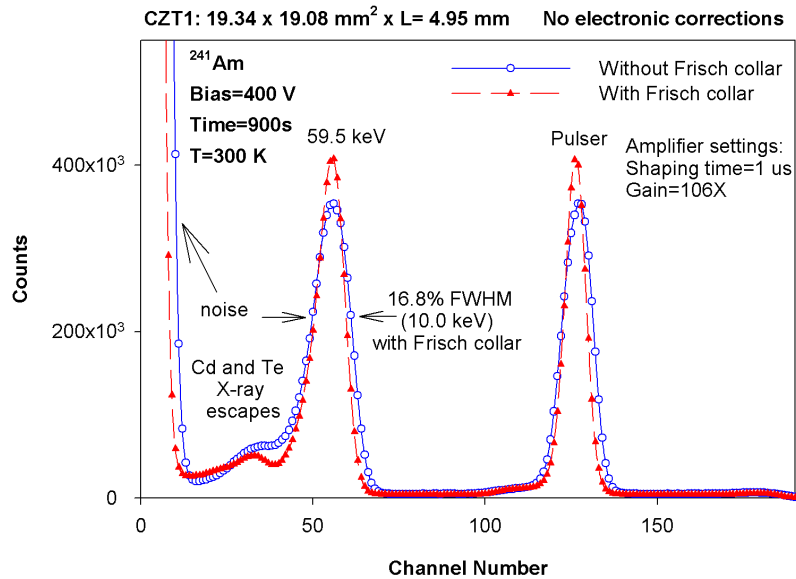


Figure 5.24: Pulse height spectra collected from CZT1 using a ^{241}Am source for both planar and Frisch collar configurations.

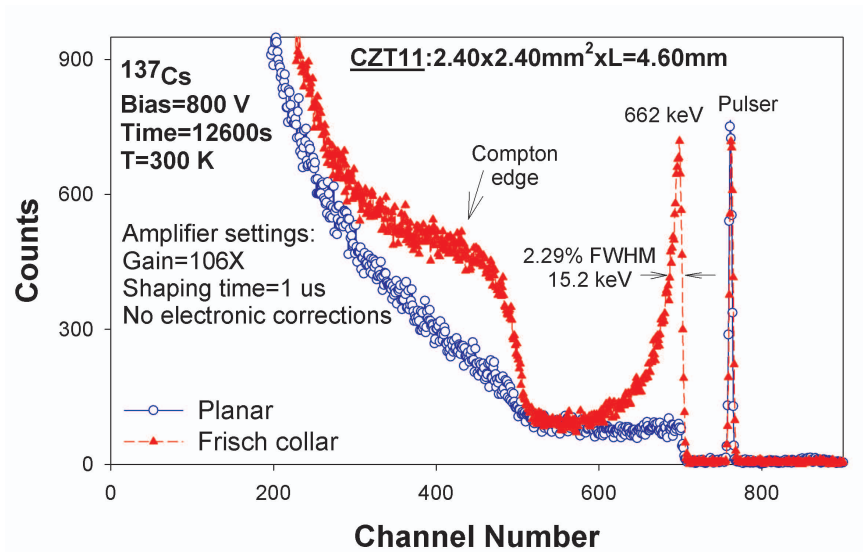


Figure 5.25: Pulse height spectra collected from CZT11 using a ^{137}Cs source for both planar and Frisch collar configurations.

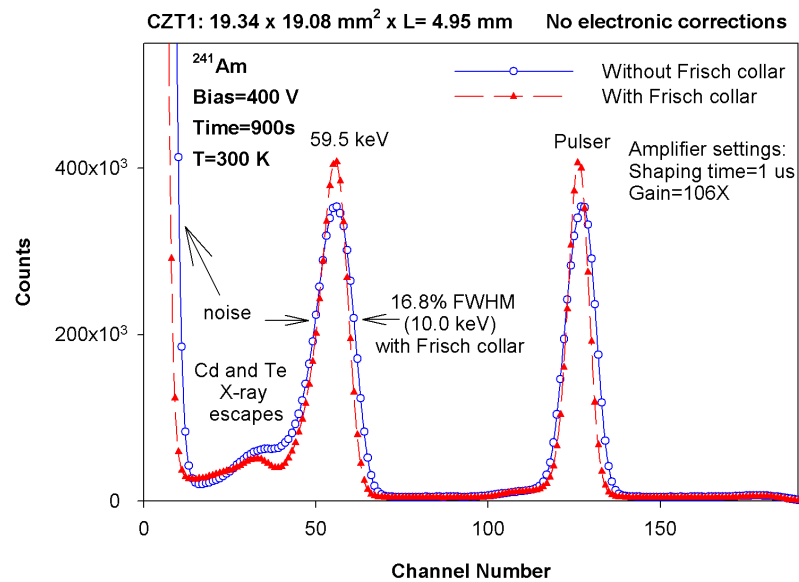


Figure 5.26: Pulse height spectra collected from CZT11 using a ^{241}Am source for both planar and Frisch collar configurations.

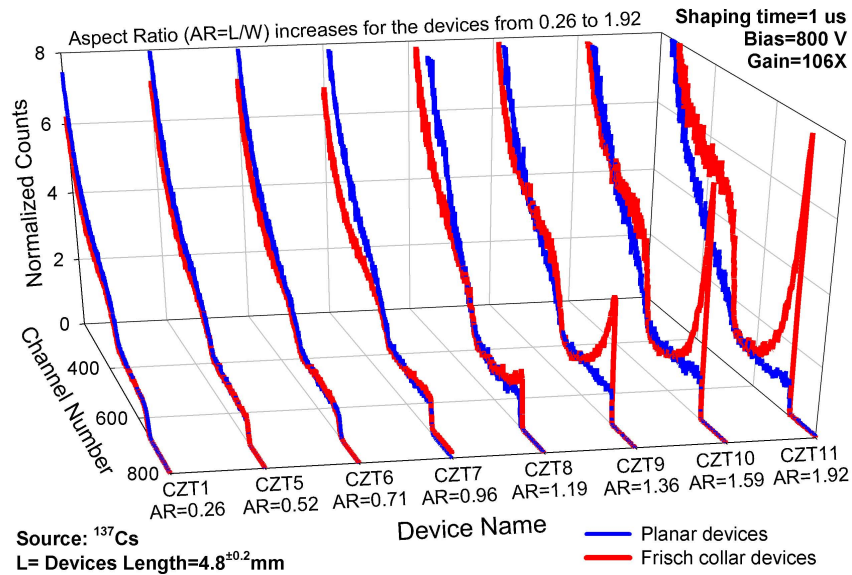


Figure 5.27: Normalized pulse height spectra collected from devices labeled as follows: CZT1, CZT5, CZT6, CZT7, CZT8, CZT9, CZT10 and CZT11 in both planar and Frisch collar configuration using an ^{137}Cs source.

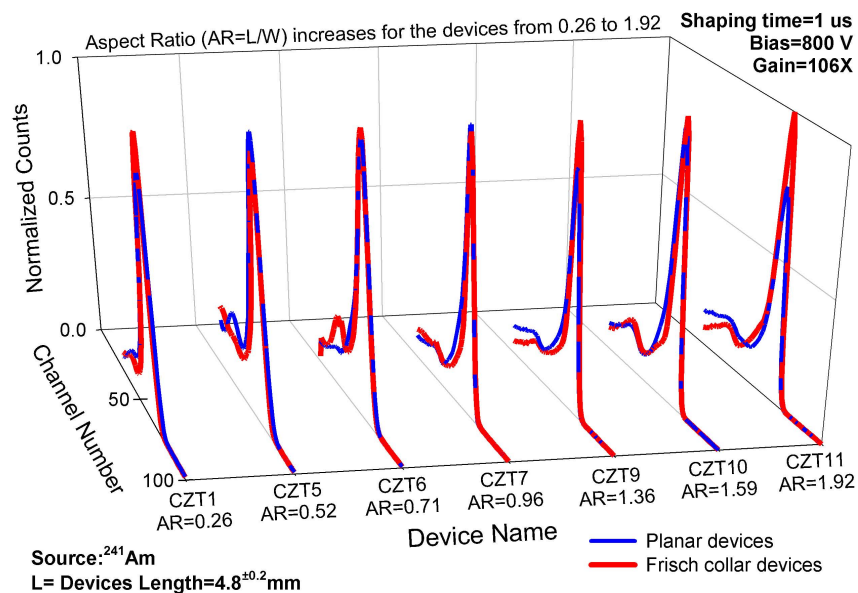


Figure 5.28: Normalized pulse height spectra collected from devices labeled as follows: CZT1, CZT5, CZT6, CZT7, CZT8, CZT9, CZT10 and CZT11 in both planar and Frisch collar configuration using an ^{241}Am source.

Energy resolution enhancement by the Frisch collar for the 59.5 keV gamma-rays is not as noticeable for the devices mentioned in Section 4.3.1 and shown in Fig. 3.9 (see Fig. 5.28). The photoelectric linear absorption coefficient for CdZnTe is approximately 40 cm^{-1} for 59.5 keV emitted by ^{241}Am [66]; therefore, 90% of the photons were absorbed in the first 575 microns of material, which limits the variance in the electronically induced signal, thereby having an effect similar to that of a single carrier device. This finding is experimentally verified by collecting the ^{241}Am energy spectra, which are demonstrated in Figs. 5.24, 5.26, and 5.28 (for CZT1 through CZT11, respectively).

This effect can be predicted from the weighting potential profiles illustrated in Figs. 3.10 through 3.17. Specifically, the Frisch collar effect improves energy resolution by negating the severe trapping effects of holes, primarily due to the nonlinear weighting potential near the anode region. Hence, the Frisch collar device performs as a single carrier device for which maintaining a sharp, nonlinear weighting potential near the anode region (collecting electrode) is vital. This becomes essential for high energy gamma-rays, where more uniform gamma-ray interactions occur throughout the entire device volume. Such interactions create an average uniform distribution of electron-hole pair excitation through the detector. A numerical solution of the weighting potential for the Frisch collar devices exhibits that the nonlinearity effect does not penetrate the bulk of the device with the $\text{AR} \leq 1.0$ (Figs. 3.10 through 3.12). Figs. 3.10 through 3.12 (devices with $\text{AR} \leq 1.0$) show that the weighting potential is nearly linear, except near the lateral surfaces, which show a distribution similar to that of a planar configuration. For that reason, the Frisch collar has little effect for $\text{AR} \leq 1.0$.

5.3.2 Results of insulator layer thickness effect on performance of the CdZnTe Frisch collar devices

The results of the study on insulator layer thickness effect on performance of the CdZnTe Frisch collar detector were published previously in [69]. The theoretical considerations for this part are in Section 3.2.1.4, and the experimental procedure and setup are in Section 4.3.2, which the results are in this section.

5.3.2.1 Current-voltage characteristic measurement results for devices used for the insulator layer thickness effect

As mentioned in Section 4.3.2, six CdZnTe devices were fabricated and used for this study. The devices' size and insulator thickness along with the setup are presented in Tables 4.2, 4.3, and 4.4. The current-voltage (IV) characteristic curves obtained for planar devices listed in Table 4.2 are in Fig. 5.29.

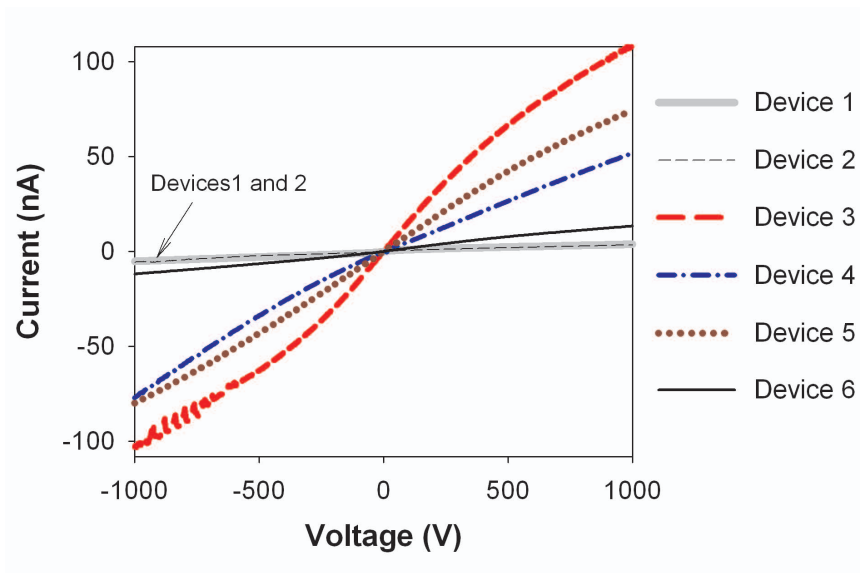


Figure 5.29: The current-voltage (IV) characteristic curve of Device 1 through Device 6 in planar configurations for the insulator layer thickness effect.

5.3.2.2 Spectral testing results for devices with different insulator layer thicknesses

Figs. 5.30 through 5.38 display the energy spectra for the devices listed in Table 4.2 with dielectric layer thicknesses presented in Table 4.3 with standard ^{137}Cs gamma-ray sources. Figs. 5.30 through 5.32 show the energy spectra for Device 1 to Device 3, respectively. The results show device improvement for the thinnest dielectric layer for Device 1 to Device 3. Notably, Device 1 and Device 2, registered little enhancement as a result of the Frisch collar effect, even with a thin dielectric layer, because the aspect ratios of the planar devices are smaller than 1.5 and do not meet the minimum required aspect ratio (as presented in Section 5.3.1).

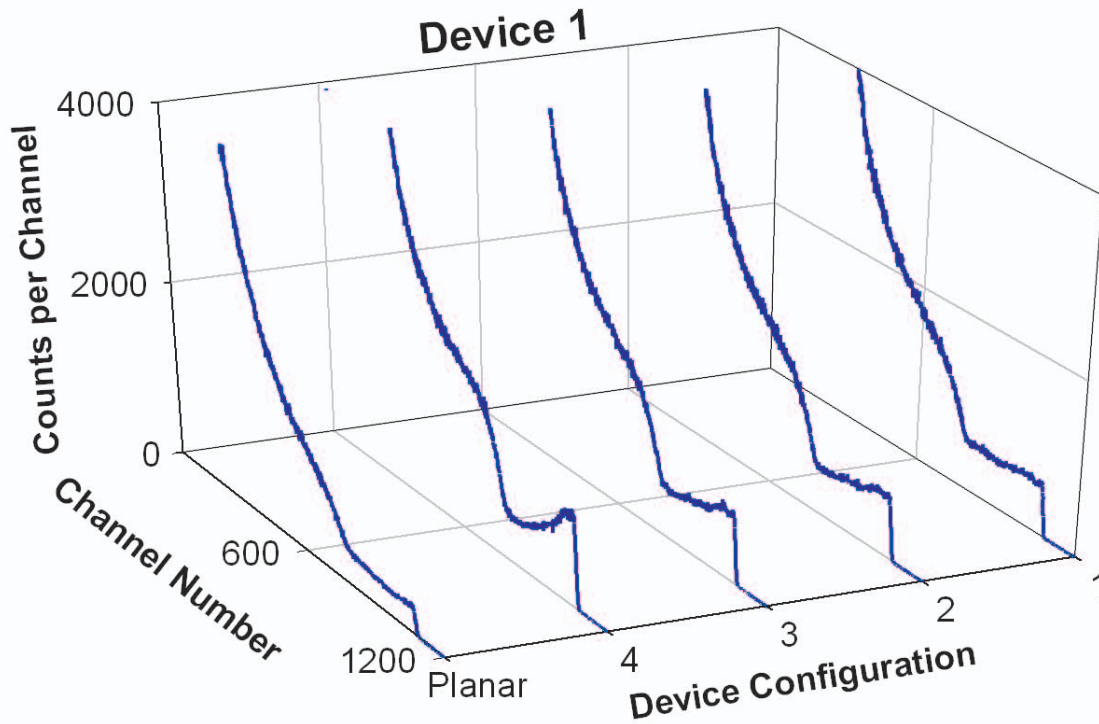


Figure 5.30: The pulse height spectra of Device 1 ($4.95 \times 4.76 \times L=4.87 \text{ mm}^3$) taken with standard gamma-ray source of ^{137}Cs . The applied bias, amplifier gain, and the spectral testing time are presented in Section 4.3.2 and Table 4.4. The dielectric thickness t is presented in Table 4.3 for Frisch collar Device 1 #1 to Device 1 #4,. The best spectral performance is for Device 1 #4 which has the thinnest dielectric layer ($t=0.05 \text{ mm}$).

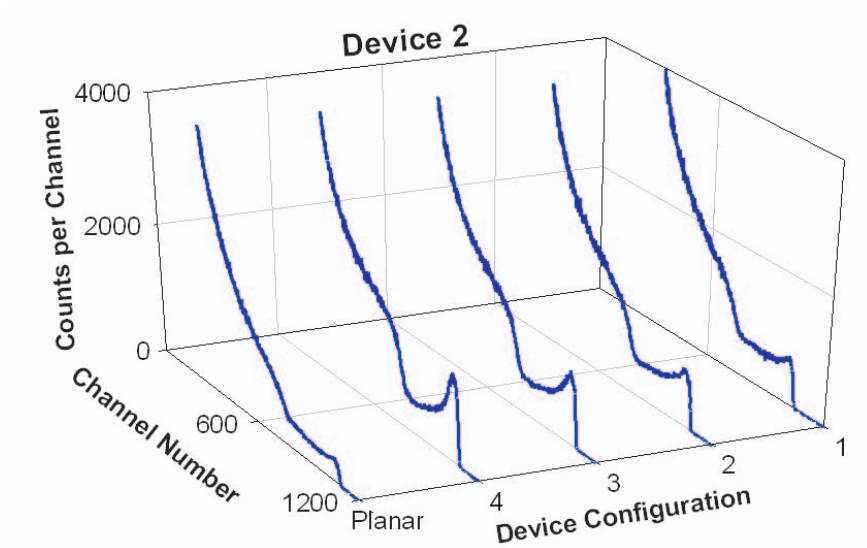


Figure 5.31: The pulse height spectra of Device 2 ($4.70 \times 4.56 \times L=6.03 \text{ mm}^3$) taken with a standard ^{137}Cs gamma-ray source. The applied bias, amplifier gain, and the spectral testing time are in Section 4.3.2 and Table 4.4. The dielectric thickness t is in Table 4.3 for Frisch collar Device 2 #1 to Device 2 #4. The best spectral performance is for Device 2 #4, which has the thinnest dielectric layer ($t=0.05 \text{ mm}$)

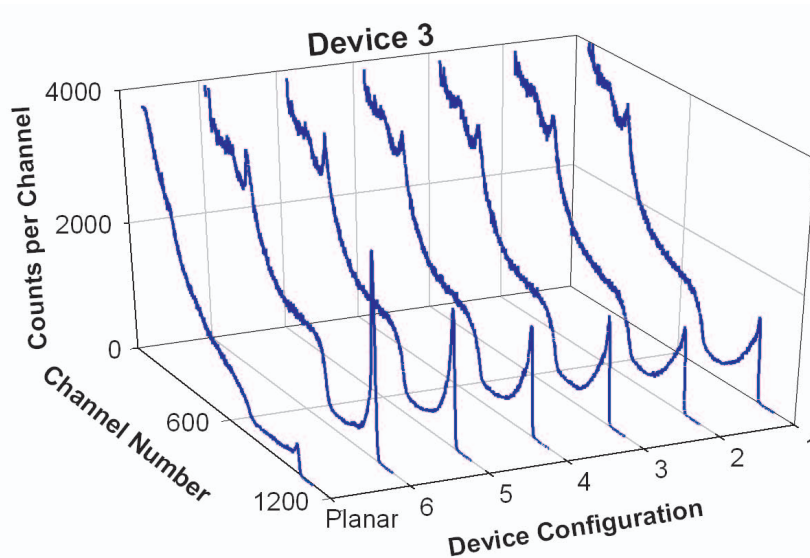


Figure 5.32: The pulse height spectra of Device 3 ($3.36 \times 3.34 \times L=5.68 \text{ mm}^3$) taken with a standard ^{137}Cs gamma-ray source. The applied bias, amplifier gain, and the spectral testing time are in Section 4.3.2 and Table 4.4. The dielectric thickness t is in Table 4.3 for Frisch collar Device 3 #1 to Device 3 #6. The best spectral performance is for Device 3 #6, which has the thinnest dielectric layer ($t=0.10 \text{ mm}$). Device 3 #6 shows $2.1\% \pm 0.1\%$ FWHM energy resolution at 662 keV.

Figs. 5.33 through 5.36 present the energy spectra for Device 4 and Device 5, in both planar and Frisch collar configuration with standard gamma-ray sources of ^{137}Cs . The results indicate an optimum dielectric layer thickness at which both Device 4 and Device 5 reach their best spectral performance. The optimum dielectric layer thickness for Device 4 is around 0.27 mm and for Device 5 around 0.39 mm. The dielectric layer thicknesses for Device 4 and Device 5 in Frisch collar configurations, the full width half maximum (FWHM) energy resolution at 662 keV, and the peak-to-valley ratio (P:V) of the full energy peak (FEP) are also summarized in Table 5.1.

Table 5.1: The FWHM and peak-to-valley of collected spectra with Device 4 and Device 5. The dielectric thickness t is in mm with the standard deviation of ± 0.005 mm. The full width half maximum (FWHM) energy resolution is at 662 keV with the standard deviation of $\pm 0.1\%$. P:V is the peak-to-valley ratio of the full energy peak (FEP) and has standard deviation of 0.1 for the lowest values and 0.7 for the highest values. The best performance of Device 5 was for Frisch collar Device 5 #8 with the optimum dielectric thickness of 0.39 mm, while the best performance of Device 4 was for Frisch collar Device 4 #10 with the optimum dielectric thickness of 0.27 mm.

Frisch collar #	Device 4			Device 5		
	t (mm)	FWHM	P:V	t (mm)	FWHM	P:V
#1	1.54	N/A	3.0	1.36	N/A	4.0
#2	1.34	4.6%	3.0	1.16	4.9%	4.1
#3	1.14	3.8%	4.2	0.95	3.4%	7.0
#4	0.94	3.0%	5.1	0.81	2.6%	8.5
#5	0.80	2.8%	6.7	0.70	2.0%	8.4
#6	0.70	2.5%	6.9	0.60	1.7%	10.7
#7	0.59	2.0%	8.3	0.50	1.5%	13.0
#8	0.50	1.9%	10.9	0.39	1.3%	14.3
#9	0.38	1.7%	11.2	0.27	1.4%	14.1
#10	0.27	1.4%	13.9	0.16	1.7%	12.1
#11	0.22	1.7%	10.7	0.08	2.0%	10.1
#12	0.16	1.9%	7.8	N/A	N/A	N/A
#13	0.08	2.2%	7.2	N/A	N/A	N/A

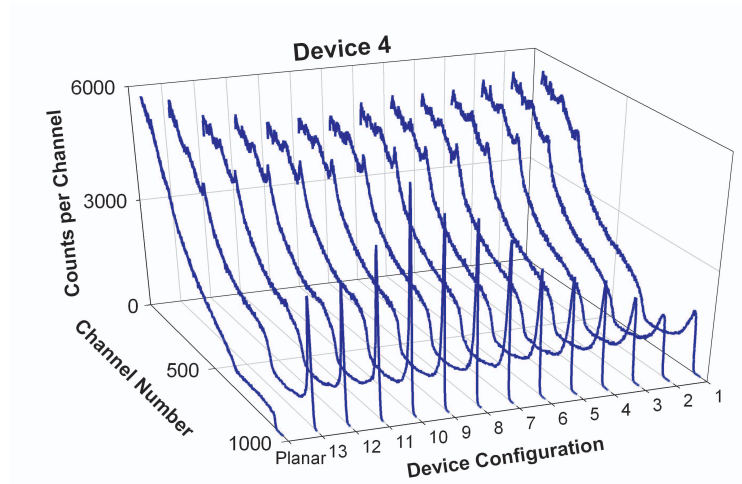


Figure 5.33: The pulse height spectra of Device 4 ($3.96 \times 4.01 \times L=11.60 \text{ mm}^3$) taken with standard ^{137}Cs gamma-ray source. The applied bias, amplifier gain, and the spectral testing time are in Section 4.3.2 and Table 4.4. The dielectric thickness t , the energy resolution, and the peak-to-valley are in Table 5.1 for Frisch collar Device 4 #1 to Device 4 #13. The best spectral performance is for Device 4 #10, which has the optimum dielectric layer thickness of 0.27 mm. Device 4 #10 shows $1.4\% \pm 0.1\%$ FWHM energy resolution at 662 keV.

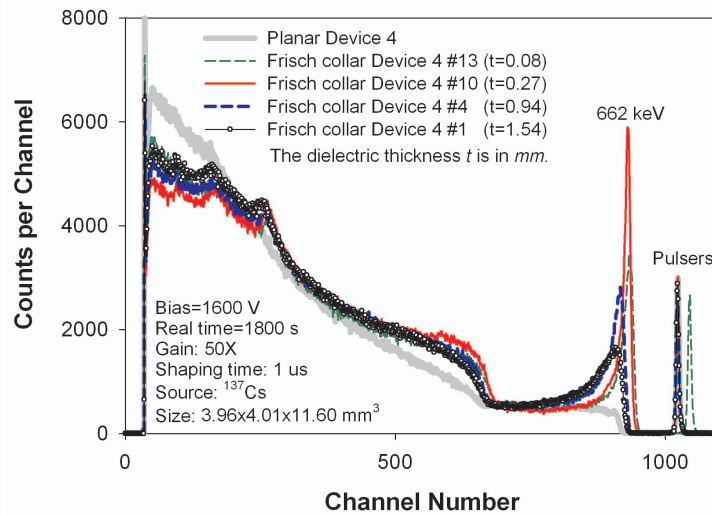


Figure 5.34: The pulse height spectra of Device 4 taken with a standard ^{137}Cs gamma-ray source. The best spectral performance is for Device 4 #10, which has the optimum dielectric layer thickness of 0.27 mm. Device 4 #10 shows $1.4\% \pm 0.1\%$ FWHM energy resolution at 662 keV and peak-to-valley of 13.9 ± 0.5

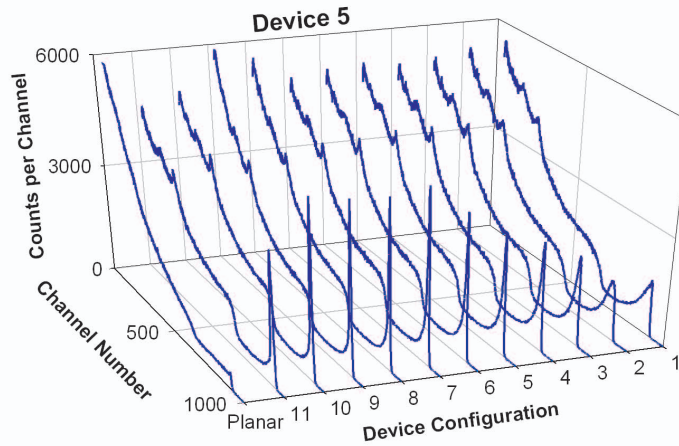


Figure 5.35: The pulse height spectra of Device 5 ($3.92 \times 3.89 \times L=10.82 \text{ mm}^3$) taken with a standard ^{137}Cs gamma-ray source. The applied bias, amplifier gain, and the spectral testing time are in Section 4.3.2 and Table 4.4. The dielectric thickness t , the energy resolution and the peak-to-valley are in Table 5.1 for Frisch collar Device 5 #1 to Device 5 #11. The best spectral performance is for Device 5 #8, which has the optimum dielectric layer thickness of 0.39 mm. Device 5 #8 shows $1.3\% \pm 0.1\%$ FWHM energy resolution at 662 keV.

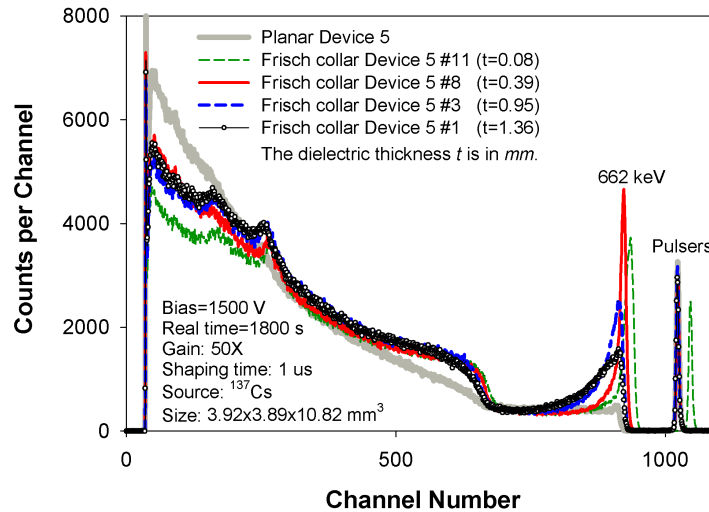


Figure 5.36: The pulse height spectra of Device 5, taken with a standard ^{137}Cs gamma-ray source, for specific dielectric thicknesses. The best spectral performance is for Device 5 #8, which has the optimum dielectric layer thickness of 0.39 mm. Device 5 #8 shows $1.3\% \pm 0.1\%$ FWHM energy resolution at 662 keV and peak-to-valley of 14.3 ± 0.7 .

A similar effect occurs for Device 6 with the different dielectric layer thicknesses in Table 4.3 as in Fig. 5.37 and Fig. 5.38 showing the energy spectra with standard ^{137}Cs gamma-ray sources. Here, the optimum dielectric layer thickness for Device 6 is around 1.10 mm. The summary of the dielectric layer thicknesses for Frisch collar Device 6, the FWHM energy resolution at 662 keV, and the P:V of the FEP are in Table 5.2.

Table 5.2: The FWHM and P:V of collected spectra with Device 6. The standard deviation for dielectric thickness t is ± 0.005 mm, and for the FWHM energy resolution is $\pm 0.1\%$. P:V has the standard deviation of 0.1 for the lowest values and 0.4 for the highest values. The best performance of Device 6 was for Frisch collar Device 6 #5.

Device 6				
Frisch collar #	t (mm)	FWHM	P:V	
#1	2.50	N/A	2.2	
#2	1.60	3.5%	10.5	
#3	1.40	1.6%	9.1	
#4	1.25	1.6%	11.0	
#5	1.10	1.6%	15.1	
#6	0.95	2.2%	8.4	
#7	0.45	4.0%	5.5	

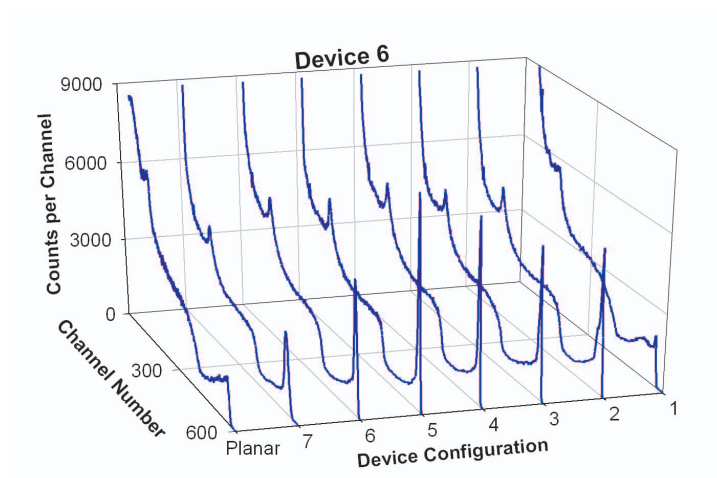


Figure 5.37: The pulse height spectra of Device 6 ($5.01 \times 4.73 \times L = 19.63 \text{mm}^3$) taken with a standard ^{137}Cs gamma-ray source. The experimental setups are in Table 4.4. The best performance is for Device 6 #5 with the optimum t of 1.10 mm, which shows $1.6\% \pm 0.2\%$ FWHM energy resolution at 662 keV.

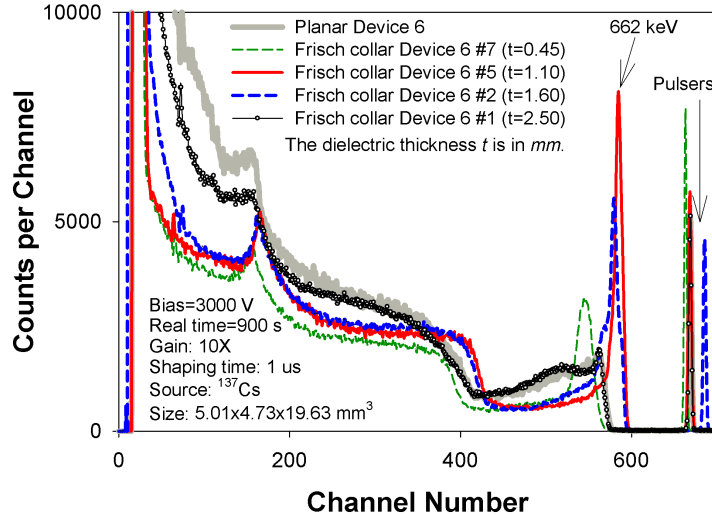


Figure 5.38: The pulse height spectra of Device 6, taken with a standard ^{137}Cs gamma-ray source, for specific dielectric thicknesses. The best spectral performance is for Device 6 #5, which has the optimum dielectric layer thickness of 1.10 mm. Device 6 #5 shows $1.6\% \pm 0.2\%$ FWHM energy resolution at 662 keV and peak-to-valley of 15.1 ± 0.4 .

Clearly, the experimental results of the six Frisch collar devices show that for those devices with the aspect ratio greater than 2.5 (Device 4 to Device 6) optimum dielectric thickness yields best performance. For the Frisch collar devices with aspect ratios smaller than 2.0, the thinnest possible dielectric thickness appears to generate better performance; however, the dielectric layer should be thick enough to stop extra leakage current from the conductive collar to the anode. Therefore, the main role of the dielectric layer in Frisch collar devices with an aspect ratio smaller than 2.0 is to prevent extra leakage current between the conductive collar and the anode.

For Frisch collar devices with an aspect ratio greater than 2.5 (Device 4 to Device 6) and very thin dielectric layers about 0.10 mm (thick enough to stop the extra leakage current), the relatively low performance of the device is due to a low electric field region in a large portion of the device. This low electric field region results in electron trapping, which degrades the device performance, an effect that becomes more important for the Frisch collar device with an aspect ratio greater than 3.0 (Frisch collar Device 6 #7). The effect

can be predicted by modeling the weighting/operating potential, the electric field, and the *CCE* for specific device and configuration. The Frisch collar devices in this study were modeled in three-dimensional geometry, and the weighting/operating potential and electric field distributions were determined using Integrated Engineering Software, LORENTZ. The weighting/operating potential and electric field distribution along the device central axis for Device 4 (which has dimensions close to Device 5) is in Figs. 5.39 and 5.40.

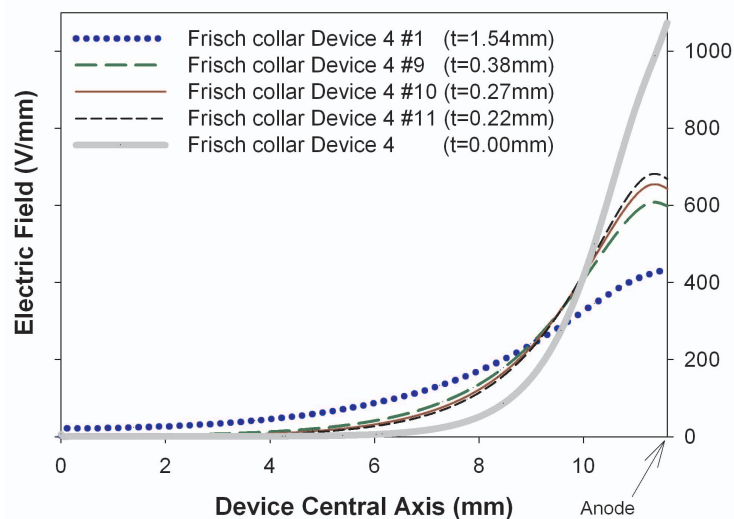


Figure 5.39: The electric field distribution for Device 4 in Frisch collar configurations along the central axis. The plot shows the electric field distribution for the maximum and minimum dielectric thickness t and in the vicinity of the optimum dielectric thickness, where the Frisch collar Device 4 #10 shows the best performance.

For a very thin dielectric layer, more than half the volume of Frisch collar Device 4 (and Device 5) suffers from extremely low electric field (close to zero as shown in Fig. 5.39). Next, Device 6 is fully modeled in Chapter 3, Section 3.2.1.4, and the results of the modeling are in Figs. 3.24, 3.25 and 3.26. The very low electric field region occurs in two-thirds of Frisch collar Device 6 with a very thin dielectric layer as shown in Fig 3.25 (note that the weighting field and electric field mimic each other for a two-terminal device). The effect makes the *CCE* of Device 6 clearly none-uniform for very thin dielectric thickness (Fig. 3.26), but when approaching optimum thickness (around 1.10 mm), the *CCE* starts to flatten, resulting in

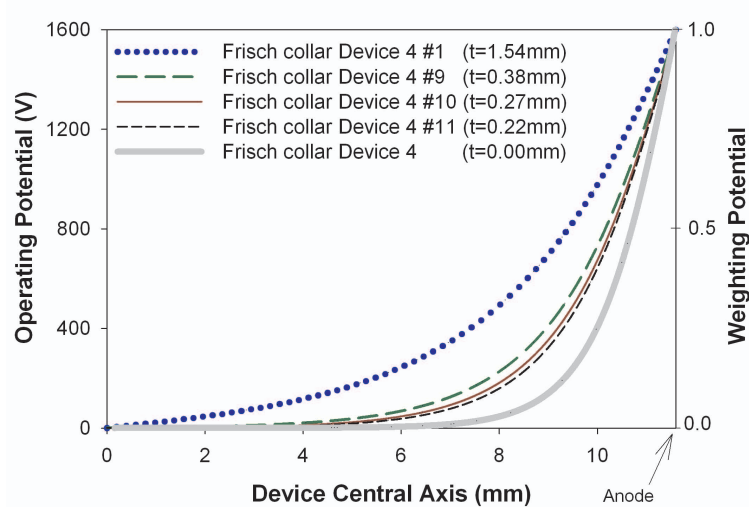


Figure 5.40: The operating and weighting potential distributions for Device 4 in Frisch collar configurations along the central axis. The plot shows the potential distributions for the maximum and minimum dielectric thickness t and in the vicinity of the optimum dielectric thickness, where the Frisch collar Device 4 #10 shows the best performance.

better performance (Device 6 #5 in Figs. 5.37 and 5.38 with more flat CCE profile in Fig. 3.26). This explains the low performance of Frisch collar Device 6 #7 with a very thin dielectric layer in Figs. 5.37 and 5.38.

As the dielectric layer thickness of the Frisch collar device further increases, a more uniform electric field distribution is achieved (Figs. 3.25 and 5.39), but the weighting potential distribution becomes more linear (Figs. 3.24 and 5.40) approaching the weighting potential of a planar device and reducing the single carrier charge induction effect for electrons. Hence, the device no longer performs as a single carrier device (Device 1 #1 through Device 6 #1), and the CCE profile of the device also approaches that of a planar device (Fig. 3.26).

5.3.3 Results of crystal length on performance of the CdZnTe Frisch collar devices

As mentioned in Section 3.2.4, crystal length has a dual impact on device performance, since it affects both device aspect ratio and the probability of charge carriers being trapped. Hence, to exclusively study the impact of length on Frisch collar device performance, the desired devices are considered to have identical aspect ratios of 1.8. Accordingly, four different Frisch collar devices are simulated and presented in Section 3.2.4. Due to a lack of large volume single crystal CdZnTe material, only three of the Frisch collar devices are fabricated and tested, labeled as Device *i*, Device *ii* and Device *iii* (Section 4.3.4 in Table 4.5). Two devices (Device *ii* to Device *iii*), however, were from the same ingot, since Device *iii* was fabricated from resizing/reshaping Device *ii*, and Device *i* was fabricated from a separate ingot. Figs. 5.41 and 5.42 display the energy spectra for the devices listed in Table 4.5 with standard ^{137}Cs gamma-ray sources.

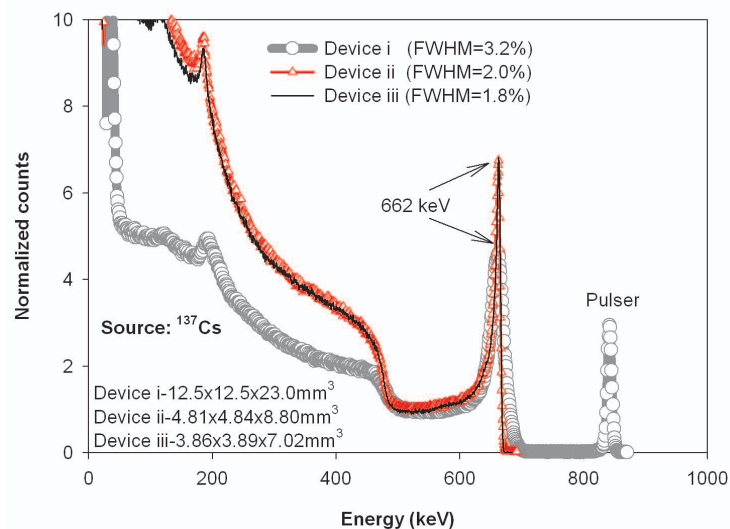


Figure 5.41: The normalized pulse height spectra of Frisch collar Device *i*, Device *ii* and Device *iii* (with the same aspect ratio of 1.8 and different lengths) taken with a standard ^{137}Cs gamma-ray source. The applied bias, amplifier gain, and the spectral testing time are in Table 4.5. The best spectral performance is for Device *iii*, which has the shortest length presenting $1.8\% \pm 0.2\%$ FWHM energy resolution at 662 keV.

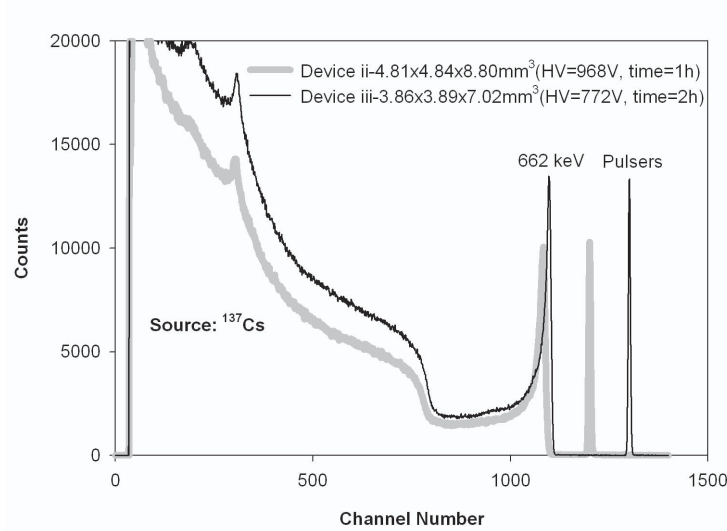


Figure 5.42: The pulse height spectra of Frisch collar Device *ii* and Device *iii* (with the same aspect ratio of 1.8 and different lengths) taken with a standard ^{137}Cs gamma-ray source. The applied bias, amplifier gain, and the spectral testing time are in Table 4.5. The best spectral performance is for Device *iii*, which has the shortest length with $1.8\% \pm 0.2\%$ FWHM energy resolution at 662 keV.

As Fig. 5.41 shows, Device *i* with longer drift length ($L = 23.00$ mm) has the worst performance. This lower performance for Device *i* is predicted in Chapter 3, Section 3.2.4 and in Fig. 3.31. Most importantly, in spite of their almost identical weighting potential profile (Fig. 3.30) due to equal aspect ratios, the shortest device performs better.

5.3.4 Post fabrication surface treatment results

The following section presents the results of the impact of final surface treatments on the energy resolution and the peak-to-valley ratio of the full energy peak, as well as the total leakage current. The results of this work were published previously [71].

Bulk leakage current and surface leakage current are the two parameters that contribute to total leakage current of the semiconductor spectrometer. Obviously, bulk leakage current is affected by material resistivity ξ ($\Omega\cdot\text{cm}$) while the surface morphology and stoichiometry of the device affects surface leakage current. It has been measured and reported [54] that total leakage current for unpassivated CdZnTe radiation detectors is dominated by surface

leakage rather than the bulk leakage. This implies that surface passivation can potentially enhance the radiation detector's spectroscopic performance. The bulk resistance R_{DB} (Ω) for a planar bar shape device is given by,

$$R_{DB} = \xi \frac{L}{A} \quad , \quad (5.2)$$

where L (cm) is the device length, and A (cm^2) is the device cross section area. Fig. 5.43 shows the simplified model of the detector-preamplifier circuit, where R_C is the detector contact resistance (normally negligible compared to the bulk resistance R_{DB} of CdZnTe detectors, if an ohmic contact is formed [72]), and R_S is the detector surface resistance. The detector total resistance R_D is given by,

$$\frac{1}{R_D} = \frac{1}{R_{DB} + 2R_C} + \frac{1}{R_S} \quad . \quad (5.3)$$

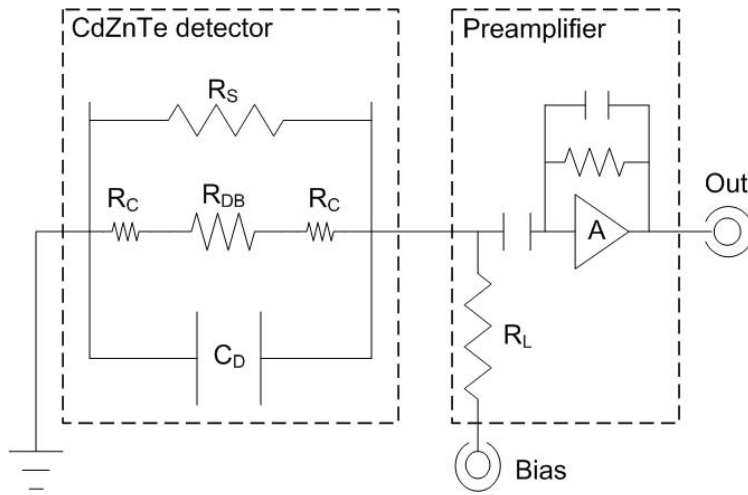


Figure 5.43: The detector-preamplifier circuit. The preamplifier has a load resistor R_L . The CdZnTe bar detector is modeled as three resistors: surface resistance R_S , bulk resistance R_{BD} and contact resistance R_C .

5.3.4.1 Mechanical treatment results

Figs. 5.44 and 5.45 display the I-V characteristic curves and also the pulse height spectra with a standard gamma-ray check source of ^{137}Cs for Detector 1 as in Section 4.3.5. The results show that the performances of Detector 1 #2 to Detector 1 #4 have deteriorated (SiC grinding treatment in Table 4.7) in both energy spectra and leakage current. However, since the lateral sides of the degraded device (Detector 1 #4) were polished with 1.0 micron alumina powders, device performance is enhanced (Detector 1 #5 in Fig. 5.45). Continued polishing of the device's lateral sides with 0.05 micron alumina powders enhanced detector performance further (Detector 1 #6 in Fig. 5.45). A summary of the full width half maximum (FWHM) energy resolution at 662 keV, the peak-to-valley ratio (P:V) of the full energy peak (FEP), and the maximum leakage current at operating bias for Detector 1 is in Table 5.3.

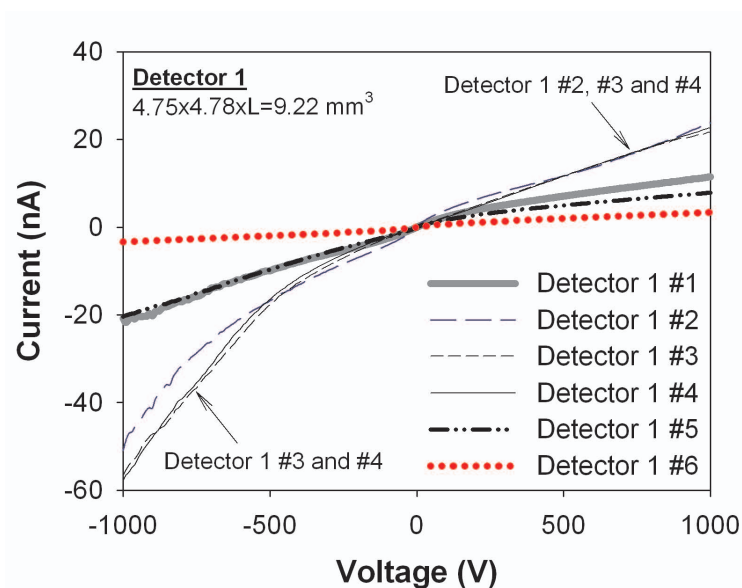


Figure 5.44: Results collected from Detector 1 ($4.75 \times 4.78 \times 9.22 \text{ mm}^3$) showing the current-voltage (I-V) characteristic curves for planar configurations. The maximum leakage current is in Table 5.3.

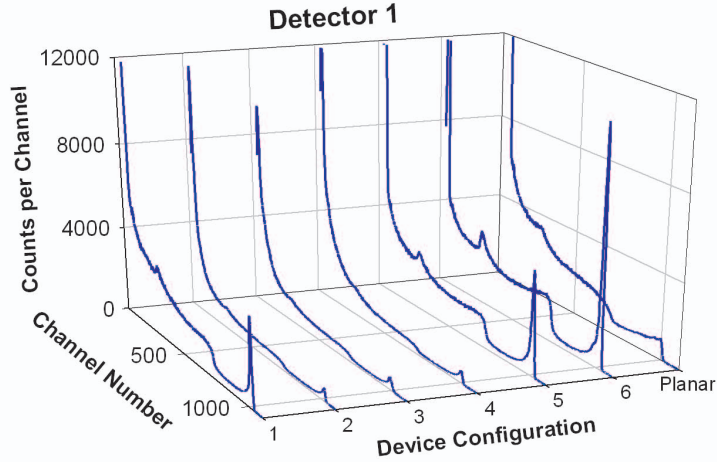


Figure 5.45: Results collected from Detector 1 ($4.75 \times 4.78 \times 9.22 \text{ mm}^3$) showing the pulse height spectra using a ^{137}Cs source. The applied bias was set to +1000 V, and the amplifier gain was set to 100X for the 900 s collecting real time. All the settings were kept the same for the entire experiment. The energy resolution and the peak-to-valley ratio are in Table 5.3 for Frisch collar Detector 1 #1 through Detector 1 #6. The best spectral performance is for Detector 1 #6, which had a final surface treatment of mechanical polishing with 0.05 micron Al_2O_3 powders. Detector 1 #6 shows a full width half maximum (FWHM) energy resolution of $1.3\% \pm 0.1\%$ at 662 keV and a peak-to-valley ratio (P:V) of 38.8.

Table 5.3: Summary of energy resolution, peak-to-valley, and maximum leakage current for Detector 2 after each surface treatment (Figs. 5.44 and 5.45). The full width half maximum (FWHM) energy resolution in % at 662 keV with the standard deviation of $\pm 0.1\%$ for each Frisch collar detector. P:V is the peak-to-valley ratio of the full energy peak (FEP) for each detector in Frisch collar configuration. The maximum leakage current is in $n\text{A}$ and is reported at +1000 V for each detector in planar configuration.

Detector 1 #	Treatment	Method	FWHM	P:V	Max leakage current ($n\text{A}$)
Detector 1 #1	Etching	2%Br/Meth	1.7%	10.4	12
Detector 1 #2	Grinding	SiC/1200 Grit	2.6%	6.7	24
Detector 1 #3	Grinding	SiC/2400 Grit	2.6%	7.3	22
Detector 1 #4	Grinding	SiC/2400 Grit	2.6%	6.1	23
Detector 1 #5	Polishing	1 micron/Alumina	1.8%	17.9	8
Detector 1 #6	Polishing	0.05 micron/Alumina	1.3%	38.8	3

5.3.4.2 Chemical treatment results

The energy spectra taken with a standard ^{137}Cs gamma-ray check source and the I-V characteristic curves for Detector 2 through Detector 5 presented in Chapter 4 and Table 4.6 are in Figs. 5.46 through 5.53. The results indicate enhanced energy spectra and reduced leakage current for the passivated Frisch collar Detector 2 through Detector 5. A summary of the FWHM energy resolution at 662 keV, the P:V of FEP, and the maximum leakage current at forward bias for Frisch collar Detector 2 through Detector 5 is in Table 5.4.

Table 5.4: Summary of FWHM energy resolution, peak-to-valley, and maximum leakage current for Detector 2 through Detector 5 (see Fig. 5.46 through Fig. 5.53). The full width half maximum (FWHM) energy resolution in % at 662 keV with the standard deviation of $\pm 0.1\%$ for each Frisch collar detector. P:V is the peak-to-valley ratio of the full energy peak (FEP) for each detector in Frisch collar configuration. The maximum leakage current is in $n\text{A}$ and is reported at +1000 V for each detector in planar configuration.

	Method applied for passivation	FWHM	P:V	Maximum leakage current ($n\text{A}$)
Detector 2	Before passivation	1.5%	6.1	42
	$\text{NH}_4\text{F}/\text{H}_2\text{O}_2$	1.2%	10.5	8
Detector 3	Before passivation	1.9%	9.4	39
	H_2O_2	1.6%	14.4	5
Detector 4	Before passivation	1.5%	5.8	30
	$\text{NaClO}_3/\text{H}_2\text{O}_2$	1.4%	11.6	3
Detector 5	Before passivation	1.3%	13.2	35
	$\text{KClO}_3/\text{H}_2\text{O}_2$	1.1%	16.8	6

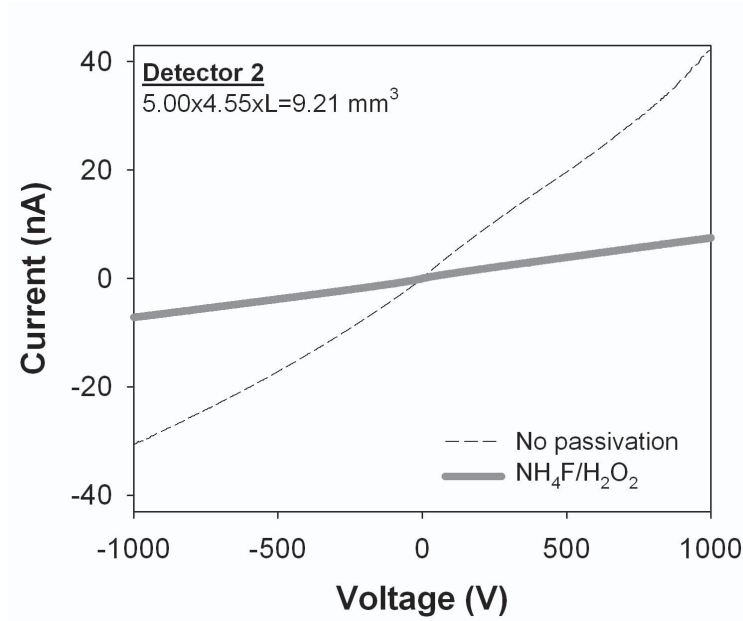


Figure 5.46: Results collected from Detector 2 ($5.00 \times 4.55 \times 9.21 \text{ mm}^3$) showing the current-voltage (I-V) characteristic curves for planar configurations. The maximum leakage current is in Table 5.4.

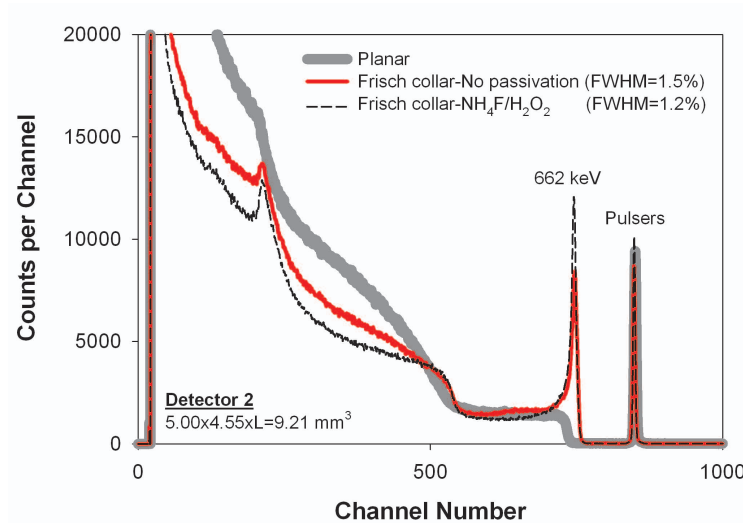


Figure 5.47: Results collected from Detector 2 ($5.00 \times 4.55 \times 9.21 \text{ mm}^3$) showing the pulse height spectra using a ^{137}Cs source. The applied bias was set to +1000 V, and the amplifier gain was set to 70X for the 3600 s collecting real time. All the settings were kept the same for the entire experiment. The energy resolution and the peak-to-valley ratio are in Table 5.4 for Frisch collar Detector 2 before and after the $\text{NH}_4\text{F}/\text{H}_2\text{O}_2$ surface treatment. The passivation enhances the detector performance.

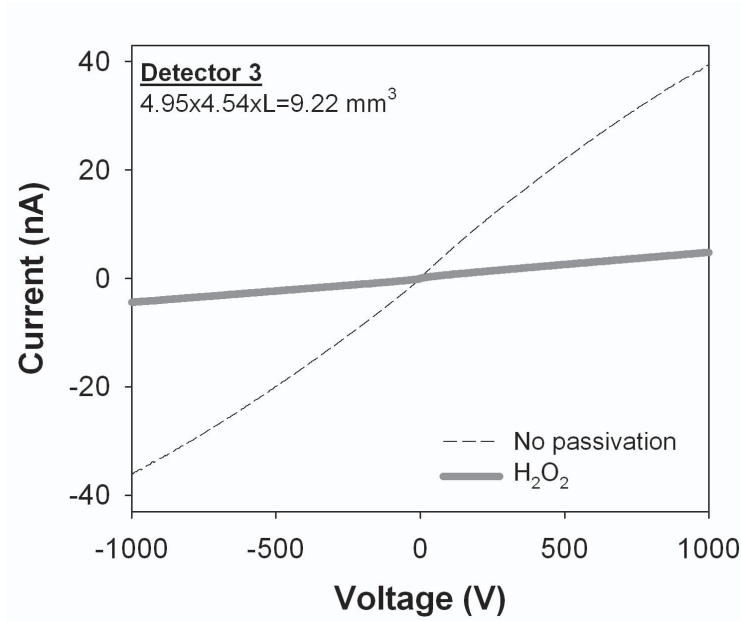


Figure 5.48: Results collected from Detector 3 ($4.95 \times 4.54 \times 9.22 \text{ mm}^3$) showing the current-voltage (I-V) characteristic curves for planar configurations. The maximum leakage current is in Table 5.4.

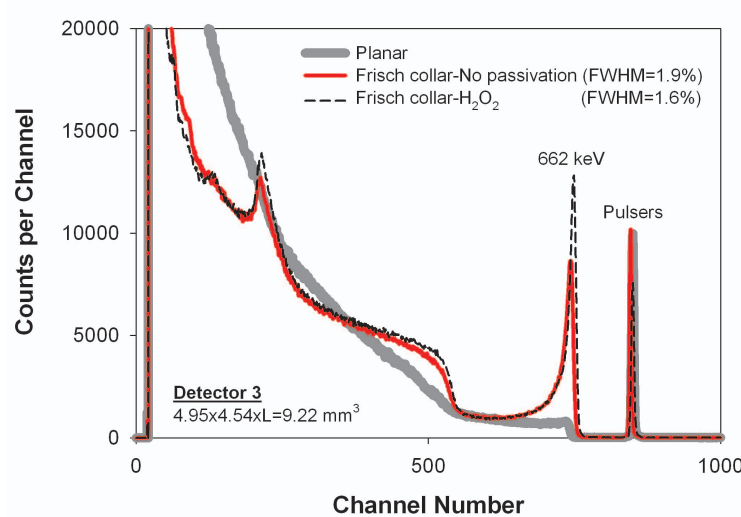


Figure 5.49: Results collected from Detector 3 ($4.95 \times 4.54 \times 9.22 \text{ mm}^3$) showing the pulse height spectra using a ^{137}Cs source. The applied bias was set to +1000 V, and the amplifier gain was set to 70X for the 3600 s collecting real time. All the settings were kept the same for the entire experiment. The energy resolution and the peak-to-valley ratio are in Table 5.4 for Frisch collar Detector 3 before and after the H_2O_2 surface treatment. The passivation enhances the detector performance.

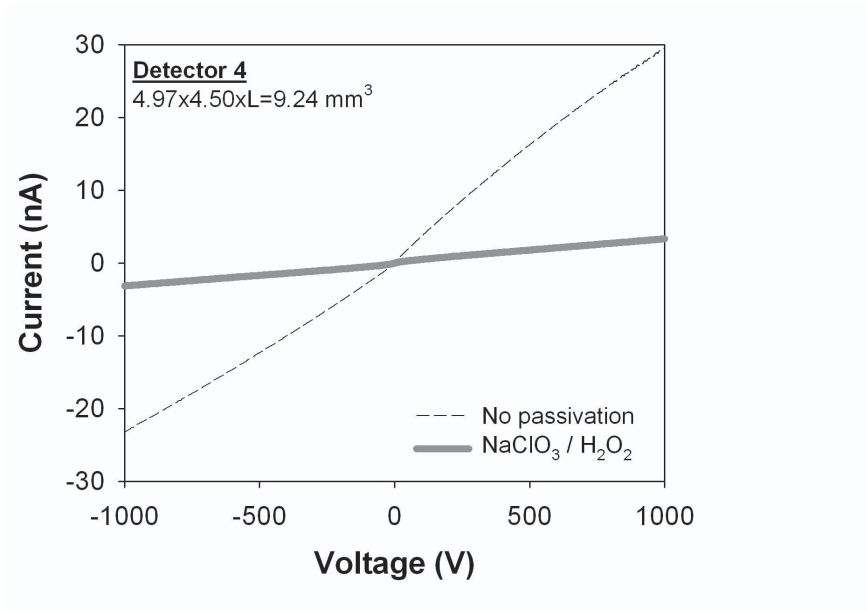


Figure 5.50: Results collected from Detector 4 ($4.97 \times 4.50 \times 9.24 \text{ mm}^3$) showing the current-voltage (I-V) characteristic curves for planar configurations. The maximum leakage current is in Table 5.4.

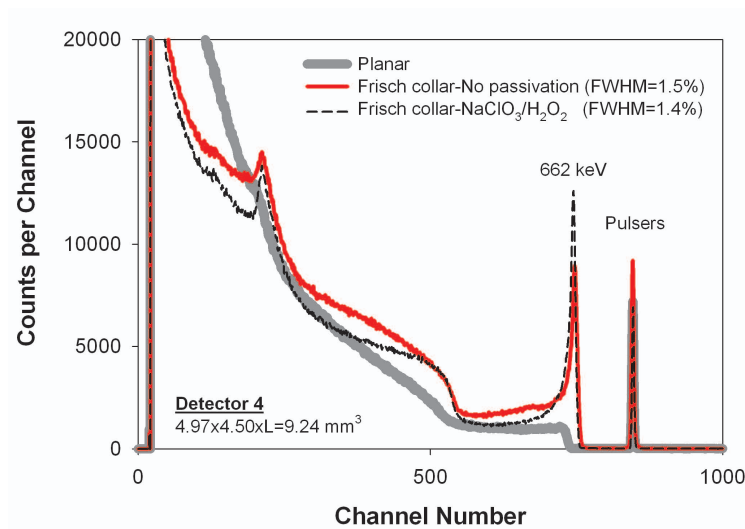


Figure 5.51: Results collected from Detector 4 ($4.97 \times 4.50 \times 9.24 \text{ mm}^3$) showing the pulse height spectra using a ^{137}Cs source. The applied bias was set to +1000 V, and the amplifier gain was set to 70X for the 3600 s collecting real time. All the settings were kept the same for the entire experiment. The energy resolution and the peak-to-valley ratio are in Table 5.4 for Frisch collar Detector 4 before and after the $\text{NaClO}_3/\text{H}_2\text{O}_2$ surface treatment. The passivation enhances the detector performance.

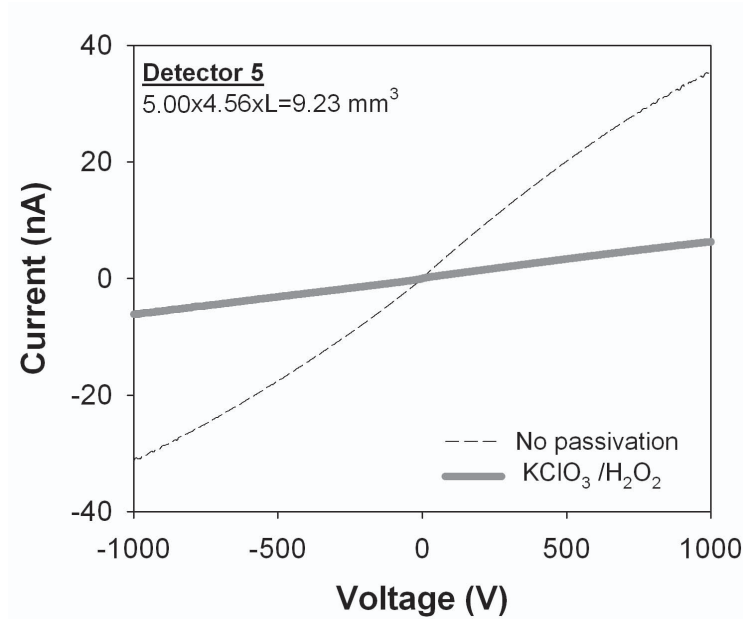


Figure 5.52: Results collected from Detector 5 ($5.00 \times 4.56 \times 9.23 \text{ mm}^3$) showing the current-voltage (I-V) characteristic curves for planar configurations. The maximum leakage current is in Table 5.4.

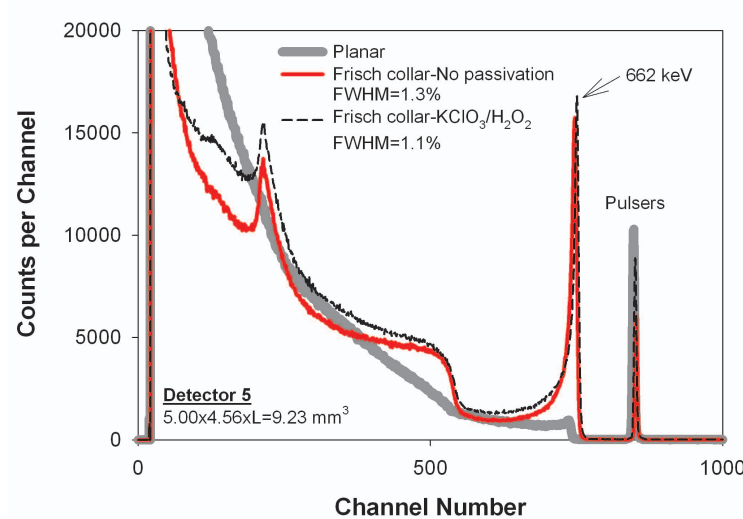


Figure 5.53: Results collected from Detector 5 ($5.00 \times 4.56 \times 9.23 \text{ mm}^3$) showing the pulse height spectra using a ^{137}Cs source. The applied bias was set to +1000 V, and the amplifier gain was set to 70X for the 3600 s collecting real time. All the settings were kept the same for the entire experiment. The energy resolution and the peak-to-valley ratio are in Table 5.4 for Frisch collar Detector 5 before and after the $\text{KClO}_3/\text{H}_2\text{O}_2$ surface treatment. The passivation enhances the detector performance.

5.3.4.3 Ion milling results

The energy spectra taken with a standard ^{137}Cs gamma-ray check source and the I-V curves for Detector 6 in Table 4.6 in Chapter 4 are in Figs. 5.54 and 5.55. The results indicate deterioration in energy spectra and an increase in leakage current for the passivated Frisch collar Detector 6 with ion milling. Specifically, the FWHM energy resolution at 662 keV deteriorates from 2.0% for the non-passivated detector to 3.4% for the passivated detector with ion milling. The P:V of FEP and the maximum leakage current at forward bias also deteriorate (Fig. 5.55). However, after the lateral surface was polished with 1.0 micron alumina powder, detector performance improved.

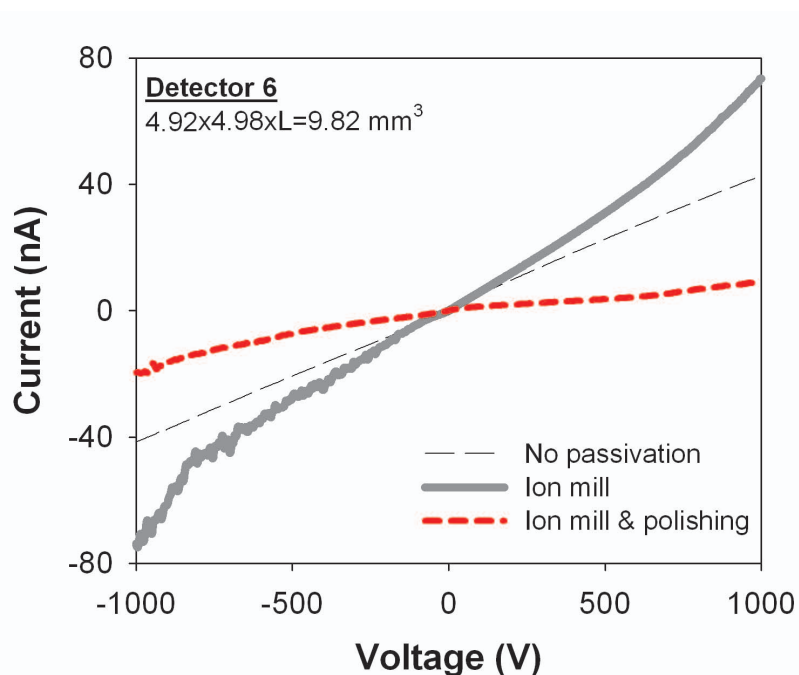


Figure 5.54: Results collected from Detector 6 ($4.92 \times 4.98 \times 9.82 \text{ mm}^3$) showing the current-voltage (I-V) characteristic curves for planar configurations.

It seems that since the leakage current increased for the passivated detector with ion milling, and later decreased as the process is followed by polishing (Fig. 5.54), there should be surface damages/contaminations due to ion milling with Xenon gas. The contamination can possibly come from the Al-jig that the detector is mounted on while ion milling, although

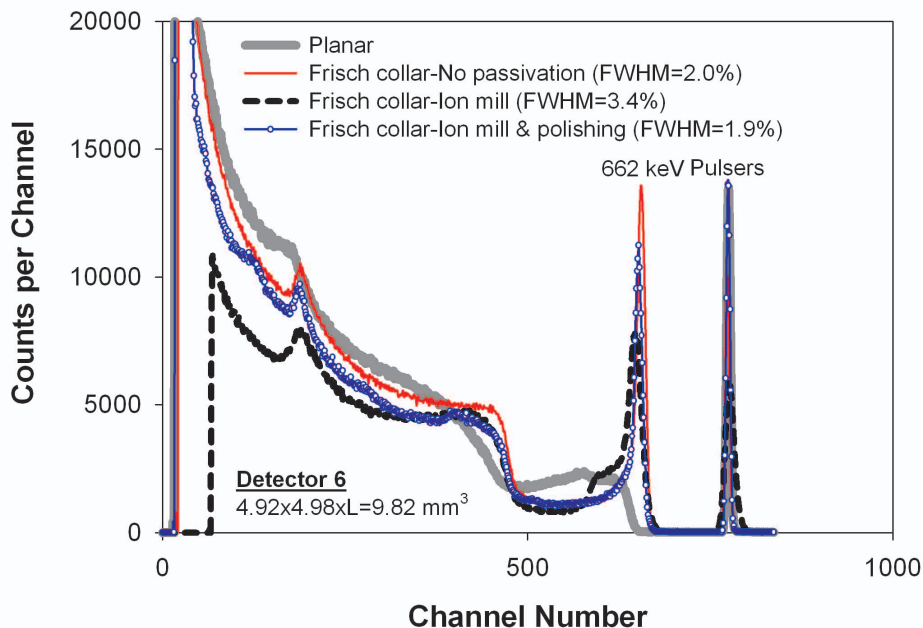


Figure 5.55: Results collected from Detector 6 ($4.92 \times 4.98 \times 9.82 \text{ mm}^3$) showing the pulse height spectra using a ^{137}Cs source. The applied bias was set to +1000 V, and the amplifier gain was set to 70X for the 3600 s collecting real time. All the settings were kept the same for the entire experiment. The ion milling passivation on Detector 6 does not enhance the detector performance, but that treatment followed by polishing (1.0 micron Al_2O_3 powder) recovers the spectral performance and reduces the leakage current. The P:V deteriorates from 12.8 to 9.9 after the ion milling passivation, and improves to 11.0 after the polishing.

no aluminum compounds or elemental aluminum were observed using Energy Dispersive Spectroscopy (EDS). It should be noted that no Au contact damages were observed, since polishing the ion milled detector recovered the spectral performance (Fig. 5.55). Other gases to be investigated such as Neon and Argon are suggested as a substitute for Xenon.

5.3.4.4 Surface characterization results

Spectral lines from three elements (Cd, Zn, and Te) were identified as part of the EDS scan to characterize the surface and analyze relative atomic concentrations. The results appear in Table 5.5 for Detector 1 through Detector 6. An attempt was made to identify oxygen or oxides on the surfaces before and after each treatment; however, there was no observable peak in the correct range. Oxygen only has one X-ray energy (K_α 505 eV), which is similar

in energy to the Cadmium M-shell (505 eV), and a very large Tellurium peak from its M-shell (450 eV), which makes low levels of oxygen difficult to discriminate using EDS. Thus, no oxygen or oxygen containing compounds were observed using EDS, although the depth profile of the electron beam (about 1.0 μm) [73] could also account for the apparent lack of elemental oxygen.

Table 5.5: EDS results of the atomic concentration from EMP technique. The results are for the maximum 1.0 μm depth from the surface.

		Atomic concentration (%)		
		Zn	Cd	Te
After surface treatment	Detector 1	4.01	46.40	49.59
	Detector 2	2.94	43.95	53.10
	Detector 3	4.31	47.29	48.40
	Detector 4	4.46	48.23	47.31
	Detector 5	3.62	49.98	46.40
	Detector 6	3.92	48.11	47.97
Before surface treatment	All detectors	4.14	46.57	49.29

5.3.4.5 Post fabrication surface treatment discussions

Clearly, a direct relation exists between the decrease in device leakage current and the improvement in spectroscopic performance. First, the increase in leakage current causes a voltage drop across the load resistor R_L (see Fig. 5.43), which can diminish the actual voltage applied to the detector. The effect becomes substantial when the leakage current is large enough. The load resistor R_L for the two preamplifiers ORTEC 142A and eV-550 used in this study are 101.5 M Ω and 110 M Ω , respectively. Therefore, with the relatively low leakage current measured for all devices, the voltage drop across the load resistor is less than 10V for the maximum reported leakage current. Therefore, the voltage drop contribution to device spectral degradation is not significant in this case. Second, the contribution of leakage current to the electronic noise is mainly due to fluctuations in leakage current, which is a component of parallel noise [65]. Therefore, higher leakage current results in more statistical

fluctuation, which causes an increase in electronic noise.

The results presented for Detector 1 with mechanical treatment indicates that highly polishing the lateral surface with fine powders results in the best improvement (Detector 1 #6 in Figs. 5.44 and 5.45). On the other hand, rough grinding of the lateral surface degrades the device causing an increase in leakage current (Detector 1 #2 through Detector 1 #4 in Figs. 5.44 and 5.45) due to an increase in the density of surface states and unbounded electrons at the surface caused by grinding. Also, Detector 1 #2 through Detector 1 #4 in Fig. 5.44 show some rectifying behaviors, which affect the uniformity of the electric field within the device, degrading the energy spectrum (Fig. 5.45). Further improvement of the devices (Detector 1 #5 and Detector 1 #6) is mainly due to reducing the mechanical damage and using fine powders, which results in removal of the highly conductive Te-rich layer from the native etched surface [53–60]. Unfortunately, due to limitations in depth profiling with the Electron Microprobe (EMP) technique, characterizing this Te-rich layer was not achieved with Energy Dispersive Spectroscopy (EDS). Note that although the grinding process (Detector 1 #2 through Detector 1 #4) removes the Te-rich layer as well, the resulting mechanical damage causes further device deterioration.

The chemical surface treatment on the lateral sides of Detector 2 through Detector 5 enhances the device performance by reducing leakage current, which results in better detector spectroscopic performance as explained. The main cause of the leakage current reduction is oxidizing the Te-rich layer [58–60]. In this study, NaClO_3 and KClO_3 were used along with H_2O_2 as the oxidizing agents, while in the previously reported study [59], only DI water was used as the solvent. For the surface characterization of Detector 2 to Detector 5, the atomic concentration of oxygen was not at a detectable level; therefore, no oxygen concentrations were reported.

Detector 6 is the only device using the ion milling surface treatment for the first documented time as a surface passivation method. Although the initial results do not show enhancement in detector performance (Figs. 5.54 and 5.55), the method seems to have po-

tential for the final surface passivation. The method is readily automatable and can be easily applied for detector fabrication in batch processing. However, the ion milling method is still under development and needs more work and characterization to advance the process as a final surface treatment. It should be noted that neither the contacts nor the bulk of the Detector 6 were degraded after the ion milling treatment, since detector performance was improved through further polishing. In addition, ion milling with Xe should theoretically allow preferential elimination of surface Cd and Te, producing a Zn rich surface [74].

In summary, the best spectroscopic enhancement was achieved through mechanical polishing with 0.05 micron alumina powders (Detector 1). The FWHM energy resolution at 662 keV improved from 1.7% to 1.3%, while the P:V improved from 10.4 to 38.8. The greatest leakage current reduction was for NaClO₃/H₂O₂ surface passivation (Detector 4 with 10 times reduction in leakage current). The surface resistance improvement for all detectors due to each treatment is summarized in Table 5.6, which shows the greatest increase in surface resistance is reported for Detector 4 with NaClO₃/H₂O₂ surface passivation.

Table 5.6: Devices' total resistance and surface resistance for Detector 1 through Detector 6. Bulk resistance R_{DB} is based on the resistivity of $1.0 \times 10^{11} \Omega \cdot \text{cm}$ for Redlen Technology CdZnTe material, using Equation 5.2. Detector total resistance R_D is evaluated based on the I-V characteristic curves. Detector surface resistance R_S is calculated applying Equation 5.3, and neglecting the contact resistance R_C . All the resistance are reported in G Ω .

	R_{DB}		R_D		R_S	
		Before	After	Before	After	
Detector 1	406	83	333	105	1861	
Detector 2	405	24	125	25	181	
Detector 3	410	26	200	27	390	
Detector 4	413	33	333	36	1725	
Detector 5	405	29	167	31	283	
Detector 6	401	23	111	25	154	

5.4 CdZnTe Device Efficiency Calculations

The intrinsic efficiency of a detector is defined as the ratio of the number of pulses produced by the detector to the number of gamma-ray quanta incident on the detector. Clearly, in gamma-ray detection, a high-quality detector must be capable of absorbing a large fraction of incident gamma-rays. Since high Z number materials result in higher attenuation coefficients for gamma-ray absorption, good gamma-ray absorption is accomplished by using materials of suitably high Z number [64, 65].

The intrinsic efficiency of the CdZnTe detector, ϵ_{int} , at a specific energy of the emitted gamma-ray can be defined as [64],

$$\epsilon_{int} = \frac{CTS}{\Omega_{ave} BR [A_0 \exp(-\lambda t)]} \quad , \quad (5.4)$$

where CTS is the total number of counts due to full energy absorption per unit time (this value was evaluated for standard sources of ^{133}Ba , ^{57}Co , ^{137}Cs , and ^{241}Am by taking the net area under the full energy peak of the corresponding spectrum over the counting time). $A_0 \exp(-\lambda t)$ is the activity of the source during the measurement, BR is the branching ratio for the specific energy of gamma-ray emitted by the source, and Ω_{ave} is the average fractional solid angle for the entire volume of CdZnTe bar detector exposed to the point source (Fig. 5.56).

To evaluate the average fractional solid angle, Ω_{ave} , requires the definition for the average of a function over an interval,

$$\Omega_{ave} = \frac{1}{L} \int_{x=d}^{d+L} \Omega(x) dx \quad . \quad (5.5)$$

In this equation, $\Omega(x)$ is the solid angle for the cross sectional area of the CdZnTe detector exposed to the point source at distance x in Fig. 5.56. The dimensions of the bar shaped

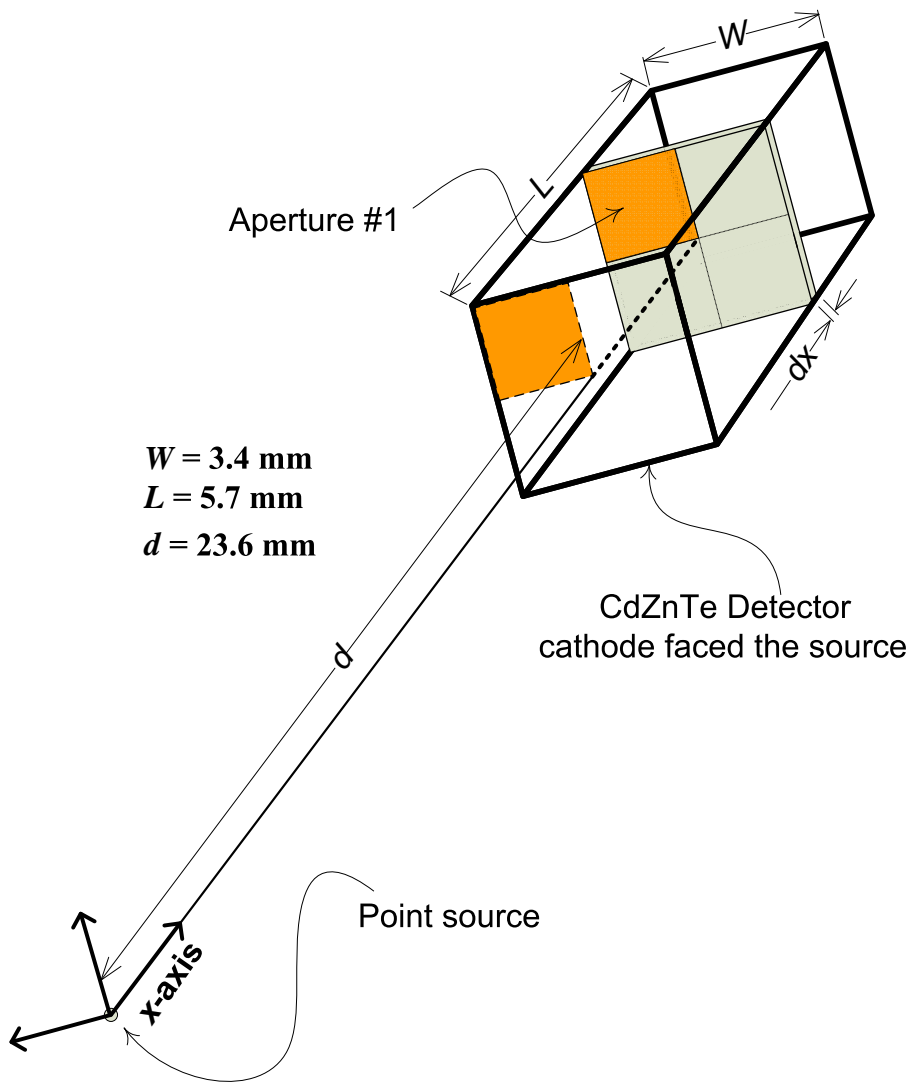


Figure 5.56: The solid angle between a point isotropic source and a CdZnTe bar detector with a rectangular aperture with the source aligned along the center of the detector.

CdZnTe detector are illustrated in Fig. 5.56 as L and W , while the point isotropic source is located at distance d away from the center of the detector. For the schematic in Fig. 5.56, one can write [64],

$$\Omega(x) = 4 \Omega_1(x) \quad , \quad (5.6)$$

where $\Omega_1(x)$ is the solid angle of the rectangular Aperture #1 shown on Fig. 5.56, while the point isotropic source is located at distance x away from Aperture #1 and aligned with its corner located in the center of the device. Then, $\Omega_1(x)$ can be evaluated from [64],

$$\Omega_1(x) = \frac{1}{4\pi} \arctan \left[\frac{(W/2)^2}{x \sqrt{2(W/2)^2 + x^2}} \right] \quad . \quad (5.7)$$

Hence, Ω_{ave} can be evaluated by applying equations 5.5 through 5.7 for the any given setup in Fig. 5.56. Since the 3.4mm \times 3.4mm \times 5.7mm CdZnTe Frisch collar detector in Section 5.1 was used for the intrinsic efficiency investigation with the setup in Fig. 5.56, the average fractional solid angle Ω_{ave} was numerically determined to be 0.00132.

To be consistent with detector-source geometry, a new set of pulse height spectra were collected with standard radionuclides. These energy spectra for ^{133}Ba , ^{57}Co , ^{137}Cs , and ^{241}Am are displayed in Figs. 5.57 through 5.60, while the intrinsic efficiency of the detector is summarized in Table 5.7. The uncertainty calculations are also shown in Table 5.7, assuming that the uncertainty is due to counting statistics alone. The results for intrinsic efficiencies are plotted for different gamma-ray energies in Fig. 5.61, showing as expected, the intrinsic efficiency decreases with energy.

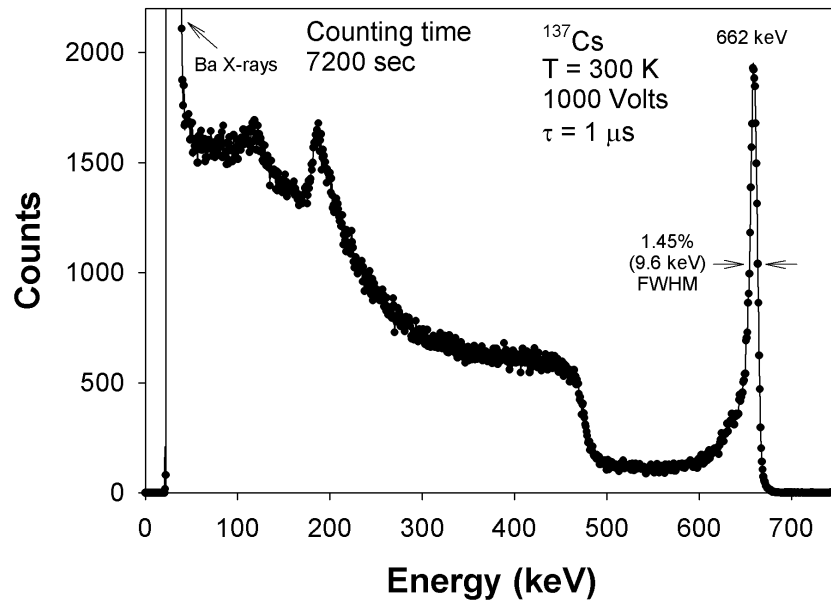


Figure 5.57: Room temperature spectrum from standard radiation source of ^{137}Cs taken with the $3.4 \times 3.4 \times 5.7 \text{ mm}^3$ CdZnTe semiconductor Frisch collar detector.

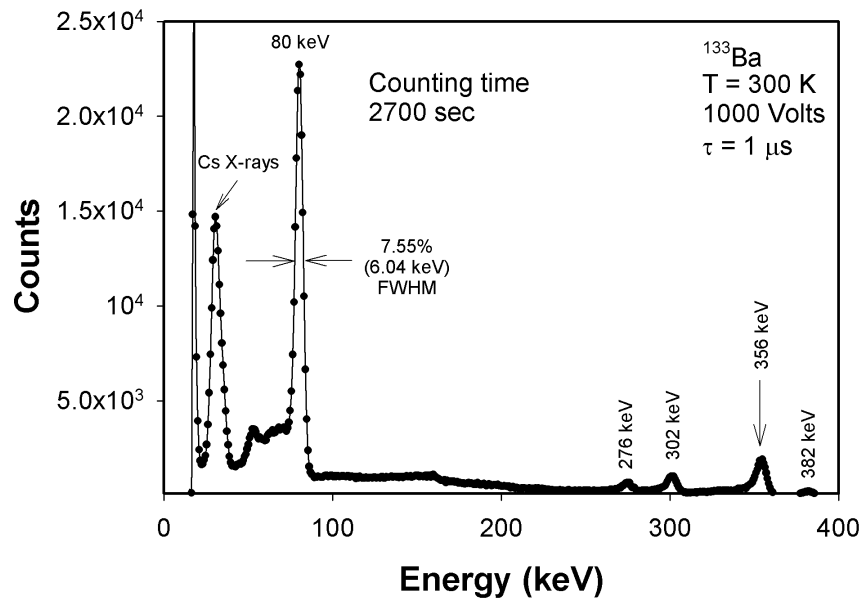


Figure 5.58: Room temperature spectrum from standard radiation source of ^{133}Ba taken with the $3.4 \times 3.4 \times 5.7 \text{ mm}^3$ CdZnTe semiconductor Frisch collar detector.

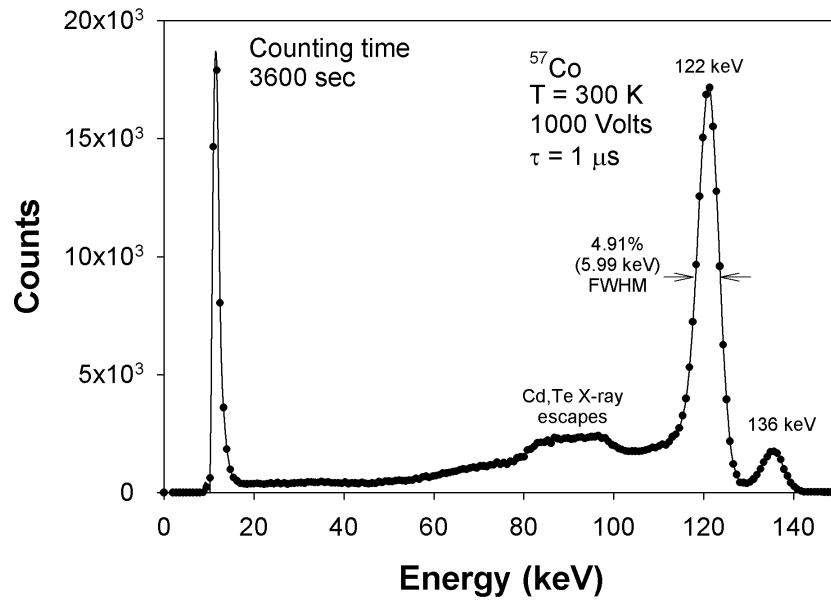


Figure 5.59: Room temperature spectrum from standard radiation source of ^{57}Co taken with the $3.4 \times 3.4 \times 5.7 \text{ mm}^3$ CdZnTe semiconductor Frisch collar detector.

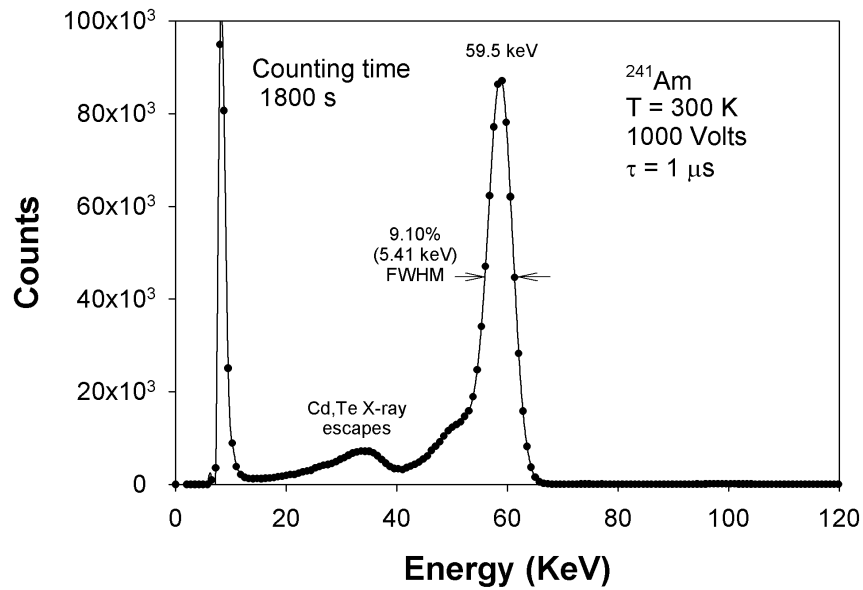


Figure 5.60: Room temperature spectrum from standard radiation source of ^{241}Am taken with the $3.4 \times 3.4 \times 5.7 \text{ mm}^3$ CdZnTe semiconductor Frisch collar detector.

Table 5.7: Summary of the values to determine the intrinsic full energy peak efficiency. The experiment was performed in June, 2005

Gamma Source	²⁴¹ Am	¹³³ Ba	⁵⁷ Co	¹³³ Ba	¹³⁷ Cs
Energy (keV)	59.5	80	122	356	662
Total counts	710165	192231	159753	23803	41137
Background	137726	43180	29738	6300	9590
Counting time (s)	1800	27000	3600	27000	7200
Activity, A0 (kBq)	1000	37	380.36	37	358.16
Assay date	9/2002	11/1998	10/2003	11/1998	10/2003
Intrinsic efficiency, ϵ_{int}	0.6743	0.5196	0.5153	0.0335	0.0114
Std. error-efficiency	0.0011	0.0017	0.0017	0.0003	0.0001

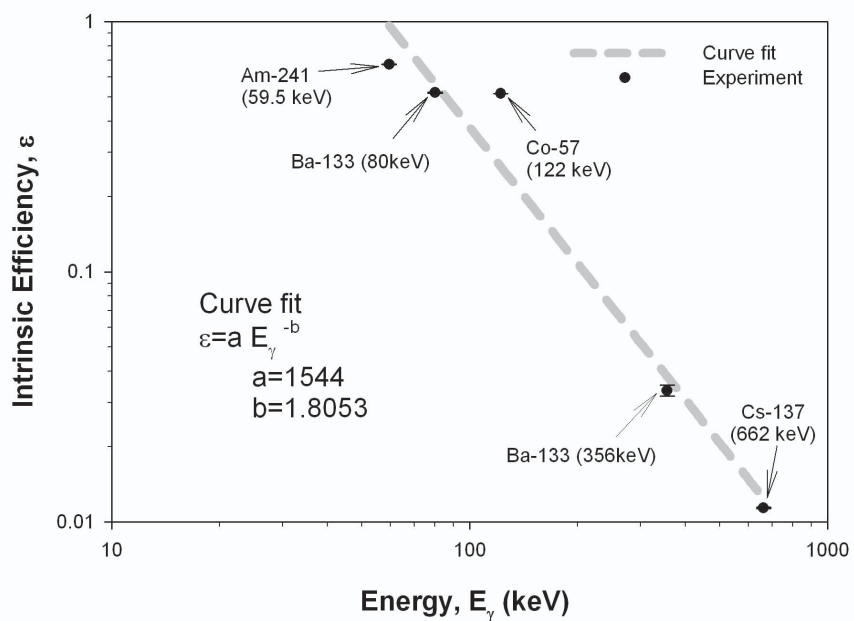


Figure 5.61: The measured CdZnTe Frisch collar detector full energy peak intrinsic efficiency at different gamma-ray energies.

5.5 Angular Response of W-Collimated CdZnTe Frisch Collar Device Results

The results of assessing angular response of a W-Collimated CdZnTe Frisch collar device to a point gamma source have been published previously in [75]. The experimental setup and procedure is presented in Section 4.4. As mentioned in Section 4.4, pulse height spectra were collected from the activated Au foils at a variety of source-detector angles, using the two different tungsten collimators. Three ^{198}Au spectra are illustrated in Fig. 5.62 for three different source-detector angles, those being 0° , 2° , and 3° using the 8 cm collimator.

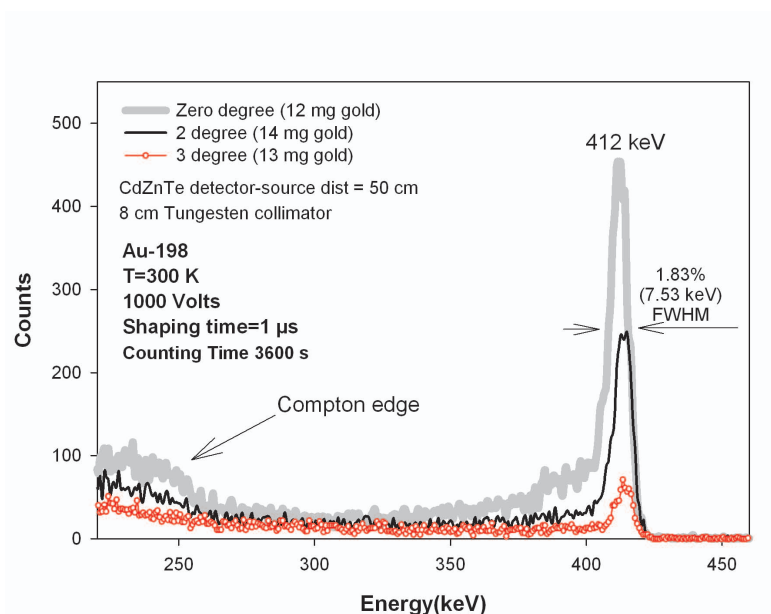


Figure 5.62: Room-temperature spectra of ^{198}Au gamma-ray emissions from the $3.4 \times 3.4 \times 5.8 \text{ mm}^3$ CdZnTe semiconductor detector inside the 8 cm long tungsten collimator at three different sourcedetector angles, showing the photopeaks and the Compton edges. Different Au foil samples were used for each measurement.

5.5.1 Angular Response Results

The total number of counts collected for a certain source-detector angle can be evaluated by finding the net counts within the full energy peak of the pulse height spectrum (minus background). Accordingly, a complete set of source-detector angles with the evaluated net

photopeak counts are presented in Tables 5.8 and 5.9 for the 8 cm and 4 cm collimators, respectively. The collected data for both 4 cm and 8 cm collimators are plotted in Fig. 5.63 to compare the directional sensitivity of the two collimators. As expected, the longer collimator is more sensitive to changes in the source-detector angle. Between the source-detector angles of $\pm 1^\circ$, the detected counts from both collimators are nearly the same. However, once the gamma-ray source was moved past the respective critical angle of each collimator, the shielding began to reduce the counts significantly. The second critical angle α_{c2} for each collimator was experimentally observed to be at $\pm 3^\circ$ and $\pm 7^\circ$ for the 4 cm and 8 cm collimators, respectively.

Table 5.8: The net counts in the full energy peak obtained from ^{198}Au sources at different source-detector angles. Also shown in the table are the actual measured Au foil sample masses. As explained, the counts from the irradiated Au foils were all normalized to that of a 13 mg sample. The CdZnTe detector used had dimensions of $3.4 \times 3.4 \times 5.8 \text{ mm}^3$ and was placed inside the 8 cm long tungsten collimator.

Angle (degrees)	Counts per 13 mg ^{198}Au	Standard counting Error (\pm)	Gold foil mass (mg)
-15	3792	148	14
-10	3083	131	13
-5	1278	61	13
-4	987	53	12
-3	493	31	12
-2	3783	158	13
-1	6170	250	13
0	6897	300	12
1	6123	231	14
2	2961	118	14
3	612	34	13
4	1058	52	13
5	1453	64	14
10	3558	149	13
15	3979	166	13

Table 5.9: The net counts in the full energy peak obtained from ^{198}Au sources at different source-detector angles. Also shown in the table are the actual measured Au foil sample masses. As explained, the counts from the irradiated Au foils were all normalized to that of a 13 mg sample. The CdZnTe detector used had dimensions of $3.4 \times 3.4 \times 5.8 \text{ mm}^3$ and was placed inside the 4 cm long tungsten collimator.

Angle (degrees)	Counts per 13 mg ^{198}Au	Standard counting Error (\pm)	Gold foil mass (mg)
-17	2796	53	12
-13	2444	49	14
-12	1864	43	12
-10	1498	39	12
-9	1400	37	11
-8	1323	36	15
-7	1202	35	14
-6	1883	43	14
-5	3296	57	14
-4	4030	63	13
-3	5468	74	13
-2	6152	78	13
-1	6349	80	12
0	6927	83	13
1	6543	81	12
2	6195	79	13
3	4736	69	14
4	4418	66	14
5	3291	57	14
6	1138	34	13
7	1057	33	14
8	1153	34	12
9	1273	36	12
10	1373	37	13
12	1957	44	14
13	1715	41	13
17	2773	53	14

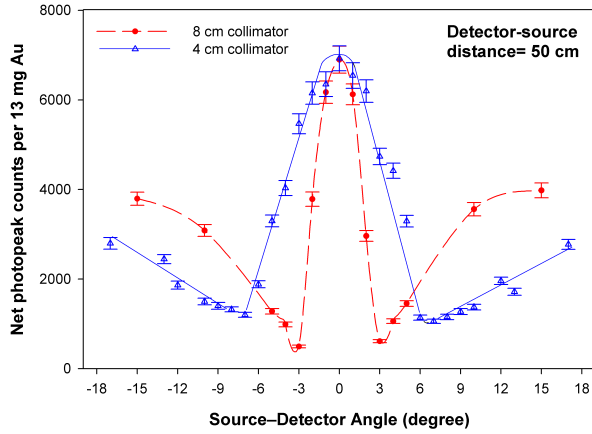


Figure 5.63: The experimental angular dependency of net photopeak counts from ^{198}Au gamma-ray sources with the $3.4\text{mm} \times 3.4\text{mm} \times 5.8\text{mm}$ CdZnTe Frisch collar detector for the 4 and 8 cm long tungsten collimators.

The normalized counts from the experiment were compared to the analytical solutions, predicted by using equations 4.8, 4.9, and 4.18, which are shown in Figs. 5.64 and 5.65 for the 4 cm and 8 cm collimators, respectively. The figures show that the two-dimensional, simple model is successful in predicting the directional sensitivity of each collimator. Therefore, based on the model, the second critical angle occurs at $\pm 6.6^\circ$ and $\pm 2.9^\circ$ for the 4 cm and 8 cm collimators, respectively. By comparison, the values of α_{c2} were experimentally verified as being $\pm 7^\circ$ for the 4 cm collimator and $\pm 3^\circ$ for the 8 cm collimator (Figs. 5.63 to 5.65). The slight disagreement between theoretical and experimental data in Figs. 5.64 and 5.65 can be explained by a few factors. The predicted small plateau in counts in the analytical model for region 1 was not experimentally observed, which suggests not to include the exposure angle and the efficiency of the CdZnTe detector, and the effects of the copper, plastic, and Teflon tape, thereby explaining, at least in part, the slight discrepancy. Subsequently, for the shielding effect of the tungsten collimator, the edge effect were not taken into consideration. In other words, it was assumed that as the source passed the critical angles, the effective thickness of the collimator was $t(\alpha)$ (Fig. 4.16). Overall, the simple analytical model predicts the performance of the collimated CdZnTe Frisch collar device quite well.

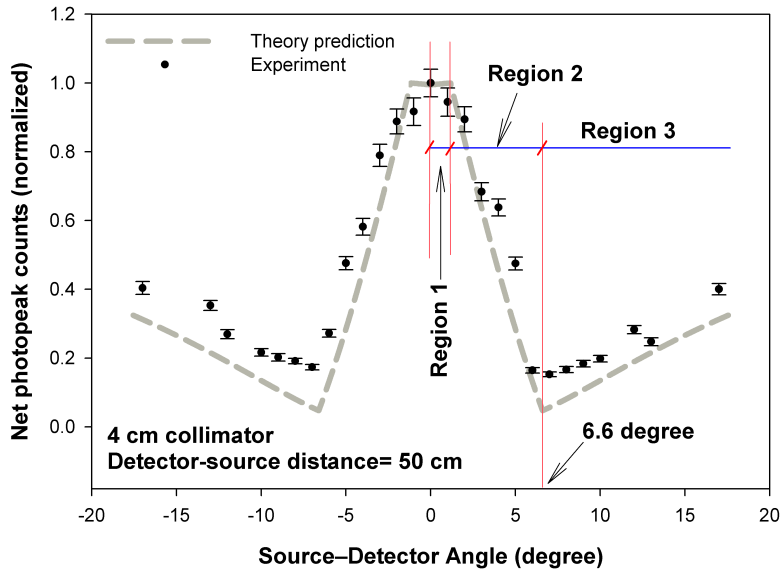


Figure 5.64: The experimental and theoretical angular dependency of net photopeak counts from ^{198}Au gamma-ray sources with the $3.4\text{mm} \times 3.4\text{mm} \times 5.8\text{mm}$ CdZnTe Frisch collar detector using the 4 cm long tungsten collimators.

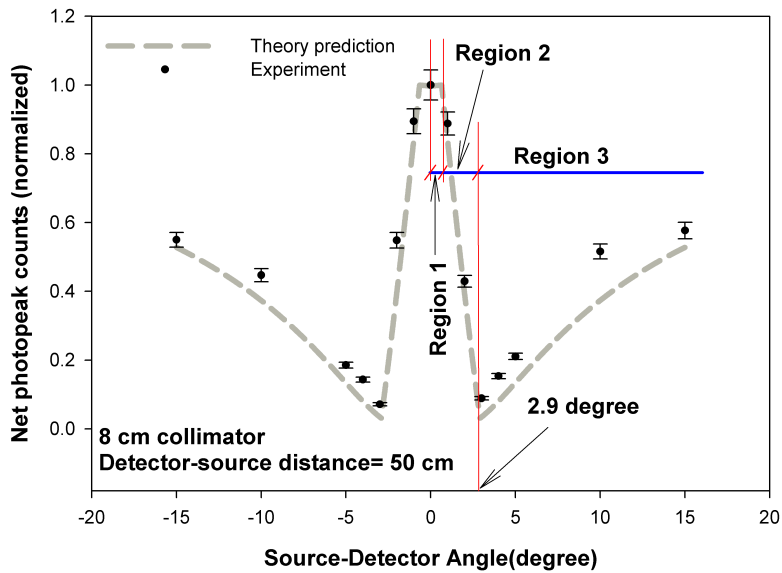


Figure 5.65: The experimental and theoretical angular dependency of net photopeak counts from ^{198}Au gamma-ray sources with the $3.4\text{mm} \times 3.4\text{mm} \times 5.8\text{mm}$ CdZnTe Frisch collar detector using the 8 cm long tungsten collimators.

5.6 Spectral Results of Array of CdZnTe Detectors

The results of the pulse height spectra taken with the array of 16 CdZnTe Frisch collar devices with a gamma-ray source have been published previously in [67]. Here, the gamma-ray responses of the array of 32 CdZnTe Frisch collar devices (two modules of 16 CdZnTe Frisch collar devices) are presented. The electronic readouts were developed at Brookhaven National Laboratory (BNL) [67] and are detailed in Section 4.5.

5.6.1 Gamma-Ray Response of Array of 16 CdZnTe Detectors

Pulse height spectra were collected with gamma-rays source of ^{137}Cs from individual CdZnTe Frisch collar detectors. The spectral responses of the individual detectors with commercial preamplifier (ORTEC 142A) and Nuclear Instrument Modules (NIM) bins equipped with amplifier and high voltage supply are presented in Appendix B. These sixteen detectors (labeled as BNL1 through BNL16) were designed, fabricated, and tested individually at the S.M.A.R.T. laboratory at KSU. Clearly, eleven of the fabricated CdZnTe Frisch collar detectors show sub-1.8% full width half maximum (FWHM) energy resolution at 662 keV with no electronic correction using commercial ORTEC 142A preamplifiers.

This section presents the results of the spectral response of the array of thirty two CdZnTe Frisch collar detectors using the electronics readouts developed at BNL (Section 4.5). The pulse height spectra collected with gamma-rays sources of ^{137}Cs , ^{241}Am , and ^{133}Ba from individual detectors using BNL electronics readouts are shown in Figs. 5.66 through 5.68.

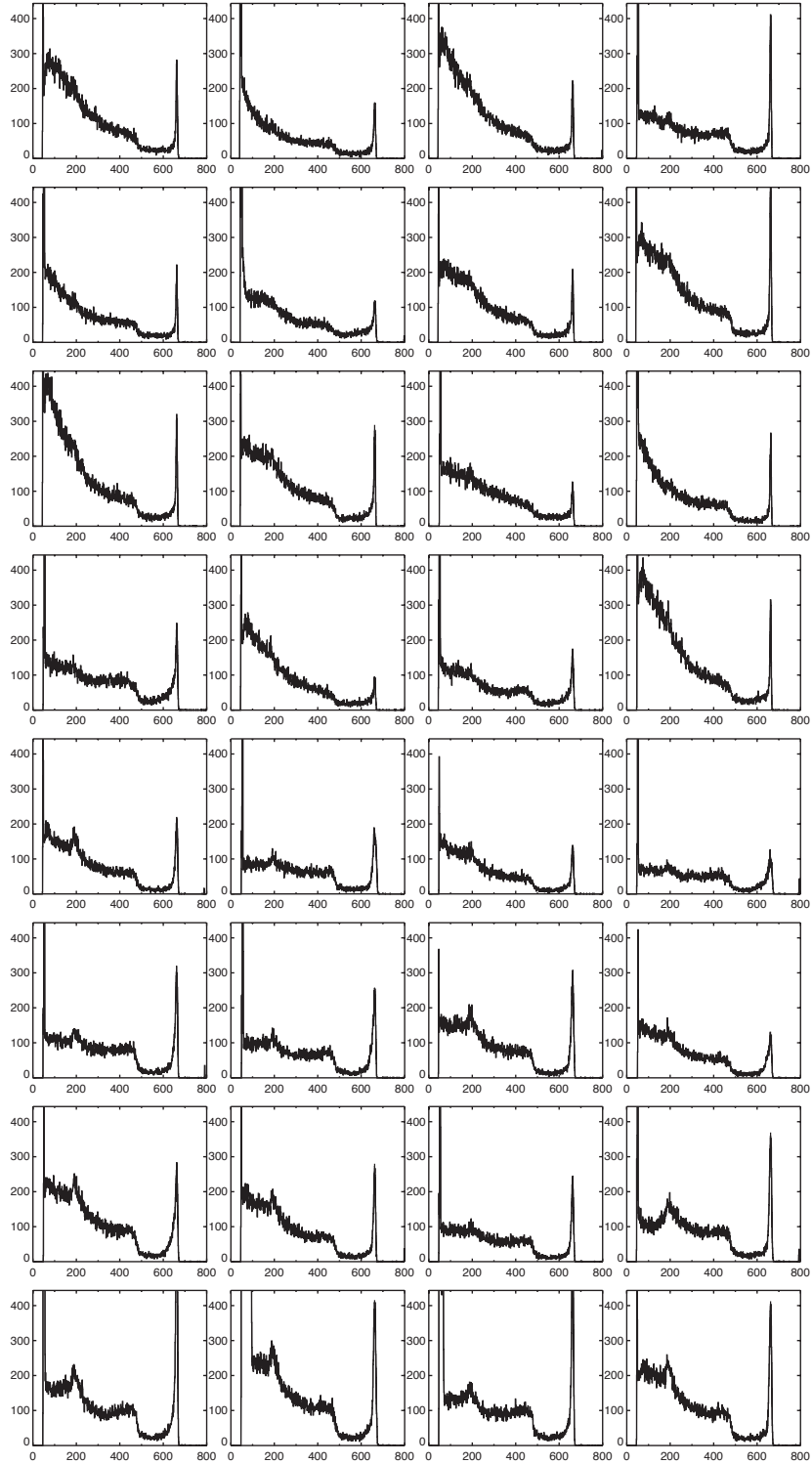


Figure 5.66: Individual responses of 32 CdZnTe Frisch collar detectors (two arrays of 4×4 device) to an uncollimated ^{137}Cs source. Courtesy of Aleksey Bolotnikov at BNL.

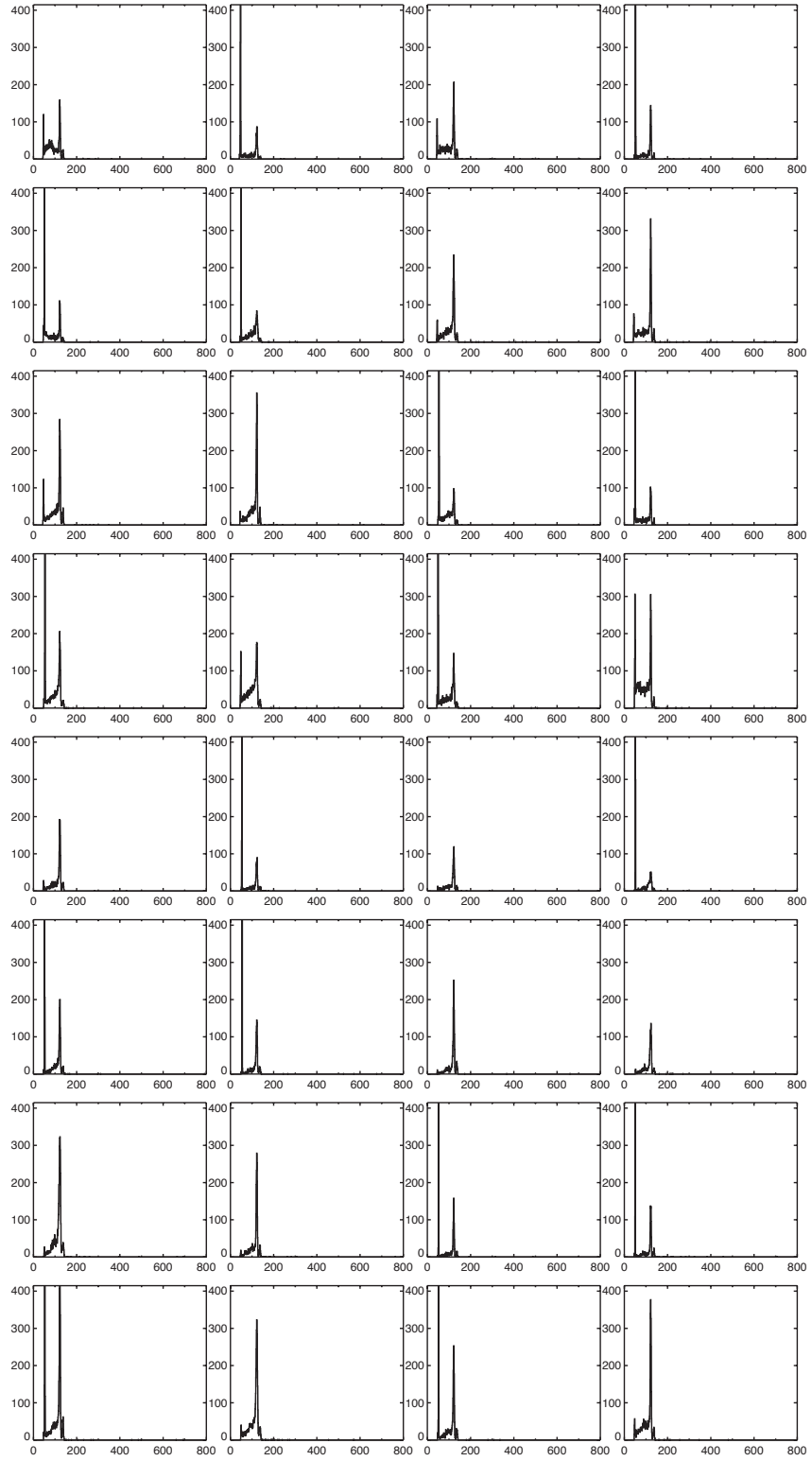


Figure 5.67: Individual responses of 32 CdZnTe Frisch collar detectors (two arrays of 4×4 device) to an uncollimated ^{241}Am source. Courtesy of Aleksey Bolotnikov at BNL.

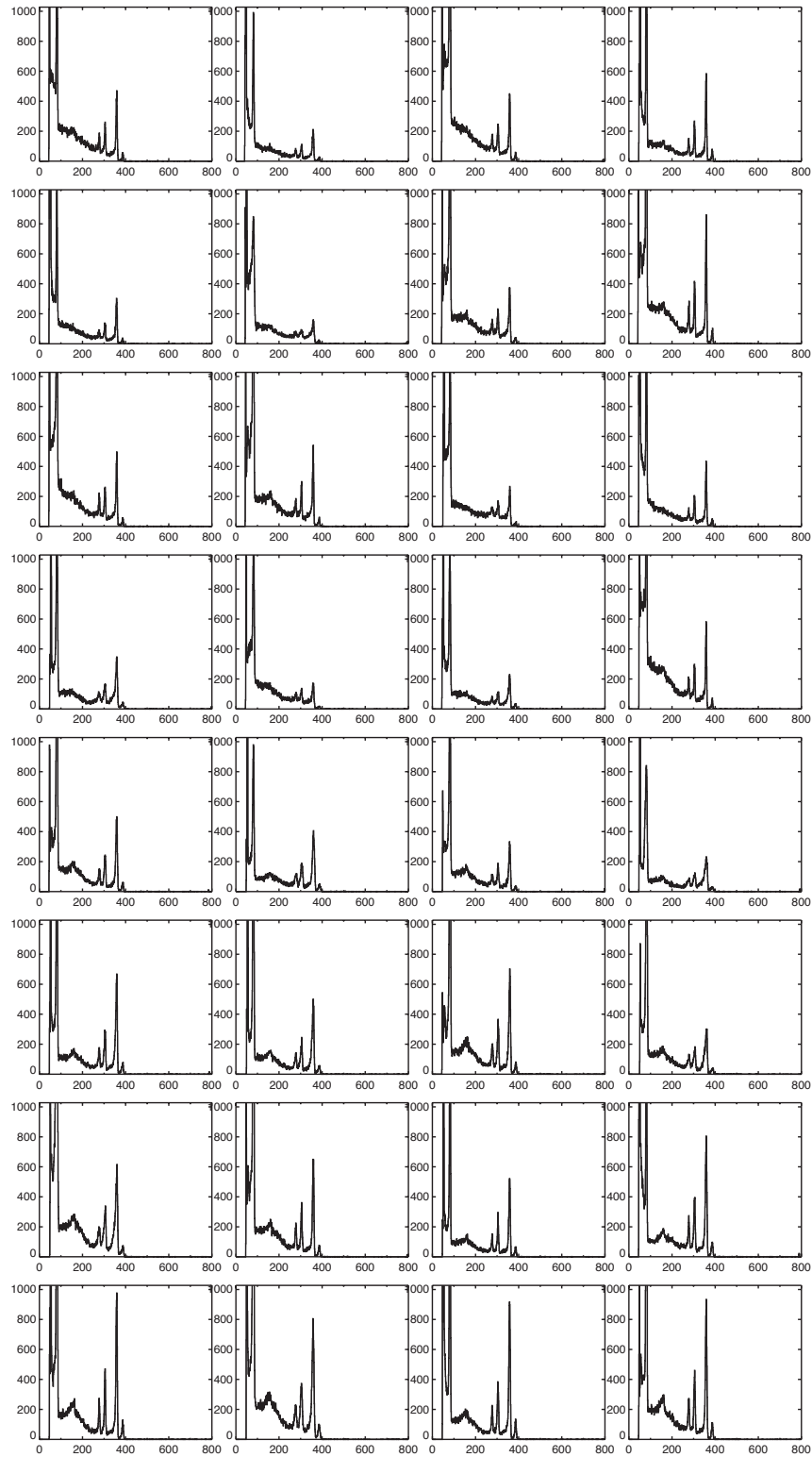


Figure 5.68: Individual responses of 32 CdZnTe Frisch collar detectors (two arrays of 4×4 device) to an uncollimated ^{133}Ba source. Courtesy of Aleksey Bolotnikov at BNL.

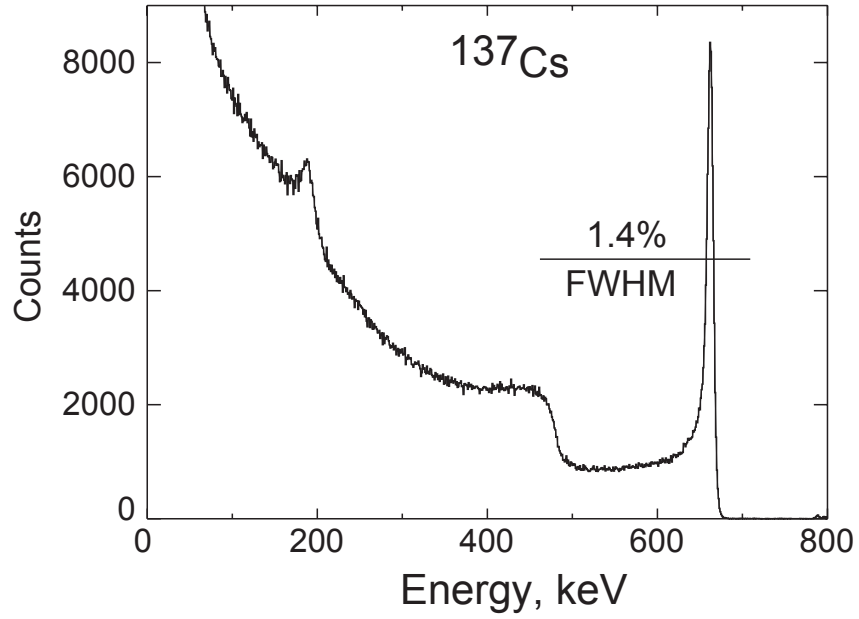


Figure 5.69: Overall responses of 16 detectors (one array of 4×4 device) to ^{137}Cs source, with no correction for gain variation and no recovery for scatter events among the detectors. Courtesy of Aleksey Bolotnikov at BNL.

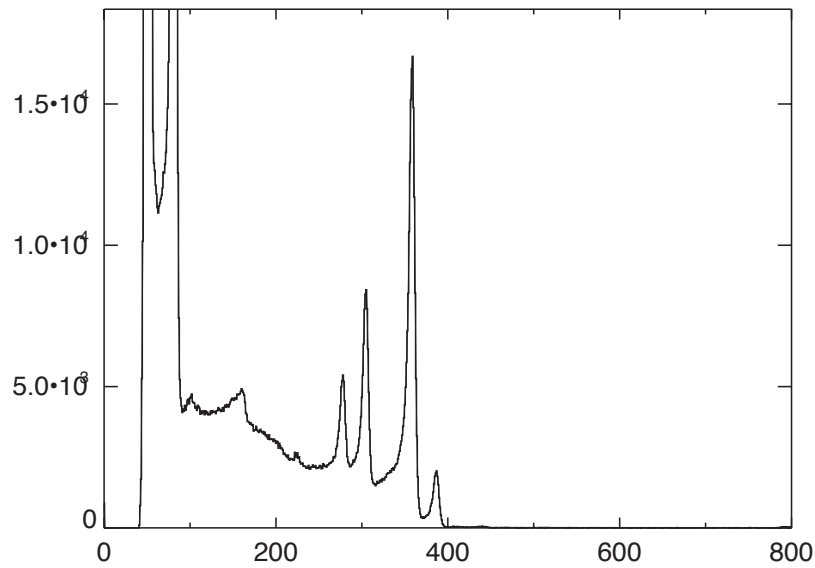


Figure 5.70: Overall responses of 16 detectors (one array of 4×4 device) to ^{133}Ba source, with no correction for gain variation and no recovery for scatter events among the detectors. The x -axis is the **Energy** in keV and the y -axis is the **counts**. Courtesy of Aleksey Bolotnikov at BNL.

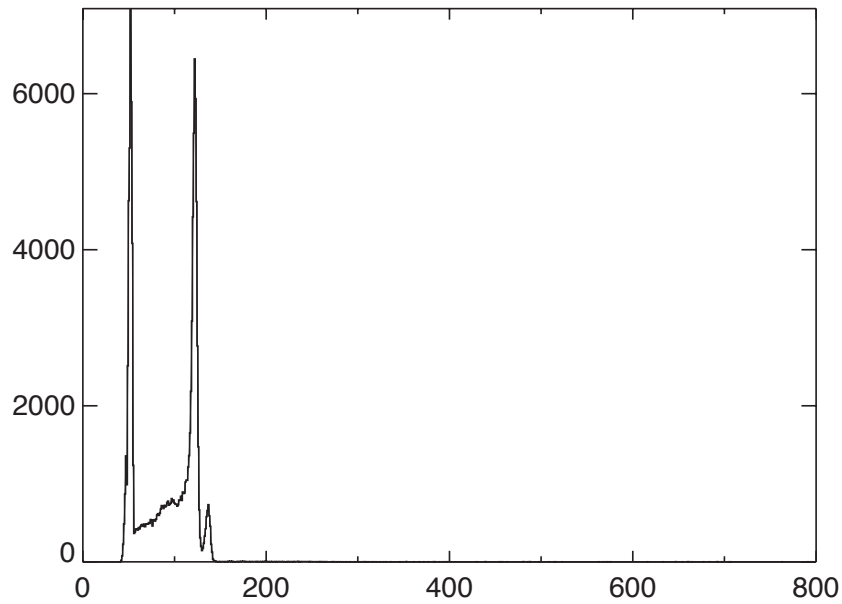


Figure 5.71: Overall responses of 16 detectors (one array of 4×4 device) to ^{241}Am source, with no correction for gain variation and no recovery for scatter events among the detectors. The x -axis is the **Energy** in keV and the y -axis is the **counts**. Courtesy of Aleksey Bolotnikov at BNL.

Figs. 5.69, 5.70 and 5.71 show the overall response of the array of 16 detectors to ^{137}Cs , ^{133}Ba and ^{241}Am gamma-ray sources. An energy resolution of 1.4% full width half maximum (FWHM) at 662 keV is achieved by combining the 16 spectra of one array of a 4×4 device, *without* correcting for variation in gain among the detectors (due to different CCE profiles for each device) and *before* recovering the scatter events among the detectors.

Chapter 6

SUMMARY AND CONCLUSIONS

This chapter summarizes all the studies in this thesis and concludes that Frisch collar technology is one of the most powerful techniques to turn a position sensitive semiconductor gamma-ray detector into a single carrier device. This chapter also provides some useful suggestions for future work on CdZnTe Frisch collar detectors and arrays of such devices.

6.1 Summary

Many bar shaped Frisch collar CdZnTe detectors were successfully fabricated and tested for gamma-ray spectroscopy, and sub-1% FWHM energy resolution at 662 keV was obtained without electronic correction (See Fig. 3.8 on Page 31). Clearly, these simple CdZnTe semiconductor detectors have excellent energy resolution at room temperature, which is useful in many applications such as remote field operations. The simple configuration of the Frisch collar device, which converts a simple planar device into a high-energy-resolution gamma-ray spectrometer, makes the devices less expensive to manufacture than other single carrier design. Further, due to CdZnTe material growth issues and problems, it is far easier to extract small samples similar to those used in the present work from a commercial ingot than to use large pieces typically used in other single carrier configurations, hence further reducing overall cost. Finally, the devices can be arranged in an array to produce gamma-ray detection devices for medical, astrophysics, and isotope identification purposes.

The summary in this section is presented in terms of optimizing the design of *two-*

terminal CdZnTe Frisch collar spectrometers to enhance induced charge/current, as well as improving the device fabrication process. The summary of optimization is presented in the following Sections 6.1.1 and 6.1.2.

6.1.1 Optimizing the Two-Terminal CdZnTe Frisch Collar Device to Enhance Induced Charge

Research shows that despite the beneficial energy resolution enhancement due to the Frisch collar effect, the effect depends heavily on the crystal geometry and aspect ratio (length over width) [70]. For instance, for the bar shape CdZnTe planar device with the aspect ratio of less than 1.0, the Frisch collar does not improve the energy resolution at 662 keV (see Sections 3.2.1.1 and 5.3.1). However, great energy resolution enhancement is achieved for aspect ratios exceeding 1.5 and close to 2.0 (Fig. 3.8 on Page 31). A numerical calculation for the weighting potential for the Frisch collar devices shows that the nonlinearity effect does not penetrate the bulk of the device with an aspect ratio of less than 1.0. Instead, the weighting potential for such a device shows a nearly linear profile, except near the lateral surfaces, a distribution similar to that of a planar configuration. For that reason, the Frisch collar has little effect for devices with an aspect ratio of less than 1.0. This nonlinearity in weighting potential uniformly penetrates the bulk of the device with an aspect ratio of 1.5 to 2.0, allowing a better charge induction as a single carrier device (Figs. 3.10 through 3.17 in Section 3.2.1.1 on Pages 35 through 38). This dependency on aspect ratio should be noted by the detector designer, and so the recommended aspect ratio of the two-terminal Frisch collar device is 1.5 to 2.0. However, if the device aspect ratio has to be smaller than 1.5 or greater than 2.5 due to other considerations, then, advanced techniques need to be applied to the device design to obtain a good single carrier spectrometer. These advanced techniques are summarized in the following paragraphs.

For Frisch collar devices with an aspect ratio smaller than 1.5 (and especially less than 1.0), the proposed method is to benefit from both the small pixel effect and the Frisch collar effect (see Section 3.2.1.3 for details). The model shows that for such a device, where the

Frisch collar effect is not strong enough, further benefiting from the small pixel effect can potentially turn the device into a single carrier device (due to enhancement in the device charge collection efficiency profile as shown in Fig. 3.23). In other words, for Frisch collar devices with an aspect ratio of less than 1.5, neither the thicker dielectric nor the shorter conductive length produces appreciable changes to improve performance. Therefore, the only other option is to take advantage of both the Frisch collar and small pixel effect and make the Frisch collar device with the anode to cathode area smaller than unity.

A Frisch collar device of aspect ratio greater than 2.5 [69] with the conductive collar covering the entire length of the device has compromised spectral performance, if too thin or thick dielectric layer is applied. Hence, the challenge is to alter parameters affecting the charge collection efficiency (CCE) profile to enhance spectral performance. Among those are the dielectric layer thickness and the Frisch collar length (or combination of both). The impact of dielectric layer thickness on the CCE profile of such a device with an aspect ratio greater than 2.5 is investigated in Sections 3.2.1.4 and 5.3.2. Such a two-terminal Frisch collar device offers a balance between improved induced charge (more nonlinear weighting potential distribution) and a more uniform electric field (more linear operating potential distribution), that ultimately results in the most uniform CCE profile. Thus, for such a device with large aspect ratio, the device needs to be optimized for this region of optimum dielectric layer thickness. This optimum dielectric layer thickness was experimentally determined for three devices with aspect ratios greater than 2.5 (Section 5.3.2). However, reaching the optimum distribution of weighting potential for such a device can be achieved by shortening the conductive collar length or with an optimal combination of both dielectric thickness and conductive collar length. These techniques allow enhanced electric field distribution, resulting in more uniform CCE profile. For the bar shape CdZnTe devices with an aspect ratio greater than 2.5, this optimum region of potential distribution was experimentally determined by changing the dielectric layer thickness.

Next, the uniformity of gamma response for a $4.7 \times 4.7 \times 9.5 \text{ mm}^3$ CdZnTe Frisch

collar device was investigated by probing the device from the lateral side along the length and width with a collimated 662 keV gamma-ray [68] (Section 5.2). The experimental results of this device show uniform charge collection efficiency (CCE) for about two-thirds of the device volume (Figs. 5.16 and 5.17 on Page 108), which is expected given CCE simulations (Fig. 3.29 on Page 50). This uniform response was investigated experimentally and theoretically for a wide range of applied voltages. The non-uniformity near the anode region is mainly due to the low mobility-lifetime product of holes. Notably, the Frisch collar configuration is designed to negate the effects of severe hole trapping and low mobility. Hence, long drift CdZnTe Frisch collar device performance can be limited by the electrons' transport properties only. As reported previously, a planar CdZnTe device shows a non-uniform response along device length [29]. Hence, planar CdZnTe detector designs can not be used for a high energy gamma-ray spectrometer (since a thick, highly efficient device is desired). Instead, poor hole transport necessitates advanced device design, for which the Frisch collar technique is one of the most inexpensive and robust methods.

6.1.2 Fabrication Enhancement

Six different techniques were applied on lateral sides of six bar shape CdZnTe detectors as the final surface treatment (passivation) [71]. The current-voltage (I-V) characteristic curves and the ^{137}Cs pulse height spectra are reported for each device before and after the surface treatment (See Sections 4.3.5 and 5.3.4 for details). The surface characterization results with the Electron Microprobe (EMP) technique are also reported for the atomic concentration of the elements using an Energy Dispersive Spectroscopy (EDS) before and after each treatment. Mechanical polishing with 0.05 μm alumina powder and $\text{NaClO}_3/\text{H}_2\text{O}_2$ treatment enhance the device performance the most, while other methods still produce acceptable results (Section 5.3.4). Notably, ion milling as a surface treatment for CdZnTe detectors is reported here for the first time and is still under development.

6.2 Conclusions

CdZnTe is one of the most promising materials for room-temperature operated gamma-ray spectroscopy. The high resistivity of the material lets the CdZnTe devices be operated at high voltage bias, which reduces the effect of trapping. In Frisch collar CdZnTe devices, using small single crystals rather than large single crystals, means less stringent material requirements since small portions of high quality CdZnTe materials are much easier to extract from an ingot than large pieces. Further, the simple Frisch collar device structure, along with less demanding materials requirements, reduces overall device cost.

In terms of directional sensitivity, bar shaped CdZnTe Frisch collar detectors can be easily collimated [75]; however, the angular resolution of a collimated CdZnTe Frisch collar gamma-ray spectrometer depends strongly on the collimator length. Also, arrays of detectors with individual collimated (or uncollimated [67]) detectors have some advantages over common pixelated devices. In the proposed array of collimated (or uncollimated) detectors, each pixel (detector) is isolated from its neighbor, resulting in little to no cross talk among the pixels from the scatter events (collimated design), with no charge sharing, unlike for current pixelated devices sharing a single crystal. A prototype of a hand-held gamma-ray spectrometer [67] using an array of uncollimated Frisch collar CdZnTe detectors is discussed in Sections 4.5 and 5.6.1. The study proves that the array of CdZnTe Frisch collar detectors can easily serve a large detecting area, maintaining relatively simple electronic readout and lower cost compared to common pixelated devices.

6.3 Future Work

Multi-terminal Frisch collar devices need to be investigated in a variety of configurations and designs, since the improvement of the *two-terminal* Frisch collar device performance is due to electric field enhancement near the cathode region. This enhancement in electric field can potentially be achieved by using the third (or fourth) terminal as another non-reading electrode with an optimum bias. For this type of multi-terminal device, the weighting poten-

tial and the normalized operating potential are no longer the same, and they are decoupled, which can potentially improve the device charge collection efficiency. This approach is important for Frisch collar devices with an aspect ratio greater than 3.0. Accordingly, taking pulse height spectra and gamma-ray probing of such a long device with different dielectric material properties and different Frisch collar length is proposed as future work. For Frisch collar devices with aspect ratios of less than 1.5, a combination of small pixel effect and Frisch collar effect is proposed (Section 3.2.1.3), which also requires further experimental investigation.

Future work on post-fabrication surface treatment should include multiple surface analysis methods. For example, combining EDS with Auger Electron Spectroscopy (AES) provides better information about the composition of the surface atomic layers. Using AES allows depth profiling at the surface, while EDS would provide composition data at a slightly lower depth. Additionally, the X-ray Photoelectron Spectroscopy (XPS) technique may provide better surface stoichiometry information. Finally, ion milling as a surface treatment for CdZnTe detectors is reported here for the first time and needs further development.

Regarding the device fabrication, a systematic study is required on contact deposition, including the surface treatment and etching prior to contact deposition. Such a study could detail the impact of several parameters prior to contact deposition on device spectral performance, such as surface roughness, type and concentration of etchant, and etching time. Other parameters that may have great impact on quality of detector contact could be concentration of gold chemical solution (AuCl_3 in this case) and duration of exposure, alternative methods of contact deposition (sputtering or evaporating), alternative metals other than gold (such as indium), and finally temperature treatment after contact deposition.

Finally, arrays of *collimated* detectors could potentially remedy the scattering effect from one detector (pixel) to the other, reducing the cross talk among the detectors. This requires a more advanced design for detector configuration with the electronics and circuit board, such as that shown in Fig. 1.1 on Page 4.

Bibliography

- [1] W. Röntgen and A. Joffé, “Electric conductivity of certain crystals,” *Annalen der Physik*, vol. 41, no. 3, pp. 449 – 498, 1913.
- [2] G. Jaffé, “Effect of α -rays on the passage of electricity through crystals,” *Physikalische Zeitschrift*, vol. 33, pp. 393 – 399, 1932.
- [3] W. Harding, C. Hilsum, M. Moncaster, D. Northrop, and O. Simpson, “Gallium arsenide for gamma-ray spectroscopy,” *Nature*, vol. 187, p. 405, 1960.
- [4] W. Akutagawa, K. Zanio, and J. Mayer, “CdTe as a gamma detector,” *Nuclear Instruments and Methods*, vol. 55, no. 2, pp. 383 – 385, 1967.
- [5] F. Doty, J. Butler, J. Schetzina, and K. Bowers, “Properties of CdZnTe crystals grown by a high pressure Bridgman method,” *Journal of Vacuum Science & Technology B: Microelectronics Processing and Phenomena*, vol. 10, no. 4, pp. 1418 – 22, 1992.
- [6] T. Prettyman, T. Reilly, M. Miller, C. Hollas, M. Pickrell, J. Prommel, and J. Dreicer, “Advances in nuclear instrumentation for safeguards,” in *Proceedings of Workshop on Science and Modern Technology for Safeguards*, (Ispra, Italy), pp. 97 – 104, 1997.
- [7] P. Russo, R. Strittmatter, E. Sandford, I. Jeter, E. McCullough, and G. Bowers, “Operation of automated NDA instruments for in-line HEU accounting at Y-12,” in *Conference on Safeguards Technology: The Process-Safeguards Interface*, vol. 45, (USA), pp. 14 – 15, 1983.
- [8] P. Russo, H. Smith, J. Sprinkle, C. Bjork, G. Sheppard, N. Ensslin, and S. Smith, “Evaluation of an integrated holdup measurement system using the GGH formalism

- with the M3CA,” in *5th International Conference on Facility Operations-Safeguards Interface*, vol. 72, (USA), pp. 29 – 30, 1995.
- [9] H. Barrett, J. Eskin, and H. Barber, “Charge transport in arrays of semiconductor gamma-ray detectors,” *Physical Review Letters*, vol. 75, no. 1, pp. 156 – 9, 1995.
- [10] P. Luke, “Unipolar charge sensing with coplanar electrodes - application to semiconductor detectors,” *IEEE Transactions on Nuclear Science*, vol. 42, no. 4 pt 1, pp. 207 – 213, 1995.
- [11] D. McGregor and R. Rojeski, “Performance of CdZnTe geometrically weighted semiconductor Frisch grid radiation detectors,” *IEEE Transactions on Nuclear Science*, vol. 46, no. 3 I, pp. 250 – 259, 1999.
- [12] D. McGregor, Z. He, H. Seifert, R. Rojeski, and D. Wehe, “CdZnTe semiconductor parallel strip Frisch grid radiation detectors,” *IEEE Transactions on Nuclear Science*, vol. 45, no. 3 pt 1, pp. 443 – 449, 1998.
- [13] H. Malm, C. Canali, J. Mayer, M. Nicolet, K. Zanio, and W. Akutagawa, “Gamma-ray spectroscopy with single-carrier collection in high-resistivity semiconductors,” *Applied Physics Letters*, vol. 26, no. 6, pp. 344 – 6, 1975.
- [14] D. McGregor, Z. He, H. Seifert, D. Wehe, and R. Rojeski, “Single charge carrier type sensing with a parallel strip pseudo-Frisch-grid CdZnTe semiconductor radiation detector,” *Applied Physics Letters*, vol. 72, no. 7, pp. 792 – 794, 1998.
- [15] D. McGregor, R. Rojeski, Z. He, D. Wehe, M. Driver, and M. Blakely, “Geometrically weighted semiconductor Frisch grid radiation spectrometers,” *Nuclear Instruments and Methods in Physics Research, Section A: Accelerators, Spectrometers, Detectors and Associated Equipment*, vol. 422,, no. 1-3, pp. 164–8, 1999.

- [16] D. McGregor, J. Nishanth, and D. Wehe, "Design considerations for trapezoid-shaped Frisch-grid semiconductor radiation detectors," in *Proceedings of the SPIE - The International Society for Optical Engineering*, vol. 4141, (USA), pp. 281 – 90, 2000.
- [17] K. Parnham, J. Glick, C. Szeles, and K. Lynn, "Performance improvement of CdZnTe detectors using modified two-terminal electrode geometry," *Journal of Crystal Growth*, vol. 214, pp. 1152 – 1154, 2000.
- [18] D. McGregor, J. Nishanth, and D. Wehe, "Low-energy gamma-ray characterization of a trapezoidal-shaped geometrically weighted Frisch grid CdZnTe gamma-ray spectrometer," *Nuclear Instruments and Methods in Physics Research, Section A: Accelerators, Spectrometers, Detectors and Associated Equipment*, vol. 457, no. 1-2, pp. 230 – 244, 2001.
- [19] D. McGregor and R. Rojeski, "High-resolution ionization detector and array of such detectors," US Patent No. 6,175,120, January 2001.
- [20] G. Montemont, M. Arques, L. Verger, and J. Rustique, "A capacitive Frisch grid structure for CdZnTe detectors," *IEEE Transactions on Nuclear Science*, vol. 48, no. 3 I, pp. 278 – 281, 2001. Frisch grid structures;
- [21] L. Cirignano, H. Kim, K. Shah, M. Klugerman, P. Wong, M. Squillante, and L. Li, "Evaluation of CZT detectors with capacitive Frisch grid structure," in *Proceedings of SPIE - The International Society for Optical Engineering*, vol. 5198, (Bellingham, WA 98227-0010, United States), pp. 1 – 8, 2004.
- [22] D. McGregor, "Collimated radiation detector assembly, array of collimated radiation detectors and collimated radiation detector module," US Patent No. 6,781,132, August 2004.
- [23] W. McNeil, D. McGregor, A. Bolotnikov, G. Wright, and R. James, "Single-charge-

- carrier-type sensing with an insulated Frisch ring CdZnTe semiconductor radiation detector,” *Applied Physics Letters*, vol. 84, no. 11, pp. 1988 – 1990, 2004.
- [24] A. Bolotnikov, G. Camarda, G. Carini, G. Wright, L. Li, A. Burger, M. Groza, and R. James, “Large area/volume CZT nuclear detectors,” *Physica Status Solidi C*, vol. 2, no. 5, pp. 1495 – 1503, 2005.
- [25] A. Kargar, A. M. Jones, W. J. McNeil, M. J. Harrison, and D. S. McGregor, “CdZnTe Frisch collar detectors for γ -ray spectroscopy,” *Nuclear Instruments and Methods in Physics Research, Section A: Accelerators, Spectrometers, Detectors and Associated Equipment*, vol. 558, no. 2, pp. 497 – 503, 2006.
- [26] O. Frisch , British atomic energy report, BR-49, (unpublished) 1944.
- [27] A. Bolotnikov, G. Camarda, G. Wright, and R. James, “Factors limiting the performance of CdZnTe detectors,” *IEEE Transactions on Nuclear Science*, vol. 52, no. 3, pp. 589 – 98, 2005.
- [28] A. Bolotnikov, G. Camarda, G. Carini, M. Fiederle, L. Li, D. Mcgregor, W. Mcneil, G. Wright, and R. James, “Performance characteristics of Frisch-ring CdZnTe detectors,” *IEEE Transactions on Nuclear Science*, vol. 53, no. 2, pp. 607 – 614, 2006.
- [29] M. J. Harrison, A. Kargar, and D. S. McGregor, “Charge collection characteristics of Frisch collar CdZnTe gamma-ray spectrometers,” *Nuclear Instruments and Methods in Physics Research, Section A: Accelerators, Spectrometers, Detectors and Associated Equipment*, vol. 579, no. 1, pp. 134 – 137, 2007.
- [30] M. Schwartz, *Principles of Electrodynamics*. McGraw-Hill, New York, 1972.
- [31] J. D. Jackson, *Classical Electrodynamics*. 3rd ed., Wiley, New York, 1999.

- [32] G. Cavalleri, E. Gatti, G. Fabri, and V. Svelto, “Extension of ramo’s theorem as applied to induced charge in semiconductor detectors,” *Nuclear Instruments and Methods*, vol. 92, no. 1, pp. 137 – 40, 1971.
- [33] V. Radeka, “Low-noise techniques in detectors,” *Annual review of nuclear and particle science*, vol. 38, pp. 217 – 77, 1988.
- [34] Integrated Engineering Software, LORENTZ, “www.integratedsoft.com.”
- [35] W. Shockley, “Currents to conductors induced by a moving point charge,” *Journal of Applied Physics*, vol. 9, pp. 635 – 636, 1938.
- [36] S. Ramo, “Currents induced by electron motion,” *IRE Proceedings*, vol. 27, pp. 584 – 585, 1939.
- [37] G. Cavalleri, G. Fabri, E. Gatti, and V. Svelto, “On the induced charge in semiconductor detectors,” *Nuclear Instruments and Methods*, vol. 21, no. 1, pp. 177 – 178, 1963.
- [38] J. Gunn, “A general expression for electrostatic induction and its application to semiconductor devices,” *Solid-State Electronics*, vol. 7, no. 10, pp. 739 – 742, 1964.
- [39] P. Tove and K. Falk, “Pulse formation and transit time of charge carriers in semiconductor junction detectors,” *Nuclear Instruments and Methods*, vol. 29, no. 1, pp. 66 – 68, 1964.
- [40] M. Martini and G. Ottaviani, “Ramo’s theorem and the energy balance equations in evaluating the current pulse from semiconductor detectors,” *Nuclear Instruments and Methods*, vol. 67, no. 1, pp. 177 – 8, 1969.
- [41] G. Knoll and D. McGregor, “Fundamentals of semiconductor detectors for ionizing radiation,” in *Proceedings of MRS - Materials Research Society*, vol. 302, pp. 3 – 17, 1993.

- [42] R. Day, G. Dearnaley, and J. Palms, “Noise, trapping and energy resolution in semiconductor gamma-ray spectrometers,” vol. NS-14, pp. 487 – 491, 1967.
- [43] W. Akutagawa and K. Zanio, “Gamma response of semi-insulating material in the presence of trapping and detrapping,” *Journal of Applied Physics*, vol. 40, no. 9, pp. 3838 – 53, 1969.
- [44] N. Stroken, V. Yeryomin, S. Lomashevich, and N. Tisnek, “Final results on the nature of the pulse-height spectrum from semiconductor detectors,” vol. S-19, (USA), pp. 365 – 79, 1972.
- [45] T. H. Prettyman, M. K. Smith, and S. E. Soldner, “Design and characterization of cylindrical CdZnTe detectors with coplanar grids,” *Proceedings of SPIE - The International Society for Optical Engineering*, vol. 3768, pp. 339 – 347, 1999.
- [46] F. Mathy, A. Gliere, E. Gros d’Aillon, P. Masse, M. Picone, J. Tabary, and L. Verger, “3D model of CZT gamma-ray spectrometer detector: validation on a monolithic pixelated detector and on a high energy spectrometric probe,” in *IEEE Nuclear Science Symposium Conference Record*, vol. Vol.5, pp. 3351 – 3355, 2004.
- [47] F. Mathy, A. Gliere, E. G. D’Aillon, P. Masse, M. Picone, J. Tabary, and L. Verger, “A Three-Dimensional Model of CdZnTe Gamma-Ray Detector and Its Experimental Validation,” *IEEE Transactions on Nuclear Science*, vol. 51, no. 5 I, pp. 2419 – 2426, 2004.
- [48] P. S. Ho, J. Leu, and W. W. Lee, *Low dielectric constant materials for IC applications*. Springer, New York, 2003.
- [49] H. Chen, J. Tong, Z. Hu, D. Shi, G. Wu, K. Chen, M. George, W. Collins, A. Burger, R. James, C. Stahle, and L. Bartlett, “Low-temperature photoluminescence of detector grade CdZnTe crystal treated by different chemical etchants,” *Journal of Applied Physics*, vol. 80, no. 6, pp. 3509 – 12, 1996.

- [50] J. Ponpon, "A review of ohmic and rectifying contacts on cadmium telluride," *Solid-State Electronics*, vol. 28, no. 7, pp. 689 – 706, 1985.
- [51] W. Akutagawa, D. Turnbull, W. Chu, and J. Mayer, "Solubility and lattice location of Au in CdTe by backscattering techniques," *Journal of the Physics and Chemistry of Solids*, vol. 36, no. 6, pp. 521 – 8, 1975.
- [52] M. J. Harrison, A. Kargar, A. C. Brooks, and D. McGregor, "Improved techniques for the fabrication of Frisch collar CdZnTe gamma ray spectrometers," in *IEEE Nuclear Science Symposium Conference Record*, vol. 3, (Honolulu, HI, United states), pp. 1816 – 1821, 2007.
- [53] M. Mescher, M. Reed, and T. Schlesinger, "Stress control in sputtered silicon nitride films," in *Materials Research Society Symposium - Proceedings*, vol. 472, (Warrendale, PA, USA), pp. 239 – 244, 1997.
- [54] Y. Nemirovsky, "Passivation with II-VI compounds," in *Proceedings of the SPIE - The International Society for Optical Engineering*, vol. 8, (USA), pp. 1185 – 7, 1990.
- [55] K.-T. Chen, D. Shi, H. Chen, B. Granderson, M. George, W. Collins, A. Burger, and R. James, "Study of oxidized cadmium zinc telluride surfaces," in *Proceedings of the SPIE - The International Society for Optical Engineering*, vol. 15, (USA), pp. 850 – 3, 1997.
- [56] J. Haring, J. Werther, R. Bube, L. Gulbrandsen, W. Jansen, and P. Luscher, "Study of cleaved, oxidized, and heat-treated CdTe surfaces," *Journal of Vacuum Science and Technology A (Vacuum, Surfaces, and Films)*, vol. 1, no. 3, pp. 1469 – 72, 1983.
- [57] A. Burger, K. Chen, D. Shi, W. Collins, and R. James, "Recent CdZnTe detector fabrication developments," in *Proceedings of the SPIE - The International Society for Optical Engineering*, vol. 3115, (USA), pp. 70 – 5, 1997.

- [58] G. Wright, R. James, D. Chinn, B. Brunett, R. Olsen, I. van Scyoc, J., M. Clift, A. Burger, K. Chattopadhyay, D. Shi, and R. Wingfield, "Evaluation of $\text{NH}_4\text{F}/\text{H}_2\text{O}_2$ effectiveness as a surface passivation agent for CdZnTe crystals," in *Proceedings of the SPIE - The International Society for Optical Engineering*, vol. 4141, (USA), pp. 324 – 35, 2000.
- [59] G. Wright, D. Chinn, B. Brunett, M. Mescher, J. Lund, R. Olsen, F. Doty, T. Schlesinger, R. James, K. Chattopadhyay, R. Wingfield, and A. Burger, "Exploratory search for improved oxidizing agents used in the reduction of surface leakage currents of CdZnTe detectors," in *Proceedings of the SPIE - The International Society for Optical Engineering*, vol. 3768, (USA), pp. 481 – 5, 1999.
- [60] G. Wright, G. Camarda, E. Kakuno, L. Li, F. Lu, C. Lee, A. Burger, J. Trombka, P. Siddons, and R. James, "Effects of surface roughness on large-volume CdZnTe nuclear radiation detectors and removal of surface damage by chemical etching," in *Proceedings of the SPIE - The International Society for Optical Engineering*, vol. 5198, pp. 306 – 313, 2004.
- [61] H. Chen, K. Chattopadhyay, K.-T. Chen, A. Burger, M. George, J. Gregory, P. Nag, J. Weimer, and R. James, "Passivation of CdZnTe surfaces by oxidation in low energy atomic oxygen," *Journal of Vacuum Science and Technology A (Vacuum, Surfaces, and Films)*, vol. 17, no. 1, pp. 97 – 101, 1999.
- [62] H. Chen, M. Hayes, K. Chattopadhyay, K.-T. Chen, A. Burger, J. Heffelfinger, and R. James, "Photoluminescence investigation of surface oxidation of CdZnTe detectors," in *Semiconductors for Room-Temperature Radiation Detector Applications II, Symposium*, (Warrendale, PA, USA), pp. 65 – 70, 1997.
- [63] A. Burger, H. Chen, K. Chattopadhyay, D. Shi, S. Morgan, W. Collins, and R. James, "Characterization of metal contacts on and surfaces of cadmium zinc telluride," *Nuclear*

Instruments and Methods in Physics Research, Section A: Accelerators, Spectrometers, Detectors and Associated Equipment, vol. 428, no. 1, pp. 8 – 13, 1999.

- [64] N. Tsoulfanidis, *Measurement and detection of radiation*. 2nd ed., Taylor & Francis, Washington, DC, 1995.
- [65] G. F. Knoll, *Radiation detection and measurement*. 3rd ed., Wiley, New York, 2000.
- [66] A. Abyzov, L. Davydov, V. Kutny, A. Rybka, M. Rowland, and C. Smith, “Correlation between spectrometric ability and physical properties of semiconductor detectors,” in *Conf. Rec. 11th International Workshop of Room Temperature Semiconductor X-and Gamma Ray Detectors and Associated Electronics*, (Vienna), pp. 11–15, 1999.
- [67] Y. Cui, A. Bolotnikov, G. Camarda, A. Hossain, R. James, G. De Geronimo, J. Fried, P. O’Connor, A. Kargar, M. Harrison, and D. McGregor, “Hand-held gamma-ray spectrometer based on high-efficiency frisch-ring cdznte detectors,” *IEEE Transactions on Nuclear Science*, vol. 55, no. 5, pp. 2765 – 9, 2008.
- [68] A. Kargar, M. J. Harrison, and D. S. McGregor, “Charge collection efficiency characterizing of CdZnTe Frisch collar spectrometer with collimated high energy gamma ray,” *Nuclear Instruments and Methods in Physics Research, Section A: Accelerators, Spectrometers, Detectors and Associated Equipment*, Submitted.
- [69] A. Kargar, A. Brooks, M. J. Harrison, K. Kohman, R. Lowell, R. Keyes, H. Chen, G. Bindley, and D. McGregor, “The effect of the dielectric layer thickness on spectral performance of CdZnTe Frisch collar gamma ray spectrometers,” *IEEE Transactions on Nuclear Science*, vol. 56, pp. 824–831, 2009.
- [70] A. Kargar, R. B. Lowell, M. J. Harrison, and D. S. McGregor, “The crystal geometry and the aspect ratio effects on spectral performance of CdZnTe Frisch collar device,” in *Proceedings of SPIE - The International Society for Optical Engineering*, vol. 6706, (San Diego, CA, United States), p. 67061J, 2007.

- [71] A. Kargar, A. Brooks, K. Kohman, R. Lowell, R. Keyes, H. Chen, S. Awadalla, G. Bindley, and D. McGregor, “Final surface treatment effect on performance of CdZnTe Frisch collar gamma-ray detectors,” in *Proceedings of SPIE - The International Society for Optical Engineering*, vol. 7079, (USA), p. 70790B (12 pp.), 2008.
- [72] P. Capper, *Properties of Narrow Gap Cadmium-based Compounds*. IEE : INSPEC, London, 1994.
- [73] D. K. Schroder, *Semiconductor material and device characterization*. Wiley, New York, 1990.
- [74] H. Kaufman and R. Robinson, *Operation of broad-beam sources*. Commonwealth Scientific Corp., Alexandria, 1987.
- [75] A. Kargar, A. M. Jones, W. J. McNeil, M. J. Harrison, and D. S. McGregor, “Angular response of a W-collimated room-temperature-operated CdZnTe Frisch collar spectrometer,” *Nuclear Instruments and Methods in Physics Research, Section A: Accelerators, Spectrometers, Detectors and Associated Equipment*, vol. 562, no. 1, pp. 262 – 271, 2006.

Appendix A

Source of the FORTRAN code for charge collection efficiency simulation

```
!generate the Q/Qo (or CCE) of the CZT (FRISCH collar) detector
!with certain values of mobility life time product for the e and holes.
!This one consider the weighting field and electric field as two vectors
!Now 1-D problem along central axis of ~1 cm long device
!-----
program EEwFrischHetchCZT
implicit none
!VARIABLES
!-----
real, dimension(1003) :: CCE, CCE_h, CCE_e, x, E, WF, Ve
!NOTE: the dim of the vectors is the same as "n"
!x is the gamma interaction distance from cathode in planar device in cm
!WF is the "Weighting field" DIM(1/cm)
!CCE_h, CCE_e are the CCE of electrons and holes-not necessary.
integer :: i, n, j, k, t
real :: meu_tau_e, meu_tau_h, L, F_h, F_e, deltaX, m, p, e_trap, Hole_trap
!-----INPUT-----INPUT-----INPUT-----
```

```

meu_tau_e=0.045      !cm2/V
  meu_tau_h=0.0001   !cm2/V
L=0.95              !cm
n=1000 !# of nodes in x-axis which is the increment of x depends
!on the number of nods in the output file of LORENTZ
  !-----INPUT-----INPUT-----INPUT-----
!Constants CALCULATION
!-----calculate the coefficient of the exponential terms-----
F_h=-L/(real(n)*meu_tau_h)
F_e=-L/(real(n)*meu_tau_e)
!-----
deltaX=L/real(n) !Now the device is divided into "n" segments
  !-----
  !OPEN two file to read from and write to
!-----
  open(unit=1,file='inputfile.txt',status='old') !read E&WF from input file
open(unit=3,file='output.txt',status='unknown') !write CCE(x) into output
  !-----
!INPUT files: READ vectors E and WF from LORENTZ OUTPUT file
!-----
x(0)=0.
DO t=1, n
  read(1,*) E(t), WF(t)
end DO
  !-----
!CALCULATE the CCE(x) which is CCE at x(i) and then write CCE(i)
!-----

```

```

DO i=1, n
!ELECTRONS
  CCE_e(i)=WF(i+1)*deltaX !the (i+1)th segments, gamma interact
  !Calculate the sum of ELECTRONS induction from x(i+1)interaction to x(n)=L
  DO k=i+2, n !+++++ELECTRONS+++++
e_trap=0.
    !Calculate the summation of ELECTRONS trapping
    DO j=i+1, k-1 !***** k-1<----->i+1
e_trap=e_trap+1.0/E(j)
      end DO !*****
    CCE_e(i)=CCE_e(i)+WF(k)*deltaX*exp(F_e*e_trap) !i+1--->j
  end DO !+++++ELECTRONS+++++
!HOLES
  CCE_h(i)=WF(i)*deltaX !HOLE the i-th segment, gamma interact
  !Calculate the sum of HOLES induction from x(i)interaction to x(0)=0
  DO k=1, i-1 !+++++HOLES+++++
    Ve(k)=k*1.0
Hole_trap=0.0
    m=0.
    !Calculate the summation of HOLES trapping
    DO j=k+1, i !*****
      Hole_trap=Hole_trap+1.0/E(j)
      m=m+1.0
    end DO !*****
    x(i)=Hole_trap
    CCE_h(i)=CCE_h(i)+WF(k)*deltaX*exp(F_h*Hole_trap)!i->j
  end DO !+++++HOLES+++++

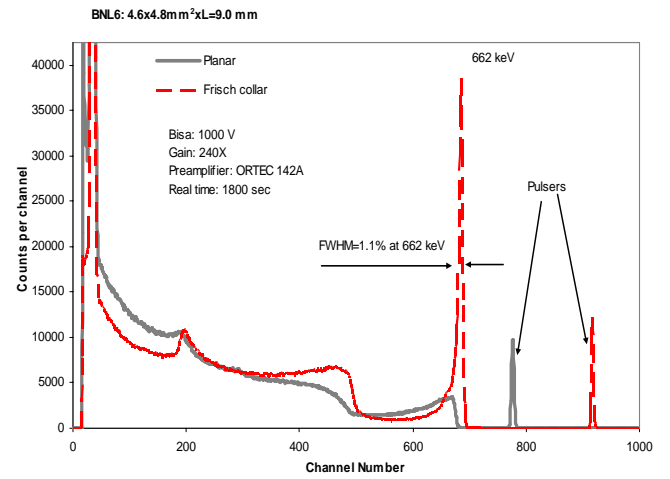
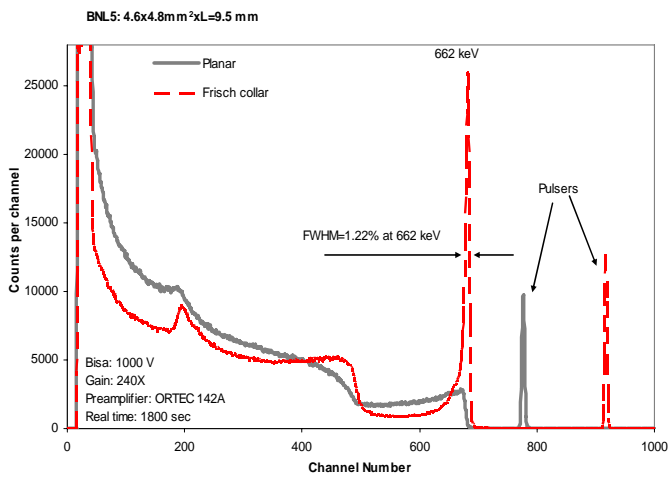
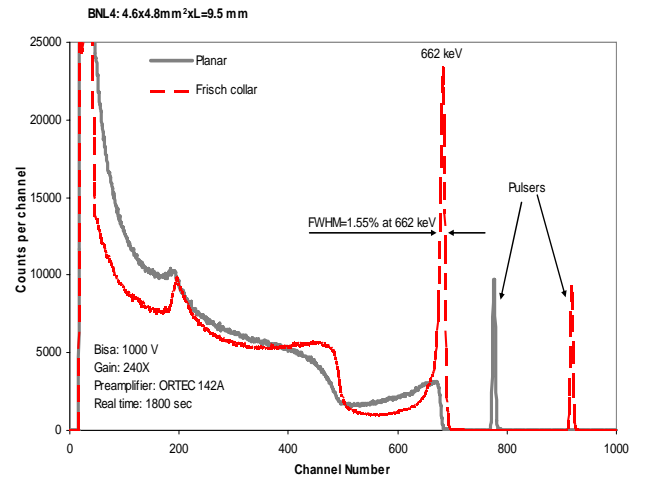
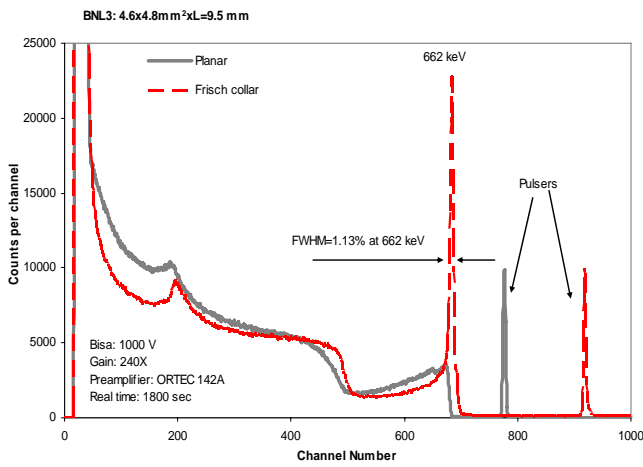
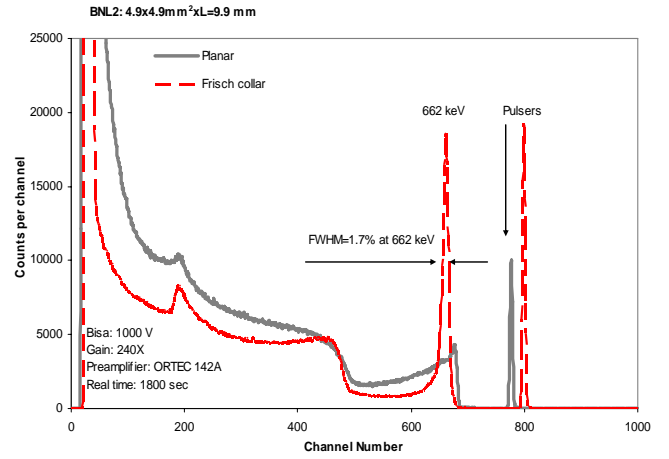
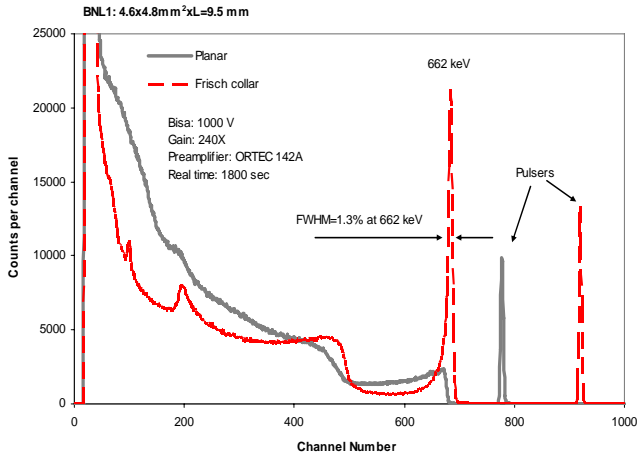
```

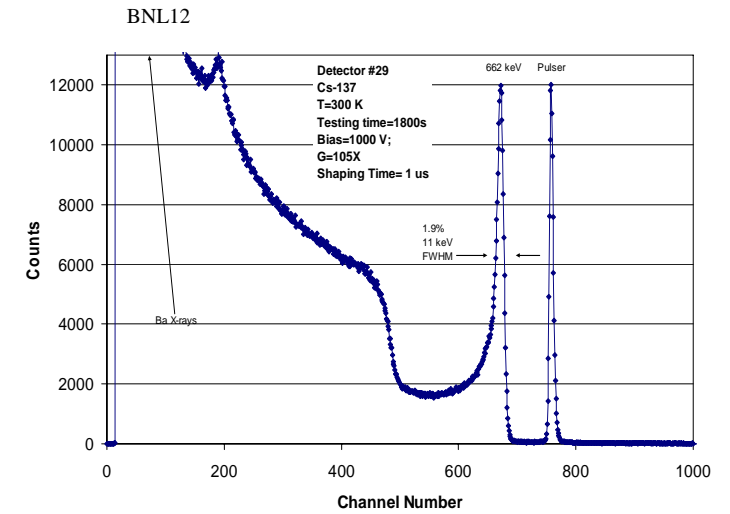
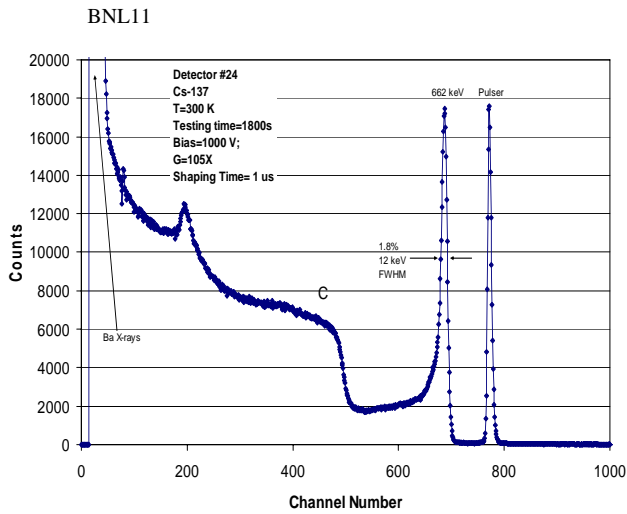
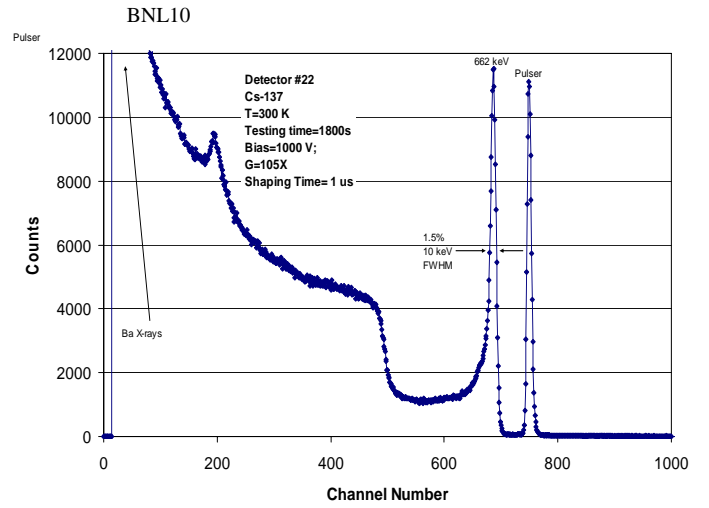
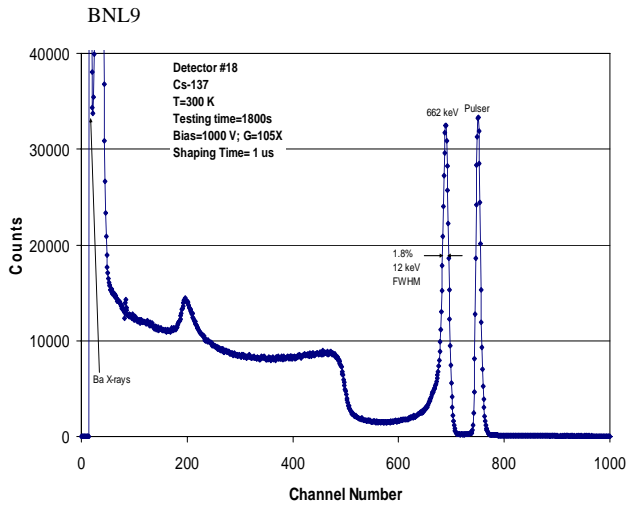
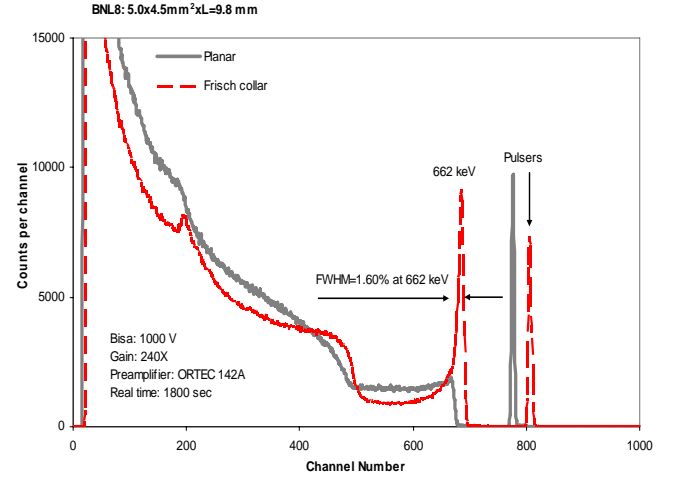
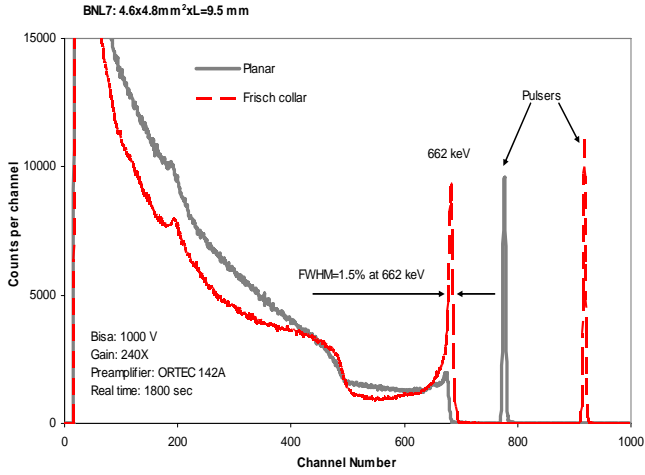
```
!BOTH ELECTRONS&HOLES
CCE(i)=CCE_e(i)+CCE_h(i) !double check the CCE of electrons
write(3,"('',1e12.4)") CCE(i)
end DO
!-----
end program EEwFrischHetchCZT
```

Appendix B

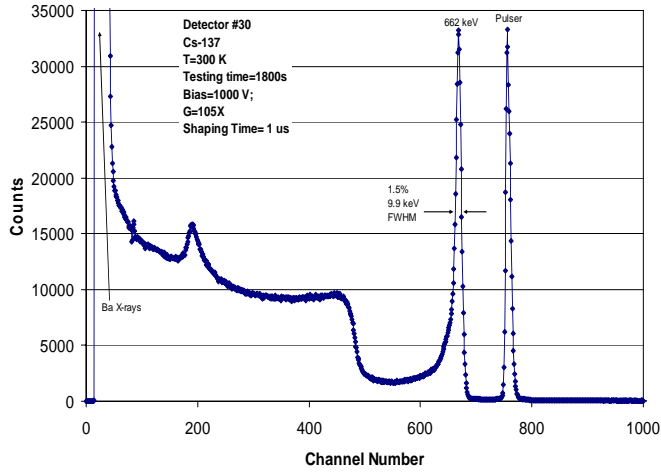
The CdZnTe Frisch Collar Detectors Fabricated at Kansas State University and Used in the Array of Detectors at Brookhaven National Laboratory

This Appendix contains the spectral results taken from a ^{137}Cs of the fabricated detectors at S.M.A.R.T. laboratory for the array of Frisch collar detectors. The array of detectors was assembled and tested at BNL as described in Section 4.5, and the results of the detector array tested with ^{137}Cs are presented in Section 5.6.

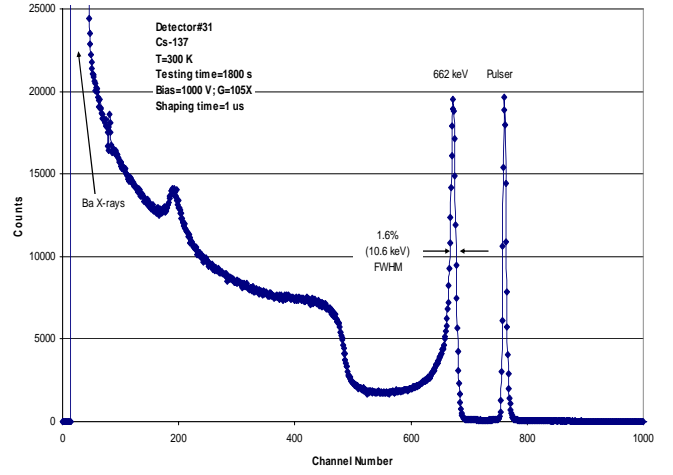




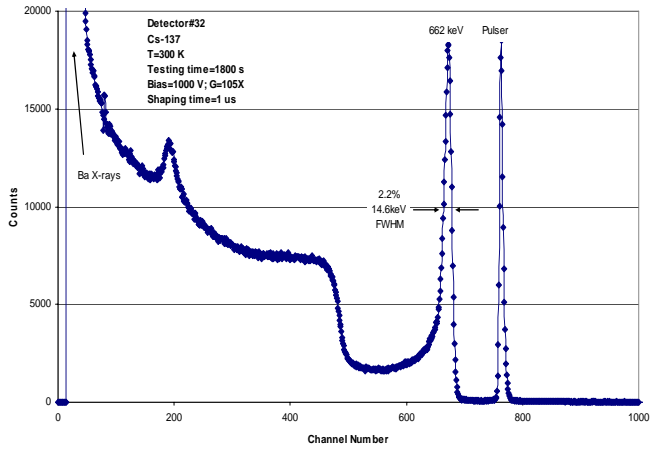
BNL13



BNL14



BNL15



BNL16

